Correlated Topological Responses In Dynamical Synthetic Quantum Matter

DISSERTATION ZUR ERLANGUNG DES
NATURWISSENSCHAFTLICHEN DOKTORGRADES
DER JULIUS-MAXIMILIANS-UNIVERSITÄT WÜRZBURG

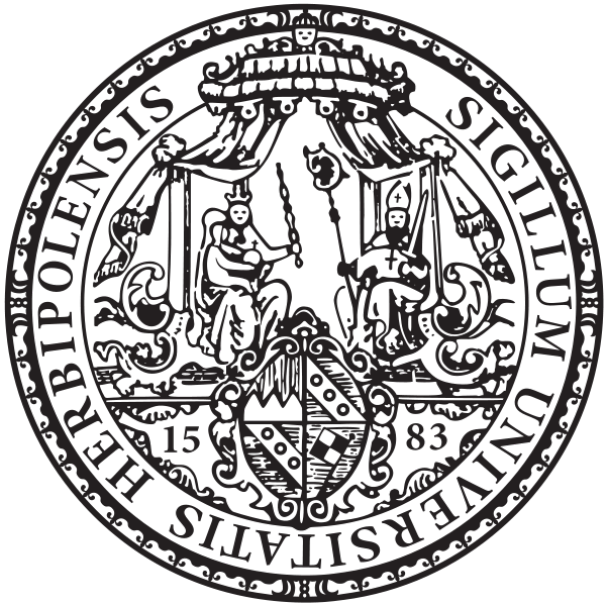

vorgelegt von

Simon Erhard Körber

aus Kitzingen

Würzburg 2022

Eingereicht am: .....

bei der Fakultät für Physik und Astronomie

1. Gutachter: Prof. Dr. Björn Trauzettel

2. Gutachter: Prof. Dr. Giorgio Sangiovanni

3. Gutachter: .....

der Dissertation

Vorsitzende(r): .....

1. Prüfer: Prof. Dr. Björn Trauzettel

2. Prüfer: Prof. Dr. Giorgio Sangiovanni

3. Prüfer: .....

im Promotionskolloquium

Tag des Promotionskolloquiums: .....

Doktorurkunde ausgehändigt am: .....

Zusammenfassung

In den letzten Jahren hat sich eine spannende Suche nach faszinierenden topologischen Phänomenen in zeitabhängigen Quantensystemen entwickelt. Ein Schlüssel zu zahlreichen Ausprägungen der Topologie in dynamischen Systemen beruht auf der effektiven Dimensionserweiterung durch zeitlich-periodische Antriebe. Ein Beispiel ist die Thouless-Pumpe in einer räumlichen Dimension, in der ein robuster und quantisierter Ladungstransport mittels eines Quanten-Hall-Effekts beschrieben werden kann, sofern Zeit als zusätzliche Dimension interpretiert wird. Durch Verallgemeinerung dieses Grundkonzepts auf Multifrequenzantriebe kann eine Vielzahl höherdimensionaler topologischer Modelle in zeitlich synthetischen Dimensionen konstruiert werden, bei denen die zugrunde liegende topologische Klassifikation zu quantisierten Pumpeffekten in den zugehörigen niederdimensionalen zeitabhängigen Systemen führt.

In dieser Dissertation wird untersucht, wie Korrelationen die topologischen Eigenschaften von zeitlich synthetischen Quantenmaterialen maßgeblich beeinflussen. Konkret wird gezeigt, dass das Zusammenspiel von Wechselwirkung und zeitlicher synthetischer Dimension zu erstaunlichen topologischen Phänomenen führt, die über nichtwechselwirkende Realisierungen hinausgehen. Als Ausgangspunkt wird das Floquet-Gegenstück eines Quanten-Hall-Szenarios genutzt, ein Zwei-Niveau-System, das von zwei inkommensurablen Frequenzen getrieben wird. In diesem Modell spiegelt sich die topologisch quantisierte Antwort in einen Prozess wider, bei dem Photonen verschiedener Frequenzen zwischen den externen Moden ausgetauscht werden, auch bekannt als topologische Frequenzumwandlung. Wir erweitern dieses prototypische Setup auf eine interagierende Version, indem wir uns auf den Minimalfall zweier korrelierter Spins konzentrieren, die gleichermaßen den externen Antrieben ausgesetzt sind. Wir zeigen, dass die topologische Invariante, die die Frequenzumwandlung bestimmt, durch ungerade ganze Zahlen verändert werden kann. Ein Zustand, der im nicht-wechselwirkenden Fall ausdrücklich verboten ist. Dieses korrelierte topologische Verhalten kann wiederum zu einer Verstärkung der quantisierten Antwort führen.

Robuste Antwortsignale, wie sie für den topologischen Frequenzumwandler vorhergesagt werden, sind von grundlegendem Interesse für potentielle technologische Anwendungen der topologischen Quantenmaterie. Basierend auf einer offenen Quantensystem-Realisierung des Frequenzumwandlers schlagen wir einen neuartigen Mechanismus der topologischen Quantisierung vor, den wir als "topologischen Brennglaseffekt" bezeichnen. Dieser Mechanismus verstärkt die lokale Antwort des getriebenen Zwei-Niveau-Systems um eine ganze Zahl, die proportional zur Anzahl der Freiheitsgrade der Umgebung ist, an die das System koppelt. Konkret werden unsere Erkenntnisse durch die Erweiterung des Frequenzumwandlers auf ein Zentralspinmodell veranschaulicht. Der lokale Energietransfer, der ausschließlich durch den zentralen Spin vermittelt wird, wird durch die kollektive Bewegung der umgebenden Spins maßgeblich verstärkt. In diesem Sinne erbt der Zentralspin die topologische Natur des Gesamtsystems in seiner nicht-unitären Dynamik, die die Korrelationen mit der Umgebung berücksichtigt.

Abstract

The last years have witnessed an exciting scientific quest for intriguing topological phenomena in time-dependent quantum systems. A key to many manifestations of topology in dynamical systems relies on the effective dimensional extension by time-periodic drives. An archetypal example is provided by the Thouless pump in one spatial dimension, where a robust and quantized charge transport can be described in terms of an integer quantum Hall effect upon interpreting time as an extra dimension. Generalizing this fundamental concept to multifrequency driving, a variety of higher-dimensional topological models can be engineered in dynamical synthetic dimensions, where the underlying topological classification leads to quantized pumping effects in the associated lower-dimensional time-dependent systems.

In this Thesis, we explore how correlations profoundly impact the topological features of dynamical synthetic quantum materials. More precisely, we demonstrate that the interplay of interaction and dynamical synthetic dimension gives rise to striking topological phenomena that go beyond noninteracting implementations. As a starting point, we exploit the Floquet counterpart of an integer quantum Hall scenario, namely a two-level system driven by two incommensurate frequencies. In this model, the topologically quantized response translates into a process in which photons of different frequencies are exchanged between the external modes, referred to as topological frequency conversion. We extend this prototypical setup to an interacting version, focusing on the minimal case of two correlated spins equally exposed to the external drives. We show that the topological invariant determining the frequency conversion can be changed by odd integers, something explicitly forbidden in the noninteracting limit of two identical spins. This correlated topological feature may, in turn, result in an enhancement of the quantized response.

Robust response signals, such as those predicted for the topological frequency converter, are of fundamental interest for potential technological applications of topological quantum matter. Based on an open quantum system implementation of the frequency converter, we propose a novel mechanism of topological quantization coined "topological burning glass effect". Remarkably, this mechanism amplifies the local response of the driven two-level system by an integer that is proportional to the number of environmental degrees of freedom to which the system is strongly coupled. Specifically, our findings are illustrated by the extension of the frequency converter to a central spin model. There, the local energy transfer mediated exclusively by the central spin is significantly enhanced by the collective motion of the surrounding spins. In this sense, the central spin adopts the topological nature of the total system in its non-unitary dynamics, taking into account the correlations with the environment.

Contents

1

Introduction

When asked what the difference is between the shape[1] of a ball (sphere) and a doughnut (torus), a child might answer that the doughnut, unlike the ball, has a hole. And although the child's answer may seem trivial at first glance, it reveals with remarkable acuity an essential geometrical discrepancy between these two objects. In fact, it is the hole that makes it impossible to transform the doughnut into a ball without irreversibly breaking its surface. Or in other words, the doughnut will never turn into a ball under continuous deformations, such as those occurring when its body is stretched, compressed, twisted, or bent. Rather, the hole has to be closed, e.g. by cutting the doughnut with a knife, before a continuous deformation into the ball can take place. In mathematics, such classification is treated within the concept of topology, in which geometrical objects are distinguished by topological invariants that are preserved under continuous deformations. In this sense, the ball and the doughnut exhibit a distinct topology, as both can be assigned a topological invariant that differs in the number of holes. On the other hand, a coffee cup and a doughnut are identical from a topological point of view, as they can be continuously deformed into each other without opening or closing a hole.

The preceding, rather pedagogical discussion raises the question whether topology offers practical applications beyond its purely mathematical formulation [Wil70, Mun00]. Here, it turns out that the solutions to many geometrical problems do not rely on the exact shape, but solely on the topological properties of the objects. Already in the early 18th century, Leonhard Euler applied the idea of topology in his discussion of the Seven Bridges of Königsberg [Eul36, Cro89]. There, four islands are ergodically connected[2] by a total number of seven bridges, with one of the islands accessible by five bridges and the remaining three by three bridges each. As each island carries an odd number of connections, Euler concluded that it is impossible to take a continuous trip

[1] In what follows, we only refer to the geometry of objects and not to their material properties, assuming that their bodies are fully pliable under mechanical action.

[2] Here, "ergodically connected" means that each island can be reached from any position on the map. This, however, does not necessarily require that the islands are directly connected to each other.

through the city of Königsberg that passes each of its seven bridges only once. This follows directly from the fact that at most two of the islands are allowed to show an odd number of bridges, as this is the maximum number of islands that can serve as the start and end points of the walk. The remaining islands, in turn, must show an even number of connections, such that they can be left on a novel path. Indeed, these arguments are topological in nature, as they do not depend on the explicit shape of the islands or the position and length of the bridges, but only on the information of how the islands are connected to each other.

Besides this historical problem, another quite modern application of topology is given by topological band theory in the context of solid state physics [CF21]. Here, the properties of electrons in a lattice-periodic potential are determined by Bloch's theorem [Blo29, Kit71, AM76], which provides the single-electron solutions of the Schrödinger equation as a function of crystal momentum. These so-called Bloch electrons form an electronic band structure in momentum space, which may result in energy bands that are well separated from each other by finite band gaps. Now, it has been figured out that Bloch electrons can assume geometrical features as well, assigning topological invariants to the respective energy bands that are preserved under continuous[3] deformations [XCN10, Van18]. This invariance, in turn, leads to robust response signals, paving the way for fascinating phenomena in physics [Tho98, Wen17]. A paradigmatic example in this context is provided by the integer quantum Hall effect [KDP80, PG90], where the transverse conductance of a two-dimensional system consists with high accuracy of integer multiples of natural constants. According to the celebrated Kubo formula [Kub57, Mah00], this quantized response originates from the first perturbative correction of the state, which in fact can be projected onto the first Chern number [Che46, TKNdN82, QHZ08], an invariant defined in terms of the adiabatic Berry curvature [Ber84] of the occupied Bloch bands [Lau81, Sim83a, Koh85, Hal88].

Inspired by this cornerstone of modern physics, a wide range of exciting topological platforms have been explored, such as topological insulators [KBWM$^+$08, QZ10, Moo10, HK10], topological superconductors [QZ11, BH13], and topological semimetals [Vol03, YF17, AMV18]. Besides these condensed matter realizations, however, recent advances in the fabrication and manipulation of topological phases in photonics [LJS14, KS17, OPA$^+$19], ultracold atomic gases [DGJbuO11, GJÖS14, GBZ16, CDS19], and Floquet insulators [CDSM13, OK19, RL20a] have triggered the quest for identifying and observing novel topological physics in synthetic dimensions [OP19]. The innovative idea behind this approach is to extend the dimensionality of a system by interpreting some of its internal degrees of freedom as an extra dimension, while controlling the motion within the synthetic direction by suitable external drives. In this sense, synthetic dimensions provide a powerful tool for the realization of exotic topological phenomena, some of which involve the simulation of higher-dimensional topological models in experimental settings of lower spatial dimensionality [PZO$^+$15, OPG$^+$16, OP19]. An archetypal example of this kind is provided by the Thouless pump [Tho83], in which a periodically driven one-dimensional system is mapped onto a two-dimensional integer quantum Hall

[3]Here, "continuous" means that the band gap remains finite during the deformation of the quantum state.

scenario upon interpreting time as an extra dimension. In this setting, the higher-dimensional topology manifests itself in a robust and quantized charge pump in the lower-dimensional time-dependent system, yielding exciting signatures that have been experimentally identified in both ultracold atomic gases [LSZ+16, NTT+16, LSP+18] and photonic systems [KLR+12, KRZ13, ZHG+18].

In the Thouless pump, the dimensional extension of the system originates from periodic driving in time, as the quantum state is dressed by all harmonics of the driving frequency. Generalizing this fundamental concept to multifrequency drives, dynamical modulations offer a highly controllable and flexible design of synthetic topological models, as the harmonics of each incommensurate driving frequency can be viewed as lattice sites along different synthetic spatial dimensions [HCT83, CT04, EA15, VPM16]. Along these lines, Martin *et al.* [MRH17] have demonstrated that quasiperiodically driven quantum systems constitute an illustrative realization of dynamical synthetic quantum matter, in which the topological features are exclusively defined in dimensions of time. Their prototypical example is given by a *topological frequency converter* (TFC), namely a single spin-1/2 driven by two circularly polarized drives, allowing the formation of a Floquet counterpart of a Chern insulator [Hal88, QWZ06, BHZ06]. There, the topologically quantized response translates into a frequency conversion between the classical modes, with a time-averaged pumping rate proportional to the Chern number classifying the synthetic Hall regime. Triggered by this pioneering work, a number of advanced discoveries have been made in this field [KNG+18, PR18, CMC19, NMR19, CMC20, CLY+20, NRRM20, LCC21, NGG+21, PR21, QRP21, SYZ22], some of which even involve the indirect measurement of the topological frequency conversion [BCCS20, MS21]. The understanding of the consequences of interparticle interactions in these dynamical settings, however, is rather limited. This Thesis is dedicated to the discovery of new insights on this field.

To this end, we extend the notion of topologically quantized frequency conversion to interacting spin systems. In doing so, we show that correlations can dramatically broaden the spectrum of topological numbers in the dynamically-induced synthetic dimensions, eventually leading to the occurrence of topological responses that are forbidden in the noninteracting regime. This feature, in turn, can improve the efficiency of the frequency conversion, as the energy transfer between the external drives gets significantly enhanced. Our findings are illustrated by two concrete and experimentally feasible settings. The first model, which we refer to as an *interacting topological frequency converter* (ITFC), represents the simplest extension of a TFC, namely two interacting spins equally exposed to two incommensurate periodic drives [KPBT20]. Despite its simplicity, this setup already provides a suitable platform for the generation of the aforementioned correlated topological phenomena. For example, while in an uncorrelated system of two identical spins the topological invariant determining the frequency conversion must be even, in the ITFC odd integers are also allowed. We then generalize these intriguing features to many spins, focusing on an open quantum system realization of the TFC in the framework of a *central spin model* (CSM) [Gau76, DPS04, CDBF19]. In this model, a central spin driven by two incommensurate frequencies statically couples to a set of surrounding spins [KPBT22]. We show that the local energy transfer is exclusively mediated by the driven central spin, exhibiting a topological quantization that is

enhanced by the collective motion of the environmental spins. As a consequence, the adiabatically defined topological invariant of the central spin fails to predict the local response signal, but is rather governed by the topology of the total system. We explain this novel mechanism of topological quantization, which we denote as *topological burning glass effect* (TBGE), by investigating the non-unitary dynamics of the (small) quantum system, revealing that the latter adopts the topological nature of the total system due to its correlations to the (larger) environment. We argue that the amplification of the TBGE not only exemplifies a general principle of topological open quantum systems, but could moreover be exploited for the direct experimental observation of the topological frequency conversion, which to our knowledge has so far only been detected indirectly [SKK$^+$14, RNC$^+$14, BCCS20, MS21].

The Thesis is organized as follows: In Chap. 2, we introduce the notion of dynamical synthetic quantum matter using fundamental concepts such as *adiabatic perturbation theory* (APT) [ROP08, WBD$^+$17] and (generalized) Floquet theory [Flo83, Shi65, Sam73]. Starting from the dynamics of a generic quantum system that temporally evolves in parameter space, we show that the first perturbative expansion around the adiabatic limit leads to a physical response proportional to the Berry curvature of the adiabatic energy band [GP12]. Based on this geometrical property, quasiperiodically driven quantum systems provide an illustrative platform for dynamical topological phenomena, where the quantized response manifests itself in a frequency conversion between the external drives. In Chap. 3, we apply these generic features to the concrete example of the TFC, demonstrating that the response signal of the driven spin is described by its adiabatically defined winding number [Vol03, QWZ06, QHZ08]. We extend this prototypical model to its simplest interacting generalization, the ITFC, and interpret the correlated topological responses by means of analytical and numerical calculations. In Chap. 4, we study the TBGE using the paradigmatic example of the quasiperiodically driven CSM, the latter motivated by experimental realizations in lateral *quantum dots* (QDs) [KAT01, HKP$^+$07, RT10, ZDM$^+$13, CSDF$^+$21] or *nitrogen-vacancy* (NV) centers [JW06, DMD$^+$13, SCLD14]. We derive the topological band structure of the CSM, demonstrating that the TBGE is a generic phenomenon that also applies to generalizations of the interacting spin system. Using numerically exact simulations, we corroborate our analytical findings and investigate the nonequilibrium phase diagrams of the CSM, revealing that the topological frequency conversion can even extend to a strongly nonadiabatic situation. This analysis allows us to identify the transient dynamics and fundamental time-scales of (pre)thermalization, showing that the nonadiabatic breakdown of the TBGE can lead to an ensemble-averaged pumping rate identical to the noninteracting regime. In Chap. 5, we conclude our results and provide an outlook for future studies. Throughout the Thesis, we set $\hbar = 1$.

2

Dynamical Synthetic Quantum Matter

Contents

Since its discovery, the Berry phase has been proven to have a crucial and intriguing impact on the electronic transport properties of solid-state quantum devices [XCN10, Van18, CF21]. This observation can be traced back to the semiclassical formulation of electron dynamics in a periodic lattice [CN95, CN96, SN99], involving the first perturbative correction of the state due to a small external field. The latter induces virtual couplings between the Bloch energy bands of the crystal [Blo29, Kit71, AM76], resulting in a transverse response proportional to the adiabatic Berry curvature [Ber84] of the occupied Bloch state. Integrating this local geometrical quantity over the closed manifold of the *Brillouin zone* (BZ), this accounts for a variety of topological response signals, such as those predicted in quantum Hall effects, quantum charge pumps, or in the modern description of electric polarization [BMK$^+$03, XCN10, Van18].

In this introductory chapter, we exploit the semiclassical approach to illustrate that quasiperiodically driven quantum systems reveal a Floquet counterpart of an integer quantum Hall scenario [MRH17]. There, the quasiperiodic dynamics can be mapped onto a higher-dimensional Floquet lattice, with lattice sites corresponding to the Fourier harmonics of the incommensurate driving frequencies [HCT83, CT04, EA15, VPM16]. Applying the semiclassical equations of motion to the Floquet lattice, this yields an anomalous response that translates into a frequency conversion between the external drives. Simultaneously, the synthetic BZ of the Floquet lattice is entirely covered during the quasiperiodic time-evolution, resulting in a quantized response that is determined by the global topological invariant of the associated synthetic energy band. We argue that the Floquet picture provides an illustrative implementation of basic geometrical concepts of dynamical synthetic quantum matter, the latter corresponding to a generic quantum system temporally evolving in parameter space and described by means of *adiabatic perturbation theory* (APT) [ROP08, WBD$^+$17]. In fact, analogous to the semiclassical formulation, the motion in an individual direction of the parameter space leads to virtual transitions to the excited states of the instantaneous spectrum, which can eventually be mapped to the Berry curvature of the adiabatic energy band [GP12]. In the concrete setting of time-quasiperiodic drives, the parameter space of the generic quantum system is discovered in the same way as the synthetic BZ of the higher-dimensional Floquet lattice, revealing a topological response equivalent to the Floquet picture.

The Chapter is organized as follows: In Sec. 2.1, we solve the quantum dynamics in parameter space using APT, showing that the geometrical response stems from the first-order corrections of the state around the adiabatic limit. In Sec. 2.2, we apply Floquet theory [Flo83, Shi65, Sam73] to periodically driven quantum systems, providing the basis for our generalization to multifrequency drives. The latter is done in Sec. 2.3, demonstrating that both the semiclassical formulation and APT yield the same topological response of the quasiperiodically driven quantum system. We argue that this observation reflects a fundamental concept of topological quantization, where linear response properties such as the (synthetic) Hall conductance are generally described by a first perturbative correction of the state due to an electric field [Kub57, Mah00]. These corrections, however, can eventually be understood in terms of the adiabatic Berry curvature of the unperturbed state alone [Lau81, TKNdN82, Sim83a, Koh85, Hal88], revealing a correspondence between adiabatically defined topological invariants and quantized response signals.

2.1 Quantum Dynamics in Parameter Space

We consider the dynamics of a generic quantum system that depends on a set of control parameters temporally evolving in parameter space. Assuming that the rate of change of these parameters is sufficiently slow, it follows from the adiabatic theorem that the quantum state remains in the instantaneous energy band to which it has been initialized [BF28, Kat50, Mes62]. Using APT [ROP08, WBD$^+$17], we demonstrate that the first-order corrections around the adiabatic limit yield virtual transitions to the excited states of the spectrum, eventually leading to a geometrical response proportional to the Berry curvature of the adiabatic energy band [GP12]. We argue that these Berry phase effects [Ber84, XCN10] reflect fundamental concepts, which apply to any system that exhibits energetically separated energy bands in its spectrum and evolves sufficiently slowly in time.

2.1.1 General Setting

We study a generic quantum system whose Hamiltonian $\hat{H}(\vec{R}_t)$ depends on a set of control parameters $\vec{R}_t = (R_{1,t},\, R_{2,t},\, \ldots,\, R_{D,t})^T$ temporally evolving in the $D-$dimensional parameter space $\vec{R}_t \in \mathbb{R}^D$. The dynamics of this system is governed by the time-dependent Schrödinger equation [Sch26, Sha08, GS18]

$$\mathrm{i}\,\frac{\mathrm{d}}{\mathrm{d}t}\,|\Psi(t)\rangle = \hat{H}(\vec{R}_t)\,|\Psi(t)\rangle\,, \tag{2.1}$$

which induces a unitary time-evolution of the quantum state $|\Psi(t)\rangle$. Given an arbitrary time-dependence $\vec{R}_t$, the dynamics of Eq. (2.1) is generally hard to solve, which is why it is often convenient to examine the spectral properties of the Hamiltonian $\hat{H}(\vec{R}_t)$:

$$\hat{H}(\vec{R}_t)\;|n(\vec{R}_t)\rangle = E_n(\vec{R}_t)\;|n(\vec{R}_t)\rangle\,. \tag{2.2}$$

At any instant, Eq. (2.2) corresponds to an eigenvalue problem with eigenstates $|n(\vec{R}_t)\rangle$ and energy eigenvalues $E_n(\vec{R}_t)$, the latter forming a synthetic band structure along the trajectory $\vec{R}_t$ in parameter space. For simplicity, we assume that the energy levels $E_n(\vec{R}_t)$ are discrete and nondegenerate, resulting in a well-defined[1] orthonormal set of basis states $\{|n(\vec{R}_t)\rangle\}_n$. The exact quantum state $|\Psi(t)\rangle$ can be expressed as

$$|\Psi(t)\rangle = \sum_n \mathrm{e}^{-\mathrm{i}\,\lambda_n(t)}\,b_n(t)\;|n(\vec{R}_t)\rangle\,, \tag{2.3}$$

where we have introduced the dynamical phase factor $\lambda_n(t) = \int_{t_0}^{t} \mathrm{d}t'\, E_n(\vec{R}_{t'})$ and the time-dependent coefficients $b_n(t)$. Based on this ansatz, we have to determine the coefficients $b_n(t)$, which contain the essential information about the dynamics of the quantum state $|\Psi(t)\rangle$. Inserting Eq. (2.3) into Eq. (2.1), the time-dependent Schrödinger equation can be transferred to a differential equation for the coefficients $b_n(t)$:

$$\dot{b}_n(t) = -b_n(t)\,\mathcal{M}_{nn}(\vec{R}_t) - \sum_{m\neq n} \mathrm{e}^{\mathrm{i}\,\lambda_{nm}(t)}\,b_m(t)\,\mathcal{M}_{nm}(\vec{R}_t), \tag{2.4}$$

[1] Apart from an overall phase factor, which we discuss in Eq. (2.6).

where we have used the shorthand notations $\dot{b}_n(t) = \frac{\mathrm{d}}{\mathrm{d}t}\, b_n(t)$ and $\lambda_{nm}(t) = \lambda_n(t) - \lambda_m(t)$. The challenge in solving Eq. (2.4) for arbitrary time-dependencies $\vec{R}_t$ comes from the fact that the coefficients $b_n(t)$ are connected by nontrivial coupling terms

$$\mathcal{M}_{nm}(\vec{R}_t) = \langle n(\vec{R}_t)|\frac{\mathrm{d}}{\mathrm{d}t}\, m(\vec{R}_t)\rangle = \dot{\vec{R}}_t\ \langle n(\vec{R}_t)|\nabla_{\vec{R}}\, m(\vec{R}_t)\rangle\,, \tag{2.5}$$

composed of the rate of change of the control parameters $\dot{\vec{R}}_t$ and the overlaps between the instantaneous eigenstates $|n(\vec{R}_t)\rangle$ and their derivatives $|\nabla_{\vec{R}}\, m(\vec{R}_t)\rangle$. Formally, the latter is only well-defined for a single-valued set of basis states $\{|n(\vec{R}_t)\rangle\}_n$, with a gauge degree of freedom

$$|n(\vec{R}_t)\rangle \mapsto \mathrm{e}^{\mathrm{i}\,\chi_n(\vec{R}_t)}\ |n(\vec{R}_t)\rangle \tag{2.6}$$

that features a smooth and differentiable phase factor $\chi_n(\vec{R}_t)$. For our derivations, however, this explicit choice is not mandatory, which manifests itself in gauge-invariant quantities that apply to any solution of Eq. (2.2).

So far, we have made no assumption about the initial condition of the differential equation (2.4). Throughout the Thesis, we suppose that the quantum state $|\Psi(t)\rangle$ is initialized in an instantaneous eigenstate $|m(\vec{R}_{t_0})\rangle$, reflected by coefficients $b_n(t_0) = \delta_{nm}$. In this case, our results work whenever the energy band $E_m(\vec{R}_t)$ is energetically separated from the other bands, yielding a less restrictive condition for Eq. (2.2). In fact, energy bands $E_{n\neq m}(\vec{R}_t)$ can pass through level crossings in the excited part of the spectrum, which is why degeneracies are explicitly allowed for these bands.

2.1.2 Adiabatic Limit

The main idea of the quantum adiabatic limit is to omit the second expression of Eq. (2.4), thus neglecting the off-diagonal coupling terms $\mathcal{M}_{nm}(\vec{R}_t)$ between the coefficients $b_n(t)$ [BF28]. Introducing the real phase factor[2]

$$\xi_n(t) = \mathrm{i}\int_{t_0}^{t} \mathrm{d}t'\, \mathcal{M}_{nn}(\vec{R}_{t'}) = \mathrm{i}\int_{\mathcal{C}_{t_0}^{t}} \mathrm{d}\vec{R}\ \langle n(\vec{R})|\nabla_{\vec{R}}\, n(\vec{R})\rangle\,, \tag{2.7}$$

the differential equation $\dot{b}_n(t) = -b_n(t)\,\mathcal{M}_{nn}(\vec{R}_t)$ can be solved as

$$b_n(t) = b_n(t_0)\,\mathrm{e}^{\mathrm{i}\,\xi_n(t)} = \delta_{nm}\,\mathrm{e}^{\mathrm{i}\,\xi_n(t)}. \tag{2.8}$$

We have used the initial condition $b_n(t_0) = \delta_{nm}$, and defined the path $\mathcal{C}_{t_0}^{t}$ that is sampled during the time-evolution of $\vec{R}_t$ in parameter space. Inserting Eq. (2.8) into Eq. (2.3), this yields the state vector of the quantum adiabatic limit [BF28, Kat50, Mes62]

$$|\Psi_m^{\mathrm{ad}}(t)\rangle = \mathrm{e}^{\mathrm{i}\,\gamma_m(t)}\ |m(\vec{R}_t)\rangle\,, \tag{2.9}$$

[2] Since $\mathcal{M}_{nm}(\vec{R}_t) = -\mathcal{M}^*_{mn}(\vec{R}_t)$, the diagonal terms $\mathcal{M}_{nn}(\vec{R}_t)$ of Eq. (2.5) are purely imaginary numbers. The phase factor $\xi_n(t)$ is thus real. We have used that $\langle\nabla_{\vec{R}}\, n(\vec{R}_t)|m(\vec{R}_t)\rangle + \langle n(\vec{R}_t)|\nabla_{\vec{R}}\, m(\vec{R}_t)\rangle = \nabla_{\vec{R}}\,\langle n(\vec{R}_t)|m(\vec{R}_t)\rangle = \nabla_{\vec{R}}\,\delta_{nm} = 0$.

with the phase factor $\gamma_m(t) = \xi_m(t) - \lambda_m(t)$. Eq. (2.9) states that the system remains in the energy band $E_m(\vec{R}_t)$ to which it has been initialized, as at each instant the quantum state $|\Psi_m^{\mathrm{ad}}(t)\rangle$ is proportional to the instantaneous eigenstate $|m(\vec{R}_t)\rangle$.

The adiabatic limit of Eq. (2.8) is based on the assumption that couplings to neighboring states of the instantaneous spectrum are completely suppressed, which is approximately satisfied under two conditions: (*i*) the time-dependence of the Hamiltonian $\hat{H}(\vec{R}_t)$ is made sufficiently slow, (*ii*) the quantum state $|\Psi(t)\rangle$ is initialized in an energy band $E_m(\vec{R}_t)$ that is energetically separated from the other bands $E_{n\neq m}(\vec{R}_t)$. We corroborate these statements by rewriting the off-diagonal coupling terms $\mathcal{M}_{nm}(\vec{R}_t)$ of Eq. (2.5) as

$$\mathcal{M}_{nm}(\vec{R}_t) = -\frac{\dot{\vec{R}}_t}{\Delta_{nm}(\vec{R}_t)}\ \langle n(\vec{R}_t)|\Big(\nabla_{\vec{R}}\,\hat{H}(\vec{R}_t)\Big)|m(\vec{R}_t)\rangle\,, \tag{2.10}$$

showing that transitions to neighboring energy bands are associated with a finite energy gap $\Delta_{nm}(\vec{R}_t) = E_n(\vec{R}_t) - E_m(\vec{R}_t)$. If the rate of change of the control parameters $|\dot{\vec{R}}_t| \ll \Delta_{nm}(\vec{R}_t)$ is sufficiently small, the excitation energy required to overcome this gap is not reached, which is why the system remains in the instantaneous eigenstate $|m(\vec{R}_t)\rangle$. We have derived Eq. (2.10) applying the identity

$$\langle n(\vec{R}_t)|\Big(\nabla_{\vec{R}}\,\hat{H}(\vec{R}_t)\Big)|m(\vec{R}_t)\rangle = \nabla_{\vec{R}}\,E_n(\vec{R}_t)\,\delta_{nm} - \Delta_{nm}(\vec{R}_t)\ \langle n(\vec{R}_t)|\nabla_{\vec{R}}\,m(\vec{R}_t)\rangle\,, \tag{2.11}$$

in which we have used that $\mathcal{M}_{nm}(\vec{R}_t) = -\mathcal{M}^*_{mn}(\vec{R}_t)$.

In addition to the dynamical phase factor $\lambda_n(t)$, the adiabatic quantum state $|\Psi_m^{\mathrm{ad}}(t)\rangle$ exhibits a phase factor $\xi_n(\mathcal{C}^t_{t_0}) \equiv \xi_n(t)$ that only depends on the geometrical properties of the path $\mathcal{C}^t_{t_0}$ in parameter space. The representation $\xi_n(\mathcal{C}^t_{t_0})$ manifests itself in the line integral of Eq. (2.7), which reveals a geometrical phase factor that transforms as

$$\xi_n(\mathcal{C}^t_{t_0}) \mapsto \xi_n(\mathcal{C}^t_{t_0}) + \chi_n(\vec{R}_{t_0}) - \chi_n(\vec{R}_t) \tag{2.12}$$

when applied to the gauge transformation of Eq. (2.6). Due to the gauge dependence of Eq. (2.12), it has been assumed that the geometrical phase $\mathrm{e}^{\mathrm{i}\,\xi_n(\mathcal{C}^t_{t_0})}$ can never be physically measured, as its phase factor $\xi_n(\mathcal{C}^t_{t_0})$ can be canceled out by a suitable choice of $\chi_n(\vec{R}_t)$ [BF28, Foc28]. This assumption, however, does not apply to a cyclic evolution around a closed path $\mathcal{C}^T_{t_0}$ with $\vec{R}_{t_0} = \vec{R}_T$, where the adiabatic quantum state $|\Psi_m^{\mathrm{ad}}(t)\rangle$ acquires a gauge-invariant Berry phase $\mathrm{e}^{\mathrm{i}\,\xi_n^{\mathrm{B}}(\mathcal{C}^T_{t_0})}$ with phase factor [Ber84]

$$\xi_n^{\mathrm{B}}(\mathcal{C}^T_{t_0}) = \mathrm{i}\oint_{\mathcal{C}^T_{t_0}} \mathrm{d}\vec{R}\ \langle n(\vec{R})|\nabla_{\vec{R}}\,n(\vec{R})\rangle\,. \tag{2.13}$$

In fact, assuming a single-valued set of basis states $\{|n(\vec{R}_t)\rangle\}_n$, the condition $\vec{R}_{t_0} = \vec{R}_T$ implies that (cf. Eq. (2.6))

$$\chi_n(\vec{R}_{t_0}) - \chi_n(\vec{R}_T) = 2\pi n, \quad n \in \mathbb{Z},$$

indicating that Eq. (2.13) can be only changed by an integer multiple of 2π (cf. Eq. (2.12)). As a result, the Berry phase $\mathrm{e}^{\mathrm{i}\,\xi_n^{\mathrm{B}}(\mathcal{C}^T_{t_0})}$ becomes a gauge-invariant physical quantity, with observable consequences that have received considerable attention in all fields of physics [Res00, XCN10].

2.1.3 Adiabatic Perturbation Theory

Assuming that the time-evolution of the system proceeds insufficiently slow, the quantum adiabatic theorem no longer applies. In this case, the differential equation (2.4) does not simplify to a diagonal form, but can be perturbatively solved using APT [ROP08, WBD+17]. The latter yields solutions $b_n(t)$ expanded in the rate of change of the control parameters $\dot{\vec{R}}_t$, with a zeroth-order term corresponding to the adiabatic limit in which the dynamics is confined to the initialized energy band $E_m(\vec{R}_t)$. Off-diagonal coupling terms $\mathcal{M}_{nm}(\vec{R}_t)$ (see Eq. (2.10)) between neighboring energy bands $E_{n\neq m}(\vec{R}_t)$ are accounted for by higher orders of the perturbative approach, resulting in corrections to Eq. (2.9) that explicitly involve overlaps with excited states of the instantaneous spectrum. We show that these transitions already appear in first-order APT, demonstrating that the latter provides a powerful tool to systematically go beyond the adiabatic limit.

We start our derivation by introducing a unitary operation[3] $\hat{V}(\vec{R}_t)$ that transforms the instantaneous eigenstates $|n(\vec{R}_t)\rangle$ of Eq. (2.2) into a set of $\vec{R}_t$-independent basis states $\{|e_n\rangle\}_n$:

$$|n(\vec{R}_t)\rangle = \hat{V}(\vec{R}_t)\,|e_n\rangle\,. \tag{2.14}$$

Eq (2.14) defines a basis transformation in which the transformed Hamiltonian $\hat{H}'(\vec{R}_t) = \hat{V}^\dagger(\vec{R}_t)\hat{H}(\vec{R}_t)\hat{V}(\vec{R}_t)$ obtains diagonal matrix elements

$$\langle e_n|\hat{H}'(\vec{R}_t)|e_m\rangle = \langle e_n|\hat{V}^\dagger(\vec{R}_t)\hat{H}(\vec{R}_t)\hat{V}(\vec{R}_t)|e_m\rangle = \langle n(\vec{R}_t)|\hat{H}(\vec{R}_t)|m(\vec{R}_t)\rangle = E_n(\vec{R}_t)\,\delta_{nm} \tag{2.15}$$

that correspond to the energy eigenvalues $E_n(\vec{R}_t)$ of Eq. (2.2). Applying the unitary transformation to the time-dependent Schrödinger equation (2.1), the exact solution $|\Psi(t)\rangle$ can be transformed to a rotated state vector $|\Psi_{\mathrm{rot}}(t)\rangle = \hat{V}^\dagger(\vec{R}_t)\,|\Psi(t)\rangle$, whose dynamics

$$\mathrm{i}\,\frac{\mathrm{d}}{\mathrm{d}t}\,|\Psi_{\mathrm{rot}}(t)\rangle = \hat{H}_{\mathrm{rot}}(\vec{R}_t)\,|\Psi_{\mathrm{rot}}(t)\rangle \tag{2.16}$$

is governed by the rotated-frame Hamiltonian $\hat{H}_{\mathrm{rot}}(\vec{R}_t) = \hat{H}'(\vec{R}_t) + \hat{\mathcal{A}}(\vec{R}_t)$. We have introduced the Hermitian operator[4] $\hat{\mathcal{A}}(\vec{R}_t) = -\mathrm{i}\,\dot{\vec{R}}_t\,\hat{V}^\dagger(\vec{R}_t)\,[\nabla_{\vec{R}}\hat{V}(\vec{R}_t)]$, which accounts for the overlaps between neighboring basis states in terms of matrix elements

$$\begin{aligned}\langle e_n|\hat{\mathcal{A}}(\vec{R}_t)|e_m\rangle = -\mathrm{i}\,\dot{\vec{R}}_t\;\langle e_n|\hat{V}^\dagger(\vec{R}_t)\left(\nabla_{\vec{R}}\hat{V}(\vec{R}_t)\right)|e_m\rangle = \\ = -\mathrm{i}\,\dot{\vec{R}}_t\;\langle n(\vec{R}_t)|\nabla_{\vec{R}}\,m(\vec{R}_t)\rangle = -\mathrm{i}\,\mathcal{M}_{nm}(\vec{R}_t).\end{aligned} \tag{2.17}$$

As the coupling terms $\mathcal{M}_{nm}(\vec{R}_t)$ of Eq. (2.5) are proportional to the rate of change of the control parameters $\dot{\vec{R}}_t$, the potential $\hat{\mathcal{A}}(\vec{R}_t)$ can be considered as a weak perturbation that

[3] The existence of a unitary operation $\hat{V}(\vec{R}_t)$ is guaranteed by the spectral theorem, which states that the eigenvectors of any Hermitian operator $\hat{H}(\vec{R}_t)$ can be chosen to form an orthonormal set of basis states $\{|n(\vec{R}_t)\rangle\}_n$. This implies that $\hat{H}(\vec{R}_t)$ can be diagonalized by a unitary operation $\hat{V}(\vec{R}_t)$, the latter generated according to the transformation relation (2.14).

[4] Since $[\nabla_{\vec{R}}\hat{V}^\dagger(\vec{R}_t)]\,\hat{V}(\vec{R}_t) + \hat{V}^\dagger(\vec{R}_t)\,[\nabla_{\vec{R}}\hat{V}(\vec{R}_t)] = \nabla_{\vec{R}}\,[\hat{V}^\dagger(\vec{R}_t)\,\hat{V}(\vec{R}_t)] = \nabla_{\vec{R}}\,[\mathbb{1}] = 0$, the potential $\hat{\mathcal{A}}(\vec{R}_t)$ is a Hermitian operator.

slightly changes the spectral properties (2.15) of the unperturbed Hamiltonian $\hat{H}'(\vec{R}_t)$. The associated modifications can be systematically derived using static perturbation theory [Sch07, SN21], in which the spectrum of the perturbed Hamiltonian

$$\hat{H}_{\mathrm{rot}}(\vec{R}_t)\ |m_{\mathrm{rot}}(\vec{R}_t)\rangle = E_m^{\mathrm{rot}}(\vec{R}_t)\ |m_{\mathrm{rot}}(\vec{R}_t)\rangle$$

gets expanded in the small parameter $\dot{\vec{R}}_t$. Using the matrix elements of Eq. (2.17), this yields first-order corrections

$$E_m^{\mathrm{rot}}(\vec{R}_t) = E_m(\vec{R}_t) + \langle e_m|\hat{\mathcal{A}}(\vec{R}_t)|e_m\rangle = E_m(\vec{R}_t) - \mathrm{i}\,\mathcal{M}_{mm}(\vec{R}_t),$$
$$|m_{\mathrm{rot}}(\vec{R}_t)\rangle = |e_m\rangle + \sum_{n\neq m} \frac{\langle e_n|\hat{\mathcal{A}}(\vec{R}_t)|e_m\rangle}{\Delta_{mn}(\vec{R}_t)}\ |e_n\rangle = |e_m\rangle + \mathrm{i}\sum_{n\neq m} \frac{\mathcal{M}_{nm}(\vec{R}_t)}{\Delta_{nm}(\vec{R}_t)}\ |e_n\rangle\,,$$

with eigenstates $|m_{\mathrm{rot}}(\vec{R}_t)\rangle$ that explicitly exhibit transitions to neighboring basis states $|e_{n\neq m}\rangle$ weighted by off-diagonal coupling terms $\mathcal{M}_{nm}(\vec{R}_t)$ (see Eq. (2.10)) and energy gaps $\Delta_{nm}(\vec{R}_t) = E_n(\vec{R}_t) - E_m(\vec{R}_t)$.

Taking into account that $\frac{\mathrm{d}}{\mathrm{d}t}\,|m_{\mathrm{rot}}(\vec{R}_t)\rangle$ only contains higher orders in $\dot{\vec{R}}_t$, a set of fundamental solutions to Eq. (2.16) is formed by $|\Psi_m^{\mathrm{rot}}(t)\rangle = \mathrm{e}^{\mathrm{i}\,\gamma_m(t)}\ |m_{\mathrm{rot}}(\vec{R}_t)\rangle$, with phase factors $\gamma_m(t) = -\int_{t_0}^{t}\mathrm{d}t'\,E_m^{\mathrm{rot}}(\vec{R}_{t'})$. Rotating back to the original basis $|\Psi(t)\rangle = \hat{V}(\vec{R}_t)\,|\Psi_{\mathrm{rot}}(t)\rangle$, and assuming that the system is initialized in an instantaneous eigenstate $|m(\vec{R}_{t_0})\rangle$, we obtain the final result of first-order APT [ROP08, WBD$^+$17]

$$|\Psi_m(t)\rangle = \mathrm{e}^{\mathrm{i}\,\gamma_m(t)}\Big[\,|m(\vec{R}_t)\rangle + \mathrm{i}\sum_{n\neq m}\frac{\mathcal{M}_{nm}(\vec{R}_t)}{\Delta_{nm}(\vec{R}_t)}\ |n(\vec{R}_t)\rangle\,\Big], \tag{2.18}$$

with an overall phase factor $\gamma_m(t) = -\int_{t_0}^{t}\mathrm{d}t'\,[E_m(\vec{R}_{t'}) - \mathrm{i}\,\mathcal{M}_{mm}(\vec{R}_{t'})]$. In the quantum adiabatic limit, the second expression of Eq. (2.18) is neglected, resulting in a zeroth-order term confined to the synthetic energy band $E_m(\vec{R}_t)$. First-order corrections, however, yield transitions to the excited states of the instantaneous spectrum, generated by the off-diagonal coupling terms $\mathcal{M}_{nm}(\vec{R}_t)$ of Eq. (2.10). The quantum state $|\Psi_m(t)\rangle$ is well-defined whenever the system is initialized in an energy band $E_m(\vec{R}_t)$ that is energetically separated from the other bands $E_{n\neq m}(\vec{R}_t)$, which is why degeneracies in the excited part of the spectrum are explicitly allowed.

2.1.4 Geometrical Response

Considering the energy transfer rate associated with the time-evolution in a given direction of the parameter space, the second expression of Eq. (2.18) reveals a first-order response proportional to the Berry curvature of the adiabatic energy band [GP12, WBD$^+$17]. This fundamental concept can be derived by analyzing the equations of motion for the total energy transfer rate [Ehr27, Bal15, GS18]

$$\frac{\mathrm{d}}{\mathrm{d}t}\,\langle\hat{H}(\vec{R}_t)\rangle = \langle\partial_t\,\hat{H}(\vec{R}_t)\rangle = \dot{\vec{R}}_t\ \langle\hat{\mathbf{I}}(\vec{R}_t)\rangle\,,\quad \hat{\mathbf{I}}(\vec{R}_t) = \nabla_{\vec{R}}\,\hat{H}(\vec{R}_t), \tag{2.19}$$

where the expectation values are calculated according to the exact solution $|\Psi(t)\rangle$ of the time-dependent Schrödinger equation (2.1). Each term $\dot{R}_{k,t}\ \langle\hat{\mathrm{I}}_k(\vec{R}_t)\rangle$ can be interpreted

as the individual pumping rate generated by temporally evolving in k direction of the parameter space, with $\hat{\mathrm{I}}_k(\vec{R}_t) = \partial_{R_k}\hat{H}(\vec{R}_t)$ resembling a current operator for the motion in the associated synthetic direction. Using the perturbed quantum state $|\Psi_m(t)\rangle$ of Eq. (2.18), the expectation value $\langle\hat{\mathrm{I}}_k(\vec{R}_t)\rangle$ can be expanded to first order in $\dot{\vec{R}}_t$ [GP12, WBD+17]:

$$\langle\hat{\mathrm{I}}_k(\vec{R}_t)\rangle_m = \langle\Psi_m(t)|\hat{\mathrm{I}}_k(\vec{R}_t)|\Psi_m(t)\rangle = \frac{\partial E_m(\vec{R}_t)}{\partial R_k} + \sum_{l=1}^{D}\dot{R}_{l,t}\,\Omega_{kl}^{(m)}(\vec{R}_t), \tag{2.20}$$

where the sum runs over the components of the $D-$dimensional parameter space $\vec{R}_t \in \mathbb{R}^D$. Eq. (2.20) demonstrates that the Berry curvature [Ber84]

$$\Omega_{kl}^{(m)}(\vec{R}_t) = -\mathrm{i}\sum_{n\neq m}\frac{\langle m(\vec{R}_t)|\hat{\mathrm{I}}_k(\vec{R}_t)|n(\vec{R}_t)\rangle\,\langle n(\vec{R}_t)|\hat{\mathrm{I}}_l(\vec{R}_t)|m(\vec{R}_t)\rangle - (l\leftrightarrow k)}{\Delta_{nm}^2(\vec{R}_t)} \tag{2.21}$$

arises as the first-order response to the current operator $\hat{\mathrm{I}}_k(\vec{R}_t)$, accompanied by the individual components of the rate of change of the control parameters $\dot{R}_{l,t}$. In this sense, the geometrical features of the dynamical synthetic quantum matter rely on the first-order corrections of APT, in which the interband excitations of Eq. (2.18) can be readily mapped onto the Berry curvature $\Omega_{kl}^{(m)}(\vec{R}_t)$ whenever the system is initialized in an energetically separated energy band and evolves sufficiently slowly in time. Couplings between synthetic energy bands are thus essential for the generation of the Berry phase effects [XCN10, CF21], as the adiabatic limit only produces Bloch oscillations $\partial_{R_k}E_m(\vec{R}_t)$ [Blo29].

The Berry curvature $\Omega_{kl}^{(m)}(\vec{R}_t)$ of Eq. (2.21) is a gauge-invariant quantity[5], which provides a purely local description of the geometrical properties of the parameter space. The latter becomes more clear by expressing Eq. (2.21) as an intrinsic property of the occupied instantaneous eigenstates

$$\Omega_{kl}^{(m)}(\vec{R}_t) = -\mathrm{i}\left[\langle\partial_{R_k}m(\vec{R}_t)|\partial_{R_l}m(\vec{R}_t)\rangle - (l\leftrightarrow k)\right] = 2\,\mathrm{Im}[\langle\partial_{R_k}m(\vec{R}_t)|\partial_{R_l}m(\vec{R}_t)\rangle], \tag{2.22}$$

where we employ the matrix elements (2.11) of the current operator $\hat{\mathbf{I}}(\vec{R}_t)$, the completeness relation $\sum_n |n(\vec{R}_t)\rangle\langle n(\vec{R}_t)| = \mathbb{1}$, and introduce the imaginary part $\mathrm{Im}[z]$ of a complex number $z \in \mathbb{C}$. Eq. (2.22) implies that the transitions to the excited states of the spectrum are virtual in nature, as the off-diagonal contributions of Eq. (2.21) are exclusively projected onto the adiabatic properties of the synthetic energy band $E_m(\vec{R}_t)$. This projection, in turn, leads to a representation of the Berry curvature $\Omega_{kl}^{(m)}(\vec{R}_t)$ that involves the incremental changes of the occupied eigenstates $|m(\vec{R}_t)\rangle$ in the synthetic directions of the parameter space. In this sense, the Berry curvature

[5] In fact, Eq. (2.21) does not depend on derivatives of the instantaneous eigenstates $|\nabla_{\vec{R}}\,m(\vec{R}_t)\rangle$, which is why a smooth and differentiable choice of gauge (cf. Eq (2.6)) is not mandatory. Moreover, it is not even necessary to choose a single-valued set of basis states $\{|n(\vec{R}_t)\rangle\}_n$, so that Eq. (2.21) holds for any solution of the instantaneous spectrum of Eq. (2.2). This becomes especially relevant for numerical calculations, in which phase relations between instantaneous eigenstates are usually hard to control by exact diagonalization routines.

$\Omega_{kl}^{(m)}(\vec{R}_t)$ represents a local geometrical quantity, whose gauge-invariance does not rely on the global condition of a closed path $\mathcal{C}_{t_0}^T$ (cf. Eq. (2.13)) in parameter space. For this reason, Eq. (2.22) can be considered as the local counterpart of the Berry phase $\xi_m^{\mathrm{B}}(\mathcal{C}_{t_0}^T)$, which becomes particularly evident for a three-dimensional parameter space ($D = 3$). In this illustrative case, the closed line integral of Eq. (2.13) can be reformulated into a surface integral according to Stokes' theorem [Gri13]

$$\xi_m^{\mathrm{B}}(\mathcal{C}_{t_0}^T) = \iint_S \mathrm{d}\vec{S} \cdot \vec{\Omega}^{(m)}(\vec{R}), \quad \vec{\Omega}^{(m)}(\vec{R}) = \mathrm{i}\, \nabla_{\vec{R}} \times \langle m(\vec{R}) | \nabla_{\vec{R}}\, m(\vec{R}) \rangle\,, \tag{2.23}$$

in which the integration is performed along a two-dimensional surface S whose boundary is given by the closed path $\mathcal{C}_{t_0}^T$ in parameter space. Using the vector calculus of $\mathbb{R}^3$, we have introduced the vector field $\vec{\Omega}^{(m)}(\vec{R})$, which reveals a flux through the surface S corresponding to the Berry phase $\xi_m^{\mathrm{B}}(\mathcal{C}_{t_0}^T)$. This geometrical structure suggests an analogy to electrodynamics, where $\vec{\Omega}^{(m)}(\vec{R})$ plays the role of a magnetic field and $\xi_m^{\mathrm{B}}(\mathcal{C}_{t_0}^T)$ represents the magnetic flux that is generated by traversing the boundary of the surface $\partial S = \mathcal{C}_{t_0}^T$. In this sense, the $r-$th component of the vector form $\Omega_r^{(m)}(\vec{R}) = \mathrm{i} \sum_{p,s} \epsilon_{rps} \langle \partial_{R_p}\, m(\vec{R}) | \partial_{R_s}\, m(\vec{R}) \rangle$ reflects the local geometrical properties of the parameter space, which eventually manifests itself in the Berry curvature relation[6]

$$\Omega_{kl}^{(m)}(\vec{R}) = \sum_{r=1}^{3} \epsilon_{lkr}\, \Omega_r^{(m)}(\vec{R}). \tag{2.24}$$

We have introduced the epsilon tensor ϵ_{lkr}, whose indices run over the components of the three-dimensional parameter space $\mathbb{R}^3$. The above statements, however, can also be extended to arbitrary dimensions of the parameter space $\vec{R}_t \in \mathbb{R}^D$. In this case, Eq. (2.23) can be generalized using the basic concepts of differential forms [Con08, Lee13], suggesting that the Berry curvature $\Omega_{kl}^{(m)}(\vec{R})$ is analogous to the field strength tensor of electrodynamics [Res00, XCN10].

Berry phase effects have attracted much attention in the condensed matter community, as they are essential for the modern description of quantum Hall effects, electric polarization, or quantum charge pumps [BMK$^+$03, XCN10, Van18]. Many of these intriguing observations can be characterized by the semiclassical formulation of electron dynamics in a periodic lattice, where the equations of motion are modified by a Berry curvature term arising from virtual couplings between energy bands [CN95, CN96, SN99]. Integrating these geometrical corrections over the *Brillouin zone* (BZ) of the crystal, this leads to topological phases that have served as the basis for the most fascinating phenomena in physics [Tho98, Wen17]. In the remainder of Chap. 2, we show that quasiperiodically driven quantum systems provide an illustrative platform for generating geometrical and topological effects in dynamical synthetic quantum matter, deriving an analogy between Eq. (2.20) and the semiclassical equations of motion in a higher-dimensional Floquet lattice [HCT83, CT04, EA15, VPM16]. The latter features a synthetic BZ that is entirely sampled during the quasiperiodic dynamics of the quantum state $|\Psi_m(t)\rangle$, yielding a quantized response proportional to the topological invariant

[6] Note that Eq. (2.24) formally includes the two-dimensional parameter space ($D = 2$) as well.

of the synthetic energy band $E_m(\vec{R}_t)$ [MRH17]. Our derivations are based on the mathematical concept of Floquet theory [Flo83, Shi65, Sam73], which is why we start with the theoretical treatment of periodically driven quantum systems.

2.2 Floquet Theory

A versatile tool for the generation of topological phenomena in nonequilibrium quantum systems involves periodic driving in time [Hol16, Eck17], leading to time-translation invariant settings theoretically explained in terms of Floquet theory [Flo83]. As Floquet theory represents the temporal analog of Bloch's theorem for spatially periodic systems [Blo29, Kit71, AM76], the associated Floquet state is characterized by both a time-periodic modulation and a stroboscopic phase evolution, the latter governed by the quasienergies of the effective time-independent Hamiltonian of the Floquet system [GH98]. We argue that this effective Hamiltonian can exhibit topological properties absent in its nondriven counterpart, revealing light-induced topological phase transitions as observed in ultracold atomic gases [GJÖS14, GBZ16, CDS19] or Floquet topological insulators [CDSM13, OK19, RL20a]. Exploiting the periodicity of the quasienergy spectrum, we show that the periodically driven quantum system can be mapped onto an eigenvalue problem in an extended Floquet Hilbert space [Sam73], allowing for an analytic calculation of the effective Hamiltonian in the context of a high-frequency expansion [BDP15, EA15]. The eigenvalue problem can be further illustrated in terms of a tight-binding model in the Floquet lattice [Shi65, RL20b], in which the quantum state is expanded in the Fourier modes of the driving frequency. This projection serves as a basis for the formation of topological phases in dynamically-induced synthetic dimensions, with linear response signals that translate into topological pumping effects in the lower-dimensional system. As the origin of Floquet theory goes back to the mathematical description of *linear differential equations* (LDEs) with periodic coefficients, we start our investigation with the mathematical concepts of Floquet theory [Chi99, Tes12, Sid13, BES13, Awr14].

2.2.1 Mathematical Background

We consider the *initial value problem* (IVP)

$$\dot{\vec{y}}(t) = \hat{A}(t)\,\vec{y}(t), \quad \vec{y}(t_0) = \vec{y}_0, \tag{2.25}$$

where we introduce the vector $\vec{y}(t) : \mathbb{R} \mapsto \mathbb{C}^n$, the shorthand $\dot{\vec{y}}(t) = \frac{\mathrm{d}}{\mathrm{d}t}\,\vec{y}(t)$, and the operator $\hat{A}(t) : \mathbb{R} \mapsto \mathbb{C}^{n\times n}$. We assume that $\hat{A}(t)$ is a locally integrable matrix-valued function, yielding a unique locally absolutely continuous solution $\vec{y}(t, t_0, \vec{y}_0) \in \mathbb{C}^n$ satisfying the initial condition of Eq. (2.25) [BES13]. A linearly independent and fundamental set of solutions $\vec{y}_i(t)$ $\{i = 1, \ldots, n\}$ of the LDE forms a vector space $\mathbb{C}^n$, such that a fundamental matrix $\hat{\Gamma}(t) : \mathbb{R} \mapsto \mathbb{C}^{n\times n}$ can be generated whose $i-$th column is given by the basis vector $\vec{y}_i(t)$. The unique solution of the IVP can be represented as

$$\vec{y}(t, t_0, \vec{y}_0) = \hat{\Phi}(t, t_0)\,\vec{y}_0, \tag{2.26}$$

where $\hat{\Phi}(t,t_0) = \hat{\Gamma}(t)\,\hat{\Gamma}^{-1}(t_0)$ corresponds to a specific fundamental operator, the transition (matricant) matrix of the system [Chi99, Sid13, Awr14]. We use that any fundamental matrix $\hat{\Gamma}(t)$ represents a regular operator[7], whose inverse matrix is given by $\hat{\Gamma}^{-1}(t)$. With $\hat{\Phi}(t,t_0)$, any fundamental matrix $\hat{\Gamma}(t)$ can be generated as

$$\hat{\Gamma}(t) = \hat{\Phi}(t,t_0)\,\hat{\Gamma}(t_0), \tag{2.27}$$

where we employ $\hat{\Gamma}^{-1}(t_0)\,\hat{\Gamma}(t_0) = \mathbb{1}$. Inserting Eq. (2.26) into the LDE of Eq. (2.25), this leads to the matrix analog of the IVP:

$$\dot{\hat{\Phi}}(t,t_0) = \hat{A}(t)\,\hat{\Phi}(t,t_0), \quad \hat{\Phi}(t_0,t_0) = \mathbb{1}. \tag{2.28}$$

Within the interval $[t_0,t_1]$, the transition matrix $\hat{\Phi}(t,t_0)$ transforms the initial vector $\vec{y}_0 = \vec{y}(t_0)$ into the time-evolved vector $\vec{y}(t_1) = \hat{\Phi}(t_1,t_0)\,\vec{y}(t_0)$ (cf. Eq. (2.26)), resulting in group properties

$$\hat{\Phi}(t_2,t_0) = \hat{\Phi}(t_2,t_1)\,\hat{\Phi}(t_1,t_0), \quad \hat{\Phi}(t_0,t_1) = \hat{\Phi}^{-1}(t_1,t_0). \tag{2.29}$$

Considering periodic coefficients $\hat{A}(t) = \hat{A}(t+NT)$ with $N \in \mathbb{Z}$, Eqs. (2.25) and (2.28) yield LDEs with periodicity $T > 0$. Assuming that $\hat{\Phi}(t,t_0)$ corresponds to the transition matrix of the periodic IVP, the operator $\hat{\Sigma}(t,t_0,NT) = \hat{\Phi}(t+NT,t_0)$ is identified as a fundamental matrix of the LDE of Eq. (2.28):

$$\dot{\hat{\Sigma}}(t,t_0,NT) = \dot{\hat{\Phi}}(t+NT,t_0) = \hat{A}(t+NT)\,\hat{\Phi}(t+NT,t_0) = \hat{A}(t)\,\hat{\Sigma}(t,t_0,NT).$$

As each fundamental matrix can be represented as shown in Eq. (2.27), the transition matrix $\hat{\Phi}(t,t_0)$ of the periodic LDE obeys the property

$$\hat{\Phi}(t+NT,t_0) = \hat{\Phi}(t,t_0)\,\hat{M}(NT,t_0), \tag{2.30}$$

where we have introduced the monodromy matrix $\hat{M}(T,t_0) = \hat{\Phi}(t_0+T,t_0)$ [Chi99, Tes12, BES13, Awr14]. The latter represents a regular operator obeying the relation

$$\hat{M}(NT,t_0) = \hat{\Phi}(t_0+NT,t_0) = \hat{\Phi}(t_0+(N-1)T,t_0)\,\hat{M}(T,t_0) = \cdots = \hat{M}^N(T,t_0),$$

which is why the monodromy matrix $\hat{M}(T,t_0)$ can be parametrized as a matrix exponential[8] of an operator $\hat{A}^F_{t_0} \in \mathbb{C}^{n\times n}$:

$$\hat{M}(T,t_0) = \hat{\Phi}(t_0+T,t_0) = \mathrm{e}^{T\hat{A}^F_{t_0}}. \tag{2.31}$$

[7] By definition, a fundamental matrix $\hat{\Gamma}(t)$ contains linearly independent columns that yield a non-vanishing determinant $\det(\hat{\Gamma}(t)) \neq 0$. This guarantees the existence of an inverse matrix $\hat{\Gamma}^{-1}(t)$, showing that $\hat{\Gamma}(t)$ represents a regular operator.

[8] In fact, any regular operator $\hat{M}(T,t_0)$ can be written as a matrix exponential $\hat{M}(T,t_0) = \mathrm{e}^{\hat{X}(T,t_0)}$ of an operator $\hat{X}(T,t_0) \in \mathbb{C}^{n\times n}$ [Chi99, Sid13, Hal15]. As $\hat{M}(NT,t_0) = \hat{M}^N(T,t_0)$, this implies that $\hat{X}(NT,t_0) = N\,\hat{X}(T,t_0)$, where the latter can be solved as $\hat{X}(T,t_0) = T\hat{A}^F_{t_0}$ by introducing a $T-$independent operator $\hat{A}^F_{t_0} \in \mathbb{C}^{n\times n}$.

Using Eqs. (2.30) and (2.31), the transition matrix $\hat{\Phi}(t,t_0)$ of the periodic IVP can be represented as

$$\hat{\Phi}(t,t_0) = \hat{\Phi}_F(t,t_0)\,\mathrm{e}^{(t-t_0)\hat{A}^F_{t_0}}, \quad \hat{\Phi}_F(t_0,t_0) = \mathbb{1}, \tag{2.32}$$

where we have introduced the $T-$periodic operator

$$\hat{\Phi}_F(t,t_0) = \hat{\Phi}(t,t_0)\,\mathrm{e}^{-(t-t_0)\hat{A}^F_{t_0}}, \quad \hat{\Phi}_F(t+NT,t_0) = \hat{\Phi}_F(t,t_0). \tag{2.33}$$

Inserting Eq. (2.32) into the LDE of Eq. (2.28), this yields a relation between the periodic coefficients $\hat{A}(t) = \hat{A}(t+NT)$ and the $t-$independent operator $\hat{A}^F_{t_0}$:

$$\hat{A}^F_{t_0} = \hat{\Phi}_F^{-1}(t,t_0)\,\hat{A}(t)\,\hat{\Phi}_F(t,t_0) - \hat{\Phi}_F^{-1}(t,t_0)\,\dot{\hat{\Phi}}_F(t,t_0), \tag{2.34}$$

where we use the inverse matrix $\hat{\Phi}_F^{-1}(t,t_0)$ of the regular operator $\hat{\Phi}_F(t,t_0)$ defined in Eq. (2.33).

Let $\vec{y}_i(t_0) \in \mathbb{C}^n$ be nontrivial eigenvectors of $\hat{A}^F_{t_0} \in \mathbb{C}^{n\times n}$ with eigenvalues[9] $\lambda_i \in \mathbb{C}$, while we assume that the algebraic equals the geometric multiplicity. The vectors $\vec{y}_i(t_0)$ $\{i = 1, \ldots, n\}$ are linearly independent, and we can identify the fundamental set of the periodic LDE as

$$\vec{y}_i(t,t_0) = \hat{\Phi}(t,t_0)\,\vec{y}_i(t_0) = \hat{\Phi}_F(t,t_0)\,\mathrm{e}^{(t-t_0)\hat{A}^F_{t_0}}\,\vec{y}_i(t_0) = \mathrm{e}^{\lambda_i(t-t_0)}\,\hat{\Phi}_F(t,t_0)\,\vec{y}_i(t_0).$$

Introducing the function

$$\vec{u}_i(t,t_0) = \hat{\Phi}_F(t,t_0)\,\vec{y}_i(t_0), \tag{2.35}$$

the Floquet solutions $\vec{y}_i(t,t_0)$ can be represented as a product of an exponential $\mathrm{e}^{\lambda_i(t-t_0)}$ and the $T-$periodic Floquet modes $\vec{u}_i(t,t_0) = \vec{u}_i(t+NT,t_0)$ [Flo83]:

$$\vec{y}_i(t,t_0) = \mathrm{e}^{\lambda_i(t-t_0)}\,\vec{u}_i(t,t_0), \quad \vec{u}_i(t_0,t_0) = \vec{y}_i(t_0). \tag{2.36}$$

The unique solution $\vec{y}(t,t_0,y_0)$ of the IVP with periodic coefficients $\hat{A}(t) = \hat{A}(t+NT)$ is given by the superposition of the Floquet solutions $\vec{y}(t,t_0,y_0) = \sum_i c_i\,\vec{y}_i(t,t_0)$, with coefficients $c_i \in \mathbb{C}$ satisfying the initial condition $\sum_i c_i\,\vec{y}_i(t_0) = \vec{y}_0$ of Eq. (2.25).

The eigenvalues $\lambda_i \in \mathbb{C}$ of Eq. (2.36) are called Floquet exponents [Chi99, Tes12, Sid13, BES13], and are explicitly independent of the initial time t_0. This stems from the fact that monodromy matrices at different initial times are connected by a basis transformation

$$\hat{M}(T,t_0') = \hat{\Phi}(t_0'+T,t_0') = \hat{\Phi}(t_0'+T,t_0)\,\hat{\Phi}(t_0,t_0') = \hat{\Phi}^{-1}(t_0,t_0')\,\hat{M}(T,t_0)\,\hat{\Phi}(t_0,t_0'), \tag{2.37}$$

yielding t_0-independent eigenvalues $\hat{M}(T,t_0)\,\vec{y}_i(t_0) = \mathrm{e}^{T\lambda_i}\,\vec{y}_i(t_0)$ denoted as Floquet multipliers of the periodic LDE [Tes12, Sid13, BES13]. Here, we employ the properties of Eqs. (2.29) and (2.30). Inserting Eq. (2.31) into Eq. (2.37), this yields the associated basis transformation for the operator $\hat{A}^F_{t_0}$:

$$\hat{A}^F_{t_0'} = \hat{\Phi}^{-1}(t_0,t_0')\,\hat{A}^F_{t_0}\,\hat{\Phi}(t_0,t_0') = \hat{\Phi}_F^{-1}(t_0,t_0')\,\hat{A}^F_{t_0}\,\hat{\Phi}_F(t_0,t_0'), \tag{2.38}$$

where we use the representation (2.32) of the transition matrix $\hat{\Phi}(t,t_0)$ of the periodic LDE.

[9] The eigenvalues $\lambda_i \in \mathbb{C}$ are explicitly independent of the initial time t_0, which directly follows from the basis transformations of Eqs. (2.37) and (2.38).

2.2.2 Periodically Driven Quantum Systems

Let a periodically driven quantum system be described by the $T-$periodic Hamiltonian $\hat{H}(t) = \hat{H}(t+T)$, where the quantum state $|\Psi(t)\rangle$ obeys the time-dependent Schrödinger equation [Sch26, Sha08, GS18]

$$\mathrm{i}\,\frac{\mathrm{d}}{\mathrm{d}t}\,|\Psi(t)\rangle = \hat{H}(t)\,|\Psi(t)\rangle\,. \tag{2.39}$$

The time-evolution of an initial state $|\Psi(t_0)\rangle$ is governed by the unitary evolution operator $\hat{U}(t,t_0)$, formally revealing the solution $|\Psi(t)\rangle = \hat{U}(t,t_0)\,|\Psi(t_0)\rangle$. Applying this approach to Eq. (2.39), the Schrödinger equation for the quantum state $|\Psi(t)\rangle$ turns into the equation for the time-evolution operator

$$\mathrm{i}\,\frac{\mathrm{d}}{\mathrm{d}t}\,\hat{U}(t,t_0) = \hat{H}(t)\,\hat{U}(t,t_0), \quad \hat{U}(t_0,t_0) = \mathbb{1}. \tag{2.40}$$

For autonomous systems with a time-independent Hamiltonian $\hat{H}(t) = \hat{H}_0$, Eq. (2.40) reduces to the evolution operator $\hat{U}(t,t_0) = \mathrm{e}^{-\mathrm{i}\,\hat{H}_0\,(t-t_0)}$, readily characterized by the energy eigenvalues E_n and eigenstates $|n\rangle$ of the Hamiltonian $\hat{H}_0$: $\hat{U}(t,t_0)\,|n\rangle = \mathrm{e}^{-\mathrm{i}\,\hat{H}_0\,(t-t_0)}\,|n\rangle = \mathrm{e}^{-\mathrm{i}\,E_n(t-t_0)}\,|n\rangle$. Expanding the initial state $|\Psi(t_0)\rangle = \sum_n c_n\,|n\rangle$ in the orthonormal set of basis states $\{|n\rangle\}_n$, the solution to Eq. (2.39) yields

$$|\Psi(t)\rangle = \hat{U}(t,t_0)\,|\Psi(t_0)\rangle = \sum_n c_n\,\mathrm{e}^{-\mathrm{i}\,\hat{H}_0\,(t-t_0)}\,|n\rangle = \sum_n c_n\,\mathrm{e}^{-\mathrm{i}\,E_n(t-t_0)}\,|n\rangle\,, \quad c_n \in \mathbb{C}. \tag{2.41}$$

For an arbitrary time-dependence $\hat{H}(t)$, the evolution operator $\hat{U}(t,t_0)$ can be formally written as

$$\hat{U}(t,t_0) = \hat{\mathrm{T}}\Big[\exp\Big(-\mathrm{i}\int_{t_0}^{t}\mathrm{d}t'\,\hat{H}(t')\Big)\Big], \tag{2.42}$$

with the time-ordering operator $\hat{\mathrm{T}}$. Finding analytical expressions for Eq. (2.42) generally proves to be very challenging, which is why the description of dynamical quantum systems often relies on numerical calculations. In what follows, however, we apply the $T-$periodicity of the Hamiltonian $\hat{H}(t) = \hat{H}(t+T)$, revealing exact solutions to Eqs. (2.39) and (2.40) in the context of Floquet theory (see Sec. 2.2.1).

Comparing Eqs. (2.28) and (2.40), the time-evolution operator $\hat{U}(t,t_0)$ can be identified as a transition matrix of a LDE with periodic coefficients $\hat{A}(t) = -\mathrm{i}\,\hat{H}(t)$. Applying Floquet theory, this yields a representation (cf. Eq. (2.32))

$$\hat{U}(t,t_0) = \hat{U}_F(t,t_0)\,\mathrm{e}^{-\mathrm{i}\,\hat{H}^F_{t_0}(t-t_0)}, \quad \hat{U}_F(t_0,t_0) = \mathbb{1}, \tag{2.43}$$

with a $T-$periodic operator $\hat{U}_F(t+T,t_0) = \hat{U}_F(t,t_0)$ (cf. Eq. (2.33)) transforming the time-dependent Hamiltonian $\hat{H}(t)$ into a time-independent operator (cf. Eq. (2.34))

$$\hat{H}^F_{t_0} = \hat{U}_F^\dagger(t,t_0)\,\hat{H}(t)\,\hat{U}_F(t,t_0) - \mathrm{i}\,\hat{U}_F^\dagger(t,t_0)\,\dot{\hat{U}}_F(t,t_0). \tag{2.44}$$

We have used the unitarity of the time-evolution operator $\hat{U}(t,t_0)$, implying that $\hat{U}_F^{-1}(t,t_0) = \hat{U}_F^\dagger(t,t_0)$ and $(\hat{H}^F_{t_0})^\dagger = \hat{H}^F_{t_0}$. A fundamental set of basis states for the time-periodic Schrödinger equation (2.39) is given by the Floquet solutions (cf. Eq. (2.36))

$$|\psi_n(t,t_0)\rangle = |u_n(t,t_0)\rangle\;\mathrm{e}^{-\mathrm{i}\,\epsilon_n(t-t_0)}, \quad |u_n(t_0,t_0)\rangle = |u_n(t_0)\rangle\,, \tag{2.45}$$

where we have introduced the $T-$periodic Floquet modes $|u_n(t+T,t_0)\rangle = |u_n(t,t_0)\rangle$ (cf. Eq. (2.35)), and the eigenvalues ϵ_n and eigenstates $|u_n(t_0)\rangle$ of the Hermitian operator $\hat{H}^F_{t_0}$. The structure of the Floquet solutions $|\psi_n(t,t_0)\rangle$ reveals an analogy to Bloch's theorem [Blo29, Kit71, AM76] for spatially-periodic systems:

1. The Floquet modes $|u_n(t,t_0)\rangle$ take the role of crystal-periodic functions, where time t is considered as a coordinate. The translation vector is given by the periodicity T, with modes satisfying the condition $|u_n(t+T,t_0)\rangle = |u_n(t,t_0)\rangle$.

2. The Hermitian operator $\hat{H}^F_{t_0}$, known as the Floquet Hamiltonian of the periodically driven quantum system [GH98, EA15, Eck17], guarantees the existence of real eigenvalues $\epsilon_n \in \mathbb{R}$ and a complete orthonormal set of Floquet solutions $\{|\psi_n(t,t_0)\rangle\}_n$. Apart from an overall phase factor, the Floquet solutions $|\psi_n(t+T,t_0)\rangle = |\psi_n(t,t_0)\rangle\ \mathrm{e}^{-\mathrm{i}\,\epsilon_n\,T}$ are periodic in time.

3. The eigenvalue ϵ_n assumes the role of a crystal wave vector, denoted as the quasienergy of the Floquet state $|\psi_n(t,t_0)\rangle$ [GH98, EA15, Hol16, Eck17]. In Sec. 2.2.3, we show that different quasienergies $\epsilon_{nm} = \epsilon_n + m\,\omega$, with $\omega = \frac{2\pi}{T}$ and $m \in \mathbb{Z}$, correspond to the same Floquet state $|\psi_n(t,t_0)\rangle$, resulting in the definition of a first BZ. The reciprocal lattice vector in the temporal case is given by $G_m = m\,\omega$, satisfying the condition $G_m\,T = 2\pi m$.

Introducing constant coefficients $c_n = \langle u_n(t_0)|\Psi(t_0)\rangle$, the dynamics of the quantum state $|\Psi(t)\rangle = \sum_n\ c_n\ |\psi_n(t,t_0)\rangle = \sum_n\ c_n\ |u_n(t,t_0)\rangle\ \mathrm{e}^{-\mathrm{i}\,\epsilon_n(t-t_0)}$ solving the time-dependent Schrödinger equation (2.39) is affected by two contributions [EA15, Eck17]:

1. The temporal dependence of the $T-$periodic Floquet modes $|u_n(t,t_0)\rangle$, referred to as the micromotion of the quantum state $|\Psi(t)\rangle$. As this time-evolution is generated by $|u_n(t,t_0)\rangle = \hat{U}_F(t,t_0)\,|u_n(t_0)\rangle$ (cf. Eq. (2.35)), the unitary operator $\hat{U}_F(t,t_0)$ is denoted as the micromotion operator of the periodically driven quantum system.

2. The relative dephasing of the phase factors $\mathrm{e}^{-\mathrm{i}\,\epsilon_n(t-t_0)}$, determined by the quasienergies ϵ_n of the Floquet states $|\psi_n(t,t_0)\rangle$. As the micromotion $|u_n(t+T,t_0)\rangle = |u_n(t,t_0)\rangle$ is temporally periodic, the dephasing reflects the stroboscopic time-evolution[10] of the periodically driven quantum system. In this sense, the quasienergies ϵ_n play a role similar to the stationary energies E_n of an autonomous system (cf. Eq. (2.41)).

Accordingly, the dynamics of a periodically driven quantum system can be divided into a short-time (micromotion) and a long-time (stroboscopic) evolution of the quantum state $|\Psi(t)\rangle$, allowing for a significant improvement in computation time as numerical simulations can be restricted to the time-interval of periodicity T. In fact, as the Floquet Hamiltonian $\hat{H}^F_{t_0}$ of Eq. (2.44) is originally defined by (cf. Eq. (2.31))

$$\hat{U}(t_0+T,t_0) = \mathrm{e}^{-\mathrm{i}\,T\hat{H}^F_{t_0}}, \tag{2.46}$$

[10]The stroboscopic time-evolution refers to times $t = t_0 + NT$ that are integer multiples $N \in \mathbb{Z}$ of the periodicity $T > 0$.

both the micromotion operator $\hat{U}_F(t,t_0)$ (cf. Eq. (2.33)) and the Floquet Hamiltonian $\hat{H}^F_{t_0}$ can be determined by diagonalizing the evolution operator $\hat{U}(t,t_0)$ over one period T. The dephasing effects of the stroboscopic time-evolution are then captured by the spectral properties of Eq. (2.46).

The Floquet Hamiltonian $\hat{H}^F_{t_0} = \sum_n \epsilon_n \, |u_n(t_0)\rangle\langle u_n(t_0)|$ formally shows a parametric dependence on the initial time t_0, generated by the Floquet modes $|u_n(t_0)\rangle$ obeying the initial condition of Eq. (2.45). This yields a unique representation[11] of $\hat{H}^F_{t_0}$, where a Floquet Hamiltonian $\hat{H}^F_{t_0'}$ at different initial time t_0' is related to $\hat{H}^F_{t_0}$ by a unitary transformation $\hat{H}^F_{t_0'} = \hat{U}^\dagger_F(t_0,t_0')\,\hat{H}^F_{t_0}\,\hat{U}_F(t_0,t_0')$ (cf. Eq. (2.38)). This unitary equivalence reveals t_0-independent quasienergies ϵ_n, suggesting that the parametrization on the initial time t_0 can be completely avoided by introducing an effective Hamiltonian[12]

$$\hat{H}_F = \hat{U}^\dagger_F(t)\,\hat{H}(t)\,\hat{U}_F(t) - \mathrm{i}\,\hat{U}^\dagger_F(t)\,\dot{\hat{U}}_F(t), \tag{2.47}$$

with a time-periodic unitary operator $\hat{U}_F(t+T) = \hat{U}_F(t)$. In Eq. (2.47), the parametric dependence on t_0 is eliminated at the price of an unitary arbitrariness in the set of operators $\hat{H}_F$ and $\hat{U}_F(t)$. In fact, the Floquet Hamiltonian $\hat{H}^F_{t_0}$ of Eq. (2.44) can be interpreted as a concrete choice of the effective Hamiltonian $\hat{H}_F$, as described by the unitary transformation $\hat{H}^F_{t_0} = \hat{U}_F(t_0)\,\hat{H}_F\,\hat{U}^\dagger_F(t_0)$. Here, the micromotion operator takes the form $\hat{U}_F(t,t_0) = \hat{U}_F(t)\,\hat{U}^\dagger_F(t_0)$, yielding a representation of the evolution operator [Shi65, EA15, Eck17]

$$\hat{U}(t,t_0) = \hat{U}_F(t)\,\mathrm{e}^{-\mathrm{i}\,\hat{H}_F(t-t_0)}\,\hat{U}^\dagger_F(t_0). \tag{2.48}$$

From this formula, the degree of freedom in the set of operators $\hat{H}_F$ and $\hat{U}_F(t)$ becomes immediately clear. Namely, multiplying $\hat{U}_F(t)$ by an arbitrary time-independent unitary operator $\hat{U}'_F(t) = \hat{U}_F(t)\,\hat{U}$, Eq. (2.48) remains invariant as long as the effective Hamiltonian transforms as $\hat{H}'_F = \hat{U}^\dagger\,\hat{H}_F\,\hat{U}$. Taking the concrete choice $\hat{U} = \hat{U}^\dagger_F(t_0)$, this yields the aforementioned unitary equivalence between the effective Hamiltonian $\hat{H}_F$ and the Floquet Hamiltonian $\hat{H}^F_{t_0}$.

As the effective Hamiltonian[13] $\hat{H}_F$ can be explicitly manipulated by suitable driving protocols of the $T-$periodic Hamiltonian $\hat{H}(t)$, this can be used to impose topological phenomena on quantum systems by engineered external fields. Following this approach, known as Floquet engineering [GD14, BDP15, EA15, Hol16, Eck17], the effective Hamiltonian $\hat{H}_F$ can be designed to induce artificial gauge-fields in ultracold atomic gases [GJÖS14, GBZ16, CDS19] or topologically nontrivial band structures in Floquet topological insulators [CDSM13, OK19, RL20a]. More precisely, in the Floquet topological insulators, conventional condensed matter materials can be driven into nontrivial quantum Hall phases by time-periodic modulations, yielding highly controllable

[11] Apart from a diagonal term, such as $m\,\omega$ with $\omega = \frac{2\pi}{T}$ and $m \in \mathbb{Z}$, as discussed in detail in Sec. 2.2.3.

[12] Assuming a finite state space of the physical system, the existence of such a transformation is ensured by Floquet theory [EA15, Eck17].

[13] In what follows, we choose between the effective Hamiltonian $\hat{H}_F$ and the Floquet Hamiltonian $\hat{H}^F_{t_0}$ according to the concrete setting in which they are used.

quantum phases with transport signatures similar to those of ordinary topological insulators [Moo10, HK10, QZ11, BH13]. In fact, these topological phase transitions stem from the long-time dynamics of the periodically driven quantum system, which is well described by the spectral properties of the effective time-independent Hamiltonian $\hat{H}_F$ as long as the period T of the external driving field represents the shortest time-scale of the experimental setup[14]. Accordingly, the topological features of the Floquet topological insulators are captured by the quasienergy spectrum of $\hat{H}_F$, characterized by topological invariants already known from equilibrium systems [Che46, TKNdN82, QHZ08]. As the topological invariants of the quasienergy spectrum can significantly differ from those of the original band structure, this allows for a light-induced quantum phase transition from a trivial to a nontrivial topological regime. An archetypal example of this kind is provided by the irradiation of graphene with circularly polarized drives [OA09, KOB$^+$11], where the originally semi-metallic band structure transforms into a gapped quasienergy spectrum whose topological properties are captured by an effective Hamiltonian $\hat{H}_F$ that successfully imitates the topological Haldane model [Hal88]. Consequently, this effect has enabled the experimental realization of the Haldane phase, with topological signatures detected in optical wave guides [RZP$^+$13] and ultracold atomic gases [JMD$^+$14], as well as in the aforementioned graphene [MSS$^+$20]. Another interesting realization of the Floquet topological insulator is based on HgTe/CdTe semiconductor quantum wells [BHZ06, KWB$^+$07], which have proven to be a suitable platform for generating the quantum spin Hall effect [KBWM$^+$08, QZ10], a topologically insulating phase originally proposed for graphene [KM05a, KM05b] and semiconductors [BZ06, QWZ06]. In the HgTe/CdTe heterostructure, the phase transition between a conventional insulating phase and a quantum spin Hall phase is controlled by the thickness of the quantum well, the latter demanding a high degree of sample control. Given this drawback, time-periodic perturbations have emerged as a versatile tool for generating topological spectra in semiconducting quantum devices, with well-controlled topological phase transitions that do not depend on changes in the material structures of the experimental sample [LRG11].

The topological invariants of the quasienergy bands do not necessarily contain all the information about the topological properties of a periodically driven quantum system [KBRD10]. A paradigmatic example is given by the anomalous Floquet topological insulator, a system that exhibits chiral edge states even though the quasienergy spectrum shows a topologically trivial band structure [RLBL13]. By introducing spatial disorder, this scenario can be even extended to an anomalous Floquet-Anderson insulator, in which robust chiral edge states appear though all bulk states are Anderson localized [TBR$^+$16]. In fact, these novel topological phenomena have no equilibrium counterpart and rely on the periodicity of the quasienergy spectrum, discussed in the next section.

[14] In this limit, analytical expressions for the effective Hamiltonian $\hat{H}_F$ can be perturbatively derived by a high-frequency expansion [BDP15, EA15], as briefly illustrated in Sec. 2.2.3. For the Floquet Hamiltonian $\hat{H}^F_{t_0}$, the Floquet-Magnus expansion [COR01, BCOR09] provides a similar approach, showing that the explicit choice of $\hat{H}^F_{t_0}$ is accompanied by a different approximation scheme.

2.2.3 Extended Hilbert Space and Floquet Lattice

Although the stroboscopic time-evolution of a periodically driven quantum system is effectively described by a time-independent Floquet Hamiltonian $\hat{H}^F_{t_0}$, the latter shows properties that are generally quite different from those of autonomous quantum systems. This stems from the fact that $\hat{H}^F_{t_0}$ is not uniquely defined, reflected in the multivaluedness of the matrix logarithm of Eq. (2.46). Namely, adding an integer multiple of the driving frequency $\omega = \frac{2\pi}{T}$, the Floquet Hamiltonian

$$\hat{H}^F_{t_0,m} = \hat{H}^F_{t_0} + m\,\omega, \quad m \in \mathbb{Z}, \tag{2.49}$$

does not change the time-evolution over the period T:

$$\hat{U}(t_0+T,t_0) = \mathrm{e}^{-\mathrm{i}\,T\hat{H}^F_{t_0,m}} = \mathrm{e}^{-\mathrm{i}\,T\hat{H}^F_{t_0}}\,\mathrm{e}^{-\mathrm{i}m\omega T} = \mathrm{e}^{-\mathrm{i}\,T\hat{H}^F_{t_0}}\,\mathrm{e}^{-\mathrm{i}2\pi m} = \mathrm{e}^{-\mathrm{i}\,T\hat{H}^F_{t_0}}.$$

At the same time, Eq. (2.44) implies that the micromotion operator transforms as

$$\hat{U}_{F,m}(t,t_0) = \hat{U}_F(t,t_0)\,\mathrm{e}^{\mathrm{i}m\omega(t-t_0)}, \tag{2.50}$$

revealing the uniquely defined time-evolution operator (cf. Eq. (2.43))

$$\hat{U}(t,t_0) = \hat{U}_{F,m}(t,t_0)\,\mathrm{e}^{-\mathrm{i}\,\hat{H}^F_{t_0,m}(t-t_0)} = \hat{U}_F(t,t_0)\,\mathrm{e}^{-\mathrm{i}\,\hat{H}^F_{t_0}(t-t_0)}.$$

Eqs. (2.49) and (2.50) form a quasienergy spectrum that is periodic in the driving frequency ω, with quasienergies

$$\hat{H}^F_{t_0,m}\,|u_n(t_0)\rangle = \epsilon_{nm}\,|u_n(t_0)\rangle\,, \quad \epsilon_{nm} = \epsilon_n + m\,\omega, \tag{2.51}$$

and Floquet modes

$$|u_{nm}(t,t_0)\rangle = \hat{U}_{F,m}(t,t_0)\,|u_n(t_0)\rangle = |u_n(t,t_0)\rangle\;\mathrm{e}^{\mathrm{i}m\omega(t-t_0)}$$

generating the Floquet solutions of Eq. (2.45):

$$|\psi_n(t,t_0)\rangle = |u_{nm}(t,t_0)\rangle\;\mathrm{e}^{-\mathrm{i}\,\epsilon_{nm}(t-t_0)} = |u_n(t,t_0)\rangle\;\mathrm{e}^{-\mathrm{i}\,\epsilon_n(t-t_0)}.$$

The Floquet solutions $|\psi_n(t,t_0)\rangle$ remain invariant under an arbitrary choice of m, revealing a periodicity of the quasienergy spectrum that has been shown to be essential for the generation of novel topological phenomena in Floquet systems [KBRD10, RLBL13, TBR+16]. Moreover, any quasienergy ϵ_n can be selected within an interval of energy size ω, motivating the definition of a first BZ, e.g. $-\omega/2 \leq \epsilon_n < \omega/2$, in analogy to the Bloch solutions [Blo29, Kit71, AM76] of spatially periodic systems.

In what follows, we use the degree of freedom in the quantum number m to formally map the periodically driven quantum system onto a time-independent eigenvalue problem in an extended Floquet Hilbert space. To this end, we insert the ansatz[15]

$$|\psi_n(t)\rangle = |u_{nm}(t)\rangle\;\mathrm{e}^{-\mathrm{i}\,\epsilon_{nm}t}, \quad |u_{nm}(t)\rangle = |u_n(t)\rangle\;\mathrm{e}^{\mathrm{i}m\omega t}, \quad m \in \mathbb{Z}, \tag{2.52}$$

[15] From now on, we consider a linearly independent and fundamental set of solutions $\{|\psi_n(t)\rangle\}_n$, ignoring the initial condition on the time t_0. Starting from these general basis states, the complete orthonormal set of Floquet solutions $\{|\psi_n(t,t_0)\rangle\}_n$ of Eq. (2.45) can be generated by suitable basis transformations.

into the time-dependent Schrödinger equation (2.39), yielding a LDE for the Floquet modes

$$\hat{Q}(t)\,|u_{nm}(t)\rangle = \epsilon_{nm}\,|u_{nm}(t)\rangle\,, \tag{2.53}$$

with the quasienergy operator $\hat{Q}(t) = \hat{H}(t) - \mathrm{i}\,\frac{\mathrm{d}}{\mathrm{d}t}$ [EA15, Hol16, Eck17]. As the Floquet modes $|u_{nm}(t)\rangle$ are time-periodic in T, time t can be considered as a coordinate under periodic boundary conditions $|u_{nm}(t+T)\rangle = |u_{nm}(t)\rangle$, suggesting the definition of a scalar product [Sam73, GH98, EA15, Eck17]

$$\langle\!\langle u|v\rangle\!\rangle = \frac{1}{T}\int_0^T \mathrm{d}t\ \langle u(t)|v(t)\rangle\,. \tag{2.54}$$

The states $|u\rangle\!\rangle$ are elements of an extended Floquet Hilbert space $\mathcal{F} = \mathcal{H}\otimes\mathcal{L}_T$, generated by the tensor product of the Hilbert space $\mathcal{H}$ of the physical quantum system and the space of square-integrable $T-$periodically functions $\mathcal{L}_T$ [Sam73, EA15]. For a state $|u\rangle\!\rangle \in \mathcal{F}$, the corresponding physical quantum state at time t is given by $|u(t)\rangle \in \mathcal{H}$, while a state $|v(t)\rangle = |v(t+T)\rangle$ is denoted $|v\rangle\!\rangle$ when it is considered to be an element of $\mathcal{F}$. For an operator $\hat{A}(t)$ that acts on $\mathcal{H}$, we analogues use the notation $\bar{A}$ in the composite space $\mathcal{F}$. Following this mathematical construction, the relation between the extended Floquet Hilbert space $\mathcal{F}$ and the physical Hilbert space $\mathcal{H}$ manifests itself in the scalar product of Eq. (2.54). Using these notations, the time-dependent equation (2.53) for the quasienergy operator $\hat{Q}(t)$ can be mapped onto an eigenvalue problem within the extended Floquet Hilbert space $\mathcal{F}$ [Sam73, EA15, Eck17]:

$$\bar{Q}\,|u_{nm}\rangle\!\rangle = \epsilon_{nm}\,|u_{nm}\rangle\!\rangle\,. \tag{2.55}$$

Eq. (2.55) resembles the form of a time-independent Schrödinger equation, allowing the application of concepts already known from autonomous quantum systems. In fact, the eigenstates and eigenvalues of the quasienergy operator $\bar{Q}$ are given by the Floquet modes $|u_{nm}\rangle\!\rangle$ and quasienergies ϵ_{nm}, similar to the stationary eigenstates and energies of a static Hamiltonian. However, there exists an essential difference between the solutions of Eq. (2.55) and those of an autonomous quantum system: While in the latter the eigenstates of the physical system are orthogonal to each other, orthonormal solutions of the quasienergy eigenvalue problem can lead to linearly dependent quantum states in the Hilbert space $\mathcal{H}$. In fact, as $\bar{Q}$ represents a Hermitian operator in $\mathcal{F}$, the Floquet modes $|u_{nm}\rangle\!\rangle$ can be chosen to build a complete orthonormal set

$$\begin{aligned}\langle\!\langle u_{n'm'}|u_{nm}\rangle\!\rangle = \frac{1}{T}\int_0^T \mathrm{d}t\ \langle u_{n'm'}(t)|u_{nm}(t)\rangle = \\ = \frac{1}{T}\int_0^T \mathrm{d}t\,\mathrm{e}^{i(m-m')\omega t}\ \langle u_{n'}(t)|u_n(t)\rangle = \delta_{nn'}\,\delta_{mm'},\end{aligned}$$

with eigenstates $|u_{nm}\rangle\!\rangle$, $|u_{nm'}\rangle\!\rangle$ $(m \neq m')$ that are orthogonal to each other in $\mathcal{F}$. However, applying Eq. (2.52), these basis states give rise to the same Floquet solution $|\psi_n(t)\rangle$ in $\mathcal{H}$. In this sense, the extended Floquet Hilbert space $\mathcal{F}$ and the associated eigenvalue problem of Eq. (2.55) contain a lot of redundant information, which is, however, compensated by the infinite number of quasienergies ϵ_{nm} and Floquet modes $|u_{nm}(t)\rangle$ with $m \in \mathbb{Z}$.

To further analyze the structure of the quasienergy operator $\bar{Q}$, we construct a complete orthonormal set of basis states $|\alpha m\rangle\!\rangle$ for the composite Hilbert space $\mathcal{F}$. This can be done by combining a complete set of orthonormal basis states $|\alpha\rangle$ of $\mathcal{H}$ with the time-periodic functions $\mathrm{e}^{\mathrm{i}m\omega t}$ [Sam73, GH98, EA15, Eck17]: $|\alpha m(t)\rangle = |\alpha\rangle\, \mathrm{e}^{\mathrm{i}m\omega t}$. Within this basis, the quasienergy operator adopts matrix elements

$$\langle\!\langle \alpha' m' | \bar{Q} | \alpha m \rangle\!\rangle = \frac{1}{T} \int_0^T \mathrm{d}t\ \langle \alpha' m'(t) | \hat{Q}(t) | \alpha m(t) \rangle = \langle \alpha' | \hat{H}^{(m-m')} | \alpha \rangle + m\,\omega\,\delta_{\alpha\alpha'}\,\delta_{mm'},$$

containing the Fourier transform of the time-periodic Hamiltonian

$$\hat{H}^{(m)} = \frac{1}{T} \int_0^T \mathrm{d}t\, \mathrm{e}^{\mathrm{i}m\omega t}\, \hat{H}(t), \quad \hat{H}(t) = \sum_m \mathrm{e}^{-\mathrm{i}m\omega t}\, \hat{H}^{(m)}. \tag{2.56}$$

The Fourier harmonic index m of the driving frequency ω provides a block structure of the quasienergy operator $\bar{Q} = \sum_{m',m} \hat{Q}^{(m',m)}\ |m'\rangle\!\rangle\langle\!\langle m|$, in which each block

$$\hat{Q}^{(m',m)} = \hat{H}^{(m-m')} + m\,\omega\,\delta_{mm'} \tag{2.57}$$

corresponds to an operator acting in the physical Hilbert space $\mathcal{H}$. This results in a block representation of the quasienergy operator

$$\bar{Q} = \begin{array}{c} \begin{array}{cccccc} m=-2 & m=-1 & m=0 & m=1 & m=2 & m=3 \end{array} \\ \left(\begin{array}{cccccc} \ddots & \vdots & \vdots & \vdots & \vdots & \iddots \\ \dots & \hat{H}^{(0)} - \omega & \hat{H}^{(1)} & \hat{H}^{(2)} & \hat{H}^{(3)} & \dots \\ \dots & \hat{H}^{(-1)} & \hat{H}^{(0)} & \hat{H}^{(1)} & \hat{H}^{(2)} & \dots \\ \dots & \hat{H}^{(-2)} & \hat{H}^{(-1)} & \hat{H}^{(0)} + \omega & \hat{H}^{(1)} & \dots \\ \dots & \hat{H}^{(-3)} & \hat{H}^{(-2)} & \hat{H}^{(-1)} & \hat{H}^{(0)} + 2\,\omega & \dots \\ \iddots & \vdots & \vdots & \vdots & \vdots & \ddots \end{array} \right) \begin{array}{c} m'=-2 \\ m'=-1 \\ m'=0 \\ m'=1 \\ m'=2 \\ m'=3 \end{array} \end{array} \tag{2.58}$$

that formally resembles the structure of a quantum system with Hilbert space $\mathcal{H}$ coupled to a photon-like mode in the classical limit of large photon numbers [EA15, Eck17, RL20b]. Based on this picture, the diagonal blocks $\hat{H}^{(0)} + m\,\omega$ of Eq. (2.58) can be considered as copies of the physical quantum system acting in the subspace of constant photon number m, while the off-diagonal blocks $\hat{H}^{(m\neq 0)}$ describe $m-$photon processes associated with the coupling to the fictitious photon-like mode. In this sense,

quasienergies ϵ_{nm} (cf. Eq. (2.51)) are generated by the absorption ($m > 0$) or emission ($m < 0$) of integer multiples of the photon energy ω, potentially revealing heating effects in the periodically driven quantum system [LDM14, DR14, Eck17, RL20a].

By exploiting a suitable unitary transformation $\bar{Q}_F = \bar{U}_F^\dagger \, \bar{Q} \, \bar{U}_F$ in the extended Floquet Hilbert space $\mathcal{F}$, the quasienergy operator $\bar{Q}$ of Eq. (2.58) can be block-diagonalized with respect to the quantum number m. This results in decoupled blocks $\hat{Q}_F^{(m',m)} = (\hat{H}_F + m\,\omega)\,\delta_{mm'}$ acting in the physical Hilbert space $\mathcal{H}$, and revealing an effective Hamiltonian $\hat{H}_F$ that provides the quasienergies (cf. Eq. (2.55)) of the periodically driven quantum system. In fact, $\bar{U}_F$ directly corresponds to a time-periodic unitary operator $\hat{U}_F(t+T) = \hat{U}_F(t)$ in the physical Hilbert space $\mathcal{H}$, generating a unitary transformation that leads to the effective Hamiltonian $\hat{H}_F$ of Eq. (2.47) [EA15, Eck17]. In this context, the unitary arbitrariness in the set of operators $\hat{H}_F$ and $\hat{U}_F(t)$ stems from the fact that multiplying $\hat{U}_F(t)$ by an arbitrary time-independent unitary operator $\hat{U}'_F(t) = \hat{U}_F(t)\,\hat{U}$ only leads to a mixing of states within the decoupled blocks, but does not destroy the block diagonal form. Thus, the block diagonalization of the quasienergy operator $\bar{Q}$ constitutes an appropriate starting point for the determination of the effective Hamiltonian $\hat{H}_F$, especially useful when the driving frequencies ω are large as compared to the energy scales of the system. In these cases, the diagonal blocks $\hat{H}^{(0)} + m\,\omega$ of Eq. (2.58) are already well separated from each other, such that the off-diagonal coupling terms $\hat{H}^{(m\neq 0)}$ can be neglected in good approximation. The effective Hamiltonian $\hat{H}_F$ is then well described by the time-averaged Hamiltonian $\hat{H}^{(0)} = \frac{1}{T}\int_0^T \mathrm{d}t\,\hat{H}(t)$, while first-order corrections around this approximation can be achieved in terms of a high-frequency expansion [BDP15, EA15]. There, couplings between the subspaces of constant photon number m are considered as virtual processes, eventually leading to light-induced topological phase transitions in the Floquet topological insulators [CDSM13, OK19, RL20a]. Generally speaking, this is at the heart of Floquet engineering [GD14, Hol16, Eck17], where analytical expressions for the effective Hamiltonian $\hat{H}_F$ are determined by means of the aforementioned approximation schemes.

Employing the block representation $\bar{Q} = \sum_{m',m} \hat{Q}^{(m',m)} \, |m'\rangle\!\rangle\langle\!\langle m|$ (cf. Eq. (2.57)), the quasienergy eigenvalue problem of Eq. (2.55) can be further reduced to a tight-binding model in frequency space [Shi65, RL20b]:

$$\sum_{m'} \left(\hat{H}^{(m-m')} - m\,\omega\,\delta_{mm'} \right) |u_n^{(m')}\rangle = \epsilon_n \, |u_n^{(m)}\rangle \,. \tag{2.59}$$

Here, we have used that

$$\langle\!\langle m'|\bar{Q}|u_{nm}\rangle\!\rangle = \sum_{m''} \hat{Q}^{(m',m'')} \, \langle\!\langle m''|u_{nm}\rangle\!\rangle = \sum_{m''} \hat{Q}^{(m',m'')} \, |u_n^{(m-m'')}\rangle \,,$$

and introduced the Fourier transform of the time-periodic Floquet mode

$$|u_n^{(m)}\rangle = \frac{1}{T}\int_0^T \mathrm{d}t\, \mathrm{e}^{\mathrm{i}m\omega t} \, |u_n(t)\rangle \,, \quad |u_n(t)\rangle = \sum_m \mathrm{e}^{-\mathrm{i}m\omega t} \, |u_n^{(m)}\rangle \,. \tag{2.60}$$

In Eq. (2.59), the Fourier harmonics of the driving frequency ω can be interpreted as the lattice sites of a Floquet lattice (for a schematic illustration see Fig. 2.1). The off-diagonal couplings constitute to time-independent hopping terms $\hat{H}^{(m\neq 0)}$ (cf. Eq. (2.56)),

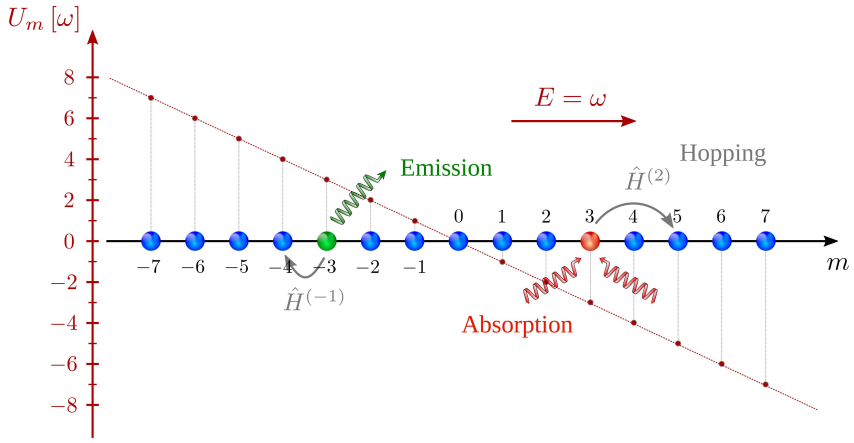

Figure 2.1: Floquet lattice of a periodically driven quantum system. Each lattice site (blue spheres) corresponds to a Fourier harmonic index m of the driving frequency ω, resembling a copy of the physical quantum system containing a relative number of photons m. The hopping terms $\hat{H}^{(m\neq 0)}$ describe processes in which the physical quantum system absorbs (red sphere, $m > 0$) or emits (green sphere, $m < 0$) a number of m photons from or to the external drive. The on-site term $\hat{H}^{(0)}$ is accompanied by a potential $U_m = -m\,\omega$ (brown line), which takes into account the energy costs of the photon processes and leads to a fictitious electric field $E = \omega$.

describing processes in which a photon is absorbed ($m > 0$) or emitted ($m < 0$) from or to the external drive. The on-site term $\hat{H}^{(0)}$ is accompanied by a potential $U_m = -m\,\omega$, which counts the photons at the corresponding site m and produces a fictitious electric field $E = \omega$. In this sense, the Floquet lattice resembles a Wannier-Stark ladder [Wan60, Wan62], with wave functions that provide physical interpretations for the Fourier coefficients $|u_n^{(m)}\rangle$ in limiting cases of the driving frequencies ω. In fact, depending on the relation between the photon energy ω and the energy scales of the Fourier components $\hat{H}^{(m)}$, the system is divided into a high- and low-frequency regime. In the high-frequency limit, the wave function in the frequency domain becomes Wannier localized at the individual Fourier harmonic index m, with a quasienergy determined by the effective Hamiltonian $\hat{H}_F$. In the low-frequency regime, however, the Fourier coefficients $|u_n^{(m)}\rangle$ are described by a Bloch wave function that experiences a small perturbation with respect to the fictitious electric field $E = \omega$. This approach is the very origin of the Thouless pump [Tho83], in which a one-dimensional system is extended to a two-dimensional quantum Hall scenario [KDP80, PG90] by inducing an additional Floquet lattice direction through a time-periodic drive. Assuming the associated Bloch Hamiltonian exhibits a nontrivial topological band structure in the composite space of crystal and time momentum, the Hall conductance generated by the fictitious electric field $E = \omega$ translates into a motion in the spatial direction of the one-dimensional system. Throughout the periodicity T, this reveals a time-averaged charge pump proportional to the topological invariant of the synthetic Hall regime [TKNdN82, Tho83, OK19]. Generalizing this fundamental concept to multifrequency drives, we demonstrate in the next section that this approach can even induce topological phenomena solely rooted in dimensions of time.

2.3 Quasiperiodically Driven Quantum Systems

We generalize Floquet theory (see Sec. 2.2) to quasiperiodically driven quantum systems, demonstrating that the latter provide a paradigmatic platform for the generation of topological phenomena in dynamically-induced synthetic dimensions. To this end, we expand the driven system in its Fourier modes, revealing a projection of the quasiperiodic dynamics to a higher-dimensional Floquet lattice [HCT83, CT04, EA15, VPM16]. Using methods already known from Bloch's theorem [Blo29, Kit71, AM76], we show that the underlying tight-binding model forms a band structure in the synthetic BZ of the Floquet lattice. We address the dynamics in the Floquet lattice by means of the semiclassical equations of motion [CN95, CN96, SN99], which account for virtual transitions between the synthetic energy bands and yield a transverse response characterized by a nontrivial Berry phase term [Ber84]. The associated motion in the frequency domain corresponds to a process in which photons of different frequencies are exchanged between the external drives, referred to as frequency conversion. The latter turns into a topological quantity once the entire synthetic BZ is sufficiently sampled, yielding a time-averaged pumping rate proportional to the topological invariant of the synthetic energy band [MRH17]. We argue that this illustrative picture is fully consistent with the results of APT (see Sec. 2.1.3), reflecting a generic mechanism of topological quantization in terms of linear response theory [Kub57, Mah00].

2.3.1 Higher-Dimensional Floquet Lattice

We investigate the dynamics of a quantum system that is exposed to a number of D external periodic drives, described by a quantum state $|\Psi(t)\rangle$ that follows the unitary evolution of the time-dependent Schrödinger equation [Sch26, Sha08, GS18]

$$\mathrm{i}\,\frac{\mathrm{d}}{\mathrm{d}t}\,|\Psi(t)\rangle = \hat{H}(\vec{\varphi}_t)\,|\Psi(t)\rangle\,. \tag{2.61}$$

The Hamiltonian $\hat{H}(\vec{\varphi}_t) = \hat{H}_0 + \sum_{j=1}^{D} \hat{H}_j(\varphi_{j,t})$ is composed of two kinds of contributions: The static Hamiltonian $\hat{H}_0$ of the autonomous quantum system, and the time-dependent Hermitian operators $\hat{H}_j(\varphi_{j,t})$ accounting for the couplings to the external drives. We assume that the time-dependent phases $\vec{\varphi}_t = (\varphi_{1,t},\, \varphi_{2,t},\, \ldots,\, \varphi_{D,t}) = \vec{\omega}\,t + \vec{\phi}$ linearly evolve in the $D-$dimensional parameter space $\vec{\varphi}_t \in \mathbb{R}^D$, with an explicit motion that is characterized by the set of frequencies $\vec{\omega} = (\omega_1,\, \omega_2,\, \ldots,\, \omega_D)$ and offset phases $\vec{\phi} = (\phi_1,\, \phi_2,\, \ldots,\, \phi_D)$ of the driving fields. The frequencies $\omega_j = \frac{2\pi}{T_j}$ correspond to the periodicities T_j of the drives, revealing a dynamical modulation of the operators $\hat{H}_j(\varphi_{j,t})$ that is $2\pi-$periodic in the individual phase components

$$\hat{H}_j(\varphi_{j,t+T_j}) = \hat{H}_j(\varphi_{j,t} + 2\,\pi) = \hat{H}_j(\varphi_{j,t}). \tag{2.62}$$

The Hamiltonian $\hat{H}(\vec{\varphi}_t)$ provides a concrete example of the generic quantum system of Sec. 2.1.1, meaning that the solutions to Eq. (2.61) can be immediately investigated using the presented techniques of Sec. 2.1. There, we have shown that the time-evolution in a given direction of the parameter space induces a geometrical response

proportional to the Berry curvature [Ber84] of the adiabatic energy band (see Sec. 2.1.4), a fundamental concept described in terms of first-order APT (see Sec. 2.1.3). In what follows, however, we solve the dynamics of the driven quantum system using concepts from Floquet theory (see Sec. 2.2), revealing an analogy between the results of Sec. 2.1 and the semiclassical equations of motion in a higher-dimensional Floquet lattice [HCT83, CT04, EA15, VPM16]. To this end, we restrict ourselves to quasiperiodic driving[16]

$$\vec{m}\,\vec{\omega} = 0, \quad \vec{m} \in \mathbb{Z}^D \quad \Leftrightarrow \quad \vec{m} = 0, \tag{2.63}$$

and argue that the geometrical properties of the dynamical synthetic quantum matter can be illustrated by means of a Floquet counterpart of an integer quantum Hall scenario [MRH17].

We start our investigation by parametrizing a fundamental and orthonormal set of basis states $\{|\psi_n(t)\rangle\}_n$ of the quasiperiodically driven quantum system in terms of the generalized Floquet solutions[17] $|\psi_n(t)\rangle = \mathrm{e}^{-\mathrm{i}\,\epsilon_n t}\,|u_n(\vec{\varphi}_t)\rangle$ (cf. Eq. (2.45)), where the Floquet modes $|u_n(\vec{\varphi}_t)\rangle$ can be expanded in the vector of Fourier harmonic indices $\vec{m} = (m_1, m_2, \ldots, m_D)$ of the driving frequencies $\vec{\omega}$ (cf. Eq. (2.60)):

$$|u_n(\vec{\varphi}_t)\rangle = \sum_{\vec{m}} \mathrm{e}^{-\mathrm{i}\,\vec{m}\,\vec{\varphi}_t}\,|u_n^{(\vec{m})}\rangle\,, \quad |u_n^{(\vec{m})}\rangle = \frac{1}{(2\pi)^D}\int\cdots\int_0^{2\pi} \mathrm{d}^D\vec{\varphi}\,\mathrm{e}^{\mathrm{i}\,\vec{m}\,\vec{\varphi}}\,|u_n(\vec{\varphi})\rangle\,. \tag{2.64}$$

Inserting this ansatz into the time-dependent Schrödinger equation (2.61), the quasienergies ϵ_n and Fourier coefficients $|u_n^{(\vec{m})}\rangle$ of the Floquet solutions $|\psi_n(t)\rangle$ are determined by a tight-binding model in frequency space (cf. Eq. (2.59))

$$\sum_{\vec{m}'}\left(\hat{H}^{(\vec{m}-\vec{m}')} - \vec{m}\,\vec{\omega}\,\delta_{\vec{m}\vec{m}'}\right)|u_n^{(\vec{m}')}\rangle = \epsilon_n\,|u_n^{(\vec{m})}\rangle\,, \tag{2.65}$$

with coupling terms $\hat{H}^{(\vec{m})}$ corresponding to the Fourier coefficients of the Hamiltonian (cf. Eq. (2.56))

$$\hat{H}^{(\vec{m})} = \frac{1}{(2\pi)^D}\int\cdots\int_0^{2\pi}\mathrm{d}^D\vec{\varphi}\,\mathrm{e}^{\mathrm{i}\,\vec{m}\,\vec{\varphi}}\,\hat{H}(\vec{\varphi}), \quad \hat{H}(\vec{\varphi}_t) = \sum_{\vec{m}}\mathrm{e}^{-\mathrm{i}\,\vec{m}\,\vec{\varphi}_t}\,\hat{H}^{(\vec{m})}. \tag{2.66}$$

Eq. (2.65) represents the quasiperiodic analog of the Floquet lattice of a periodically driven quantum system (cf. Fig. 2.1). In fact, the vector of Fourier harmonic indices $\vec{m}$ provides a position in a higher-dimensional Floquet lattice (for a schematic illustration see Fig. 2.2), in which the number of Floquet lattice dimensions equals the number of incommensurate driving frequencies ω_j, as described by Eq. (2.63). Each lattice site $\vec{m} = (m_1, m_2, \ldots, m_D)$ corresponds to a copy of the quantum system acting in the

[16] In case of two external periodic drives ($D = 2$), Eq. (2.63) translates into frequencies ω_1 and ω_2 that are irrationally related to each other: $\frac{\omega_1}{\omega_2} \notin \mathbb{Q}$.

[17] Note that such an ansatz is justified because of the $2\pi-$periodicity of the Hamiltonian $\hat{H}(\vec{\varphi}_t)$ in each phase component $\varphi_{j,t}$, as described in Eq. (2.62). In fact, this implies an expansion of $\hat{H}(\vec{\varphi}_t)$ in its Fourier modes (cf. Eq. (2.66)), and suggests that the Floquet modes $|u_n(\vec{\varphi}_t)\rangle$ obey the same periodicity (cf. Eq. (2.64)).

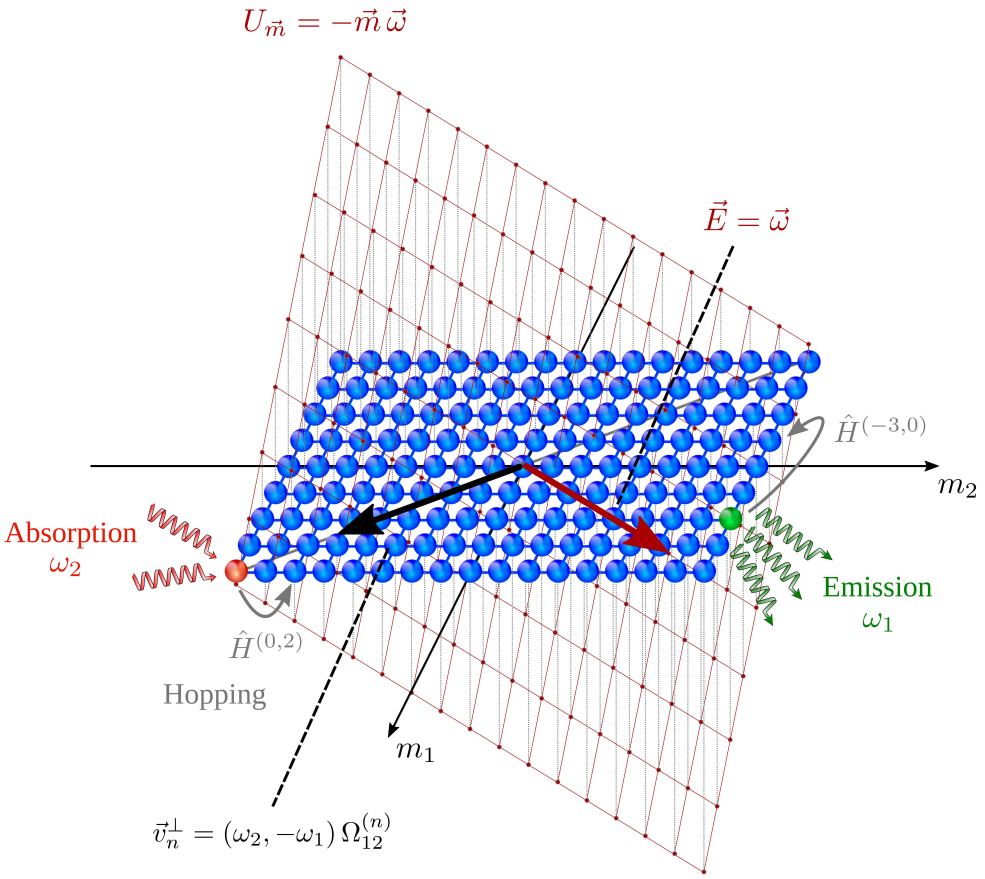

Figure 2.2: Higher-dimensional Floquet lattice of a quasiperiodically driven quantum system. For illustration, we restrict ourselves to the case of two external driving fields with incommensurate frequencies ω_1 and ω_2. Each lattice site (blue spheres) corresponds to the vector of Fourier harmonic indices $\vec{m} = (m_1, m_2)$ of the driving frequencies $\vec{\omega} = (\omega_1, \omega_2)$, resembling a copy of the quantum system containing a relative number of m_j photons of the individual drives. The hopping terms $\hat{H}^{(\vec{m}\neq 0)}$ describe processes in which the quantum system absorbs (red sphere, $m_j > 0$) or emits (green sphere, $m_j < 0$) a number of m_j photons from or to the external fields with frequencies ω_j. The on-site term $\hat{H}^{(\vec{m}=0)}$ is accompanied by a potential $U_{\vec{m}} = -\vec{m}\,\vec{\omega}$, which takes into account the energy costs of the photon processes and leads to a fictitious electric field $\vec{E} = \vec{\omega}$. If the system exhibits a nontrivial topological band structure in the synthetic 2D *Brillouin zone* (BZ) of the two-dimensional Floquet lattice (cf. Fig. 2.3), the semiclassical equations of motion yield an anomalous velocity $\vec{v}_n^{\perp} = (\omega_2, -\omega_1)\,\Omega_{12}^{(n)}$ (cf. Eq. (2.69)) along the equipotential lines of the potential $U_{\vec{m}} = -m_1\,\omega_1 - m_2\,\omega_2 = \text{const.}$, translating into an energy pumping between the driving fields.

subspace of constant photon numbers m_j, while off-diagonal couplings constitute to time-independent hopping terms $\hat{H}^{(\vec{m}\neq 0)}$ that describe processes in which photons are absorbed ($m_j > 0$) or emitted ($m_j < 0$) from or to the external drives with frequencies ω_j. The on-site term $\hat{H}^{(\vec{m}=0)}$ is accompanied by a potential $U_m = -\vec{m}\,\vec{\omega}$, which counts the photons at the corresponding site $\vec{m}$ and produces a fictitious electric field $\vec{E} = \vec{\omega}$.

As for the extended Hilbert space of a periodically driven quantum system (see Sec. 2.2.3), the higher-dimensional Floquet lattice contains a lot of redundant information. In fact, assuming that $|u_n^{(\vec{m})}\rangle$ is a solution to the tight-binding model with quasienergy ϵ_n, it is straightforward to show that $|u_{n\vec{m}'}^{(\vec{m})}\rangle = |u_n^{(\vec{m}+\vec{m}')}\rangle$ with quasienergy $\epsilon_{n\vec{m}'} = \epsilon_n + \vec{m}'\,\vec{\omega}$ solves Eq. (2.65) for any combination of $\vec{m}'$ as well. Apart from an unimportant total phase factor, this leads to the same Floquet state

$$|\psi_{n\vec{m}'}(t)\rangle = \mathrm{e}^{-\mathrm{i}\,\epsilon_{n\vec{m}'}\,t} \sum_{\vec{m}} \mathrm{e}^{-\mathrm{i}\,\vec{m}\,\vec{\varphi}_t}\ |u_{n\vec{m}'}^{(\vec{m})}\rangle = \mathrm{e}^{-\mathrm{i}\,\epsilon_n\,t} \sum_{\vec{m}} \mathrm{e}^{-\mathrm{i}\,\vec{m}\,\vec{\phi}}\,\mathrm{e}^{-\mathrm{i}\,(\vec{m}+\vec{m}')\,\vec{\omega}\,t}\ |u_n^{(\vec{m}+\vec{m}')}\rangle =$$
$$= \mathrm{e}^{\mathrm{i}\,\vec{m}'\,\vec{\phi}}\,\mathrm{e}^{-\mathrm{i}\,\epsilon_n\,t} \sum_{\vec{m}} \mathrm{e}^{-\mathrm{i}\,\vec{m}\,\vec{\varphi}_t}\ |u_n^{(\vec{m})}\rangle = \mathrm{e}^{\mathrm{i}\,\vec{m}'\,\vec{\phi}}\ |\psi_n(t)\rangle\,.$$

In the next section, we use this degree of freedom to implement topological phenomena solely rooted in the synthetic dimensions of frequency space, concentrating on the case of two external driving fields ($D = 2$) for simplicity. By assuming a nontrivial band structure in the synthetic 2D BZ of the two-dimensional Floquet lattice, the semiclassical equations of motion [CN95, CN96, SN99] reveal an anomalous velocity $\vec{v}_n^{\perp} = (\omega_2, -\omega_1)\,\Omega_{12}^{(n)}$ (cf. Eq. (2.69)) transverse to the fictitious electric field $\vec{E} = \vec{\omega}$. As the anomalous response runs along the equipotential lines of the potential $U_{\vec{m}} = -m_1\,\omega_1 - m_2\,\omega_2 = \text{const.}$, this Hall scenario translates into an energy pumping between the external driving fields [MRH17].

2.3.2 Semiclassical Equations of Motion

Assuming that the fictitious electric field $\vec{E} = \vec{\omega}$ shows energy scales much smaller than those of the Fourier components $\hat{H}^{(\vec{m})}$ of Eq. (2.66), the dynamics in the higher-dimensional Floquet lattice can be described in terms of the semiclassical formulation of electron dynamics in a spatially periodic lattice [XCN10, CF21]. In its original form, this approach reveals Bloch electrons that behave almost like free particles in vacuum, provided that their energy dispersion $E(\vec{\varphi}) = |\vec{\varphi}|^2/2$ ($m = 1$) with Bloch quasimomenta $\vec{\varphi}$ is replaced by the band dispersion $E_n(\vec{\varphi})$ of the crystal [Kit71, AM76]. The latter results in a band group velocity $\partial_{\varphi_k} E_n(\vec{\varphi})$, which has been shown to be essential for the generation of Bloch oscillations in the periodic lattice [Blo29]. However, if the crystal is exposed to a static electric field, Bloch electrons can even show phenomena that go beyond Bloch oscillations [Blo62]. In this context, it has been demonstrated that couplings between energy bands can induce corrections to the band group velocity of the Bloch wave function, eventually revealing an anomalous velocity transverse to the electric field [KL54, KL57, AB59]. While these first-order corrections already provided insights on the Hall conductance of the anomalous Hall effect [JNM02, NSO$^+$10], it has later been shown that the anomalous response can even be projected onto a local geometrical

quantity, the Berry curvature of the occupied energy band [CN95, CN96, SN99]. This observation paved the way for a variety of intriguing Berry phase effects [Ber84] in condensed matter materials, including the modern description of quantum Hall effects, electric polarization, or quantum charge pumps [BMK+03, XCN10, Van18].

We apply the semiclassical formulation of electron dynamics to the Bloch solutions of the two-dimensional Floquet lattice ($D = 2$), revealing a Floquet counterpart of an integer quantum Hall scenario [MRH17]. For vanishing frequency $\vec{\omega} = 0$, the Floquet lattice becomes periodic in the synthetic space, which is why Bloch's theorem [Blo29, Kit71, AM76] can be applied to diagonalize the tight-binding model of Eq. (2.65). The wave functions of the Fourier coefficients $|u_n^{(\vec{m})}\rangle$ (cf. Eq. (2.60)) are then described by Bloch solutions

$$|u_n^{(\vec{m})}\rangle = \mathrm{e}^{\mathrm{i}\,\vec{m}\,\vec{\varphi}}\;|\tilde{u}_n(\vec{\varphi})\rangle\,, \tag{2.67}$$

leading to quasienergies $\epsilon_n(\vec{\varphi}) = E_n(\vec{\varphi})$ that correspond to the energy eigenvalues of the physical quantum system: $\hat{H}(\vec{\varphi})\;|\tilde{u}_n(\vec{\varphi})\rangle = E_n(\vec{\varphi})\;|\tilde{u}_n(\vec{\varphi})\rangle$. As the individual phase components φ_j of the Hamiltonian $\hat{H}(\vec{\varphi})$ can be projected to an interval of size 2π (cf. Eq. (2.62)), the phases $\vec{\varphi} = (\varphi_1, \varphi_2)$ can be interpreted as Bloch quasimomenta, revealing a synthetic 2D BZ of the two-dimensional Floquet lattice (for a schematic illustration see Fig. 2.3). In this sense, the Hamiltonian $\hat{H}(\vec{\varphi})$ constitutes to the Bloch Hamiltonian of the periodic system, with energy levels $\{E_n(\vec{\varphi})\}_n$ that generate a Bloch band structure in the synthetic 2D BZ. Assuming the Bloch wave functions of Eq. (2.67) form a wave-packet restricted to the synthetic energy band $E_n(\vec{\varphi})$, the dynamics of the Fourier harmonic indices m_k is governed by the semiclassical equations of motion [CN95, CN96, SN99]

$$\dot{m}_k^{(n)}(\vec{\varphi}) = \frac{\partial E_n(\vec{\varphi})}{\partial \varphi_k} - \sum_{l=1}^{D}\sum_{r=1}^{3} \epsilon_{klr}\,\omega_l\,\Omega_r^{(n)}(\vec{\varphi}), \quad \text{with} \quad \dot{\vec{\varphi}} = \vec{\omega}. \tag{2.68}$$

At zeroth order, the band group velocity of the wave-packet generates Bloch oscillations $\partial_{\varphi_k} E_n(\vec{\varphi})$ [Blo29], while first-order corrections involve a Berry phase term associated with the $r-$th component of the Berry curvature[18] $\vec{\Omega}^{(n)}(\vec{\varphi}) = \mathrm{i}\,\nabla_{\vec{\varphi}} \times \langle \tilde{u}_n(\vec{\varphi})|\nabla_{\vec{\varphi}}\,\tilde{u}_n(\vec{\varphi})\rangle$ (cf. Eq. (2.23)). The latter implies synthetic Hall physics in the frequency domain, with an anomalous velocity

$$\vec{v}_n^{\perp}(\vec{\varphi}) = \begin{pmatrix} \omega_2 \\ -\omega_1 \end{pmatrix} \Omega_{12}^{(n)}(\vec{\varphi}) \tag{2.69}$$

transverse to the fictitious electric field $\vec{E} = \vec{\omega}$. The anomalous response is proportional to the Berry curvature $\Omega_{kl}^{(n)}(\vec{\varphi}) = 2\,\mathrm{Im}[\langle \partial_{\varphi_k}\,\tilde{u}_n(\vec{\varphi})|\partial_{\varphi_l}\,\tilde{u}_n(\vec{\varphi})\rangle]$ (cf. Eqs. (2.22) and (2.24)), and translates into an energy transfer between the external drives that goes along the equipotential lines of the potential $U_{\vec{m}} = -m_1\,\omega_1 - m_2\,\omega_2 = \text{const.}$ (for a schematic illustration see Fig. 2.2). At the same time, the Bloch quasimomenta $\vec{\varphi} = (\varphi_1, \varphi_2)$ undergo an evolution $\vec{\varphi}_t = \vec{\omega}\,t + \vec{\phi}$, revealing the original dynamics of the quasiperiodically driven quantum system.

[18] Note that we assume a complete orthonormal set of Bloch modes $\{|\tilde{u}_n(\vec{\varphi})\rangle\}_n$.

Let us take a closer look at the energy pumping effect. The total energy transfer rate of the quasiperiodically driven quantum system with Hamiltonian $\hat{H}(\vec{\varphi}_t) = \hat{H}_0 + \sum_{k=1}^{D} \hat{H}_k(\varphi_{k,t})$ is given by (cf. Eq. (2.19))

$$\frac{\mathrm{d}}{\mathrm{d}t} \langle \hat{H}(\vec{\varphi}_t) \rangle = \langle \partial_t \hat{H}(\vec{\varphi}_t) \rangle = \sum_{k=1}^{D} \omega_k \, \langle \hat{\mathrm{I}}_k(\vec{\varphi}_t) \rangle \,, \quad \hat{\mathrm{I}}_k(\vec{\varphi}_t) = \partial_{\varphi_k} \hat{H}_k(\varphi_{k,t}),$$

where the expectation values are calculated according to the exact solution $|\Psi(t)\rangle$ of the time-dependent Schrödinger equation (2.61). The semiclassical equations of motion (2.68) apply whenever the energy gaps of the synthetic band structure exceed the energy scales of the frequencies ω_j, which is why the expectation value of the $k-$th component of the current operator $\langle \hat{\mathrm{I}}_k(\vec{\varphi}_t) \rangle$ can be expanded by means of first-order APT (cf. Eq. (2.20)):

$$\langle \hat{\mathrm{I}}_k(\vec{\varphi}_t) \rangle_n = \frac{\partial E_n(\vec{\varphi}_t)}{\partial \varphi_k} + \sum_{l=1}^{D} \omega_l \, \Omega_{kl}^{(n)}(\vec{\varphi}_t). \tag{2.70}$$

Comparing this result with the semiclassical equations of motion (2.68), we find that the dynamics of the Fourier harmonic indices $\dot{m}_k^{(n)}$ exactly corresponds[19] to the expectation value of Eq. (2.70). In this sense, the fictitious electric field $\vec{E} = \vec{\omega}$ of the higher-dimensional Floquet lattice couples to the current operator $\hat{\mathbf{I}}(\vec{\varphi}_t) = \nabla_{\vec{\varphi}} \hat{H}(\vec{\varphi}_t)$ of the underlying quantum system (cf. Eq. (2.19)), allowing for additional insights into the physics of Eq. (2.68): As $\hat{\mathbf{I}}(\vec{\varphi}_t)$ exhibits off-diagonal matrix elements (cf. Eq. (2.11)), its coupling to $\vec{E}$ induces virtual transitions between the synthetic energy bands (cf. Eq. (2.18)), which can eventually be projected onto the Berry curvature $\Omega_{kl}^{(n)}(\vec{\varphi}_t)$ of the adiabatic energy band $E_n(\vec{\varphi}_t)$ (cf. Eq. (2.20)). The dynamics of the Bloch wave-packet of Eq. (2.68) then induces processes in which photons of different frequencies ω_k are absorbed or emitted by the quantum system, revealing energy pumping rates

$$\dot{W}_k^{(n)}(t) = \omega_k \, \langle \hat{\mathrm{I}}_k(\vec{\varphi}_t) \rangle_n = \omega_k \, \dot{m}_k^{(n)}(\vec{\varphi}_t) \tag{2.71}$$

for the individual driving fields. Analogous to first-order APT (see Sec. 2.1.3), the semiclassical equations of motion (2.68) and the associated energy pumping rates (2.71) are thus associated with a first-order perturbative expansion with respect to the fictitious electric field $\vec{E} = \vec{\omega}$.

2.3.3 Topological Response

The anomalous response of Eq. (2.70) strongly depends on the explicit details of the quasiperiodically driven quantum system. Namely, modifying the properties of the Bloch Hamiltonian $\hat{H}(\vec{\varphi})$ changes both the Bloch mode $|\tilde{u}_n(\vec{\varphi})\rangle$ of Eq. (2.67) and the associated Berry curvature $\Omega_{kl}^{(n)}(\vec{\varphi}) = 2\,\mathrm{Im}[\langle \partial_{\varphi_k} \tilde{u}_n(\vec{\varphi}) | \partial_{\varphi_l} \tilde{u}_n(\vec{\varphi}) \rangle]$ (cf. Eq. (2.22)). To

[19] Although the semiclassical equations of motion (2.68) are usually applied in two ($D = 2$) or three ($D = 3$) dimensions, the representation of Eq. (2.70) also holds for arbitrary dimensions of the parameter space $\vec{\varphi}_t \in \mathbb{R}^D$ (cf. Eq. (2.20)).

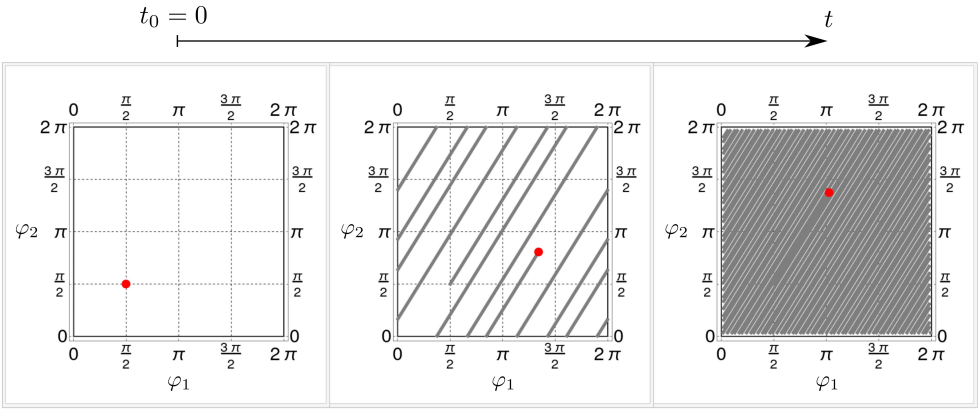

Figure 2.3: Schematic illustration of the synthetic 2D *Brillouin zone* (BZ) of the two-dimensional Floquet lattice (cf. Fig. 2.2). The phases $\vec{\varphi} = (\varphi_1, \varphi_2)$ take the role of Bloch quasimomenta, undergoing a time-evolution $\vec{\varphi}_t = \vec{\omega}\, t + \vec{\phi}$ (illustrated by gray lines and red dot) described by the semiclassical equations of motion (2.68). Starting from $t_0 = 0$, the quasiperiodic dynamics entirely covers the torus structure $\mathbb{T}^2$ of the 2D BZ, such that the geometrical response in terms of the anomalous velocity $\vec{v}_n^{\perp}(\vec{\varphi}) = (\omega_2, -\omega_1)\, \Omega_{12}^{(n)}(\vec{\varphi})$ (cf. Eq. (2.69)) turns into a topological quantity. In two dimensions, this yields a topological frequency conversion proportional to the first Chern number $C_n = \frac{1}{2\pi} \int\!\!\int_0^{2\pi} \mathrm{d}^2\vec{\varphi}\, \Omega_{12}^{(n)}(\vec{\varphi})$ of the associated Bloch energy band $E_n(\vec{\varphi})$ (cf. Eq. (2.73)).

observe robust and quantized transport signatures, such as those predicted for the integer quantum Hall effect [KDP80, PG90], the Berry curvature $\Omega_{kl}^{(n)}(\vec{\varphi})$ has to be integrated over the closed manifold of the synthetic BZ of the higher-dimensional Floquet lattice. In this case, the geometrical response turns into a global topological quantity robust to continuous deformations of the synthetic energy bands $E_n(\vec{\varphi})$, thus revealing quantized response signals in a variety of topological systems [Tho98, Wen17].

In Fig. 2.3, we provide a schematic illustration of the synthetic 2D BZ of the two-dimensional Floquet lattice (cf. Fig. 2.2). The phases $\vec{\varphi} = (\varphi_1, \varphi_2)$ characterize the Bloch solutions of Eq. (2.67), and can be interpreted as the Bloch quasimomenta defined on the two-dimensional surface of a torus $\mathbb{T}^2$ (cf. Eq. (2.62)). Applying the semiclassical equations of motion (2.68), the 2D BZ is discovered by the time-dependent phases $\vec{\varphi}_t = \vec{\omega}\, t + \vec{\phi}$, the latter revealing the original phase evolution of the quasiperiodically driven quantum system. As the two frequencies $\frac{\omega_1}{\omega_2} \notin \mathbb{Q}$ are incommensurate, this yields a situation in which the quasiperiodic dynamics of the Bloch wave-packet entirely samples the synthetic 2D BZ of the system. Averaging the pumping rates of Eqs. (2.20) and (2.70) over a long period of time[20], this translates into an integration over the

[20] In Eq. (2.72), the limit $t \mapsto \infty$ formally requires vanishing frequencies $\omega_k \mapsto 0$, such that the semiclassical equations of motion (2.68) apply throughout the whole time process. In the numerical simulations performed in this Thesis, we choose the time scales and frequencies such that both the synthetic BZ is adequately sampled and the semiclassical formulation holds at all times for broad parameter ranges of the system.

closed manifold of the two-dimensional torus $\mathbb{T}^2$:

$$P_{n,k} = \lim_{t\mapsto\infty} \frac{\omega_k}{t} \int_0^t \mathrm{d}t' \, \langle \hat{\mathrm{I}}_k(\vec{\varphi}_{t'}) \rangle_n = \frac{\omega_k}{(2\pi)^2} \iint_0^{2\pi} \mathrm{d}^2\vec{\varphi} \, \langle \hat{\mathrm{I}}_k(\vec{\varphi}) \rangle_n \,. \tag{2.72}$$

Due to the symmetry of the synthetic energy bands $E_n(\vec{\varphi})$ (cf. Eq. (2.61)), the Bloch oscillations $\partial_{\varphi_k} E_n(\vec{\varphi})$ do not contribute to this integration. The first-order corrections, however, provide an integrated Berry curvature $\Omega_{kl}^{(n)}(\vec{\varphi})$ that results in a time-averaged pumping rate [MRH17]

$$P_n^{12} = -P_n^{21} = \frac{C_n}{2\pi} \, \omega_1 \, \omega_2 \tag{2.73}$$

proportional to the first Chern number [Che46, TKNdN82, QHZ08]

$$C_n = \frac{1}{2\pi} \iint_0^{2\pi} \mathrm{d}^2\vec{\varphi} \, \Omega_{12}^{(n)}(\vec{\varphi}). \tag{2.74}$$

The Chern number C_n is nothing else than the Berry phase calculated along the torus structure $\mathbb{T}^2$ of the 2D BZ, divided by 2π (cf. Eqs. (2.23) and (2.24)). The associated result only takes integer values, which is why changes of C_n can only occur discontinuously. In fact, the Chern number C_n remains invariant as long as the energy gaps of the synthetic band structure are finite, revealing a quantization of the time-averaged pumping rate P_n^{12} that is robust to smooth modifications of the Hamiltonian $\hat{H}(\vec{\varphi}_t)$ of the quasiperiodically driven quantum system.

Eq. (2.73) demonstrates that the quantized energy pumping effects of the dynamical synthetic quantum matter are governed by the topological properties of the underlying Bloch Hamiltonian $\hat{H}(\vec{\varphi})$, an observation that arises from the coupling of a small perturbation to the off-diagonal terms of the current operator $\hat{\mathbf{I}}(\vec{\varphi}) = \nabla_{\vec{\varphi}} \hat{H}(\vec{\varphi})$ (cf. Eqs. (2.11) and (2.19)). Remarkably, these off-diagonal coupling terms can eventually be projected onto the adiabatic Berry curvature $\Omega_{kl}^{(n)}(\vec{\varphi}) = 2\,\mathrm{Im}[\langle \partial_{\varphi_k} \tilde{u}_n(\vec{\varphi}) | \partial_{\varphi_l} \tilde{u}_n(\vec{\varphi}) \rangle]$ of the occupied Bloch modes $|\tilde{u}_n(\vec{\varphi})\rangle$ (cf. Eqs. (2.20) and (2.70)), while integration over the closed manifold of the BZ yields robust response signals proportional to the topological invariants of the associated synthetic energy bands $E_n(\vec{\varphi})$ (cf. Eqs. (2.72) and (2.73)). We have illustrated this mechanism using two equivalent methods, APT (see Sec. 2.1.3) and the semiclassical formulation of electron dynamics (see Sec. 2.3.2), showing that virtual couplings between (synthetic) energy bands are indeed essential for the generation of the aforementioned features. We argue that these results reflect a fundamental concept of topological quantization, already applied in the theoretical development of the integer quantum Hall effect [KDP80, PG90]. There, the linear response signal can be derived in terms of the celebrated Kubo formula [Kub57, Mah00], in which first-order corrections of the state due to an external field produce a (synthetic) Hall conductance that is directly related to the adiabatically defined topological invariant of the occupied (synthetic) Bloch bands [Lau81, TKNdN82, Sim83a, Koh85, Hal88]. In this sense, both the Kubo formula and the aforementioned methods reveal a correspondence between quantized physical observables and adiabatically defined topological invariants, a mechanism that finds applications in a variety of (synthetic) condensed matter materials [Tho98, XCN10, Van18, CF21]. In the remainder of this Thesis, we

apply these generic topological concepts to the Floquet counterpart of a Chern insulator [MRH17], and show that interacting extensions of this dynamical setup can even lead to intriguing topological phenomena solely induced by correlation effects between the constituents [KPBT20, KPBT22]. An outstanding example of this kind is the TBGE (see Sec. 4.2), which states that the aforementioned topological correspondence can be fundamentally modified in open quantum systems.

3

Correlations in Dynamical Synthetic Dimensions

Contents

The emergence of topological phenomena in dynamical synthetic quantum matter often relies on the effective dimensional extension of the system by time-periodic drives, as anticipated by Thouless in the topologically quantized charge pump [Tho83]. Following this line of reasoning, Martin *et al.* [MRH17] have demonstrated that quasiperiodically driven quantum systems provide a paradigmatic platform for the generation of synthetic quantum Hall physics in the frequency domain, with a transverse response that translates into a robust and quantized energy transfer between the quasiperiodic external drives (see Sec. 2.3). Starting from this illustrative picture, they have applied the geometrical concepts of dynamical synthetic dimensions to the concrete example of a *topological frequency converter* (TFC), which can be interpreted as the Floquet counterpart of a Chern insulator [Hal88, QWZ06, BHZ06]. In the TFC, a single spin-1/2 subjected to two circularly polarized drives mediates a frequency conversion between the classical modes, the latter occurring at a topologically quantized rate proportional to the adiabatic winding number [Vol03, QWZ06, QHZ08] of the driven spin. However, for both the Thouless pump and the TFC, there is limited understanding of the consequences of interparticle interactions on the associated linear response signals. Typically, the effects of interactions are addressed only with respect to the robustness of the dynamical topological response. What needs to be better understood is what topological effects can be interaction-driven in such time-dependent settings.

In this Chapter, we present a simple and feasible example of how interactions can qualitatively change the topological properties of a quantum system with dynamically-induced synthetic dimensions, revealing correlated topological phases that have no counterpart to the noninteracting regime. To this end, we add spin-spin interaction to the TFC, showing that the aforementioned correlated features already appear for the simplest generalization, namely two interacting spins exposed to two incommensurate periodic drives. As the quantized response is associated with both the frequency conversion and the interplay of interaction and synthetic dimension, we coin this minimal setup an *interacting topological frequency converter* ITFC. An experimental realization of the ITFC could be achieved in gated double quantum dots [PJT$^+$05, BFT$^+$15, SPF$^+$19] or in superconducting quantum circuits [SKK$^+$14, RNC$^+$14]. By calculating the topological phase diagrams of the ITFC as a function of interaction strength, we demonstrate the appearance of topological responses that are explicitly forbidden in the noninteracting case of two identical spins: The topological invariants determining the frequency conversion can take odd integer values. This extended set of topological numbers, in turn, can result in an enhancement of the dynamical response of the ITFC.

The Chapter is organized as follows: In Sec. 3.1, we introduce the TFC and relate its topological response to the adiabatically defined winding number of the driven spin. The quantized response signal only arises as long as the spin dynamics is described by first-order *adiabatic perturbation theory* APT (see Sec. 2.1.3), which we illustrate by numerically calculating the exact dynamics and the related frequency conversion of the TFC. In Sec. 3.2, we discover the topological features of the ITFC, providing a simple explanation of the correlated topological responses in terms of two-body spin configurations. Again, we corroborate our analytical findings by numerical simulations. Parts of this Chapter have been published as a Rapid Communication in Physical Review Research [KPBT20].

3.1 Topological Frequency Converter

We apply the synthetic Hall physics of quasiperiodically driven quantum systems (see Sec. 2.3) to the prototypical model of a two-frequency driven spin, the latter revealing a Floquet counterpart of a quantum anomalous Hall scenario [WYH$^+$15, LZQ16, CLM22]. The physics of this topologically nontrival phase is theoretically described by a Chern insulator [Hal88, QWZ06, BHZ06], whose topological properties translate into a synthetic Hall conductance in the two-dimensional Floquet lattice of the dynamical synthetic quantum matter (cf. Fig. 2.2). As the associated energy transfer between the classical modes is solely mediated by the two-level quantum system, we refer to the driven spin as a TFC [MRH17]. The time-averaged response of the TFC is proportional to the adiabatically defined topological invariant of the Chern insulator, which can be interpreted as the winding number [Vol03, QWZ06, QHZ08] obtained by projecting the two-level quantum states onto the associated Bloch sphere [NC10]. Following the adiabatic time-evolution of the Bloch vector, this yields a mapping of the spin configurations at *high-symmetry points* HSPs of the synthetic 2D BZ to the winding number of the Bloch sphere, with topological phase transitions exclusively induced by band inversions between the associated spin-polarized states. We corroborate our analysis by exact numerical calculations, showing that the topological frequency conversion can be suppressed by nonadiabatic excitation processes between the Bloch energy bands of the synthetic 2D BZ. In these cases, the description of the quasiperiodic dynamics by means of first-order APT (see Sec. 2.1.3) breaks down.

3.1.1 Quasiperiodically Driven Spin-1/2

We consider the dynamics of a single spin-1/2 subjected to a static magnetic field $\mathbf{B}_0 \in \mathbb{R}^3$ and two quasiperiodic drives[1] $\mathbf{B}_j(\varphi_{j,t}) \in \mathbb{R}^3$ $\{j = 1, 2\}$, the latter parametrized by a set of control parameters $\vec{\varphi}_t = (\varphi_{1,t}, \varphi_{2,t}) = \vec{\omega}\, t + \vec{\phi}$ linearly evolving in the two-dimensional parameter space $\vec{\varphi}_t \in \mathbb{R}^2$. As the driving fields $\mathbf{B}_j(\varphi_{j,t})$ underlie periodicities $T_j = \frac{2\pi}{\omega_j}$, the vectors of frequencies $\vec{\omega} = (\omega_1, \omega_2)$ and offset phases $\vec{\phi} = (\phi_1, \phi_2)$ reveal a dynamical modulation that is $2\pi-$periodic in the individual phase components (cf. Eq. (2.62))

$$\mathbf{B}_j(\varphi_{j,t+T_j}) = \mathbf{B}_j(\varphi_{j,t} + 2\,\pi) = \mathbf{B}_j(\varphi_{j,t}),$$

thus inducing a torus structure of the parameter space $\vec{\varphi}_t \in \mathbb{T}^2$. Introducing the total field vector $\mathbf{B}(\vec{\varphi}_t) = \mathbf{B}_0 + \sum_{j=1}^{2} \mathbf{B}_j(\varphi_{j,t})$, the magnetic coupling to the spin operator $\hat{\mathbf{S}} = \frac{1}{2}\,\hat{\boldsymbol{\sigma}}$ can be parametrized by a Zeeman term [Sch07, Sha08, SN21]

$$\hat{H}(\vec{\varphi}_t) = g^*\,\mu_B\,\mathbf{B}(\vec{\varphi}_t)\cdot\hat{\mathbf{S}} = g^*\,\mu_B \sum_{i=x,y,z} B_i(\vec{\varphi}_t)\,\hat{S}_i, \tag{3.1}$$

where we use the vector of Pauli matrices $\hat{\boldsymbol{\sigma}} = (\hat{\sigma}_x, \hat{\sigma}_y, \hat{\sigma}_z)$. The magnetic moment produced by the spin operator $\hat{\mathbf{S}}$ is proportional to Bohr's magneton μ_B and the

[1] Throughout the Thesis, we assume that the external periodic drives correspond to photon-like modes in the classical limit of large photon numbers [EA15, Eck17, RL20b], consistent with the derivations of Chap. 2. For a generalization to the few-photon quantum limit, we refer to Refs. [NMR19, NRRM20, PR21].

effective g^*-factor of the spin, the latter potentially realized by an electron spin trapped in lateral QDs [KAT01, HKP$^+$07, RT10, ZDM$^+$13, CSDF$^+$21] or NV centers in diamond[2] [JW06, DMD$^+$13, SCLD14]. Alternatively, the Hamiltonian $\hat{H}(\vec{\varphi}_t)$ of Eq. (3.1) might be implemented using superconducting quantum circuits, in which the physical Hilbert space $\mathcal{H} = \mathbb{C}^2$ of the single spin-1/2 can be resembled by suitable Josephson-junction devices [MSS01, YN05, SG08, CW08].

As shown in Sec. 2.3.1, the quasiperiodic modulation with incommensurate driving frequencies $\frac{\omega_1}{\omega_2} \notin \mathbb{Q}$ allows projection onto a two-dimensional Floquet lattice (see Fig. 2.2), in which a fictitious electric field $\vec{E} = \vec{\omega}$ divides the system into a high- and low-frequency regime. In the low-frequency limit, the dynamics in the Floquet lattice is adequately described by the semiclassical equations of motion (cf. Eq. (2.68)), revealing an anomalous response that translates into a topological frequency conversion between the external drives (see Sec. 2.3.3). The associated time-averaged pumping rate (cf. Eq. (2.73))

$$P_{\pm}^{12} = \frac{C_{\pm}}{2\pi}\,\omega_1\,\omega_2 \tag{3.2}$$

is proportional to the first Chern number (cf. Eq. (2.74))

$$C_{\pm} = \frac{1}{2\pi}\iint_0^{2\pi} \mathrm{d}^2\vec{\varphi}\,\Omega_{12}^{(\pm)}(\vec{\varphi}), \tag{3.3}$$

a topological invariant defined in terms of the adiabatic Berry curvature $\Omega_{kl}^{(\pm)}(\vec{\varphi}) = 2\,\mathrm{Im}[\langle\partial_{\varphi_k}\Phi_{\pm}(\vec{\varphi})|\partial_{\varphi_l}\Phi_{\pm}(\vec{\varphi})\rangle]$ (cf. Eq. (2.22)) of the occupied Bloch modes $|\Phi_{\pm}(\vec{\varphi})\rangle$. The Bloch modes $|\Phi_{\pm}(\vec{\varphi})\rangle$ correspond to eigenstates of the Bloch Hamiltonian $\hat{H}(\vec{\varphi})$: $\hat{H}(\vec{\varphi})\,|\Phi_{\pm}(\vec{\varphi})\rangle = E_{\pm}(\vec{\varphi})\,|\Phi_{\pm}(\vec{\varphi})\rangle$, with phases $\vec{\varphi} = (\varphi_1, \varphi_2)$ resembling the Bloch quasimomenta of a spatially periodic system. Accordingly, the parameter space $\vec{\varphi}_t \in \mathbb{T}^2$ of the driven quantum system can be interpreted as a synthetic 2D BZ of the two-dimensional Floquet lattice, entirely covered during the quasiperiodic dynamics of the time-dependent phases $\vec{\varphi}_t = \vec{\omega}\,t + \vec{\phi}$ (see Fig. 2.3). If now the associated Bloch band structure is gapped throughout the entire synthetic 2D BZ, each energy band $E_{\pm}(\vec{\varphi})$ can be assigned a Chern number $C_{\pm}$ (see Eq. (3.3)), revealing a physical observable that is given by the time-averaged pumping rate $P_{\pm}^{12}$ of Eq. (3.2). In this sense, Eq. (3.1) can mimic two-dimensional topological models of condensed matter systems, with adopted topological features that manifest themselves in quantized energy pumping effects between the external drives.

We exploit the aforementioned approach by designing the external field vector $\mathbf{B}(\vec{\varphi}_t)$ such that it induces topological properties to the synthetic band structure of the driven two-level system. To this end, we choose a static magnetic field $\mathbf{B}_0 = B_0\,\hat{\mathbf{z}}$ with amplitude $B_0 > 0$, and two circularly polarized drives with incommensurate frequencies ω_1 and ω_2 (for a schematic illustration see Fig. 3.1). Using the natural basis $\{\hat{\mathbf{x}}, \hat{\mathbf{y}}, \hat{\mathbf{z}}\}$

[2] In both systems, the lateral QDs and the NV centers, the trapped electron spin potentially couples to the surrounding nuclear spins of the host material by hyperfine interaction (see Sec. 4.1.1). For simplicity, however, we assume that the electron spin is well isolated from its environment, such that the model of Eq. (3.1) constitutes an appropriate starting point for our investigations. An extended analysis taking into account environmental effects is studied in the context of a CSM in Chap. 4.

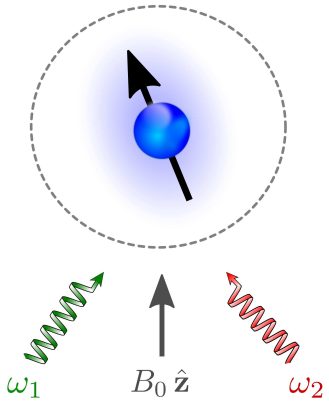

Figure 3.1: *Topological frequency converter* (TFC) as a prototypical example of a quasiperiodically driven quantum system. A single spin-1/2 subjected to a static magnetic field with amplitude B_0 and two circularly polarized drives with incommensurate frequencies ω_1 and ω_2 generates synthetic quantum Hall physics in the frequency domain (see Sec. 2.3). The associated quantized response translates into a topological frequency conversion between the dynamical drives, with a time-averaged pumping rate proportional to the adiabatically defined topological invariant of a Chern insulator.

of the three-dimensional space $\mathbb{R}^3$, the dynamical field vectors are chosen as

$$\mathbf{B}_1(\varphi_{1,t}) = B_1 \Big(\sin(\varphi_{1,t})\,\hat{\mathbf{x}} - \cos(\varphi_{1,t})\,\hat{\mathbf{z}} \Big), \quad \mathbf{B}_2(\varphi_{2,t}) = B_2 \Big(\sin(\varphi_{2,t})\,\hat{\mathbf{y}} - \cos(\varphi_{2,t})\,\hat{\mathbf{z}} \Big),$$

with amplitudes $B_{1/2} > 0$. Setting $B_{1/2} = B_c$, this yields a Bloch Hamiltonian

$$\hat{H}(\vec{\varphi}) = \lambda\, \mathbf{d}(\vec{\varphi}) \cdot \hat{\mathbf{S}}, \quad \mathbf{d}(\vec{\varphi}) = \begin{pmatrix} \sin(\varphi_1) \\ \sin(\varphi_2) \\ M - \cos(\varphi_1) - \cos(\varphi_2) \end{pmatrix}, \tag{3.4}$$

resembling the momentum-space representation of a Chern insulator [Hal88, QWZ06, BHZ06] with mass parameter $M = B_0/B_c$ and energy scale[3]

$$\lambda = g^*\, \mu_B\, B_c.$$

Using the correspondence between linear response signals and adiabatically defined topological invariants (see discussion below Eq. (2.74)), this model explains the quantization of the transverse Hall conductance in the quantum anomalous Hall effect [WYH$^+$15, LZQ16, CLM22], the quantized version of the anomalous Hall effect [JNM02, NSO$^+$10]. In fact, each of the two Bloch energy bands $E_\pm(\vec{\varphi})$ of Eq. (3.4) can be characterized by a Chern number $C_\pm = \mp\nu_{gr}$, with $\nu_{gr} = \pm 1$ (nontrivial) for $|M| < 2$, $M \neq 0$ or $\nu_{gr} = 0$ (trivial) for $|M| > 2$ [Vol03, QWZ06, QHZ08]. Applying this topological classification to the quasiperiodically driven spin-1/2 of Eq. (3.1), the Hall conductance of the Chern insulator translates into a topological frequency conversion between the dynamical drives, which is why we coin this concrete setup a TFC [MRH17].

[3] We assume $\lambda > 0$ for simplicity.

3.1.2 Winding Number

In the previous section, we have claimed that the topological features of the Chern insulator can induce quantum anomalous Hall responses to the driven quantum system, characterized by topological invariants that strongly depend on the explicit values of the mass parameter M (see discussion below Eq. (3.4)). In what follows, we argue that this topological classification can be visually illustrated by projecting the associated quantum states onto the two-dimensional surface $\mathbb{S}^2$ of the Bloch sphere of the two-level quantum system [NC10]. We start our investigation by introducing the spectrum of the Bloch Hamiltonian $\hat{H}(\vec{\varphi})$ of Eq. (3.4):

$$\hat{H}(\vec{\varphi})\ |\Phi_{\pm}(\vec{\varphi})\rangle = E_{\pm}(\vec{\varphi})\ |\Phi_{\pm}(\vec{\varphi})\rangle\,.$$

Assuming the Bloch energy bands $E_{\pm}(\vec{\varphi})$ are nondegenerate throughout the entire (synthetic) 2D BZ, the local geometrical properties of the parameter space are carried by the well-defined Berry curvature $\Omega_{kl}^{(\pm)}(\vec{\varphi}) = 2\,\mathrm{Im}[\langle\partial_{\varphi_k}\,\Phi_{\pm}(\vec{\varphi})|\partial_{\varphi_l}\,\Phi_{\pm}(\vec{\varphi})\rangle]$ (cf. Eqs. (2.21) and (2.22)). Introducing the density matrices $\hat{\rho}_{\pm}(\vec{\varphi}) = |\Phi_{\pm}(\vec{\varphi})\rangle\langle\Phi_{\pm}(\vec{\varphi})|$ of the associated Bloch modes $|\Phi_{\pm}(\vec{\varphi})\rangle$, the Berry curvature can be further rewritten as

$$\Omega_{kl}^{(\pm)}(\vec{\varphi}) = -\mathrm{i}\ \mathrm{Tr}\left(\hat{\rho}_{\pm}(\vec{\varphi})\left[\partial_{\varphi_k}\,\hat{\rho}_{\pm}(\vec{\varphi}), \partial_{\varphi_l}\,\hat{\rho}_{\pm}(\vec{\varphi})\right]\right). \tag{3.5}$$

Here, Tr denotes the trace operating on the physical Hilbert space $\mathcal{H}^2$, and $[\hat{A},\hat{B}] = \hat{A}\hat{B} - \hat{B}\hat{A}$ is the commutator between operators $\hat{A}$ and $\hat{B}$. In what follows, we exploit the elementary approach that density matrices of a generic two-level quantum system can be parametrized by a Bloch vector $\mathbf{u} \in \mathbb{R}^3$: $\hat{\rho} = \frac{1}{2}\,(\mathbb{1} + \mathbf{u}\cdot\hat{\boldsymbol{\sigma}})$, with $|\mathbf{u}| \leq 1$ [NC10]. To this end, we introduce $SU(2)$ matrices $\hat{U}(\vec{\varphi})$ that rotate the z quantization axes of Eq. (3.4) in the z' direction of the dimensionless field vector $\mathbf{d}(\vec{\varphi})$: $\hat{U}^{\dagger}(\vec{\varphi})\,\mathbf{d}(\vec{\varphi})\cdot\hat{\boldsymbol{\sigma}}\,\hat{U}(\vec{\varphi}) = |\mathbf{d}(\vec{\varphi})|\,\hat{\sigma}_{z'}$. Within the rotated basis $\{|\uparrow\rangle_{z'}, |\downarrow\rangle_{z'}\}$, this yields a transformed Bloch Hamiltonian

$$\hat{H}'(\vec{\varphi}) = \hat{U}^{\dagger}(\vec{\varphi})\,\hat{H}(\vec{\varphi})\,\hat{U}(\vec{\varphi}) = \lambda\,|\mathbf{d}(\vec{\varphi})|\,\hat{S}_{z'},$$

with spectral properties given by the energy eigenvalues $E_{\pm}(\vec{\varphi}) = \pm\frac{\lambda}{2}\,|\mathbf{d}(\vec{\varphi})|$ and density matrices $\hat{\varrho}_{\pm} = \frac{1}{2}\,(\mathbb{1} \pm \hat{\sigma}_{z'})$. Performing the inverse transformation $\hat{\rho}_{\pm}(\vec{\varphi}) = \hat{U}(\vec{\varphi})\,\hat{\varrho}_{\pm}\,\hat{U}^{\dagger}(\vec{\varphi})$, the density matrices $\hat{\varrho}_{\pm}$ can be rotated back to the original basis of Eq. (3.4):

$$\hat{\rho}_{\pm}(\vec{\varphi}) = \frac{1}{2}\left(\mathbb{1} \pm \tilde{\mathbf{d}}(\vec{\varphi})\cdot\hat{\boldsymbol{\sigma}}\right), \tag{3.6}$$

with $\tilde{\mathbf{d}}(\vec{\varphi}) = \frac{\mathbf{d}(\vec{\varphi})}{|\mathbf{d}(\vec{\varphi})|}$. Inserting Eq. (3.6) into Eq. (3.5), and integrating over the closed manifold of the synthetic 2D BZ (cf. Eq. (3.3)), this yields a Chern number $C_{\pm} = \mp\nu_{gr}$, with [Vol03, QWZ06, QHZ08]

$$\nu_{gr} = -\frac{1}{4\pi}\iint_0^{2\pi}\mathrm{d}^2\vec{\varphi}\,\tilde{\mathbf{d}}(\vec{\varphi})\left(\partial_{\varphi_1}\tilde{\mathbf{d}}(\vec{\varphi})\times\partial_{\varphi_2}\tilde{\mathbf{d}}(\vec{\varphi})\right). \tag{3.7}$$

Let's work out a visual interpretation of Eq. (3.7). The density matrices $\hat{\rho}_{\pm}(\vec{\varphi})$ of Eq. (3.6) are parametrized by normalized Bloch vectors[4] $|\tilde{\mathbf{d}}(\vec{\varphi})| = 1$, revealing a

[4]Provided that $|\mathbf{d}(\vec{\varphi})| \neq 0$, which is the case whenever the Bloch energy bands $E_{\pm}(\vec{\varphi}) = \pm\frac{\lambda}{2}\,|\mathbf{d}(\vec{\varphi})|$ remain gapped throughout the entire synthetic 2D BZ.

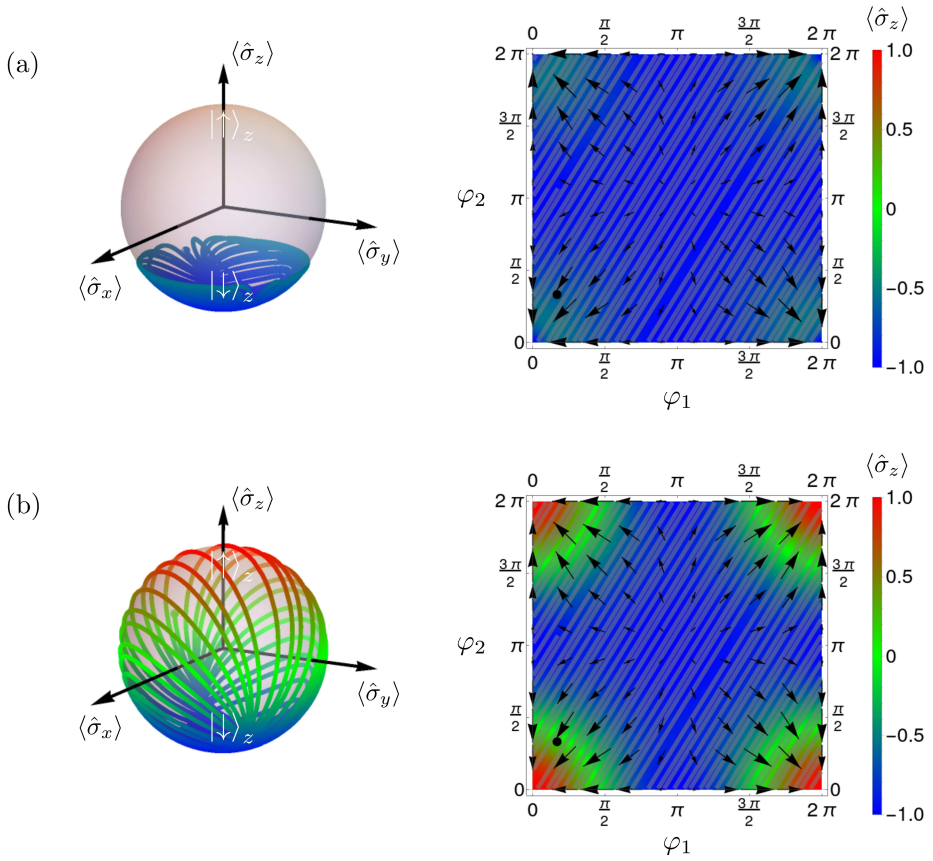

Figure 3.2: Adiabatic spin polarization $\langle\hat{\boldsymbol{\sigma}}(\vec{\varphi}_t)\rangle_- = -\tilde{\mathbf{d}}(\vec{\varphi}_t)$ represented on the Bloch sphere (left side) and in the two-dimensional parameter space $\vec{\varphi} = (\varphi_1, \varphi_2) \in \mathbb{T}^2$ (right side) for mass parameters (a) $M = 2.2$ and (b) $M = 1.2$. The temporal evolution of the phases $\vec{\varphi}_t = \vec{\omega}\, t + \vec{\phi}$ is illustrated up to times $T = \frac{40\pi}{\omega}$, with a vector of frequencies $\vec{\omega} = (1,\, \gamma)\, \omega$ and offset-phases $\vec{\phi} = (\pi/6,\, \pi/3)$. We set $\omega = 0.1\,\lambda$ and $\gamma = \frac{1}{2}\,(1 + \sqrt{5})$. As the quasiperiodic dynamics entirely samples the torus structure $\mathbb{T}^2$ of the synthetic 2D *Brillouin zone* (BZ) (illustrated by gray lines and black dot on the right side, cf. Fig. 2.3), the coverage of the two-dimensional surface $\mathbb{S}^2$ of the Bloch sphere can be approximated by the projection $\tilde{\mathbf{d}}(\vec{\varphi}) : \mathbb{T}^2 \mapsto \mathbb{S}^2$, revealing winding numbers (a) $\nu_{gr} = 0$ and (b) $\nu_{gr} = 1$. Besides numerical calculations (cf. Fig. 3.4), this topological classification can be determined by the spin configurations at *high-symmetry points* (HSPs) of the synthetic 2D BZ (cf. Fig. 3.3). There, the spin-1/2 points in the z direction of the Bloch sphere: $\hat{\sigma}_z\,|\uparrow\rangle_z = |\uparrow\rangle_z$ or $\hat{\sigma}_z\,|\downarrow\rangle_z = -\,|\downarrow\rangle_z$. Note that the black arrows on the right side correspond to vectors $-(\tilde{d}_x,\, \tilde{d}_y)$.

mapping from the torus structure $\mathbb{T}^2$ of the synthetic 2D BZ to the two-dimensional surface $\mathbb{S}^2$ of the Bloch sphere, denoted as

$$\tilde{\mathbf{d}}(\vec{\varphi}) : \mathbb{T}^2 \mapsto \mathbb{S}^2. \tag{3.8}$$

In fact, this mapping reveals an illustrative explanation of the Chern number ν_{gr} of Eq. (3.7): As the integrand $\tilde{\mathbf{d}}(\vec{\varphi})\,(\partial_{\varphi_1}\tilde{\mathbf{d}}(\vec{\varphi}) \times \partial_{\varphi_2}\tilde{\mathbf{d}}(\vec{\varphi}))$ corresponds to the oriented

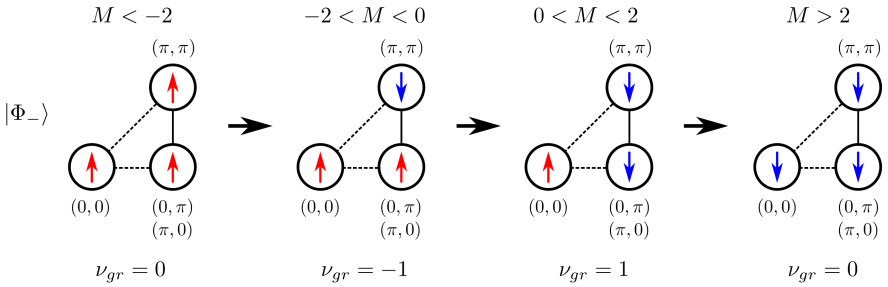

Figure 3.3: Spin configurations of the ground state $|\Phi_-(\vec{\varphi})\rangle$ at *high-symmetry points* (HSPs) of the synthetic 2D *Brillouin zone* (BZ) for different mass parameters M. As the Bloch Hamiltonian (3.4) commutes with $\hat{S}_z$ at HSPs, there exists a mapping (see also Appendix A.1) from the spin configurations at HSPs to the winding number ν_{gr} of Eq. (3.7). This allows an illustrative explanation for the topological classification of Fig 3.2. For $M = 2.2$, the spin configurations at HSPs only point in negative z direction of the Bloch sphere, revealing a winding number $\nu_{gr} = 0$. For $M = 1.2$, however, the spin in $(0,0)$ is polarized in opposite direction with respect to the other HSPs, resulting in a winding number $\nu_{gr} = 1$ as the Bloch sphere is covered once. Our mapping is corroborated by exact numerical calculations in Fig. 3.4.

Jacobian[5] of the projection (3.8), the integral over the closed manifold of the torus $\mathbb{T}^2$ reveals the relative area covered by the vector $\tilde{\mathbf{d}}(\vec{\varphi})$. However, as the Chern number $C_\pm = \mp\nu_{gr}$ only takes integer values [Che46, TKNdN82, QHZ08], fractional surfaces do not contribute to this integration, meaning that the covered area can only assume multiples of the entire two-dimensional surface $\mathbb{S}^2$. As the latter equals 4π, Eq. (3.7) corresponds to the definition of a winding number ν_{gr}, indicating how many times the Bloch sphere is covered by the projection (3.8). In what follows, we use the terminology of the winding number ν_{gr} whenever the topology of a two-level quantum system is addressed.

Following the aforementioned approach, we can determine the winding number ν_{gr} by considering the adiabatic time-evolution of the driven quantum system of Eq. (3.1). In Fig. 3.2, the adiabatic spin polarization $\langle\hat{\boldsymbol{\sigma}}(\vec{\varphi}_t)\rangle_- = -\tilde{\mathbf{d}}(\vec{\varphi}_t)$ of the single spin-1/2 is represented on the Bloch sphere (left side) and in the two-dimensional parameter space $\vec{\varphi} = (\varphi_1, \varphi_2) \in \mathbb{T}^2$ (right side) for mass parameters (a) $M = 2.2$ and (b) $M = 1.2$. Assuming sufficiently long time scales, the time-dependent phases $\vec{\varphi}_t = \vec{\omega}\, t + \vec{\phi}$ entirely sample the closed manifold of the torus $\mathbb{T}^2$ (cf. Fig. 2.3), such that the coverage of the two-dimensional surface $\mathbb{S}^2$ of the Bloch sphere can be approximated by the mapping (3.8). Setting $\omega = 0.1\,\lambda$ and $\gamma = \frac{1}{2}(1 + \sqrt{5})$, we illustrate the temporal evolution up to times $T = \frac{40\pi}{\omega}$, with a vector of frequencies $\vec{\omega} = (1, \gamma)\,\omega$ and offset-phases[6]

[5]The Jacobian of the mapping (3.8) is defined as $\sqrt{\det(\hat{J}^T\,\hat{J})}$, with the Jacobian matrix $\hat{J}$ that involves matrix elements $J_{ij} = \frac{\partial \tilde{d}_i}{\partial_{\varphi_j}}$ [Fed69, Sim83b, KP08, Mor16]. It is straightforward to show that this definition equals the absolute value of the integrand $\tilde{\mathbf{d}}(\vec{\varphi})\,(\partial_{\varphi_1}\tilde{\mathbf{d}}(\vec{\varphi}) \times \partial_{\varphi_2}\tilde{\mathbf{d}}(\vec{\varphi}))$.

[6]In the remainder of this Thesis, the explicit values of the offset phases $\vec{\phi} = (\phi_1, \phi_2)$ play a minor role, as we are interested in the quasiperiodic dynamics that entirely covers the synthetic 2D BZ of the system (cf. Fig. 2.3). Accordingly, the topological response of Eq. (2.73) is independent of the explicit

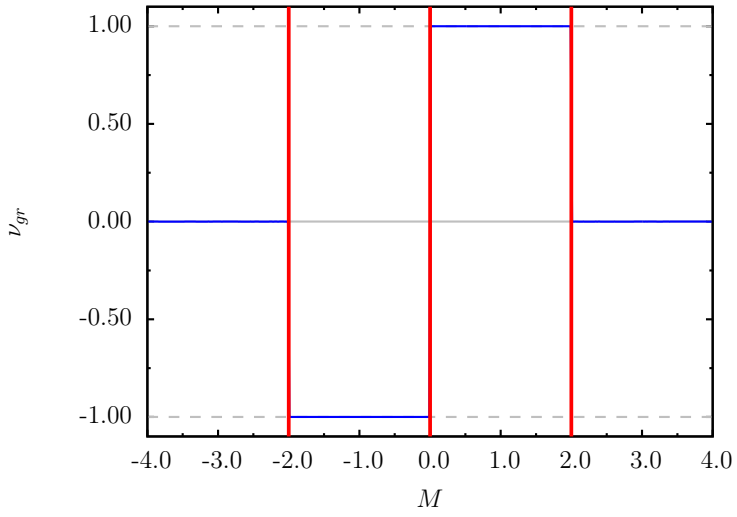

Figure 3.4: Numerically calculated winding number ν_{gr} (cf. Eq. (3.7)) as a function of mass parameter M. Due to its topological origin, the winding number ν_{gr} remains invariant as long as the minimum band gap between the energy levels $E_{\pm}(\vec{\varphi}) = \pm\frac{\lambda}{2}\,|\mathbf{d}(\vec{\varphi})|$ is finite. For mass parameters $|M| = 2.0$, $M = 0.0$ (vertical red lines), the energy gaps close at *high-symmetry points* (HSPs) of the synthetic 2D *Brillouin zone* (BZ) (cf. Tab. 3.1), resulting in topological phase transitions with discontinuous changes in the winding number ν_{gr}.

$\vec{\phi} = (\pi/6,\, \pi/3)$. For $M = 2.2$, the Bloch sphere is only partially covered, resulting in a winding number $\nu_{gr} = 0$. For $M = 1.2$, however, the spin polarization at HSPs of the synthetic 2D BZ implies a winding number $\nu_{gr} = 1$: At $(0, 0)$, the spin is polarized in opposite direction with respect to the other HSPs, which is why the Bloch sphere is covered once. This simple explanation stems from the fact that the Bloch Hamiltonian (3.4) at HSPs commutes with $\hat{S}_z$, revealing a mapping (see also Appendix A.1) between the spin configurations at HSPs and the winding number ν_{gr} of Eq. (3.7). For the ground state $|\Phi_{-}(\vec{\varphi})\rangle$, these spin configurations are illustrated in Fig. 3.3 for different mass parameters M. Topological phase transitions lead to inversions between states $|\uparrow\rangle_z$ and $|\downarrow\rangle_z$, changing both the spin configuration at HSPs and the winding number ν_{gr}. Notably, gap closings and reopenings at $(0, \pi)$ and $(\pi, 0)$ occur simultaneously, such that the change in the winding number ν_{gr} is twice as large as in $(0, 0)$ or (π, π).

We corroborate our visualization on the Bloch sphere by exact numerical calculations in Fig. 3.4. The results are consistent with our previous discussion. The winding number ν_{gr} remains invariant as long as the minimum band gap between the energy levels $E_{\pm}(\vec{\varphi}) = \pm\frac{\lambda}{2}\,|\mathbf{d}(\vec{\varphi})|$ is finite, which is the case whenever $|\mathbf{d}(\vec{\varphi})| \neq 0$ throughout the entire synthetic 2D BZ. For mass parameters $|M| = 2.0$, $M = 0.0$ (cf. Tab. 3.1), however, the Bloch vector $\tilde{\mathbf{d}}(\vec{\varphi})$ is not well-defined, revealing a discontinuity in the definition of Eq. (3.7). As a consequence, Dirac gap closings and reopenings are accompanied with discrete changes in the winding number ν_{gr}, explaining the topological phase transitions in Fig. 3.4.

starting point in parameter space at $t_0 = 0$.

HSP	$(0,0)$	$(0,\pi),(\pi,0)$	(π,π)
M	2	0	-2

Table 3.1: Mass parameter M for which a Dirac gap closing happens at *high-symmetry points* (HSPs) of the synthetic 2D *Brillouin zone* (BZ). The associated topological phase transitions are induced by band inversions between states $|\uparrow\rangle_z$ and $|\downarrow\rangle_z$ (cf. Fig. 3.3), accompanied by discrete changes in the winding number ν_{gr} (cf. Fig. 3.4). As gap closings and reopenings at $(0,\pi)$ and $(\pi,0)$ occur simultaneously, the change in ν_{gr} is twice as large as in the other HSPs.

3.1.3 Topological Frequency Conversion

Having determined the winding number ν_{gr} as a function of mass parameter M (see Fig. 3.4), we investigate whether the correspondence between adiabatically defined topological invariants and linear response signals (see discussion below Eq. (2.74)) actually holds in the driven two-level quantum system of Eq. (3.1). To this end, we numerically solve the time-dependent Schrödinger equation [Sch26, Sha08, GS18]

$$\mathrm{i}\,\frac{\mathrm{d}}{\mathrm{d}t}\,|\Psi(t)\rangle = \hat{H}(\vec{\varphi}_t)\,|\Psi(t)\rangle \tag{3.9}$$

associated with the Hamiltonian[7] $\hat{H}(\vec{\varphi}_t) = \lambda\,\mathbf{d}(\vec{\varphi}_t)\cdot\hat{\mathbf{S}}$ (cf. Eq. (3.4)), and determine the related frequency conversion by means of the equations of motion (cf. Eq. (2.19))

$$\frac{\mathrm{d}}{\mathrm{d}t}\,\langle\hat{H}(\vec{\varphi}_t)\rangle = \langle\partial_t\,\hat{H}(\vec{\varphi}_t)\rangle = \vec{\omega}\,\langle\hat{\mathbf{I}}(\vec{\varphi}_t)\rangle\,, \quad \hat{\mathbf{I}}(\vec{\varphi}_t) = \nabla_{\vec{\varphi}}\,\hat{H}(\vec{\varphi}_t).$$

The expectation values are calculated according to the exact solution $|\Psi(t)\rangle$ of Eq. (3.9), while each term[8] $\dot{W}_k(t) = \omega_k\,\langle\hat{\mathrm{I}}_k(\vec{\varphi}_t)\rangle$ can be interpreted as the energy pumping rate provided by the individual driving field (cf. Eq. (2.71)). If the initial state at $t_0 = 0$ corresponds to the ground state $|\Phi_-(\vec{\varphi}_{t_0})\rangle$ of the Bloch Hamiltonian (3.4), the time-averaged pumping rates $P_{-,k}$ (cf. Eq. (2.72)) can be extrapolated by the gradient[9] of the associated energy transfers $W_k(t) = \omega_k\,\int_0^t \mathrm{d}t'\,\langle\hat{\mathrm{I}}_k(\vec{\varphi}_{t'})\rangle$. Throughout the numerics, we choose the vectors of frequencies $\vec{\omega} = (1,\,\gamma)\,\omega$ and offset phases $\vec{\phi} = (\pi/10,\,0)$, with $\omega = 0.1\,\lambda$ and $\gamma = \frac{1}{2}(1+\sqrt{5})$. To ensure that the entire synthetic 2D BZ is adequately sampled (cf. Fig. 2.3), we calculate the exact dynamics up to times $\lambda\,T = 10^4$.

Fig. 3.5(a) shows the energy transfers $W_k(t)$ of the individual drives as a function of time t for different mass parameters M, with an offset in time inserted for each value of

[7] We have multiplied (3.4) by an overall factor $\eta = 4.0$, which formally increases the minimum band gap of the system and thus improves the ability to stay within the associated energy level $E_\pm(\vec{\varphi}_t)$ during the quasiperiodic dynamics. This allows us to choose a larger frequency $\omega = 0.1\,\lambda$, such that the entire synthetic 2D BZ is sufficiently sampled for a time evolution up to times $\lambda\,T = 10^4$. This leads to a reduction of computation time.

[8] Since the expectation value of the current operator $\langle\hat{\mathrm{I}}_k(\vec{\varphi}_t)\rangle$ is determined by the exact solution $|\Psi(t)\rangle$ of the time-dependent Schrödinger equation (3.9), the individual energy puming rates $\dot{W}_k(t) = \omega_k\,\langle\hat{\mathrm{I}}_k(\vec{\varphi}_t)\rangle$ also involve the higher orders in the perturbative expansion of APT (see Sec. 2.1.3). This reveals a significant difference from Eq. (2.71), where only first-order terms in APT are considered.

[9] We obtain the gradient by computing $P_{-,k} = \frac{2}{T}\,(\bar{W}_k^T - \bar{W}_k^{T/2})$ with the associated time-averaged energy transfers $\bar{W}_k^{T/2} = \frac{2}{T}\,\int_0^{T/2}\mathrm{d}t\,W_k(t)$ and $\bar{W}_k^T = \frac{2}{T}\,\int_{T/2}^T \mathrm{d}t\,W_k(t)$.

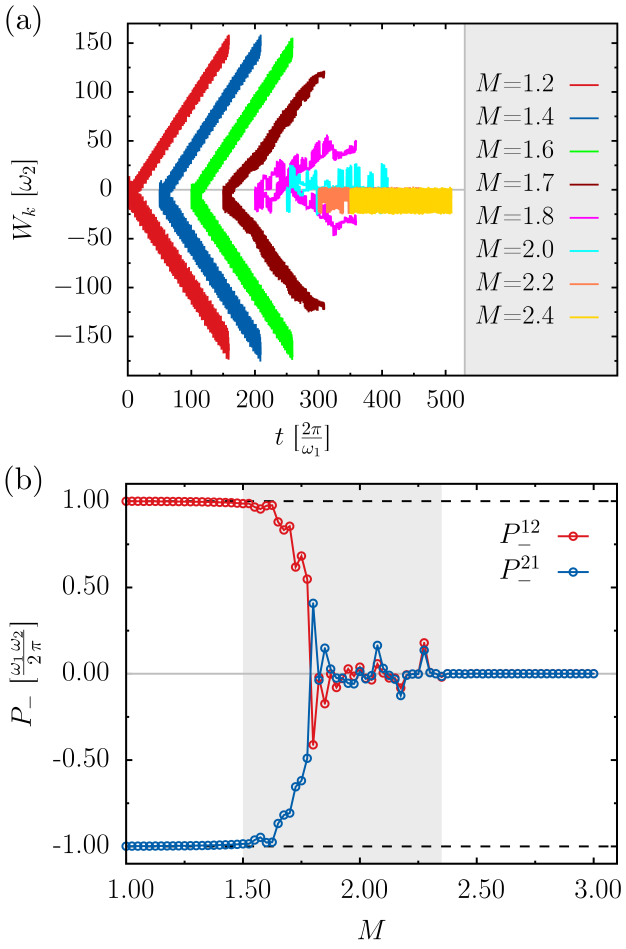

Figure 3.5: Numerical results for the exact dynamics of the *topological frequency converter* (TFC) (for a schematic illustration see Fig. 3.1). (a) Energy transfers $W_k(t)$ as a function of time t for different mass parameters M, with an offset in time inserted for each value of M for illustrative reasons. Assuming the exact dynamics in the nontrivial topological regime (cf. Fig. 3.4) is well described within first-order *adiabatic perturbation theory* (APT), the driven spin mediates a linear energy transfer between the external drives. In the trivial regime, contributions to the energy transfers $W_k(t)$ are mainly provided by Bloch oscillations $\partial_{\varphi_k} E_-(\vec{\varphi}_t)$. Near the Dirac gap closing at $M = 2.0$, the quantized pumping effect is suppressed due to nonadiabatic excitation processes between the synthetic energy bands $E_\pm(\vec{\varphi}_t)$ of the two-level system. (b) Extrapolated energy pumping rate P_- as a function of mass parameters M. The quantization $P_-^{12} = \frac{\nu_{gr}}{2\pi}\,\omega_1\,\omega_2$ (cf. Eq. (3.2)) occurs in excellent agreement (white regimes) with the topological classification of Fig. 3.4. This applies as long as the TFC shows quasiadiabaticity, while otherwise the topological response breaks down (gray regimes).

M for illustrative reasons. Besides the contributions from Bloch oscillations $\partial_{\varphi_k} E_-(\vec{\varphi}_t)$ (cf. Eq. (2.70)), the energies $W_k(t)$ exhibit a linear time-dependence for mass parameters $M = 1.2$ to $M = 1.6$. Accordingly, the driven spin absorbs photons of frequency ω_1 from the first mode, and emits the same amount of energy in form of photons of frequency

ω_2 to the second mode (or vice versa). The associated frequency conversion occurs at a topologically quantized rate as long as the dynamics of the system is well described within first-order APT (see Sec. 2.1.3), while for mass parameters $M = 1.7$ and $M = 1.8$ the energy transfer becomes suppressed. As these parameters are close to the Dirac gap closing at $M = 2.0$ (see Tab. 3.1), the energy scales of the frequencies ω_k can exceed the minimum band gap of the Bloch energy levels $E_{\pm}(\vec{\varphi})$, leading to nonadiabatic excitation processes between these bands. As a consequence, the quantized energy pumping effect breaks down whenever the mass parameters M sufficiently approach an associated topological phase transition of Fig. 3.4. Although a mass parameter $M = 2.4$ reveals quasiadiabatic dynamics[10], the associated energy transfers $W_k(t)$ are mainly described by the contributions from Bloch oscillations $\partial_{\varphi_k} E_{-}(\vec{\varphi}_t)$. This, however, can be explained by the topological properties of the synthetic energy bands $E_{\pm}(\vec{\varphi})$, in which mass parameters $M > 2$ correspond to trivial regimes. The extrapolated time-averaged pumping rates P_{-} as a function of mass parameter M are illustrated in Fig. 3.5(b). As long as the TFC shows quasiadiabaticity (white regimes), a quantized energy pumping effect $P_{-}^{12} = \frac{\nu_{gr}}{2\pi}\,\omega_1\,\omega_2$ (cf. Eq. (3.2)) occurs in excellent agreement with the topological classification of Fig. 3.4. Otherwise, the dynamical response is suppressed (gray regimes), and perfect quantization breaks down.

Fig. 3.5 corroborates that the topological observable of the dynamical synthetic quantum matter is proportional to the adiabatically defined winding number of the driven spin (cf. Fig. 3.3), the latter mediating a process in which photons of incommensurate frequencies are exchanged between the external drives at a topologically quantized rate. Inspired by this observation, a number of advanced studies have been emerged [KNG$^+$18, PR18, CMC19, NMR19, CMC20, BCCS20, CLY$^+$20, NRRM20, LCC21, MS21, NGG$^+$21, PR21, QRP21, SYZ22], such as the generalization to quantum cavity modes [NMR19, NRRM20, PR21], the investigation of topological semimetallic regimes [CMC20, QRP21], or the indirect measurement of the quantized energy pumping effect [BCCS20, MS21]. In the next section, we extend the prototypical example of a TFC to an interacting two-spin model and show that correlations in dynamical synthetic dimensions give rise to novel topological responses in quasiperiodically driven quantum systems.

3.2 Interacting Topological Frequency Converter

By adding spin-spin interactions to the TFC (see Sec. 3.1), we extend the notion of topologically quantized frequency conversion to correlated spin systems. To this end, we focus on a minimal model of two interacting spins equally exposed to two circularly polarized incommensurate drives. Despite its simplicity, this setup already offers a striking example of how the interplay of interaction and the dynamical dimensional extension of a quantum system can have a profound impact on the resulting topological properties. Most prominently, while in a noninteracting system of two identical spins

[10] Throughout the Thesis, we use equivalent terminologies for the dynamics associated with the first-order corrections of APT (see Sec. 2.1.3). These include, for example, the terms quasiadiabaticity, quasiadiabatic dynamics, or strong coupling regime.

the topological charge determining the frequency conversion is constrained to be even, in the interacting case also odd integers are allowed. This feature may, in turn, result in an enhancement by interactions of the topological response. For these reasons, we call our setup an ITFC. We provide a simple interpretation of our results in terms of two-body spin configurations and corroborate the observed topological phase transitions with an explicit calculation of the system's dynamics and the related frequency conversion. Throughout this Section, we closely follow the derivations and results presented in Ref. [KPBT20]. *Copyright (2022) by the American Physical Society.*

3.2.1 Interacting Two-Spin Model

We analyze the ITFC schematically as shown in Fig. 4.3, in which two spins coupled by spin-spin interaction are equally exposed to a dynamical magnetic field $\mathbf{B}(\vec{\varphi}_t)$. The corresponding Hamiltonian is given by (cf. Eq. (3.1))

$$\hat{H}(\vec{\varphi}_t) = \frac{g^*\,\mu_B}{2}\,\mathbf{B}(\vec{\varphi}_t)\cdot(\hat{\boldsymbol{\sigma}}_A + \hat{\boldsymbol{\sigma}}_B) + \sum_{i=x,y,z} J_i\,\hat{\sigma}_A^i\,\hat{\sigma}_B^i, \tag{3.10}$$

where we introduce the vector of Pauli matrices $\hat{\boldsymbol{\sigma}}_\alpha = (\hat{\sigma}_\alpha^x,\, \hat{\sigma}_\alpha^y,\, \hat{\sigma}_\alpha^z)$ acting on the individual constituents $\alpha = A/B$, and assume anisotropic Heisenberg interaction with coupling parameters J_i $\{i = x, y, z\}$. We focus on the case of spin-1/2, generating a Zeeman coupling term proportional to Bohr's magneton μ_B and the effective g^*-factor of the spin. An experimental realization of Eq. (3.10) could be implemented in gated double quantum dots [PJT+05, BFT+15, SPF+19], in which spin-orbit coupling can potentially induce anisotropies in the interaction between the trapped electron spins [FSC+20, FVV+22]. Alternatively, superconducting quantum circuits allow for the realization of this type of interaction, with a substantial degree of tunability of the anisotropy [SKK+14, RNC+14]. In addition to a static magnetic field with amplitude $B_0 > 0$ in z direction, the external field

$$\mathbf{B}(\vec{\varphi}_t) = \begin{pmatrix} B_1\,\sin(\varphi_{1t}) \\ B_2\,\sin(\varphi_{2t}) \\ B_0 - B_1\,\cos(\varphi_{1t}) - B_2\,\cos(\varphi_{2t}) \end{pmatrix} \tag{3.11}$$

is composed of two circularly polarized drives with time-dependent phases $\vec{\varphi}_t = (\varphi_{1,t},\, \varphi_{2,t}) = \vec{\omega}\,t + \vec{\phi}$ and amplitudes $B_{1/2} > 0$. The frequencies and offset phases are parametrized by $\vec{\omega} = (\omega_1,\, \omega_2)$ and $\vec{\phi} = (\phi_1,\, \phi_2)$. In what follows, we set $B_{1/2} = B_c$ for simplicity.

The interaction favors ferromagnetic ($J_i < 0$) or antiferromagnetic ($J_i > 0$) alignment of the spins along the respective quantization axis in the ground state. The interplay of interaction and magnetic field $\mathbf{B}(\vec{\varphi}_t)$ can be conveniently investigated by introducing the total spin operator $\hat{\mathbf{S}} = \frac{1}{2}\,(\hat{\boldsymbol{\sigma}}_A + \hat{\boldsymbol{\sigma}}_B)$ and the associated eigenstates $|\psi_{s,m_z}\rangle$ determined by quantum numbers (s, m_z) [Sch07, Sha08, GS18]:

$$\hat{\mathbf{S}}^2\,|\psi_{s,m_z}\rangle = s\,(s+1)\,|\psi_{s,m_z}\rangle\,, \quad \hat{S}_z\,|\psi_{s,m_z}\rangle = m_z\,|\psi_{s,m_z}\rangle\,,$$

where $\{s = 0, 1\}$ and $\{m_z = -s, \ldots, s\}$. The Hamiltonian of Eq. (3.10) commutes with the total spin $[\hat{H}(\vec{\varphi}_t), \hat{\mathbf{S}}^2] = 0$, such that the total spin quantum number s is

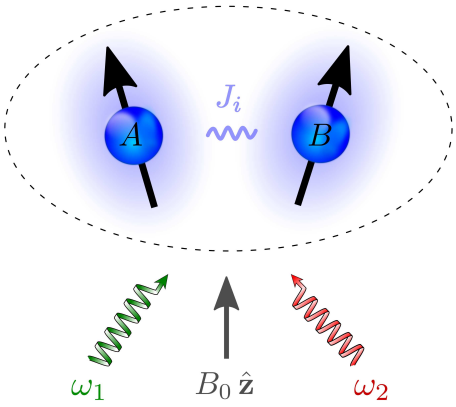

Figure 3.6: *Interacting topological frequency converter* (ITFC) as a minimal interacting extension of the *topological frequency converter* (TFC). The spins A/B (blue spheres) coupled by spin-spin interaction are equally exposed to a static magnetic field with amplitude B_0 and two circularly polarized drives with incommensurate frequencies ω_1 and ω_2. The interaction is controlled by the coupling parameters J_i $\{i = x, y, z\}$, allowing the realization of correlated topological phases in synthetic dimensions (cf. Fig. 3.7). *Reprinted figure with permission from Ref. [KPBT20]. Copyright (2022) by the American Physical Society.*

a constant of motion of the interacting spin system[11]. Accordingly, the singlet state $|\psi_{0,0}\rangle$ constitutes to a solution of the time-dependent Schrödinger equation with trivial dynamics, which is why we restrict ourselves to study the Hilbert subspace with $s = 1$. In this case, apart from a global constant, the Hamiltonian (3.10) can be written in the basis of triplet states $\{|\psi_{1,1}\rangle, |\psi_{1,0}\rangle, |\psi_{1,-1}\rangle\}$:

$$\hat{H}_T = \lambda' \begin{pmatrix} 2\,\frac{B_z}{B_c} + \mathcal{J}_z & \sqrt{2}\,\frac{B_-}{B_c} & \mathcal{J}_{x-y} \\ \sqrt{2}\,\frac{B_+}{B_c} & -\mathcal{J}_z & \sqrt{2}\,\frac{B_-}{B_c} \\ \mathcal{J}_{x-y} & \sqrt{2}\,\frac{B_+}{B_c} & -2\,\frac{B_z}{B_c} + \mathcal{J}_z \end{pmatrix}, \tag{3.12}$$

with the energy scale[12]

$$\lambda' = \frac{g^*\,\mu_B\,B_c}{2},$$

the transverse components $B_\pm = B_x \pm i\,B_y$, and the effective interaction strengths

$$\mathcal{J}_{x\pm y} = \frac{J_x \pm J_y}{\lambda'}, \quad \mathcal{J}_z = \frac{J_z}{\lambda'} - \frac{\mathcal{J}_{x+y}}{2}.$$

The interaction enters $\hat{H}_T$ with the parameters $\mathcal{J}_z$ and $\mathcal{J}_{x-y}$, while the third parameter $\mathcal{J}_{x+y}$ only affects the energy $E_{0,0} = -\lambda'\,(2\,\mathcal{J}_{x+y} + \mathcal{J}_z)$ of the decoupled singlet state $|\psi_{0,0}\rangle$. With isotropic exchange interaction, the interacting part of Eq. (3.10) commutes with

[11] This can be seen from the equations of motion [Ehr27, Bal15, GS18]: $\frac{\mathrm{d}}{\mathrm{d}t}\,\langle\hat{\mathbf{S}}^2\rangle = \mathrm{i}\,\langle[\hat{H}(\vec{\varphi}_t), \hat{\mathbf{S}}^2]\rangle + \langle\partial_t\,\hat{\mathbf{S}}^2\rangle = 0$, where the expectation values are calculated according to the exact solution of the time-dependent Schrödinger equation of the interacting spin system.

[12] We assume $\lambda' > 0$ for simplicity.

$\hat{S}_z$, effectively resulting in interaction strengths $\mathcal{J}_z = \mathcal{J}_{x-y} = 0$. Below, we focus on the anisotropic case, setting $\mathcal{J}_{x-y} = 0$ for simplicity[13]. Additional results for nonvanishing $\mathcal{J}_{x-y}$ are presented in the Appendix A.2, showing that our main predictions are not qualitatively affected.

3.2.2 Topological Phase Diagrams

For each spin, the noninteracting part of Eq. (3.10) is equivalent to a Chern insulator with mass parameter $M = B_0/B_c$ (cf. Eq. (3.4)). The time-dependent phases $\varphi_{1,t}$ and $\varphi_{2,t}$ play the role of Bloch quasimomenta: as they vary between 0 and 2π, they define a two-dimensional torus $\mathbb{T}^2$, analogous to a 2D BZ (cf. Fig. 2.3). Hence, the dynamics of the magnetic field $\mathbf{B}(\vec{\varphi}_t)$ of Eq. (3.11) can induce nontrivial topological responses in the single-spin subspaces for quasiperiodic driving (see Sec. 2.3.3). Each of the two Bloch energy bands of the single-spin Hamiltonian can be characterized by a winding number $\nu_{gr} = -\nu_{ex} = \pm 1$ (nontrivial) for $|M| < 2$, $M \neq 0$ or $\nu_{gr} = \nu_{ex} = 0$ (trivial) for $|M| > 2$, where ν_{gr} (ν_{ex}) corresponds to the single-spin ground (excited) energy band (cf. Fig. 3.4). In the interacting case, we can diagonalize the projected Bloch Hamiltonian of Eq. (3.12): $\hat{H}_T(\vec{\varphi})\ |\Psi_n(\vec{\varphi})\rangle = E_n(\vec{\varphi})\ |\Psi_n(\vec{\varphi})\rangle$, and determine the Chern number (cf. Eqs. (2.22) and (2.74))

$$C_n = \frac{1}{2\pi \mathrm{i}} \iint_0^{2\pi} \mathrm{d}^2\vec{\varphi}\, [\langle \partial_{\varphi_1} \Psi_n(\vec{\varphi}) \,|\, \partial_{\varphi_2} \Psi_n(\vec{\varphi})\rangle - \langle \partial_{\varphi_2} \Psi_n(\vec{\varphi}) \,|\, \partial_{\varphi_1} \Psi_n(\vec{\varphi})\rangle] \tag{3.13}$$

of the respective synthetic energy bands $E_n(\vec{\varphi})$. Here, the associated Bloch states of the synthetic 2D BZ are given by $|\Psi_n(\vec{\varphi})\rangle$ $\{n = 0, 1, 2\}$. The resulting topological phase diagrams as a function of mass parameter M and effective interaction strength $\mathcal{J}_z$ ($\mathcal{J}_{x-y} = 0$) are displayed in Fig. 3.7. Interactions have two striking effects on the topological properties of the synthetic energy bands $E_n(\vec{\varphi})$. First, phases with odd Chern numbers $C_n = \pm 1, \pm 3$ emerge. This observation is a genuine interaction effect since for $\mathcal{J}_z = 0$ the two spins are independently exposed to the same magnetic field $\mathbf{B}(\vec{\varphi})$, such that the global topological invariant can only change by an even number $\Delta C_n = \pm 2, \pm 4$. Second, a finite interaction strength $\mathcal{J}_z \neq 0$ can induce a nontrivial topology for states that were trivial in the noninteracting regime.

The topological phase transitions in Fig. 3.7 are caused by band inversions at HSPs of the synthetic 2D BZ (for a schematic illustration see Fig. 3.8), accompanied by Dirac gap closings for mass parameters $|M| = 2$ or $M = 0$ (cf. Fig. 3.4), and effective interaction strengths $\mathcal{J}_z$ shown in Tab. 3.2. Notably, gap closings and reopenings at $(0, \pi)$ and $(\pi, 0)$ occur simultaneously, such that the change in the global Chern number C_n is twice as large as in $(0, 0)$ or (π, π). At HSPs, the Hamiltonian (3.10) commutes with $\hat{S}_z$, making $\hat{H}_T$ diagonal in the $|\psi_{s,m_z}\rangle$ basis: Gap closings caused by $\mathcal{J}_z$ ($M = \text{const.}$) lead to inversions between the ferromagnetic triplet states $|\psi_{1,1}\rangle$, $|\psi_{1,-1}\rangle$ and the antiferromagnetic triplet state $|\psi_{1,0}\rangle$. The corresponding topological phases are bounded by straight lines in Fig. 3.7. Topological phase transitions for mass parameters $|M| = 2$ or $M = 0$, however, only involve the ferromagnetic states $|\psi_{1,1}\rangle$

[13] For $\mathcal{J}_{x-y} = 0$, the interacting part of Eq. (3.10) still commutes with $\hat{S}_z$.

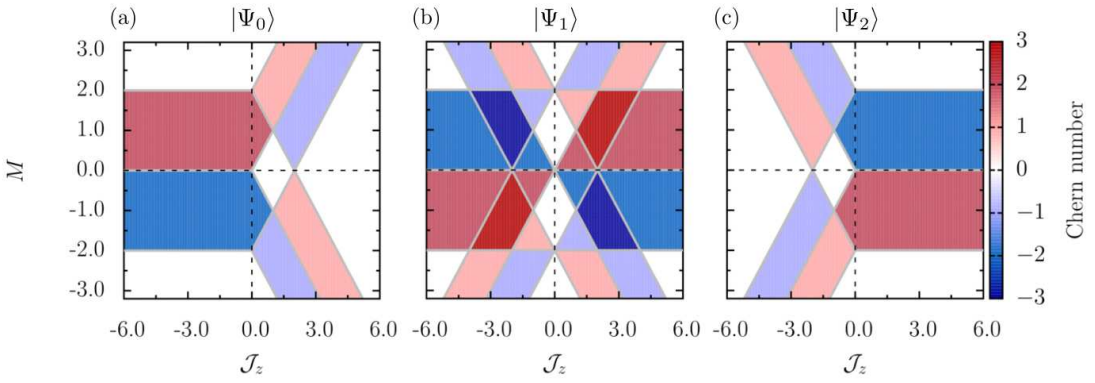

Figure 3.7: Topological phase diagrams associated with Bloch eigenstates $|\Psi_n(\vec{\varphi})\rangle$ $\{n = 0, 1, 2\}$ as a function of mass parameter M and effective interaction strength $\mathcal{J}_z$ ($\mathcal{J}_{x-y} = 0$). Due to many-body effects, interactions can drive the system into correlated topological phases with odd Chern numbers $C_n = \pm 1, \pm 3$. Furthermore, a finite interaction strength $\mathcal{J}_z \neq 0$ can induce a nontrivial topology for states that were trivial in the noninteracting regime. The associated topological phase transitions are accompanied by band inversions at *high-symmetry points* (HSPs) of the synthetic 2D *Brillouin zone* (BZ) (cf. Fig. 3.8). *Reprinted figure with permission from Ref. [KPBT20]. Copyright (2022) by the American Physical Society.*

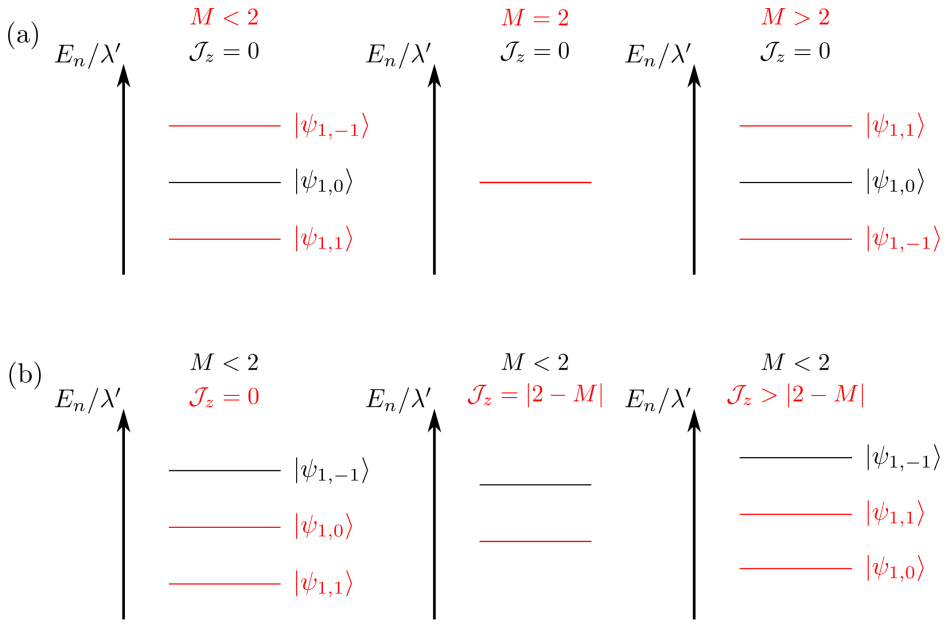

Figure 3.8: Schematic illustration of the energy levels E_n/λ' at *high-symmetry points* (HSPs) of the synthetic 2D *Brillouin zone* (BZ). We restrict ourselves to the HSP $(0, 0)$, while similar observations can be obtained for the other HSPs as well (cf. Tab. 3.2). For $\mathcal{J}_z = 0$, a topological phase transition can only occur for the mass parameter $M = 2$, revealing an inversion between the ferromagnetic triplet states $|\psi_{1,1}\rangle$ and $|\psi_{1,-1}\rangle$. Assuming antiferromagnetic couplings between the spins, the effective interaction strength $\mathcal{J}_z = |2 - M|$ induces an inversion between the ferromagnetic state $|\psi_{1,1}\rangle$ (as $M < 2$) and the antiferromagnetic state $|\psi_{1,0}\rangle$, corresponding to a linear phase boundary in Fig. 3.7.

HSP	$(0,0)$	$(0,\pi),(\pi,0)$	(π,π)
$\mathcal{J}_z$	$\pm\lvert 2-M\rvert$	$\pm\lvert M\rvert$	$\pm\lvert 2+M\rvert$

Table 3.2: Interaction strength $\mathcal{J}_z$ (as a function of M) for which a Dirac gap closing happens at *high-symmetry points* (HSPs) of the synthetic 2D *Brillouin zone* (BZ). Positive (negative) $\mathcal{J}_z$ correspond to inversions between the ferromagnetic ground (highest excited) state and the antiferromagnetic state $|\psi_{1,0}\rangle$ (cf. Fig. 3.8(b)). Since gap closings and reopenings at $(0,\pi)$ and $(\pi,0)$ occur simultaneously, the change in the global Chern number C_n is twice as large as in the other HSPs. *Adapted table with permission from Ref. [KPBT20]. Copyright (2022) by the American Physical Society.*

and $|\psi_{1,-1}\rangle$, which is why the polarization of both spins reverses upon band inversion at the respective HSP. The global topological invariant then changes by an even number $\Delta C_n = \pm 2, \pm 4$. Conversely, a band inversion containing the antiferromagnetic state $|\psi_{1,0}\rangle$ is the reason for the generation of the odd topological phases with $C_n = \pm 1, \pm 3$.

3.2.3 Two-Body Spin Configurations

From the previous considerations, it seems illuminating to investigate the relationship between the spin configurations of the Bloch eigenstates $|\Psi_n(\vec{\varphi})\rangle$ and the respective topological invariants of the synthetic energy bands $E_n(\vec{\varphi})$. In our case, it suffices to focus on HSPs, which completely determine the topology of the system[14]. In Fig. 3.9, the spin configurations at HSPs are schematically shown for an increasing interaction strength $\mathcal{J}_z \geq 0$ and fixed mass parameter $M = 1.2$ (cf. Fig. 3.7). For $\mathcal{J}_z = 0$, the ground state $|\Psi_0(\vec{\varphi})\rangle$ is always a separable state, and the global topological features can be interpreted by examining the spins separately: each spin exhibits a well-defined single-particle Chern number corresponding to the winding number ν_{gr}, the latter describing the coverage of the single-spin Bloch sphere as $\vec{\varphi}$ varies (cf. Fig. 3.2). The global Chern number $C_0 = 2\,\nu_{gr}$ is then simply the sum of the two single-particle ones. Since the two spins at $(0,0)$ are polarized in opposite directions with respect to the other HSPs, each spin winds once around its Bloch sphere ($\nu_{gr} = 1$, cf. Fig. 3.3), resulting in the combined Chern number $C_0 = 2$.

By increasing the interaction strength $\mathcal{J}_z > 0$, a phase transition into the correlated topological phase $C_0 = 1$ is achieved. Within this phase, the separable ground state $|\psi_{1,1}\rangle$ (as $M < 2$) at $(0,0)$ is substituted by the maximally entangled state $|\psi_{1,0}\rangle$ (cf. Fig. 3.8(b)). Thus, since it is no longer possible to specify a winding number for the individual constituents[15], we exploit the following idea: We examine the topological

[14] Since the Hamiltonian (3.10) commutes with $\hat{S}_z$ at HSPs, there exists a mapping (see Fig. 3.9) from the spin configurations at HSPs to the topological invariant of Eq. (3.13). This applies whenever $\mathcal{J}_z \neq 0$ and $\mathcal{J}_{x-y} = 0$, while for nonvanishing $\mathcal{J}_{x-y}$ this argument breaks down. The topological invariant then needs to be explicitly calculated by Eq. (3.13), but as discussed in the Appendix A.2, this does not qualitatively change the phenomenological results obtained for the ITFC.

[15] As a maximally entangled state $|\psi_{1,0}\rangle$ entails vanishing Bloch vectors for the associated reduced density matrices [NC10], a winding number for the individual constituents of the ITFC is not well defined (see discussion around Eq. (B.8)).

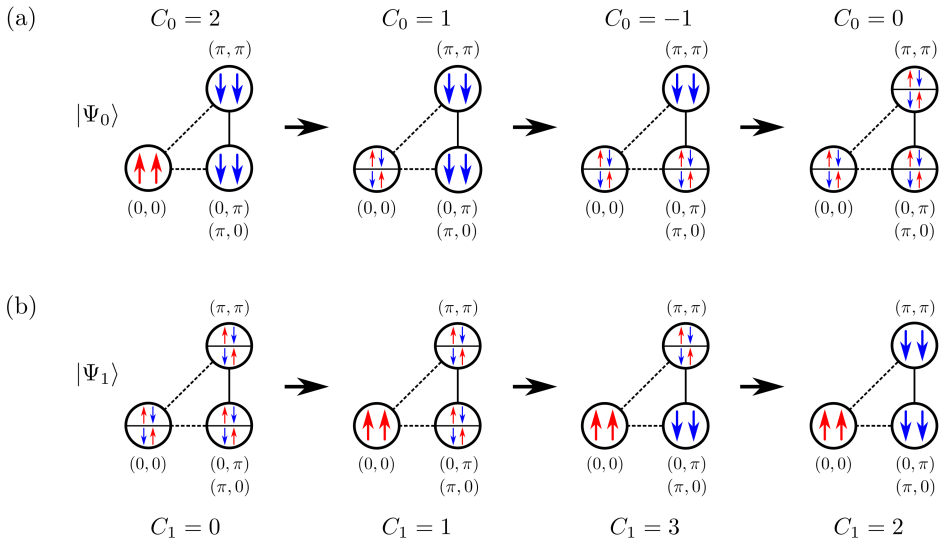

Figure 3.9: Spin configurations of (a) the ground state $|\Psi_0(\vec{\varphi})\rangle$ and (b) the first excited state $|\Psi_1(\vec{\varphi})\rangle$ at *high-symmetry points* (HSPs) for interaction strengths $\mathcal{J}_z \geq 0$ and a fixed mass parameter $M = 1.2$ (cf. Fig. 3.7). Topological phase transitions caused by $\mathcal{J}_z$ lead to inversions between separable $|\psi_{1,1}\rangle$, $|\psi_{1,-1}\rangle$ and maximally entangled states $|\psi_{1,0}\rangle$ (cf. Fig. 3.8), which is why it is no longer possible to specify a winding number for the individual constituents. To describe the topology, we consider each separable state that contributes to the linear combination in $|\psi_{1,0}\rangle$ individually according to its topological features. Depending on the number $\{k = 0, \ldots, 3\}$ of HSPs containing a maximally entangled state $|\psi_{1,0}\rangle$, this leads to 2^k combinations for the spin configurations formed by the equally weighted quantum states $|\uparrow\downarrow\rangle$ and $|\downarrow\uparrow\rangle$ at different HSPs. *Adapted figure with permission from Ref. [KPBT20]. Copyright (2022) by the American Physical Society.*

features of each separable state that contributes to the linear combination in $|\psi_{1,0}\rangle$ individually. For instance, for the phase of $C_0 = 1$ the topology associated with the equally weighted quantum states (I) $|\uparrow\downarrow\rangle^{(0,0)}$ and (II) $|\downarrow\uparrow\rangle^{(0,0)}$ at $(0,0)$ is examined. Each separable state reveals a single-spin winding number $\nu_A^{(\mathrm{I})} = 1$ or $\nu_A^{(\mathrm{II})} = 0$ for spin A. Moreover, spin B is antiferromagnetically correlated to spin A, resulting in the winding number $\nu_B^{(\mathrm{I})} = 0$ or $\nu_B^{(\mathrm{II})} = 1$. In both cases (I) and (II), the single-particle winding numbers add up to a global Chern number $C_0 = 1$. This picture provides an intuitive explanation for the odd topological phase: each band inversion between an antiferromagnetic (maximally entangled) state $|\psi_{1,0}\rangle$ and a ferromagnetic (separable) state $|\psi_{1,1}\rangle$, $|\psi_{1,-1}\rangle$ causes a change in the global Chern number by $\Delta C_n = \pm 1$.

When the interaction strength $\mathcal{J}_z > 0$ is increased up to the phase $C_0 = -1$, the separable ground states $|\psi_{1,-1}\rangle$ (as $M > 0$) at $(0,\pi)$, $(\pi,0)$ are replaced by the maximally entangled states $|\psi_{1,0}\rangle$. By applying the previous picture, we have to consider four[16] combinations for the spin configurations formed by the equally weighted quantum states $|\uparrow\downarrow\rangle$ and $|\downarrow\uparrow\rangle$ at different HSPs: $|\uparrow\downarrow\rangle^{(0,0)}\,|\uparrow\downarrow\rangle^{(0,\pi)}$, $|\uparrow\downarrow\rangle^{(0,0)}\,|\downarrow\uparrow\rangle^{(0,\pi)}$, $|\downarrow\uparrow\rangle^{(0,0)}\,|\uparrow\downarrow\rangle^{(0,\pi)}$,

[16]Due to the symmetry of the Hamiltonian $\hat{H}(0,\pi) = \hat{H}(\pi,0)$, the quantum states at $(0,\pi)$, $(\pi,0)$ show the same spin configuration.

and $|{\downarrow\uparrow}\rangle^{(0,0)}$ $|{\downarrow\uparrow}\rangle^{(0,\pi)}$. For each combination, the corresponding single-spin winding numbers[17] add up to the combined Chern number $C_0 = -1$. This mechanism is quite generic and applies whenever $\mathcal{J}_z \neq 0$ and $\mathcal{J}_{x-y} = 0$: If $\{k = 0, \ldots, 3\}$ is the number of HSPs containing a maximally entangled state $|\psi_{1,0}\rangle$, we have to examine 2^k equally weighted combinations of spin configurations individually (see Fig. 3.9). Topological phase transitions in Fig. 3.7 are thus associated with a change in the spin configuration of the Bloch eigenstate $|\Psi_n(\vec{\varphi})\rangle$ under consideration. Remarkably, in the first excited state $|\Psi_1(\vec{\varphi})\rangle$, this generic concept can produce a correlated topological phase $C_1 = 3$ in which one of the spins effectively winds twice around its Bloch sphere (see Appendix A.1), a situation that is impossible in the noninteracting case (cf. Fig. 3.3).

3.2.4 Correlated Topological Response

The dynamics of the system can be described in a two-dimensional Floquet lattice with fictitious electric field $\vec{E} = \vec{\omega}$, the latter inducing a linear Hall response that gives rise to a transverse current in the frequency domain (for a schematic illustration see Fig. 2.2). For a system initially prepared in a Bloch eigenstate $|\Psi_n(\vec{\varphi})\rangle$ of $\hat{H}_T$, the topological features of Fig. 3.7 then translate into a quantized frequency conversion between the circularly polarized drives (see Sec. 2.3.3). As first realized in Ref. [MRH17], energy is pumped between the two fields at a time-averaged rate (cf. Eq. (2.73))

$$P_n^{12} = -P_n^{21} = \frac{C_n}{2\,\pi}\,\omega_1\,\omega_2,$$

provided the dynamics is approximately confined to a Bloch energy band $E_n(\vec{\varphi})$ of Chern number C_n (see Eq. 3.13). A necessary condition for the observation of a quantized rate, besides quasiadiabaticity, is that the two frequencies $\frac{\omega_1}{\omega_2} \notin \mathbb{Q}$ are incommensurate in such a way that the dynamics effectively samples the entire synthetic 2D BZ of the two-dimensional Floquet lattice (cf. Fig. 2.3). Here, we have used the terminology of quasiadiabaticity, corresponding to dynamics well described by first-order APT (see Sec. 2.1.3). Thus, quasiadiabaticity is given for frequencies ω_1 and ω_2 that are much smaller than the minimum band gaps between the synthetic energy bands $E_n(\vec{\varphi})$ of the Hamiltonian (3.12), so that over time nonadiabatic excitations are suppressed. In this regime, the topological phase with Chern number $C_n = \pm 3$ generates an enhancement of the frequency conversion as a direct consequence of the correlated spin configurations in the ITFC. Remarkably, this amplification is found to be more pronounced as the number of spins increases, as we explicitly confirm in the Appendix A.3 for the example of three interacting spins. There, global Chern numbers up to $C_n = \pm 5$ are observed.

We investigate the topological energy pumping effect by numerically solving the time-dependent Schrödinger equation associated with the Hamiltonian (3.10) of the interacting spin system[18] (cf. Sec. 3.1.3). To this end, we compute the expectation value

[17] A mapping of all possible single-spin configurations at HSPs to the winding number ν is given in the Appendix A.1.

[18] We have multiplied (3.10) by an overall factor $\eta = 2.0$, which formally increases the minimum band gaps of the system and thus improves the ability to stay within the associated energy level $E_n(\vec{\varphi}_t)$ during the quasiperiodic dynamics. This allows us to choose a larger frequency $\omega = 0.1\,\lambda'$, such that

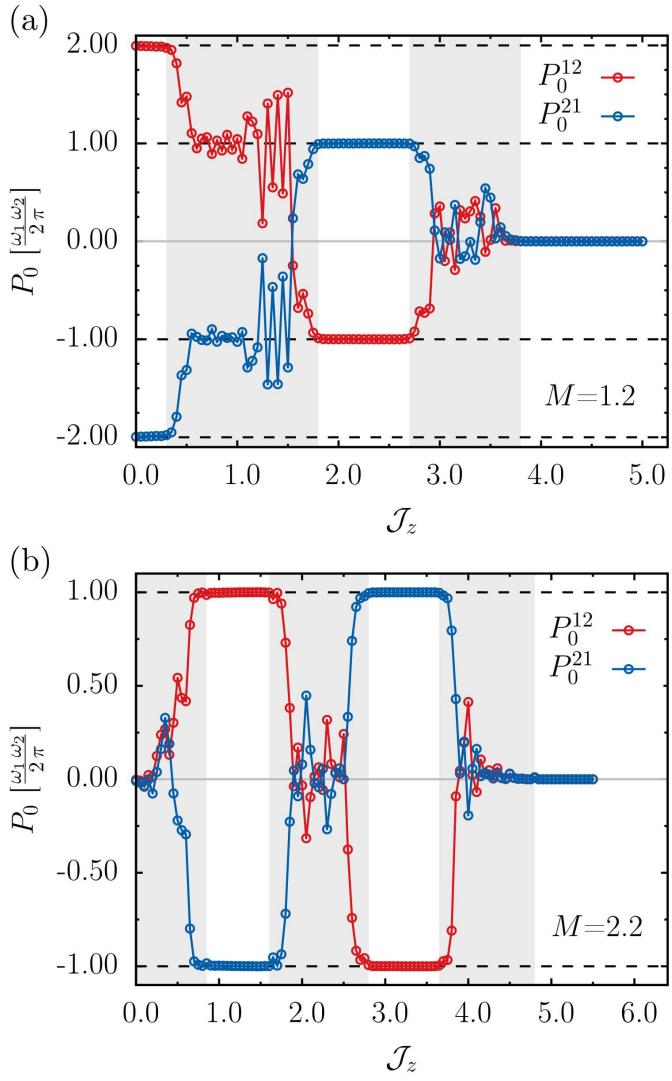

Figure 3.10: Extrapolated energy pumping rate P_0 as a function of $\mathcal{J}_z$ for mass parameters (a) $M = 1.2$ and (b) $M = 2.2$. The quantization occurs in an excellent agreement (white regimes) with the topological phase diagrams of Fig. 3.7. This applies as long as the system shows quasiadiabaticity, while otherwise the topological response breaks down (gray regimes). *Reprinted figure with permission from Ref. [KPBT20]. Copyright (2022) by the American Physical Society.*

of the current operator $\hat{\mathbf{I}}(\vec{\varphi}_t) = \nabla_{\vec{\varphi}}\,\hat{H}(\vec{\varphi}_t)$, which is associated with the total energy transfer rate as can be seen from the equations of motion (cf. Eq. (2.19)): $\frac{\mathrm{d}}{\mathrm{d}t}\,\langle\hat{H}(\vec{\varphi}_t)\rangle = \langle\partial_t\,\hat{H}(\vec{\varphi}_t)\rangle = \vec{\omega}\,\langle\hat{\mathbf{I}}(\vec{\varphi}_t)\rangle$. If the initial state at $t_0 = 0$ is the eigenstate $|\Psi_n(\vec{\varphi}_{t_0})\rangle$,

the entire synthetic 2D BZ is sufficiently sampled for a time evolution up to times $\lambda' T = 10^4$. This leads to a significant reduction of computation time.

the averaged pumping rates $P_{n,k}$ (cf. Eq. (2.72)) can be extrapolated through linear regression of the associated energy transfers $W_k(t) = \omega_k \int_0^t \mathrm{d}t' \, \langle \hat{\mathrm{I}}_k(\vec{\varphi}_{t'}) \rangle$ (cf. Fig. 3.5). Throughout the numerics, we choose the vectors of frequencies $\vec{\omega} = (1, \gamma)\,\omega$ and offset phases $\vec{\phi} = (\pi/10, 0)$, with $\omega = 0.1\,\lambda'$ and $\gamma = \frac{1}{2}(1 + \sqrt{5})$. To ensure that the entire synthetic 2D BZ is adequately sampled (cf. Fig. 2.3), we calculate the exact dynamics up to times $\lambda' T = 10^4$. In Fig. 3.10, the extrapolated pumping rate P_0 associated with the ground state $|\Psi_0(\vec{\varphi}_{t_0})\rangle$ is shown as a function of $\mathcal{J}_z$ for mass parameters (a) $M = 1.2$ and (b) $M = 2.2$. A quantized frequency conversion occurs in an excellent agreement (white regimes) with the topological phase diagrams of Fig. 3.7. This applies as long as the ITFC shows quasiadiabaticity. Otherwise, the topological response is suppressed (gray regimes), and perfect quantization breaks down.

4

Open Quantum System Perspective

Contents

A key ingredient of many manifestations of topology in physics is the appearance of impressively robust and quantized linear response signals, such as those predicted for the transverse conductance in the integer quantum Hall effect [KDP80, PG90]. According to the well-known Kubo formula [Kub57, Mah00], the linear response due to an external field originates from the first perturbative correction of the state, which can eventually be projected onto a topological invariant characterizing the occupied Bloch bands of the system [Lau81, TKNdN82, Sim83a, Koh85, Hal88]. Following this line of reasoning, the topologically quantized response of an isolated quantum system is characterized by its adiabatically defined topological invariant, revealing a correspondence that has been applied to a variety of topological systems [Tho98, XCN10, Van18, CF21].

In this chapter, we show how this correspondence between adiabatically defined topological invariants and quantized response properties can be profoundly modified in open quantum systems. In this context, we propose a *topological burning glass effect* (TBGE) in which the local response of a system exhibits a topological quantization that is amplified by its environmental coupling. The (small) quantum system coupled to a (larger) environment adopts the topological nature of the total system in its non-unitary dynamics, imposing a local response that is not captured by the adiabatically defined topological invariant of the quantum system. As a paradigmatic platform, we extend the Floquet counterpart of a Chern insulator, namely the *topological frequency converter* (TFC) of Sec. 3.1, by statically coupling it to a set of $N-1$ surrounding spins by means of a *central spin model* (CSM) [Gau76, DPS04, CDBF19]. In the strong coupling regime, the collective motion of the environmental spins is readily understood to imprint on the TFC an N-fold enhanced topological frequency conversion between the two driving frequencies, while the adiabatic winding number (see Sec. 3.1.2) of the driven spin remains equal to one. Given this discrepancy, we argue that the TBGE is induced by the non-unitary dynamics of the TFC, which locally involves the collective motion of the surrounding spins and leads to fluctuations around the adiabatic spin polarization that significantly differ from those of the single spin case. Besides using basic concepts of quantum information theory [NC10], our results are derived in the framework of *adiabatic perturbation theory* (APT) (see Sec. 2.1.3) and fully corroborated by exact numerical simulations, the latter allowing for a systematic investigation of the nonadiabatic breakdown of the strong coupling regime in our concrete model.

The Chapter is organized as follows: In Sec. 4.1, we study the hyperfine interactions in lateral *quantum dots* (QDs) [KAT01, HKP$^+$07, RT10, ZDM$^+$13, CSDF$^+$21] or *nitrogen-vacancy* (NV) centers [JW06, DMD$^+$13, SCLD14], elaborating a parametrization of the environmental effects in terms of the CSM. Taking this interacting system, we analytically derive the topological band structure in the synthetic 2D *Brillouin zone* (BZ), with energy gaps that are robust to variations in the interaction strength and scale with $1/N$ due to spin-wave excitations. Based on these calculations, we examine the TBGE in its full glory in Sec. 4.2, using fundamental concepts that imply a generic validity of our results. In Sec. 4.3, we analyze the transient dynamics of the nonequilibrium phases diagrams, predicting (pre)thermalization into a dynamical quantum phase with ensemble-averaged pumping rate identical to the single spin case. Parts of this Chapter have been published as a Letter in Physical Review B [KPBT22].

4.1 Central Spin Model

Trapped electron spins in lateral QDs [KAT01, HKP$^+$07, RT10, ZDM$^+$13, CSDF$^+$21] or NV centers [JW06, DMD$^+$13, SCLD14] can serve as building blocks for quantum computation [LD98, DiV00, NC10], in which fundamental concepts of quantum mechanics, such as coherent superposition or entanglement, can be applied to solve complex problems by powerful quantum algorithms [Sho94, EJ96, Gro97, Wil11]. In these systems, the spin degree of freedom of the electron can be employed to build a two-level system, the quantum version of a classical bit [NC10]. However, since the electron wave function is not perfectly localized, its spatial extent induces interactions with the surrounding nuclear spins of the host material [UMA$^+$13, KL13]. As a consequence, the electron spin is not isolated from its environment, revealing decoherence effects that can be properly described in the framework of a CSM [Gau76, DPS04, CDBF19]. Apart from being of fundamental interest for the study of quantum integrability [CDBF19, VCC20, VCP$^+$20], the CSM can address the hyperfine interactions between a central spin and an arbitrary number of environmental spins in the lateral QDs or NV centers [SKL03, CB09]. If we restrict ourselves to a star-like geometry, in which a central spin exposed to a time-quasiperiodic magnetic field statically couples to the surrounding spins by a homogeneous and isotropic interaction strength, the CSM exhibits a block diagonal form in its Hamiltonian. Concentrating on the block that contains the overall ground state of the system, we analytically derive the topological band structure in the synthetic BZ. The latter reveals a gapped spectrum robust to variations in the interaction strength, with a minimum band gap that scales inversely with the total number of spins due to spin wave excitations. This analysis provides fruitful insights into the topological properties of the CSM, essential for the subsequent discussion of the TBGE (see Sec. 4.2) and the associated nonequilibrium phase diagrams (see Sec. 4.3). Parts of this Section are based on the Supplemental Material of Ref. [KPBT22].

4.1.1 Hyperfine Interactions

Quasiperiodically driven few-spin devices, such as the TFC or ITFC proposed in Chap. 3, provide an intriguing platform for the generation of topological phenomena in dynamically-induced synthetic dimensions. While in the TFC only a single spin is exposed to the time-quasiperiodic external fields, the correlated topological responses in the ITFC are induced by additional Heisenberg interactions between the two driven spins. A possible implementation of the TFC is given by a driven electron spin captured in a lateral QD [KAT01, HKP$^+$07, RT10, ZDM$^+$13, CSDF$^+$21] or NV center in diamond [JW06, DMD$^+$13, SCLD14], while an extension to a gated double quantum dot [PJT$^+$05, BFT$^+$15, SPF$^+$19] can realize the ITFC. In both models, however, we have supposed that the electron spins are perfectly isolated from their environment, an assumption that does not hold under realistic experimental conditions. There, interactions with the environment can significantly modify the spin dynamics of the electron, eventually revealing decoherence effects for the associated quantum states [SKL03, HKP$^+$07, CB09, KL13]. In what follows, we briefly outline the fundamental interactions in solid-state QDs, and derive a minimal model that accounts for

the environmental effects.

In QDs, the spatial degrees of freedom of an electron can be constrained by suitable geometric arrangements and electronic gates, resulting in discrete states similar to those of a conventional atom [KAT01, HKP$^+$07, UMA$^+$13]. By filling such a zero-dimensional state with a single electron, its spin degree of freedom can serve as the building block of a quantum computer [LD98, DiV00, NC10]. There, the classical bit is replaced by a two-level quantum system, which can be initialized in any superposition of the two classical outputs of the bit. This enables the application of fundamental concepts of quantum mechanics, where the coherent superposition and entanglement between several two-level systems can provide the basis for fascinating quantum algorithms [Sho94, EJ96, Gro97, Wil11]. In these algorithms, successful quantum computation requires coherent manipulation of the spin state over sufficiently long time-scales. Interaction with the environment, however, eventually leads to a loss of this coherence. In fact, as the electron spin wave function is not perfectly confined to the zero-dimensional structure, these decoherence effects are mainly induced by the hyperfine interactions between the trapped electron spin and the nuclear spins of the host material [HKP$^+$07, UMA$^+$13, KL13].

Two of the most relevant interaction mechanisms in solid-state QDs involve the Zeeman coupling of an external field to the magnetic moments of the underlying spins, and the hyperfine interactions of the electron spin to the surrounding nuclear spins. Accordingly, a proper theoretical model for a quasiperiodically driven QD is provided by the Hamiltonian [SKL03, CB09, KL13]

$$\hat{H}(\vec{\varphi}_t) = g^* \, \mu_B \, \mathbf{B}(\vec{\varphi}_t) \cdot \hat{\mathbf{S}}_0 - g_N \, \mu_N \sum_{k=1}^{N-1} \mathbf{B}(\vec{\varphi}_t) \cdot \hat{\mathbf{S}}_k - \sum_{k=1}^{N-1} A_k \sum_{\mu,\nu} \hat{X}_{\mu\nu} \, \hat{S}_0^{\mu} \, \hat{S}_k^{\nu}. \tag{4.1}$$

The spin operators $\hat{\mathbf{S}}_0 = \frac{1}{2}\,\hat{\boldsymbol{\sigma}}_0$ and $\hat{\mathbf{S}}_k = \frac{1}{2}\,\hat{\boldsymbol{\sigma}}_k$ constitute to the central electron spin and the surrounding nuclear spins of the host material, where we restrict ourselves to spin-1/2 for both components. The vector of Pauli matrices acting on the individual subspaces of the constituents is given by $\hat{\boldsymbol{\sigma}}_i = (\hat{\sigma}_i^x, \hat{\sigma}_i^y, \hat{\sigma}_i^z)$. The Zeeman coupling terms associated with the dynamical magnetic field $\mathbf{B}(\vec{\varphi}_t)$ are proportional to Bohr's magneton μ_B (the nuclear magneton μ_N) and the effective g^*-factor of the central spin (the nuclear g_N-factor of the environmental spins) [SKL03, CB09, UMA$^+$13]. The relative sign difference in the Zeeman coupling terms is due to the opposite charge of the corresponding constituents, while we assume that there only exists one nuclear spin species in the QD. The central electron spin couples to a set of $N-1$ nuclear spins via hyperfine interactions, the latter parametrized by a Heisenberg term with inhomogeneous coupling strengths A_k. In this context, we further introduce the dimensionless tensor $\hat{X}_{\mu\nu}$ $\{\mu, \nu = x, y, z\}$, which accounts for possible anisotropies in the interaction [CB09, RT10]. We neglect the dipole-dipole coupling between the nuclear spins, as their energy scales are typically much smaller than those of the hyperfine interaction between the electron spin and the environmental spins [SKL03, HKP$^+$07, KL13].

The details of the interaction can significantly vary according to the choice of the host material of the QD. In fact, prototype materials such as GaAs QDs [HKP$^+$07, UMA$^+$13, KL13] or graphene QDs [TBLB07, RT10, RGB$^+$11] differ in several aspects. For instance, while the hyperfine interaction in graphene is generally anisotropic in nature, it is isotropic in GaAs. However, the probably most crucial difference between

these two substrates appears in the size of the associated spin environments. While in GaAs there typically exists up to 10^6 nuclear spins in the QDs [KAT01, HKP$^+$07, UMA$^+$13, KL13], isotopic purification [TLAR03, BNT$^+$09, CSDF$^+$21] in carbon based materials allows for a variable size in the number of environmental spins. In this sense, isotopic purification offers the opportunity to explore the physical limits of both large and small spin environments, which could find application in QDs based on graphene [TBLB07, RT10, RGB$^+$11] or SiGe [ZDM$^+$13, CSDF$^+$21]. Alternatively, NV centers in diamond can provide a moderately small number of environmental spins as well [JW06, DMD$^+$13, SCLD14].

We choose the dynamical modulation of the external field $\mathbf{B}(\vec{\varphi}_t) = B_c\,\mathbf{d}(\vec{\varphi}_t)$ as (cf. Eq. (3.4))

$$\mathbf{d}(\vec{\varphi}_t) = \begin{pmatrix} \sin(\varphi_{1t}) \\ \sin(\varphi_{2t}) \\ M - \cos(\varphi_{1t}) - \cos(\varphi_{2t}) \end{pmatrix},$$

consisting of a static magnetic field with amplitude $B_s = B_c\,M$ in z direction, and two circularly polarized drives with amplitudes B_c. The associated time-dependent phases $\vec{\varphi}_t = (\varphi_{1t}, \varphi_{2t}) = \vec{\omega}\,t + \vec{\phi}$ are generated by the vector of incommensurate frequencies $\vec{\omega} = (\omega_1,\, \omega_2)$ and offset phases $\vec{\phi} = (\phi_1,\, \phi_2)$. Introducing the relation $\Delta x = \frac{g_N\,\mu_N}{g^*\,\mu_B}$, the energy scale[1]

$$\lambda = g^*\,\mu_B\,B_c,$$

and the renormalized interaction strength $\mathcal{A}_k = A_k/\lambda$, the Hamiltonian (4.1) can be rewritten as

$$\hat{H}(\vec{\varphi}_t) = \lambda\left[\mathbf{d}(\vec{\varphi}_t)\cdot\hat{\mathbf{S}}_0 - \Delta x\sum_{k=1}^{N-1}\mathbf{d}(\vec{\varphi}_t)\cdot\hat{\mathbf{S}}_k - \sum_{k=1}^{N-1}\mathcal{A}_k\sum_{\mu,\nu}\hat{X}_{\mu\nu}\,\hat{S}_0^{\mu}\,\hat{S}_k^{\nu}\right].$$

Typically, the Zeeman splitting between the nuclear spin states is much smaller than that of the central electron spin, revealing a relation $|\Delta x| \ll 1$ [SKL03, HKP$^+$07, UMA$^+$13]. If we consider rather small spin environments, we can thus neglect the Zeeman coupling terms of the environmental spins. For simplicity, we further assume homogeneous $\mathcal{A}_k = \mathcal{A}$ and isotropic $\hat{X}_{\mu\nu} = \delta_{\mu\nu}$ Heisenberg interactions between the central electron spin and the surrounding spins, eventually leading to the quasiperiodically driven CSM [Gau76, DPS04, CDBF19]

$$\hat{H}(\vec{\varphi}_t) = \lambda\,[\mathbf{d}(\vec{\varphi}_t)\cdot\hat{\mathbf{S}}_0 - \mathcal{A}\,\hat{\mathbf{S}}_0\cdot\hat{\mathbf{J}}]. \tag{4.2}$$

Although this minimal model may not reflect the physics of real experimental setups, the Hamiltonian (4.2) shows an important symmetry based on the star-geometry of the homogeneous interaction: $[\hat{H}(\vec{\varphi}_t), \hat{\mathbf{J}}^2] = 0$, with $\hat{\mathbf{J}} = \sum_{k=1}^{N-1}\hat{\mathbf{S}}_k$. As a consequence, the total system can be transformed into a block diagonal form, with each block characterized

[1] We assume $\lambda > 0$ for simplicity.

by a constant of motion[2]

$$j = \begin{cases} \frac{N-1}{2},\, \frac{N-1}{2}-1,\, \ldots,\, \frac{1}{2} & ;\, N \text{ even} \\ \frac{N-1}{2},\, \frac{N-1}{2}-1,\, \ldots,\, 0 & ;\, N \text{ odd} \end{cases}$$

corresponding to the total spin $\hat{\mathbf{J}}^2$ of the surrounding spins with $N \geq 2$. In the remainder of Sec. 4.1, we explicitly analyze this block diagonal form, showing that the overall ground state is contained in the block $j = \frac{N-1}{2}$. Restricting ourselves to this block, we derive the topological band structure in the synthetic 2D BZ, and demonstrate that it leads to a gapped spectrum robust to variations in the interaction strength. The minimum band gaps of the synthetic band structure scale with the inverse of the total number of spins, described by the collective behavior of spin wave excitations. This analysis forms the basis for the subsequent discussion of the TBGE (see Sec. 4.2) and the associated nonequilibrium phase diagrams (see Sec. 4.3), which are derived from the quasiperiodic dynamics of the system. In what follows, however, we derive the instantaneous spectrum of the Hamiltonian (4.2) for fixed values of the phases $\vec{\varphi}_t$, that is at a given point of the synthetic 2D BZ. To this end, we suppress the subscript t from $\vec{\varphi}_t$.

4.1.2 Block diagonal form

Rewriting Eq. (4.2) by means of the total spin $\hat{\mathbf{S}}_{\text{tot}} = \hat{\mathbf{S}}_0 + \hat{\mathbf{J}}$, it becomes clear that the interaction is invariant under the transformation

$$\hat{H}'(\vec{\varphi}) = \Big(\bigotimes_{i=0}^{N-1} \hat{U}^\dagger(\vec{\varphi}) \Big)\, \hat{H}(\vec{\varphi})\, \Big(\bigotimes_{i=0}^{N-1} \hat{U}(\vec{\varphi}) \Big) = \lambda \Big[|\mathbf{d}(\vec{\varphi})|\, \hat{S}_0^{z'} - \frac{\mathcal{A}}{2} \Big(\hat{\mathbf{S}}_{\text{tot}}^2 - \hat{\mathbf{J}}^2 - \frac{3}{4} \Big) \Big]. \quad (4.3)$$

The $SU(2)$ matrices $\hat{U}(\vec{\varphi})$ rotate the z quantization axes of the subspaces in the z' direction of the field vector $\mathbf{d}(\vec{\varphi})$: $\hat{U}^\dagger(\vec{\varphi})\, \mathbf{d}(\vec{\varphi}) \cdot \hat{\boldsymbol{\sigma}}\, \hat{U}(\vec{\varphi}) = |\mathbf{d}(\vec{\varphi})|\, \hat{\sigma}^{z'}$. By introducing raising and lowering operators $\hat{S}_0'^{\pm} = \hat{S}_0^{x'} \pm \mathrm{i}\, \hat{S}_0^{y'}$ and $\hat{J}'^{\pm} = \hat{J}^{x'} \pm \mathrm{i}\, \hat{J}^{y'}$ within the rotated basis, Eq. (4.3) can be rewritten as

$$\hat{H}'(\vec{\varphi}) = \lambda \Big[|\mathbf{d}(\vec{\varphi})|\, \hat{S}_0^{z'} - \frac{\mathcal{A}}{2} \Big(\hat{S}_0'^{+}\, \hat{J}'^{-} + \hat{S}_0'^{-}\, \hat{J}'^{+} + 2\, \hat{S}_0^{z'}\, \hat{J}^{z'} \Big) \Big]. \quad (4.4)$$

Eq. (4.4) immediately reveals the symmetries of the model: $[\hat{H}'(\vec{\varphi}), \hat{\mathbf{J}}^2] = [\hat{H}(\vec{\varphi}), \hat{\mathbf{J}}^2] = 0$ and $[\hat{H}'(\vec{\varphi}), \hat{S}_{\text{tot}}^{z'}] = 0$, where we use that the total spin $\hat{\mathbf{J}}^2$ of the environmental spins is invariant under the transformation defined in Eq. (4.3). The associated quantum numbers are given by

$$j = \begin{cases} \frac{N-1}{2},\, \frac{N-1}{2}-1,\, \ldots,\, \frac{1}{2} & ;\, N \text{ even} \\ \frac{N-1}{2},\, \frac{N-1}{2}-1,\, \ldots,\, 0 & ;\, N \text{ odd} \end{cases} \quad \text{and} \quad m_s = -j - \frac{1}{2}, -j + \frac{1}{2}, \ldots, j + \frac{1}{2}.$$

[2] This can be seen from the equations of motion [Ehr27, Bal15, GS18]: $\frac{\mathrm{d}}{\mathrm{d}t} \langle \hat{\mathbf{J}}^2 \rangle = \mathrm{i}\, \langle [\hat{H}(\vec{\varphi}_t), \hat{\mathbf{J}}^2] \rangle + \langle \partial_t\, \hat{\mathbf{J}}^2 \rangle = 0$, where the expectation values are calculated according to the exact solution of the time-dependent Schrödinger equation of the interacting spin system.

Due to the symmetries of the Hamiltonian $\hat{H}'(\vec{\varphi})$, it seems convenient to represent Eq. (4.4) within the rotated basis of product states between the central spin-1/2 and the total spin $\hat{\mathbf{J}}^2$ of the surrounding spins: $|m_{s_0}, j, m_j, \eta\rangle = |m_{s_0}\rangle \otimes |j, m_j, \eta\rangle$. We introduce the eigenstates within the rotated basis

$$\hat{S}_0^{z'}\ |m_{s_0}\rangle = m_{s_0}\ |m_{s_0}\rangle\,, \quad \hat{\mathbf{J}}^2\ |j, m_j, \eta\rangle = j\,(j+1)\ |j, m_j, \eta\rangle\,, \\ \hat{J}^{z'}\ |j, m_j, \eta\rangle = m_j\ |j, m_j, \eta\rangle\,, \quad (4.5)$$

with quantum numbers $m_{s_0} = \pm\frac{1}{2}$, $m_j = -j, -j+1, \ldots, j$, and $\eta = 1, 2, \ldots, \eta_{\max}$. The quantum numbers η distinguish orthogonal states $\langle j, m_j, \eta | j, m_j, \tilde{\eta}\rangle = \delta_{\eta,\tilde{\eta}}$, having identical quantum numbers j and m_j. Consequently, $\eta_{\max}$ equals the dimension of the degenerated subspace formed by states $|j, m_j, \eta\rangle$ [WM02, BBP04]. The rotated basis states $|m_{s_0}, j, m_j, \eta\rangle$ form an orthonormal set with

$$\langle m_{s_0}, j, m_j, \eta | \tilde{m}_{s_0}, \tilde{j}, \tilde{m}_j, \tilde{\eta}\rangle = \delta_{m_{s_0},\tilde{m}_{s_0}}\ \delta_{j,\tilde{j}}\ \delta_{m_j,\tilde{m}_j}\ \delta_{\eta,\tilde{\eta}}. \quad (4.6)$$

We would like to emphasize that the quantum numbers j are constants of motion, while the quantum numbers m_s are not. This follows from the fact that $\hat{S}_{\mathrm{tot}}^{z'}$ becomes explicitly time-dependent when rotated back into the original basis of Eq. (4.2). Dynamical excitations into states of different m_s are then possible during the nonequilibrium evolution of the system. Concerning the exact dynamics, we can thus restrict ourselves to the basis states with fixed quantum numbers j. The Hamiltonian $\hat{H}'(\vec{\varphi})$ is transformed into a block diagonal form, with each block characterized by the constants of motion j. The explicit representation of the blocks within the rotated basis $\langle m_{s_0}, j, m_j, \eta | \hat{H}'(\vec{\varphi}) | \tilde{m}_{s_0}, j, \tilde{m}_j, \tilde{\eta}\rangle$ can be derived using the properties of Eqs. (4.5), (4.6) and

$$\hat{S}_0'^{\pm}\ |\pm\frac{1}{2}\rangle = 0, \quad \hat{S}_0'^{\pm}\ |\mp\frac{1}{2}\rangle = |\pm\frac{1}{2}\rangle\,, \\ \hat{J}'^{\pm}\ |j, m_j, \eta\rangle = \sqrt{j\,(j+1) - m_j\,(m_j \pm 1)}\ |j, m_j \pm 1, \eta\rangle\,.$$

This yields the only nonvanishing matrix elements

$$\langle m_{s_0}, j, m_j, \eta | \hat{H}'(\vec{\varphi}) | m_{s_0}, j, m_j, \eta\rangle = \lambda\, m_{s_0}\,(|\mathbf{d}(\vec{\varphi})| - \mathcal{A}\, m_j) \quad (4.7)$$

and

$$\langle \mp\frac{1}{2}, j, m_j \pm 1, \eta | \hat{H}'(\vec{\varphi}) | \pm\frac{1}{2}, j, m_j, \eta\rangle = -\frac{\lambda\,\mathcal{A}}{2}\sqrt{j\,(j+1) - m_j\,(m_j \pm 1)}. \quad (4.8)$$

By proper arrangement of the nonvanishing matrix elements of Eqs. (4.7) and (4.8), the block j can be further separated into one- and two-dimensional blocks characterized by quantum numbers m_s (and η). It should be noted that the Hamiltonian $\hat{H}'(\vec{\varphi})$ is degenerate in the quantum numbers η. The one-dimensional blocks correspond to eigenstates $|E, j, m_s, \eta\rangle$ with minimal and maximal values $m_s = \pm\frac{1}{2} \pm j$:

$$|E_{\pm}^{(1)}, j, \pm\frac{1}{2} \pm j, \eta\rangle = |\pm\frac{1}{2}, j, \pm j, \eta\rangle\,, \quad E_{\pm}^{(1)}(\vec{\varphi}, j) = \pm\frac{\lambda}{2}\Big[|\mathbf{d}(\vec{\varphi})| \mp \mathcal{A}\, j\Big]. \quad (4.9)$$

We have introduced quantum numbers E corresponding to the energy eigenvalues of the associated eigenstates $|E, j, m_s, \eta\rangle$. The remaining quantum numbers $m_s = -j + \frac{1}{2}, -j + \frac{3}{2}, \ldots, j - \frac{1}{2}$ define two-dimensional blocks within the rotated basis $\{|\frac{1}{2}, j, m_s - \frac{1}{2}, \eta\rangle, |-\frac{1}{2}, j, m_s + \frac{1}{2}, \eta\rangle\}$, resulting in equations

$$\lambda \left(\frac{\mathbf{l}\,\hat{\boldsymbol{\sigma}}'}{2} + \frac{\mathcal{A}}{4} \right) |E_{\pm}^{(2)}, j, m_s, \eta\rangle = E_{\pm}^{(2)}(\vec{\varphi}, j, m_s)\, |E_{\pm}^{(2)}, j, m_s, \eta\rangle \tag{4.10}$$

with

$$\mathbf{l}(\vec{\varphi}, j, m_s) = \begin{pmatrix} -\mathcal{A}\sqrt{j\,(j+1) - (m_s^2 - \frac{1}{4})} \\ 0 \\ |\mathbf{d}(\vec{\varphi})| - \mathcal{A}\, m_s \end{pmatrix}.$$

The solutions of Eq. (4.10) are given by

$$|E_{\pm}^{(2)}, j, m_s, \eta\rangle = \begin{cases} |\pm\frac{1}{2}, j, m_s \mp \frac{1}{2}, \eta\rangle & ; \mathcal{A} = 0 \\ \frac{|\mathbf{l}| \pm \mathbf{l}\,\hat{\boldsymbol{\sigma}}'}{\sqrt{2\,|\mathbf{l}|\,(|\mathbf{l}| \pm l_z)}} \begin{pmatrix} 1 \\ 0 \end{pmatrix} & ; \mathcal{A} \neq 0 \end{cases},$$

$$E_{\pm}^{(2)}(\vec{\varphi}, j, m_s) = \pm\frac{\lambda}{2}\left[|\mathbf{l}(\vec{\varphi}, j, m_s)| \pm \frac{\mathcal{A}}{2} \right]. \tag{4.11}$$

The representation of the instantaneous eigenstates can be further simplified to

$$|E_{\pm}^{(2)}, j, m_s, \eta\rangle = \frac{1}{\sqrt{2}}\left[\sqrt{1 \pm \frac{l_z}{|\mathbf{l}|}}\; |\frac{1}{2}, j, m_s - \frac{1}{2}, \eta\rangle \mp \mathrm{sgn}(\mathcal{A}) \sqrt{1 \mp \frac{l_z}{|\mathbf{l}|}}\; |-\frac{1}{2}, j, m_s + \frac{1}{2}, \eta\rangle \right], \tag{4.12}$$

with the sign-function

$$\mathrm{sgn}(x) = \begin{cases} +1 & ; x \geq 0 \\ -1 & ; x < 0 \end{cases}.$$

Assuming that $|\mathbf{d}(\vec{\varphi})| \neq 0$, $\mathcal{A} \neq 0$ and $\lambda > 0$, we examine the overall ground state of Eqs. (4.9) and (4.11). By formally performing the derivative

$$\frac{\partial E_{-}^{(2)}(\vec{\varphi}, j, m_s)}{\partial m_s} = \frac{\lambda\,|\mathbf{d}(\vec{\varphi})|\,\mathcal{A}}{2\,|\mathbf{l}(\vec{\varphi}, j, m_s)|}$$

at a given point of the synthetic 2D BZ, we can conclude that for ferromagnetic/antiferromagnetic interaction strength $\mathcal{A} > 0/\mathcal{A} < 0$ the lowest energy level $E_{-}^{(2)}$ within each block j is given by the minimal/maximal quantum number $m_s = -j + \frac{1}{2}/m_s = j - \frac{1}{2}$. Moreover, it can be shown that

$$\lim_{m_s \mapsto -\frac{1}{2} - j} E_{-}^{(2)}(\vec{\varphi}, j, m_s) = \frac{\lambda}{4}\left(\mathcal{A} - \left| 2\,|\mathbf{d}(\vec{\varphi})| + (2\,j+1)\,\mathcal{A} \right| \right) \begin{cases} = E_{-}^{(1)}(\vec{\varphi}, j) & ; \mathcal{A} > 0 \\ \leq E_{-}^{(1)}(\vec{\varphi}, j) & ; \mathcal{A} < 0 \end{cases},$$

which implies that the local ground state energy level within each block j is given by $E_{-}^{(1)}(\vec{\varphi}, j)/E_{-}^{(2)}(\vec{\varphi}, j, j - \frac{1}{2})$ for ferromagnetic/antiferromagnetic interaction strength

$\mathcal{A} > 0/\mathcal{A} < 0$. By additionally performing the derivatives

$$\frac{\partial E_{-}^{(1)}(\vec{\varphi}, j)}{\partial j} = -\frac{\lambda\,\mathcal{A}}{2}, \quad \frac{\partial E_{-}^{(2)}(\vec{\varphi}, j, j-\frac{1}{2})}{\partial j} = \frac{\lambda\,\mathcal{A}\,[2\,|\mathbf{d}(\vec{\varphi})| - (2\,j+1)\,\mathcal{A}]}{4\,|\mathbf{l}(\vec{\varphi}, j, m_s)|},$$

it becomes obvious that the block $j = \frac{N-1}{2}$ contains the overall ground state for interaction strengths $\mathcal{A} \neq 0$. The associated instantaneous spectrum is not degenerate ($\eta_{\max} = 1$) [WM02, BBP04].

4.1.3 Topological Band Structure

Since the Hamiltonian $\hat{H}'(\vec{\varphi})$ of Eq. (4.3) commutes with $\hat{S}^{z'}_{\mathrm{tot}}$, the block $j = \frac{N-1}{2}$ can be further separated into one- and two-dimensional blocks characterized by quantum numbers $m_s = -\frac{N}{2}, -\frac{N}{2}+1, \ldots, \frac{N}{2}$. The one-dimensional blocks correspond to the minimal and maximal values $m_s = \pm N/2$, resulting in energy bands (see Eq. (4.9))

$$E_{\pm}^{(1)}(\vec{\varphi}) = \pm\frac{\lambda}{4}\Big[2\,|\mathbf{d}(\vec{\varphi})| \mp \mathcal{A}\,(N-1)\Big]. \tag{4.13}$$

The remaining quantum numbers m_s define two-dimensional blocks with energy bands (see Eq. (4.11))

$$E_{\pm}^{(2)}(\vec{\varphi}, m_s) = \pm\frac{\lambda}{4}\left[\sqrt{\mathcal{A}^2\,N^2 + 4\,|\mathbf{d}(\vec{\varphi})|\,(|\mathbf{d}(\vec{\varphi})| - 2\,\mathcal{A}\,m_s)} \pm \mathcal{A}\right]. \tag{4.14}$$

The invariance of the interaction under the transformation of Eq. (4.3) stems from the isotropy of the interaction, leading to a gapped band structure robust to variations in the interaction strength $\mathcal{A}$. Namely, the spectrum of Eqs. (4.13) and (4.14) is gapped throughout the entire synthetic 2D BZ for $|\mathbf{d}(\vec{\varphi})| \neq 0$ and $\mathcal{A} \neq 0$. The dependence on the phases $\vec{\varphi}$ can then be addressed by introducing the ($\vec{\varphi}$-dependent) interaction strength $\mathcal{A}_{\vec{\varphi}} = \mathcal{A}/|\mathbf{d}(\vec{\varphi})|$ and the dimensionless energy eigenvalues

$$\mathcal{E}_{\pm}^{(1)}(\mathcal{A}_{\vec{\varphi}}) = \frac{E_{\pm}^{(1)}(\vec{\varphi})}{\lambda\,|\mathbf{d}(\vec{\varphi})|}, \quad \mathcal{E}_{\pm,n}^{(2)}(\mathcal{A}_{\vec{\varphi}}) = \frac{E_{\pm}^{(2)}(\vec{\varphi}, -\frac{N}{2}+n)}{\lambda\,|\mathbf{d}(\vec{\varphi})|}. \tag{4.15}$$

The eigenvalues $\mathcal{E}_{\pm}^{(1)}$ and $\mathcal{E}_{\pm,n}^{(2)}$ depend only on the interaction strength $\mathcal{A}_{\vec{\varphi}}$, but not on the explicit phases $\vec{\varphi}$. Instead of the quantum numbers m_s, we have introduced the number $n = 1, 2, \ldots, N-1$ of flipped spins as compared to the ferromagnetic state $m_s = -\frac{N}{2}$ for illustration. The instantaneous eigenstates within the rotated basis are given by

$$|\mathcal{E}_{\pm}^{(1)}\rangle = \left|\pm\frac{1}{2}, \pm\frac{N-1}{2}\right\rangle, \quad |\mathcal{E}_{\pm,n}^{(2)}\rangle = \sqrt{\frac{1 \pm \chi_n}{2}}\,\left|\frac{1}{2}, -\frac{N+1}{2}+n\right\rangle \mp$$
$$\mp\,\mathrm{sgn}(\mathcal{A}_{\vec{\varphi}})\,\sqrt{\frac{1 \mp \chi_n}{2}}\,\left|-\frac{1}{2}, -\frac{N-1}{2}+n\right\rangle, \tag{4.16}$$

with

$$\chi_n(\mathcal{A}_{\vec{\varphi}}) = \frac{2 + \mathcal{A}_{\vec{\varphi}}\,(N-2\,n)}{\sqrt{4 - 8\,\mathcal{A}_{\vec{\varphi}}\,n + \mathcal{A}_{\vec{\varphi}}\,N\,(4 + \mathcal{A}_{\vec{\varphi}}\,N)}}. \tag{4.17}$$

We have used the definitions of Eqs. (4.9), (4.12) and introduced the rotated basis $|m_{s_0}, m_j\rangle = |m_{s_0}\rangle \otimes |m_j\rangle$, neglecting the constant quantum numbers $j = \frac{N-1}{2}$ and $\eta = 1$. Flipping a spin represents a collective excitation in the spin structure. However, as far as the physical explanation permits, we simply refer to a (local) flipping of spins: either a flip of the central spin or a (local) flip in the environment. Both flipping mechanisms are defined by the same quantum number n, but produce different energy contributions manifested in the two eigenvalues $\mathcal{E}^{(2)}_{\pm,n}$. In fact, the associated eigenstates (4.16) are described by linear combinations of both flipping mechanisms, reflecting the collective behavior of the spin excitations.

Fig. 4.1(a) shows the schematic structure of the instantaneous spectrum $\mathcal{E}$ as a function of ferromagnetic interaction strength $\mathcal{A}_{\vec{\varphi}} \geq 0$. The ground state corresponds to $m_s = -\frac{N}{2}$, and is separated from the state $m_s = \frac{N}{2}$ by the Zeeman energy term equal to 1 (in units of $\lambda\,|\mathbf{d}(\vec{\varphi})|$). Excited states $|\mathcal{E}^{(2)}_{\pm,n}\rangle$ are generated by flipping a number of n spins relatively to the ground state. For $\mathcal{A}_{\vec{\varphi}} \gg \frac{2}{N}$, the energy difference between high-$|\mathcal{E}^{(2)}_{+,n}\rangle$ and low-lying states $|\mathcal{E}^{(2)}_{-,n}\rangle$ goes linearly with the interaction strength $\mathcal{A}_{\vec{\varphi}}$ (see Sec. 4.1.4). In what follows, we focus on gaps

$$\Delta_n(\mathcal{A}_{\vec{\varphi}}) = \mathcal{E}^{(2)}_{-,n}(\mathcal{A}_{\vec{\varphi}}) - \mathcal{E}^{(1)}_{-}(\mathcal{A}_{\vec{\varphi}}). \tag{4.18}$$

Exact results for Δ_n and $\Delta_f = 1 - \Delta_{N-1}$ are shown in Fig. 4.1(b) for $N = 6$. The underlying processes can be roughly divided into the following ranges of interaction strengths $\mathcal{A}_{\vec{\varphi}}$. For $\mathcal{A}_{\vec{\varphi}} \ll \frac{2}{N}$, the gaps $\Delta_n = \frac{n}{2}\,\mathcal{A}_{\vec{\varphi}} + \mathcal{O}(\mathcal{A}^2_{\vec{\varphi}})$ are properly described by (locally) flipping n environmental spins[3]. By increasing the interaction strength to $\mathcal{A}_{\vec{\varphi}} \approx \frac{2}{N}$, it becomes energetically more favorable to have collective excitations similar to spin waves: a rotation in the environment manifests itself in a rotation of the central spin (and vice versa). Energy costs associated with flipping of spins are then reduced by distributing the excitation across the total system. As shown in Sec. 4.1.4, this leads to low-energy states $|\mathcal{E}^{(2)}_{-,n}\rangle$ that exhibit ferromagnetic ordering $\langle \hat{\mathbf{S}}_0 \cdot \hat{\mathbf{J}} \rangle \approx \frac{N-1}{4}$ for $\mathcal{A}_{\vec{\varphi}} \gg \frac{2}{N}$. Gaps $\Delta_n \approx \frac{n}{N}$ then arise from Zeeman splittings induced by the misalignment $\langle \hat{S}^{z'}_0 \rangle \approx -\frac{1}{2} + \frac{n}{N}$ of the central spin. From these considerations, it becomes clear why we have defined the crossover interaction strength $\mathcal{A}^{\mathrm{cr}}_{\vec{\varphi}} = \frac{2}{N}$ as the intersection of the approximations $\Delta_f \approx 1 - \frac{N-1}{2}\,\mathcal{A}_{\vec{\varphi}}$ and $\Delta_f \approx \frac{1}{N}$.

The previous observations can be straightforwardly expanded to antiferromagnetic interaction strengths $\mathcal{A} \leq 0$, which is why subsequent results are not limited to the ferromagnetic case (see Appendix B.4). For example, the topological classification of the synthetic energy bands is independent of the sign of interaction strength $\mathcal{A}$. For $\mathcal{A} = 0$, the instantaneous spectrum formally leads to degenerate eigenvalues $\mathcal{E}^{(2)}_{\pm,n} = \mathcal{E}^{(1)}_{\pm}$. Nevertheless, in the noninteracting case, Eq. (4.2) is in fact a single-spin Hamiltonian equivalent to a Chern insulator with mass parameter M (cf. Eq. (3.4)). Thus, each of the two single-spin energy bands can be characterized by a winding number (provided that $|\mathbf{d}(\vec{\varphi})| \neq 0$): $\nu_{gr} = -\nu_{ex} = \pm 1$ (nontrivial) for $|M| < 2$, $M \neq 0$ or $\nu_{gr} = \nu_{ex} = 0$ (trivial) for $|M| > 2$, where ν_{gr} (ν_{ex}) corresponds to the single-spin ground (excited) energy band (cf. Fig. 3.4). In the interacting case $\mathcal{A} \neq 0$, the spectrum is explicitly

[3] Note that a flip of the central spin would lead to a high-energy excitation.

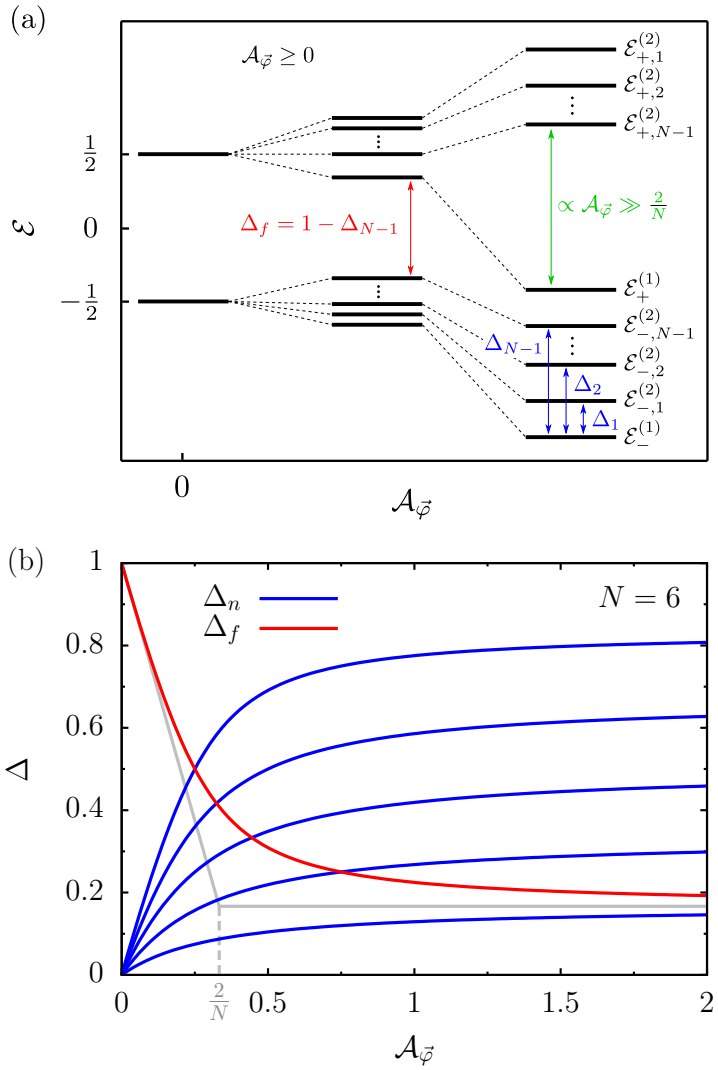

Figure 4.1: Spectrum $\mathcal{E}$ and gaps Δ as a function of interaction strength $\mathcal{A}_{\vec{\varphi}} \geq 0$. (a) The ground state corresponds to $m_s = -\frac{N}{2}$, separated from the state $m_s = \frac{N}{2}$ by the Zeeman term equal to 1 (in units of $\lambda |\mathbf{d}(\vec{\varphi})|$). Flipping a number of n spins with respect to the ground state yields low- and high-energy states $|\mathcal{E}^{(2)}_{\pm,n}\rangle$. For $\mathcal{A}_{\vec{\varphi}} \gg \frac{2}{N}$, the high-energy excited states $|\mathcal{E}^{(2)}_{+,n}\rangle$ are well separated ($\propto \mathcal{A}_{\vec{\varphi}}$) from the other states. (b) Exact results for Δ_n and $\Delta_f = 1 - \Delta_{N-1}$ for $N = 6$. For $\mathcal{A}_{\vec{\varphi}} \ll \frac{2}{N}$, gaps $\Delta_n \approx \frac{n}{2}\,\mathcal{A}_{\vec{\varphi}}$ are described by (locally) flipping n environmental spins. For $\mathcal{A}_{\vec{\varphi}} \gg \frac{2}{N}$, the gaps converge to $\Delta_n \approx \frac{n}{N}$ due to collective spin wave excitations. We have defined the crossover interaction strength $\mathcal{A}^{\mathrm{cr}}_{\vec{\varphi}} = \frac{2}{N}$ as the intersection of the approximations $\Delta_f \approx 1 - \frac{N-1}{2}\,\mathcal{A}_{\vec{\varphi}}$ and $\Delta_f \approx \frac{1}{N}$. *Reprinted figure with permission from Ref. [KPBT22]. Copyright (2022) by the American Physical Society.*

gapped (provided that $|\mathbf{d}(\vec{\varphi})| \neq 0$) and a total Chern number $C_n = (N - 2\,n)\,\nu_{gr}$ can be assigned to the synthetic energy bands of Eq. (4.15). We have introduced indices $n = 0, 1, \ldots, N$ representing (again) the number of flipped spins as compared to the ferromagnetic state $m_s = -\frac{N}{2}$. The total Chern number C_n only depends on the quantum number n, yielding the same topology of low- and high-energy bands $\mathcal{E}^{(2)}_{\pm,n}$ for (anti)ferromagnetic interaction strengths $\mathcal{A} \neq 0$. The topological classification can be explained by the effective interaction-induced extension of the magnetic coupling to the surrounding spins. As a result, the environmental spins also rotate along the direction of the external magnetic field $\mathbf{B}(\vec{\varphi}_t)$, producing adiabatic topological properties beyond those of the central spin. For $n = 0$, this yields the total Chern number $C_0 = N\,\nu_{gr}$: The adiabatic spin polarizations of the environmental spins point in the same direction as that of the central spin, such that each spin contributes to the many-body wave function by the single-spin Chern number ν_{gr} (cf. Fig. 3.2). Starting from this state, each flip of a spin leads to an even change in the total Chern number $\Delta C = C_{n+1} - C_n = -2\,\nu_{gr}$.

4.1.4 Spin-Wave Excitations

In the following, we investigate the nature of spin excitations in the instantaneous spectrum. We start our consideration by determining the expectation values $\langle \hat{S}^{z'}_0 \rangle$, $\langle \hat{\mathbf{S}}_0 \cdot \hat{\mathbf{J}} \rangle$ associated with the instantaneous eigenstates of the Hamiltonian (4.3):

$$\chi = \langle \hat{S}^{z'}_0 \rangle = \frac{1}{\lambda} \left\langle \frac{\partial \hat{H}'(\vec{\varphi})}{\partial |\mathbf{d}(\vec{\varphi})|} \right\rangle = \frac{1}{\lambda} \frac{\partial E(\vec{\varphi})}{\partial |\mathbf{d}(\vec{\varphi})|},$$

$$\xi = \langle \hat{\mathbf{S}}_0 \cdot \hat{\mathbf{J}} \rangle = -\frac{1}{\lambda} \left\langle \frac{\partial \hat{H}'(\vec{\varphi})}{\partial \mathcal{A}} \right\rangle = -\frac{1}{\lambda} \frac{\partial E(\vec{\varphi})}{\partial \mathcal{A}}. \quad (4.19)$$

We apply the Hellmann-Feynman theorem, which relates the expectation values χ, ξ to the synthetic energy bands $E(\vec{\varphi})$ of the Hamiltonian $\hat{H}'(\vec{\varphi})$. Further, we use that the interaction $\hat{\mathbf{S}}_0 \cdot \hat{\mathbf{J}}$ is invariant under the transformation defined in Eq. (4.3). By inserting the energy bands of Eqs. (4.13), (4.14) into Eq. (4.19), this yields expectation values $\chi^{(1)}_{\pm} = \pm\frac{1}{2}$, $\xi^{(1)}_{\pm} = \frac{N-1}{4}$ for the one-dimensional blocks, and expectation values

$$\chi^{(2)}_{\pm,n}(\mathcal{A}_{\vec{\varphi}}) = \pm\frac{1}{2}\,\chi_n(\mathcal{A}_{\vec{\varphi}}), \quad \xi^{(2)}_{\pm,n}(\mathcal{A}_{\vec{\varphi}}) = -\frac{1}{4} \pm \frac{4\,n - N\,(2 + \mathcal{A}_{\vec{\varphi}}\,N)}{4\,\sqrt{4 - 8\,\mathcal{A}_{\vec{\varphi}}\,n + \mathcal{A}_{\vec{\varphi}}\,N\,(4 + \mathcal{A}_{\vec{\varphi}}\,N)}} \quad (4.20)$$

for the two-dimensional blocks. We have used the values $\chi_n(\mathcal{A}_{\vec{\varphi}})$ of Eq. (4.17), which have now been assigned a physical meaning. Using the relations of Eqs. (4.19) and (4.20), the dimensionless energy eigenvalues (4.15) can be solely expressed by the associated expectation values χ, ξ: $\mathcal{E}^{(1)}_{\pm} = \chi^{(1)}_{\pm} - \mathcal{A}_{\vec{\varphi}}\,\xi^{(1)}_{\pm}$ and $\mathcal{E}^{(2)}_{\pm,n} = \chi^{(2)}_{\pm,n} - \mathcal{A}_{\vec{\varphi}}\,\xi^{(2)}_{\pm,n}$. Restricting ourselves to ferromagnetic interaction strengths $\mathcal{A}_{\vec{\varphi}} \geq 0$, the gaps (4.18) can be described by $\Delta_n = \Delta\chi_n + \mathcal{A}_{\vec{\varphi}}\,\Delta\xi_n$, with expectation values

$$\Delta\chi_n(\mathcal{A}_{\vec{\varphi}}) = \chi^{(2)}_{-,n}(\mathcal{A}_{\vec{\varphi}}) - \chi^{(1)}_{-}, \quad \Delta\xi_n(\mathcal{A}_{\vec{\varphi}}) = \xi^{(1)}_{-} - \xi^{(2)}_{-,n}(\mathcal{A}_{\vec{\varphi}}). \quad (4.21)$$

The formation of gaps Δ_n can be explained according to the separation into spin expectation values $\Delta\chi_n$, $\Delta\xi_n$: one contribution is given by the Zeeman splittings

induced by the interaction-driven rotation of the central spin (indicated by $\Delta\chi_n$), while the other part explicitly originates from the interaction $\hat{\mathbf{S}}_0 \cdot \hat{\mathbf{J}}$ (indicated by $\Delta\xi_n$). Fig. 4.2 shows exact results for the expectation values $\Delta\chi_n$, $\Delta\xi_n$ of Eq. (4.21), and $\Delta\chi_f = 1 - \Delta\chi_{N-1}$, as a function of ferromagnetic interaction strength $\mathcal{A}_{\vec{\varphi}} \geq 0$ and $N = 6$. As in Sec. 4.1.3, the underlying processes can be roughly divided into the following ranges of interaction strengths $\mathcal{A}_{\vec{\varphi}}$. For $\mathcal{A}_{\vec{\varphi}} \ll \frac{2}{N}$, the expectation values $\Delta\chi_n = \mathcal{O}(\mathcal{A}_{\vec{\varphi}}^2)$ indicate that the central spin is hardly affected by interactions, which is why gaps Δ_n can only arise due to rotations in the environment. Indeed, the expectation values $\Delta\xi_n = \frac{n}{2} + \mathcal{O}(\mathcal{A}_{\vec{\varphi}})$ are properly described by (locally) flipping n environmental spins, which finally leads to gaps $\Delta_n = \frac{n}{2}\,\mathcal{A}_{\vec{\varphi}} + \mathcal{O}(\mathcal{A}_{\vec{\varphi}}^2)$. By increasing the interaction strength to $\mathcal{A}_{\vec{\varphi}} \approx \frac{2}{N}$, the expectation values $\Delta\chi_n/\Delta\xi_n$ increase/decrease with the interaction strength $\mathcal{A}_{\vec{\varphi}}$, indicating the collective behavior of the excitations similar to spin waves. As explicitly shown in Fig. 4.2(b), this leads to vanishing expectation values $\Delta\xi_n \approx 0$, $\mathcal{A}_{\vec{\varphi}}\,\Delta\xi_n \approx 0$ for interaction strengths $\mathcal{A}_{\vec{\varphi}} \gg \frac{2}{N}$, revealing that the low-energy states $|\mathcal{E}^{(2)}_{-,n}\rangle$ exhibit ferromagnetic ordering. Gaps $\Delta_n \approx \frac{n}{N}$ then arise solely from the Zeeman splittings induced by the misalignment $\Delta\chi_n \approx \frac{n}{N}$ of the central spin. High-energy states $|\mathcal{E}^{(2)}_{+,n}\rangle$ exhibit antiferromagnetic ordering $\xi^{(2)}_{+,n} \approx -\frac{N+1}{4}$, which is why they separate linearly ($\propto \mathcal{A}_{\vec{\varphi}}$) from the low-energy states $|\mathcal{E}^{(2)}_{-,n}\rangle$ for interaction strengths $\mathcal{A}_{\vec{\varphi}} \gg \frac{2}{N}$.

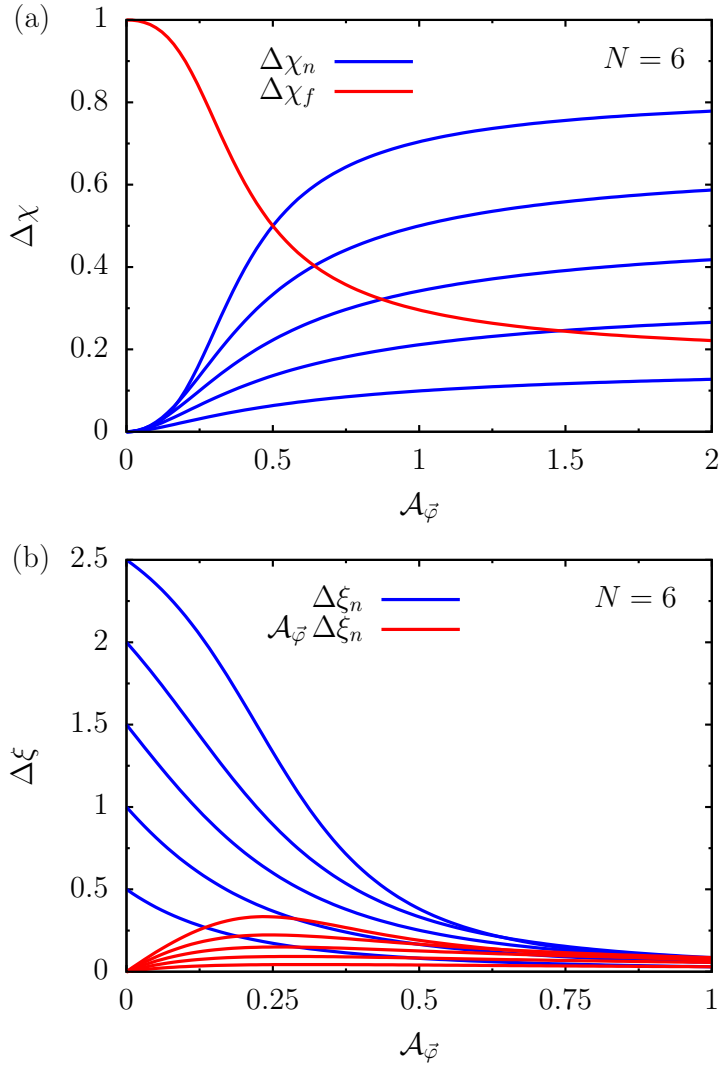

Figure 4.2: Spin expectation values (a) $\Delta\chi_n$, $\Delta\chi_f = 1 - \Delta\chi_{N-1}$ and (b) $\Delta\xi_n$, $\mathcal{A}_{\vec{\varphi}}\,\Delta\xi_n$ as a function of ferromagnetic interaction strength $\mathcal{A}_{\vec{\varphi}} \geq 0$ and $N = 6$. For $\mathcal{A}_{\vec{\varphi}} \ll \frac{2}{N}$, expectation values $\Delta\chi_n \approx 0$ indicate that the central spin is hardly affected by interactions. Expectation values $\Delta\xi_n \approx \frac{n}{2}$ are then described by (locally) flipping n environmental spins. For $\mathcal{A}_{\vec{\varphi}} \gg \frac{2}{N}$, the expectation values converge to $\Delta\chi_n \approx \frac{n}{N}$ and $\Delta\xi_n \approx 0$, $\mathcal{A}_{\vec{\varphi}}\,\Delta\xi_n \approx 0$, which shows that low-energy states $|\mathcal{E}^{(2)}_{-,n}\rangle$ exhibit ferromagnetic ordering. The central spin is then rotated due to interactions, demonstrating the collective nature of the spin wave excitations: rotations in the environment manifest themselves in rotations of the central spin (and vice versa).

4.2 Topological Burning Glass Effect

We extend the TFC of Sec. 3.1 by statically coupling it to a set of surrounding spins in the framework of a CSM (see Sec. 4.1). There, the topologically quantized response is given by the energy transfer between the two driving modes, which represents a local observable of the driven central spin. Yet, the adiabatically defined winding number (see Sec. 3.1.2) of the central spin fails to predict the linear response signal, which can instead only be topologically understood from the adiabatic state of the total system. In this sense, the topological properties of the environmental spins are focused to the local response of the TFC, motivating the terminology of a topological burning glass. In our concrete topological burning glass scenario, the quantized energy transfer is found to be N-fold enhanced by the collective motion of N spins, while the adiabatic winding number of the driven spin remains equal to one. By investigating the fluctuations around the adiabatic spin polarization of the central spin-1/2, we argue that the collective motion of the surrounding spins crucially affects the non-unitary dynamics of the TFC, which is the very origin of the TBGE. Throughout this Section, we closely follow the derivations and results presented in Ref. [KPBT22]. *Copyright (2022) by the American Physical Society.*

4.2.1 Concrete Model

We consider the dynamics of a central spin that is subjected to a time-quasiperiodic magnetic field $\mathbf{B}(\vec{\varphi}_t)$, and interacts in a static fashion with its environment. A minimal framework for this scenario is provided by the following driven CSM (see Fig. 4.3 for an illustration):

$$\hat{H}(\vec{\varphi}_t) = g^* \, \mu_B \, \mathbf{B}(\vec{\varphi}_t) \cdot \hat{\mathbf{S}}_0 - A \, \hat{\mathbf{S}}_0 \cdot \hat{\mathbf{J}}, \tag{4.22}$$

where $\hat{\mathbf{S}}_0 = \frac{1}{2}\,\hat{\boldsymbol{\sigma}}_0$ represents the central spin-1/2 and $\hat{\mathbf{J}} = \sum_{k=1}^{N-1} \hat{\mathbf{S}}_k = \sum_{k=1}^{N-1} \frac{\hat{\boldsymbol{\sigma}}_k}{2}$ the surrounding spins. The environment is composed of a number of $N-1$ spin-1/2, and is assumed to interact homogeneously with the central spin with coupling strength A. We further introduce the vector of Pauli matrices $\hat{\boldsymbol{\sigma}}_i = (\hat{\sigma}_i^x, \hat{\sigma}_i^y, \hat{\sigma}_i^z)$ acting on the individual subspaces of the constituents. The Zeeman term generated by the magnetic field $\mathbf{B}(\vec{\varphi}_t)$ is proportional to Bohr's magneton μ_B and the effective g^*-factor of the central spin. This model effectively applies for instance to driven electron spins trapped in lateral QDs in SiGe or NV centers in diamond[4]. In these systems, the (central) electron spin couples in a star-like fashion to the surrounding nuclear spins of the host material, with a hyperfine interaction that is typically three orders of magnitude larger than the dipole-dipole coupling between the nuclear spins themselves (cf. Sec. 4.1.1).

[4] In lateral QDs or NV centers, the Heisenberg interaction to the surrounding spins is not necessarily homogeneous or isotropic (cf. Sec. 4.1.1), as assumed for simplicity in Eq. (4.22). However, as our main statements about the TBGE reflect fundamental concepts that do not depend on the details of the model (cf. Appendix B.1), our results generally apply to inhomogeneous and anisotropic interactions as well.

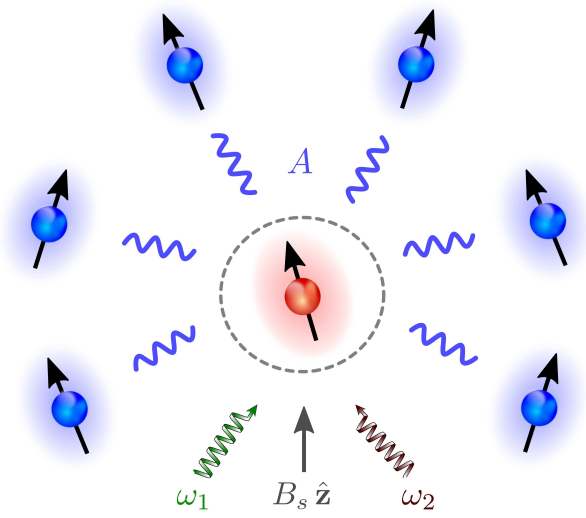

Figure 4.3: Quasiperiodically driven *central spin model* (CSM) as a topological burning glass. A central spin (red sphere) couples in star-geometry to $N-1$ surrounding spins (blue spheres). The isotropic interaction is parametrized by the homogeneous coupling constant A. The central spin is subjected to a static magnetic field with amplitude B_s and two circularly polarized drives with incommensurate frequencies ω_1 and ω_2, so as to induce a topological frequency conversion. *Reprinted figure with permission from Ref. [KPBT22]. Copyright (2022) by the American Physical Society.*

The time-dependence of the external field $\mathbf{B}(\vec{\varphi}_t) = B_c\,\mathbf{d}(\vec{\varphi}_t)$ is chosen as (cf. Eq. (3.4))

$$\mathbf{d}(\vec{\varphi}_t) = \begin{pmatrix} \sin(\varphi_{1t}) \\ \sin(\varphi_{2t}) \\ M - \cos(\varphi_{1t}) - \cos(\varphi_{2t}) \end{pmatrix}.$$

It consists of a static magnetic field with amplitude $B_s = B_c\,M$ in z direction, and two circularly polarized drives, with amplitudes B_c and time-dependent phases $\vec{\varphi}_t = (\varphi_{1t}, \varphi_{2t}) = \vec{\omega}\,t + \vec{\phi}$. The offset phases and incommensurate frequencies are parametrized by $\vec{\phi} = (\phi_1, \phi_2)$ and $\vec{\omega} = (\omega_1, \omega_2)$.

In order to cope with the influence of the surrounding spins, we take advantage of the homogeneity of the interaction based on the star-like symmetry of Eq. (4.22), that entails $[\hat{H}(\vec{\varphi}_t), \hat{\mathbf{J}}^2] = 0$ (see also Sec. 4.1). The Hamiltonian $\hat{H}(\vec{\varphi}_t)$ may thus be transformed into a block diagonal form, with each block characterized by a constant of motion

$$j = \begin{cases} \frac{N-1}{2},\ \frac{N-1}{2} - 1,\ \ldots,\ \frac{1}{2} & ;\ N \text{ even} \\ \frac{N-1}{2},\ \frac{N-1}{2} - 1,\ \ldots,\ 0 & ;\ N \text{ odd} \end{cases}$$

corresponding to the total spin $\hat{\mathbf{J}}^2$ of the surrounding spins with $N \geq 2$. As we want to focus on the dynamics originating from the ground state, we restrict ourselves to the

block[5] $j = \frac{N-1}{2}$. The associated block matrix size is $2N \times 2N$, and the instantaneous spectrum is obtained by solving

$$\hat{H}(\vec{\varphi}_t)\ |\Phi_\alpha(\vec{\varphi}_t)\rangle = E_\alpha(\vec{\varphi}_t)\ |\Phi_\alpha(\vec{\varphi}_t)\rangle\,. \tag{4.23}$$

The energies $E_\alpha(\vec{\varphi}_t)$ are ordered from low to high values by ascending indices $\alpha = 0, 1, \ldots, 2N-1$, where $\alpha = 0$ denotes the ground state. For an incommensurate pair of frequencies $\frac{\omega_1}{\omega_2} \notin \mathbb{Q}$, the phases φ_{1t} and φ_{2t} entirely sample the surface of a two-dimensional torus, analogously to a synthetic 2D BZ (cf. Fig. 2.3). The energy levels $\{E_\alpha(\vec{\varphi}_t)\}_\alpha$ then resemble a Bloch band structure in parameter space, with the phases $\vec{\varphi}_t$ taking the role of Bloch quasimomenta.

4.2.2 Collective Motion Picture

Assuming that the interacting spin system of Eq. (4.22) is gapped[6] and initially prepared in an instantaneous eigenstate $|\Phi_\beta(\vec{\varphi}_{t_0})\rangle$ of Eq. (4.23), the dynamics can be expanded to first order in $\vec{\omega}$ using APT (cf. Eq. (2.18)):

$$|\Psi_\beta(t)\rangle = \mathrm{e}^{\mathrm{i}\gamma_\beta(t)}\Big[\,|\Phi_\beta(\vec{\varphi}_t)\rangle + \mathrm{i}\sum_{\alpha\neq\beta}\frac{\mathcal{M}_{\alpha\beta}(\vec{\varphi}_t)}{\Delta_{\alpha\beta}(\vec{\varphi}_t)}\,|\Phi_\alpha(\vec{\varphi}_t)\rangle\,\Big]. \tag{4.24}$$

At zeroth order, the quantum state $|\Psi_\beta(t)\rangle$ is restricted to the synthetic energy band $E_\beta(\vec{\varphi}_t)$. First-order corrections, however, yield virtual transitions to the excited states of the instantaneous spectrum, weighted by the terms $\mathcal{M}_{\alpha\beta}(\vec{\varphi}_t) = \vec{\omega}\ \langle\Phi_\alpha(\vec{\varphi}_t)|\nabla_{\vec{\varphi}}\,\Phi_\beta(\vec{\varphi}_t)\rangle$ and the energy gaps $\Delta_{\alpha\beta}(\vec{\varphi}_t) = E_\alpha(\vec{\varphi}_t) - E_\beta(\vec{\varphi}_t)$. We have also introduced the overall phase factor $\gamma_\beta(t) = -\int_{t_0}^{t}\mathrm{d}t'\,[E_\beta(\vec{\varphi}_{t'}) - \mathrm{i}\,\mathcal{M}_{\beta\beta}(\vec{\varphi}_{t'})]$.

As shown in Sec. 2.3.3, a feature of quasiperiodically driven quantum systems is energy pumping, a process in which photons of different frequencies are exchanged between the external drives. The total energy transfer rate is determined by the equations of motion (cf. Eq. (2.19)): $\frac{\mathrm{d}}{\mathrm{d}t}\,\langle\hat{H}(\vec{\varphi}_t)\rangle = \langle\partial_t\,\hat{H}(\vec{\varphi}_t)\rangle = \vec{\omega}\ \langle\hat{\mathbf{I}}(\vec{\varphi}_t)\rangle$, with $\hat{\mathbf{I}}(\vec{\varphi}_t) = \nabla_{\vec{\varphi}}\,\hat{H}(\vec{\varphi}_t)$. Each term $\dot{W}_k(t) = \omega_k\,\langle\hat{\mathrm{I}}_k(\vec{\varphi}_t)\rangle$ can be interpreted as the pumping rate provided by the individual drive (cf. Eq. (2.71)), where $\hat{\mathrm{I}}_k(\vec{\varphi}_t) = \partial_{\varphi_k}\hat{H}(\vec{\varphi}_t)$ resembles a current operator in k direction of the parameter space. Using the perturbed quantum state $|\Psi_\beta(t)\rangle$ from Eq. (4.24), the expectation value $\langle\hat{\mathrm{I}}_k(\vec{\varphi}_t)\rangle$ can be expanded to first order in $\vec{\omega}$ (cf. Eq. (2.20)):

$$\langle\hat{\mathrm{I}}_k(\vec{\varphi}_t)\rangle_\beta = \langle\Psi_\beta(t)|\hat{\mathrm{I}}_k(\vec{\varphi}_t)|\Psi_\beta(t)\rangle = \frac{\partial E_\beta(\vec{\varphi}_t)}{\partial\varphi_k} + \sum_{l=1}^{2}\omega_l\,\Omega_{kl}^{(\beta)}(\vec{\varphi}_t). \tag{4.25}$$

This result emphasizes that virtual couplings between bands are essential for the generation of geometrical and topological effects, as the adiabatic limit only produces

[5] The block $j = \frac{N-1}{2}$ contains the overall ground state for both ferromagnetic and antiferromagnetic coupling strengths $A \neq 0$, as explicitly derived in Sec. 4.1.2.

[6] As shown in Sec. 4.1.3 and in the Appendix B.4, the Bloch band structure of the CSM is gapped throughout the entire synthetic 2D BZ for both ferromagnetic and antiferromagnetic coupling strengths $A \neq 0$ (provided that $|\mathbf{d}(\vec{\varphi})| \neq 0$).

Bloch oscillations $\partial_{\varphi_k} E_\beta(\vec{\varphi}_t)$ (cf. Sec. 2.3.2). In fact, the virtual interband excitations of Eq. (4.24) can be readily shown to be identical to the Berry curvature $\Omega_{kl}^{(\beta)}(\vec{\varphi}_t) = 2\,\mathrm{Im}[\langle\partial_{\varphi_k}\Phi_\beta(\vec{\varphi}_t)|\partial_{\varphi_l}\Phi_\beta(\vec{\varphi}_t)\rangle]$ (cf. Eq. (2.22)) of the synthetic energy band $E_\beta(\vec{\varphi}_t)$ to which the quasiadiabatic dynamics is confined. This phenomenon demonstrates that, in an isolated quantum system, the Berry curvature $\Omega_{kl}^{(\beta)}(\vec{\varphi}_t)$ arises as the adiabatic first-order response of the physical observable $\hat{\mathrm{I}}_k(\vec{\varphi}_t) = \partial_{\varphi_k}\hat{H}(\vec{\varphi}_t)$ to the rate of change of the external parameter $\dot{\vec{\varphi}}_t = \vec{\omega}$ (cf. Sec. 2.1.4).

As the two frequencies $\frac{\omega_1}{\omega_2} \notin \mathbb{Q}$ are incommensurate, the entire synthetic 2D BZ is sampled during the time-evolution of the quantum state $|\Psi_\beta(t)\rangle$ (cf. Fig. 2.3). Averaging the pumping rates of Eq. (4.25) over a long period of time, this translates into an integration over the closed manifold of the two-dimensional torus (cf. Eq. (2.72)). The Bloch oscillations $\partial_{\varphi_k} E_\beta(\vec{\varphi}_t)$ do not contribute to this integration, while the integrated Berry curvature $\Omega_{kl}^{(\beta)}(\vec{\varphi}_t)$ produces a topological frequency conversion between the dynamical drives that is proportional to the first Chern number $C^{(\beta)} = \frac{1}{2\pi}\iint_0^{2\pi}\mathrm{d}^2\vec{\varphi}\,\Omega_{12}^{(\beta)}(\vec{\varphi})$ (cf. Eq. (2.74)). As explicitly shown in Sec. 4.1.3, this topological invariant is governed by the collective motion of the central spin and the environmental spins: The interactions in the CSM effectively extend the magnetic coupling to the environmental spins, which is why the latter also rotate along the direction of the external magnetic field $\mathbf{B}(\vec{\varphi}_t)$ at every point in time. This leads to adiabatic topological properties beyond those of the central spin, revealing a time-averaged pumping rate determined by the collective motion of all spins of the CSM (cf. Eq. (2.73)):

$$P_\beta^{12} = -P_\beta^{21} = \frac{C^{(\beta)}}{2\,\pi}\,\omega_1\,\omega_2. \tag{4.26}$$

The topologically quantized response of the total quantum system of Eq. (4.22) is thus characterized by its adiabatically defined topological invariant $C^{(\beta)}$. We contrast this behavior with its counterpart in an open quantum system in the next section.

4.2.3 Non-Unitary Dynamics

We take an open quantum system perspective, in which a physical observable of interest operates locally on the (small) quantum system that is coupled to a (larger) environment. Specifically, in Eq. (4.22), only the central spin is exposed to the quasiperiodic field $\mathbf{B}(\vec{\varphi}_t)$, resulting in a current operator $\hat{\mathrm{I}}_k(\vec{\varphi}_t) = \lambda\,\frac{\partial\mathbf{d}(\vec{\varphi}_t)}{\partial\varphi_k}\cdot\hat{\mathbf{S}}_0$ that acts exclusively on the central spin-1/2. Accordingly, the expectation value

$$\langle\hat{\mathrm{I}}_k(\vec{\varphi}_t)\rangle_\beta = \mathrm{Tr}[\hat{\rho}_\beta^{\mathrm{dy}}(t)\,\hat{\mathrm{I}}_k(\vec{\varphi}_t)] = \mathrm{Tr}_0[\hat{\rho}_{0,\beta}^{\mathrm{dy}}(t)\,\hat{\mathrm{I}}_k(\vec{\varphi}_t)] \tag{4.27}$$

can be fully determined by the non-unitary dynamics of the central spin, expressed by the reduced density matrix $\hat{\rho}_{0,\beta}^{\mathrm{dy}}(t) = \mathrm{Tr}_{\hat{\mathbf{J}}}[\hat{\rho}_\beta^{\mathrm{dy}}(t)]$ [NC10]. Here, we have introduced the total density matrix $\hat{\rho}_\beta^{\mathrm{dy}}(t) = |\Psi_\beta(t)\rangle\langle\Psi_\beta(t)|$, where $|\Psi_\beta(t)\rangle$ represents the perturbed quantum state[7] of Eq. (4.24). The reduced density matrix $\hat{\rho}_{0,\beta}^{\mathrm{dy}}(t)$ is calculated by tracing

[7] Note that Eq. (4.27) also holds for the exact dynamics of the system, involving the higher orders in the perturbative expansion of Eq. (4.24).

out the environment $\hat{\mathbf{J}}$ (denoted as $\mathrm{Tr}_{\hat{\mathbf{J}}}$), while Tr ($\mathrm{Tr}_0$) denotes the trace operating on the total system (the central spin-1/2). We have further introduced the energy scale

$$\lambda = g^* \mu_B B_c,$$

assuming $\lambda > 0$ for simplicity.

Eq. (4.27) illustrates that the frequency conversion is entirely carried by the central spin. The topological quantization of the local response, however, is determined by the geometrical and topological properties of the total system, namely the Berry curvature $\Omega_{kl}^{(\beta)}(\vec{\varphi}_t)$ and the Chern number $C^{(\beta)}$ of the synthetic energy band $E_\beta(\vec{\varphi}_t)$ to which the quasiadiabatic dynamics is confined (see Sec. 4.2.2). Thus, the non-unitary dynamics of the central spin effectively inherits the topological nature of the total system. Employing the perturbed quantum state $|\Psi_\beta(t)\rangle$ of Eq. (4.24), this phenomenon can be further analyzed by a first-order expansion in $\vec{\omega}$ of the reduced density matrix

$$\hat{\rho}_{0,\beta}^{\mathrm{dy}}(t) = \hat{\rho}_{0,\beta}^{\mathrm{ad}}(\vec{\varphi}_t) + \sum_{\alpha\neq\beta} \frac{\hat{T}_{\alpha\beta}(\vec{\varphi}_t)}{\Delta_{\alpha\beta}(\vec{\varphi}_t)}. \tag{4.28}$$

Here, we introduce the adiabatic limit of the reduced density matrix $\hat{\rho}_{0,\beta}^{\mathrm{ad}}(\vec{\varphi}_t) = \mathrm{Tr}_{\hat{\mathbf{J}}}[|\Phi_\beta(\vec{\varphi}_t)\rangle\langle\Phi_\beta(\vec{\varphi}_t)|]$, which corresponds to the zeroth order of Eq. (4.24), and results in Bloch oscillations $\partial_{\varphi_k} E_\beta$ of Eq. (4.25). The local response, however, arises from the operators $\hat{T}_{\alpha\beta}(\vec{\varphi}_t) = \mathrm{i}\,\mathcal{M}_{\alpha\beta}(\vec{\varphi}_t)\ \mathrm{Tr}_{\hat{\mathbf{J}}}[|\Phi_\alpha(\vec{\varphi}_t)\rangle\langle\Phi_\beta(\vec{\varphi}_t)|] + \mathrm{h.c.}$ accounting for the virtual transitions to the excited states in the instantaneous spectrum of the total system. In fact, the correlations of the total system are manifested in the matrix elements of $\hat{T}_{\alpha\beta}(\vec{\varphi}_t)$, thus imposing a topological quantization that is not captured by basic geometrical or topological aspects of the reduced adiabatic density matrix $\hat{\rho}_{0,\beta}^{\mathrm{ad}}(\vec{\varphi}_t)$. In this sense, the adiabatic topological properties of the total system are focused to the local response of the central spin, which motivates the terminology of a topological burning glass. This mechanism is quite generic, since Eqs. (4.23) to (4.28) reflect fundamental concepts that do not depend on the details of the model. In fact, the TBGE generically occurs in any static extension of the CSM under the following three conditions: (*i*) the initial state of the interacting spin system is energetically separated from the other bands, (*ii*) the dynamics is well described within first-order APT (see Sec. 2.1.3), (*iii*) the time-quasiperiodic fields only act on the central spin. The robustness of our results to more generic couplings is corroborated in the Appendix B.1.

In the open quantum system perspective of the TFC, the correspondence between the adiabatically defined winding number of the central spin (cf. Sec. 3.1.2) and its local response signal is fundamentally modified. This discrepancy, however, can be explained by the non-unitary quantum formalism of Eq. (4.28), which, due to Eq. (4.27), shows an identical response to that of the collective motion description of Sec. 4.2.2. Accordingly, both pictures can be treated at the same level, while the collective motion of the environmental spins is locally imprinted in the non-unitary dynamics of the central spin. This manifests itself in fluctuations around the adiabatic spin polarization of the central spin-1/2, which can be illustrated by parametrizing the reduced density matrix $\hat{\rho}_{0,\beta}^{\mathrm{dy}}(t)$ by vectors $\mathbf{u}_\beta^{\mathrm{dy}}(t)$ [NC10]:

$$\hat{\rho}_{0,\beta}^{\mathrm{dy}}(t) = \frac{1}{2}\left(\mathbb{1} + \mathbf{u}_\beta^{\mathrm{dy}}(t)\cdot\hat{\boldsymbol{\sigma}}\right). \tag{4.29}$$

A first-order expansion in $\vec{\omega}$ yields $\mathbf{u}_\beta^{\mathrm{dy}}(t) = \mathbf{u}_\beta^{\mathrm{ad}}(\vec{\varphi}_t) + \Delta\mathbf{u}_\beta(\vec{\varphi}_t)$, separated in terms of the adiabatic spin polarization $\mathbf{u}_\beta^{\mathrm{ad}}(\vec{\varphi}_t)$ and the corrections $\Delta\mathbf{u}_\beta(\vec{\varphi}_t)$. Using the notation of Eq. (4.28), the associated contributions to the reduced density matrix $\hat{\rho}_{0,\beta}^{\mathrm{dy}}(t)$ can be written as

$$\hat{\rho}_{0,\beta}^{\mathrm{ad}}(\vec{\varphi}_t) = \frac{1}{2}\left(\mathbb{1} + \mathbf{u}_\beta^{\mathrm{ad}}(\vec{\varphi}_t)\cdot\hat{\boldsymbol{\sigma}}\right), \quad \sum_{\alpha\neq\beta}\frac{\hat{T}_{\alpha\beta}(\vec{\varphi}_t)}{\Delta_{\alpha\beta}(\vec{\varphi}_t)} = \frac{1}{2}\,\Delta\mathbf{u}_\beta(\vec{\varphi}_t)\cdot\hat{\boldsymbol{\sigma}},$$

showing that the operators $\hat{T}_{\alpha\beta}(\vec{\varphi}_t)$ induce corrections $\Delta\mathbf{u}_\beta(\vec{\varphi}_t)$ around the adiabatic spin polarization $\mathbf{u}_\beta^{\mathrm{ad}}(\vec{\varphi}_t)$ of the central spin-1/2. Remarkably, these corrections contribute to the expectation value of the current operator $\hat{\mathrm{I}}_k(\vec{\varphi}_t) = \lambda\,\frac{\partial\mathbf{d}(\vec{\varphi}_t)}{\partial\varphi_k}\cdot\hat{\mathbf{S}}_0$. This can be directly seen by applying the parametrization of the reduced density matrix $\hat{\rho}_{0,\beta}^{\mathrm{dy}}(t)$ of Eq. (4.29) to Eq. (4.27):

$$\langle\hat{\mathrm{I}}_k(\vec{\varphi}_t)\rangle_\beta = \frac{\lambda}{2}\,\frac{\partial\mathbf{d}(\vec{\varphi}_t)}{\partial\varphi_k}\cdot\mathbf{u}_\beta^{\mathrm{ad}}(\vec{\varphi}_t) + \frac{\lambda}{2}\,\frac{\partial\mathbf{d}(\vec{\varphi}_t)}{\partial\varphi_k}\cdot\Delta\mathbf{u}_\beta(\vec{\varphi}_t). \tag{4.30}$$

Comparing Eq. (4.30) with Eq. (4.25), this yields

$$\frac{\partial E_\beta(\vec{\varphi}_t)}{\partial\varphi_k} = \frac{\lambda}{2}\,\frac{\partial\mathbf{d}(\vec{\varphi}_t)}{\partial\varphi_k}\cdot\mathbf{u}_\beta^{\mathrm{ad}}(\vec{\varphi}_t), \quad \sum_{l=1}^{2}\omega_l\,\Omega_{kl}^{(\beta)}(\vec{\varphi}_t) = \frac{\lambda}{2}\,\frac{\partial\mathbf{d}(\vec{\varphi}_t)}{\partial\varphi_k}\cdot\Delta\mathbf{u}_\beta(\vec{\varphi}_t), \tag{4.31}$$

demonstrating that the corrections $\Delta\mathbf{u}_\beta(\vec{\varphi}_t)$ include the topological information of the total system in terms of the Berry curvature $\Omega_{kl}^{(\beta)}(\vec{\varphi}_t)$. In the next section, we illustrate this behavior by concentrating on the concrete topological burning glass scenario in which the dynamics of the system is initialized in the ferromagnetic ground state $|\Phi_0(\vec{\varphi}_{t_0})\rangle$.

4.2.4 Spin Polarization

To further analyze the TBGE, we contrast the dynamics of a decoupled central spin with the collective dynamics in the strong coupling regime[8]. We start with the noninteracting case, where Eq. (4.22) transforms into a single-spin Hamiltonian resembling the momentum-space representation of a Chern insulator with mass parameter M (cf. Eq. (3.4)). Thus, each of the two single-spin energy bands can be characterized by a winding number $\nu_{gr} = -\nu_{ex} = \pm 1$ (nontrivial) for $|M| < 2$, $M \neq 0$ or $\nu_{gr} = \nu_{ex} = 0$ (trivial) for $|M| > 2$, where ν_{gr} (ν_{ex}) corresponds to the single-spin ground (excited) energy band (cf. Fig. 3.4). Starting from the single-spin ground state, the quasiadiabatic dynamics produces a topological frequency conversion that is proportional to $\nu_{gr} = -\frac{1}{4\pi}\iint_0^{2\pi}\mathrm{d}^2\vec{\varphi}\,\tilde{\mathbf{d}}(\vec{\varphi})\left(\partial_{\varphi_1}\tilde{\mathbf{d}}(\vec{\varphi})\times\partial_{\varphi_2}\tilde{\mathbf{d}}(\vec{\varphi})\right)$ with $\tilde{\mathbf{d}}(\vec{\varphi}) = \frac{\mathbf{d}(\vec{\varphi})}{|\mathbf{d}(\vec{\varphi})|}$ (see Eq. (3.7)). In the interacting case, the interaction effectively extends the magnetic coupling to the

[8] Throughout the Thesis, we use equivalent terminologies for the dynamics associated with the first-order corrections of APT (see Sec. 2.1.3). These include, for example, the terms quasiadiabaticity, quasiadiabatic dynamics, or strong coupling regime.

surrounding spins, forcing them to rotate along the direction of the external field $\mathbf{B}(\vec{\varphi}_t)$ as well. In the strong coupling regime and for ferromagnetic coupling strength[9] $A > 0$, this collective behavior imposes a topological frequency conversion that is proportional (cf. Eq. (4.26)) to the total Chern number

$$C^{(0)} = N\,\nu_{gr} \tag{4.32}$$

of the ferromagnetic ground state[10] $|\Phi_0(\vec{\varphi}_{t_0})\rangle$. This behavior affords a simple interpretation (see also Sec. 4.1.3): In the adiabatic limit, the spin polarizations of the surrounding spins point in the same direction as that of the central spin, such that each spin contributes to the many-body wave function by the same single-spin Chern number ν_{gr} (cf. Fig. 3.2). Importantly, the adiabatic ground state is a product state at all times, such that the reduced adiabatic density matrix $\hat{\rho}^{\mathrm{ad}}_{0,0}(\vec{\varphi}) = \frac{1}{2}\,(\mathbb{1} - \tilde{\mathbf{d}}(\vec{\varphi}) \cdot \hat{\boldsymbol{\sigma}})$ yields a Chern number ν_{gr} that is given by that of a single spin-1/2 (cf. Sec. 3.1.2). The latter thus fails to capture the topological quantization and enhancement of the local response, revealing a burning glass effect in which the aforementioned collective motion of all spins is locally imprinted in the non-unitary dynamics of the central spin. In fact, as we have described in Sec. 4.2.3, the operators $\hat{T}_{\alpha\beta}(\vec{\varphi}_t)$ of Eq. (4.28) induce fluctuations around the adiabatic spin polarization of the central spin-1/2, including the topological information of the total system, and affecting the indirect measurement of the topological frequency conversion [SKK$^+$14, RNC$^+$14, MS21].

In Fig. 4.4, we illustrate the numerically exact simulations of the spin polarization $\mathbf{u}^{\mathrm{dy}}_0(t) = (u^{\mathrm{dy}}_{0,x}(t), u^{\mathrm{dy}}_{0,y}(t), u^{\mathrm{dy}}_{0,z}(t))$ as a function of time $\omega\,t$ for different ferromagnetic interaction strengths $\mathcal{A} = 0.0$ (green), $\mathcal{A} = 0.5$ (blue), $\mathcal{A} = 4.0$ (red). Here, we introduce the renormalized interaction strength $\mathcal{A} = A/\lambda$ and the vector of frequencies $\vec{\omega} = (1,\,\gamma)\,\omega$, with $\gamma = \frac{1}{2}(1+\sqrt{5})$. We initialize the system at $t_0 = 0$ in the ferromagnetic ground state $|\Phi_0(\vec{\varphi}_{t_0})\rangle$ (cf. Eq. (4.23)), selecting a total number of spins $N = 5$ and a frequency $\omega/\lambda = 5 \cdot 10^{-3}$. The remaining parameters are chosen as $\phi_1 = \pi/10$, $\phi_2 = 0$, and $M = 1.2$, while the adiabatic spin polarization $\mathbf{u}^{\mathrm{ad}}_0(\vec{\varphi}_t) = -\tilde{\mathbf{d}}(\vec{\varphi}_t)$ (cf. Fig. 3.2) is represented as a solid black line. In the interacting case $\mathcal{A} \neq 0$, the spin polarization $\mathbf{u}^{\mathrm{dy}}_0(t)$ differs from the single spin case ($\mathcal{A} = 0$), indicating that the non-unitary dynamics of the central spin is crucially affected by the geometrical properties of the total system (cf. Eq. 4.31). Note that this information is contained in the enhanced fluctuations (compared to the single spin case) around the black line in Fig. 4.4.

[9] Results for antiferromagnetic coupling strength $A < 0$ are presented in the Appendix B.4.

[10] For simplicity, we restrict ourselves to the dynamics originating from the ferromagnetic ground state $|\Phi_0(\vec{\varphi}_{t_0})\rangle$, leading to a concrete topological burning glass scenario in which the quantized frequency conversion is maximally amplified by a factor N. However, as the Bloch band structure in the synthetic 2D BZ is explicitly gapped (cf. Sec. 4.1.3), the TBGE can be also observed for the excited states of the interacting spin system (4.22), as explicitly discussed in the Appendix B.3.

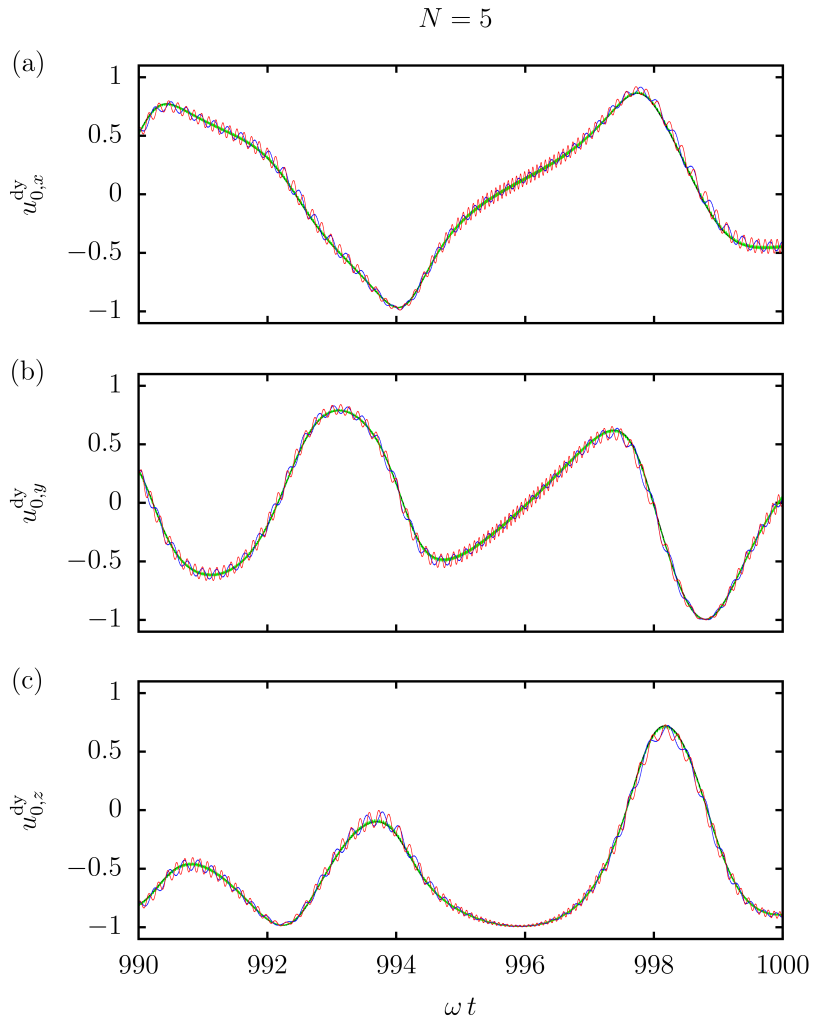

Figure 4.4: Spin polarization $\mathbf{u}_0^{\mathrm{dy}}(t) = (u_{0,x}^{\mathrm{dy}}(t), u_{0,y}^{\mathrm{dy}}(t), u_{0,z}^{\mathrm{dy}}(t))$ as a function of time $\omega\, t$ for different interaction strengths $\mathcal{A} = 0.0$ (green), $\mathcal{A} = 0.5$ (blue), $\mathcal{A} = 4.0$ (red). In the interacting case $\mathcal{A} \neq 0$, the collective motion of the environmental spins crucially affects the non-unitary dynamics of the central spin, as can be seen from the enhanced fluctuations (compared to the single spin case) around the adiabatic spin polarization $\mathbf{u}_0^{\mathrm{ad}}(\vec{\varphi}_t) = -\tilde{\mathbf{d}}(\vec{\varphi}_t)$ (solid black line). We have selected a total number of spins $N = 5$ and a frequency $\omega/\lambda = 5 \cdot 10^{-3}$. Note that the green line only slightly deviates from the black line. *Reprinted figure with permission from Ref. [KPBT22]. Copyright (2022) by the American Physical Society.*

4.3 Nonequilibrium Phase Diagrams

Performing exact numerical calculations, we explore the parameter ranges of the CSM (see Sec. 4.1) for which the strong coupling regime breaks down. To this end, we investigate the associated nonequilibrium phase diagrams as a function of interaction strength, driving frequencies, time-scales of the quasiperiodic dynamics, and the total number of spins in the CSM. The TBGE (see Sec. 4.2) is suppressed whenever the driving frequencies approach the size of the energy gap above the many-body ground state, the latter generally scaling with the inverse of the total number of spins in the CSM (see Sec. 4.1.3). Accordingly, there exists an ideal choice of environmental spins such that the TBGE is as pronounced as possible, but the energy gaps are still large enough to allow for a strong coupling regime under realistic driving frequencies and interactions. Although this observation indicates that the TBGE constitutes a finite size effect in our model, the quantized energy transfer between the external drives is not immediately gone after the breakdown of the quasiadiabatic dynamics. Rather, the system (pre)thermalizes into an intermediate dynamical quantum phase in which the topological frequency conversion even extends to a strongly nonadiabatic situation, with an ensemble-averaged pumping rate similar to that of the decoupled central spin case. Characterizing the nonequilibrium quantum phases by the time-averaged von Neumann entropy of the central spin, we further identify the transient dynamics and fundamental time-scales of (pre)thermalization. Parts of this Section are based on the Supplemental Material of Ref. [KPBT22].

4.3.1 Nonadiabatic Breakdown

We corroborate the formation of a topological burning glass by numerically solving the Schrödinger equation associated with the Hamiltonian (4.22) up to times[11] $\lambda T = 5 \cdot 10^5$. If the initial state at $t_0 = 0$ corresponds to the ferromagnetic ground state $|\Phi_0(\vec{\varphi}_{t_0})\rangle$ (cf. Eq. (4.23)), the time-averaged pumping rate P^{12} can be extrapolated by the gradient[12] of the energy transfer $W_1(t) = \omega_1 \int_0^t \mathrm{d}t' \, \langle \hat{\mathrm{I}}_1(t') \rangle$ (cf. Fig. 3.5). In Fig. 4.5, the pumping rate P^{12} is shown as a function of ferromagnetic interaction strength[13] $\mathcal{A} > 0$ and frequency ω for different total spin numbers N, where we introduce the renormalized interaction strength $\mathcal{A} = A/\lambda$. The mass parameter $M = 1.2$ is selected such that the system is in the nontrivial topological regime, yielding an adiabatic Chern number $\nu_{gr} = 1$ of the driven spin (cf. Fig. 3.4). We further choose the frequencies $\omega_1 = \omega$ and $\omega_2 = \gamma\,\omega$, with $\gamma = \frac{1}{2}(1 + \sqrt{5})$ the golden ratio, and the offset phases $\phi_1 = \pi/10$, $\phi_2 = 0$. A finite interaction strength drives the system into the burning glass regime with an N-fold enhanced topological frequency conversion determined by the Chern number $C^{(0)} = N\,\nu_{gr}$ of Eq. (4.32) (red regime). Away from the zero-frequency limit, there exists parameter ranges at which the strong coupling regime of Eq. (4.26)

[11] For a time $\lambda T = 5 \cdot 10^5$, the entire synthetic 2D BZ is sufficiently sampled for our choice of parameters.

[12] We obtain the gradient by computing $P^{12} = \frac{2}{T}\,(\bar{W}_1^T - \bar{W}_1^{T/2})$ with the time-averaged energy transfers $\bar{W}_1^{T/2} = \frac{2}{T}\int_0^{T/2} \mathrm{d}t\, W_1(t)$ and $\bar{W}_1^T = \frac{2}{T}\int_{T/2}^{T} \mathrm{d}t\, W_1(t)$.

[13] Results for antiferromagnetic interaction strength $\mathcal{A} < 0$ are presented in the Appendix B.4.

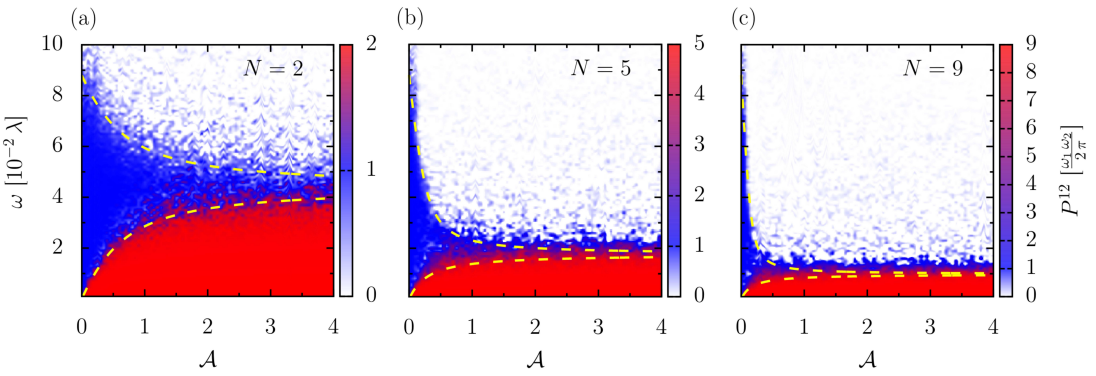

Figure 4.5: Nonequilibrium phase diagrams as a function of interaction strength $\mathcal{A} > 0$ and frequencies $\omega_1 = \omega$, $\omega_2 = \gamma\,\omega$ for different total spin numbers N. The mass parameter $M = 1.2$ is chosen in the nontrivial topological regime ($\nu_{gr} = 1$). Provided the quasiadiabatic dynamics is confined to the ferromagnetic ground state $|\Phi_0(\vec{\varphi}_{t_0})\rangle$, the time-averaged pumping rate P^{12} is proportional to the Chern number $C^{(0)} = N\,\nu_{gr}$ (red regime). Nonadiabatic excitation processes can result in dynamical transitions to intermediate/featureless quantum phases with pumping rates $\bar{P}^{12} = \frac{\nu_{gr}}{2\,\pi}\,\omega_1\,\omega_2$ (blue regimes)/$P^{12} = 0$ (white regimes). The critical frequencies ω_c scale with the energy gaps separating the spectrum into the aforementioned dynamical quantum phases (see Fig. 4.1), roughly illustrated by phase boundaries $\omega_c = 0.11\,\Delta^{\min}_{1/f}$ (dashed yellow lines). *Reprinted figure with permission from Ref. [KPBT22]. Copyright (2022) by the American Physical Society.*

breaks down. The dynamics leads to nonadiabatic excitation processes between the instantaneous eigenstates of the spectrum, yielding a suppression of the dynamical response. Finally, the system enters an ergodic regime that leads to a featureless state with pumping rate $P^{12} = 0$ (white regime). Interestingly, in the CSM, there exists an intermediate dynamical quantum phase in which the spectrum is only partially occupied. The topological frequency conversion then even extends to a nonadiabatic situation, with a pumping rate $\bar{P}^{12} = \frac{\nu_{gr}}{2\,\pi}\,\omega_1\,\omega_2$ (see Eq. (4.33)) similar to that of the single spin (blue regime).

The nonadiabatic breakdown of the strong coupling regime can be described in terms of the topological band structure of Fig. 4.1. Starting from the ferromagnetic ground state energy band $\mathcal{E}^{(1)}_{-}$, the dynamical breakdown occurs in two main stages[14]. (I) The exact quantum state shows equal time-averaged overlaps with the instantaneous eigenstates of the energy bands $\mathcal{E}^{(1)}_{-}$ and $\mathcal{E}^{(2)}_{-,n}$, resulting in an intermediate dynamical quantum phase with an ensemble-averaged pumping rate $\bar{P}^{12} = \frac{\nu_{gr}}{2\,\pi}\,\omega_1\,\omega_2$ identical to that of a single spin (cf. Sec. 3.1). The remaining stage (II) divides into two featureless phases (IIa) and (IIb) with zero time-averaged pumping rate $P^{12} = 0$. (IIa) In addition to the overlaps of the intermediate phase, also the energy band $\mathcal{E}^{(1)}_{+}$ is equally occupied on time-average. (IIb) Within the block $j = \frac{N-1}{2}$, an ergodic situation arises in which the exact quantum state additionally exhibits equal time-averaged overlaps with the instantaneous eigenstates of the high-energy bands $\mathcal{E}^{(2)}_{+,n}$. The stages (I)-(II) can be

[14] Again, we restrict ourselves to ferromagnetic interaction strengths $\mathcal{A} > 0$, while similar results can be also obtained for the antiferromagnetic case (see Appendix B.4).

considered as (pre)thermalization processes, while the ergodic situation (IIb) in this analogy corresponds to a featureless "infinite-temperature" state.

Let us analyze the above statements in more detail. Starting from the ferromagnetic ground state energy band $\mathcal{E}_{-}^{(1)}$, the nonequilibrium evolution can drive the system into the dynamical quantum phase (I) with integer-quantized energy current

$$\bar{P}^{12} = -\bar{P}^{21} = \frac{1}{N}\sum_{n=0}^{N-1} P_n^{12} = \frac{\nu_{gr}}{2\,\pi}\,\omega_1\,\omega_2. \tag{4.33}$$

Each occupied energy band contributes by a time-averaged pumping rate $P_n^{12} = -P_n^{21} = \frac{C_n}{2\,\pi}\,\omega_1\,\omega_2$ determined by the total Chern number $C_n = (N-2\,n)\,\nu_{gr}$ (cf. Sec. 4.1.3). The ensemble-averaged pumping rate of Eq. (4.33) can be observed for interaction strengths $\mathcal{A}_{\vec{\varphi}} > 0$ that induce low-energy gaps $\Delta_1 \ll \Delta_f$ (cf. Fig. 4.1): once the dynamics leads to nonadiabatic excitation processes to the first excited energy band $\mathcal{E}_{-,1}^{(2)}$, subsequent energy bands $\mathcal{E}_{-,n}^{(2)}$ are gradually occupied as gaps Δ_1 and $\Delta_{n+1} - \Delta_n$ are of similar size. Populations in the instantaneous ground $\mathcal{E}_{-}^{(1)}$ and low-energy bands $\mathcal{E}_{-,n}^{(2)}$ then become equal within an intermediate (pre)thermal regime, while transitions to the energy band $\mathcal{E}_{+}^{(1)}$ are suppressed. For $\mathcal{A}_{\vec{\varphi}} \gg \frac{2}{N}$, however, all low-energy gaps $\Delta_1 \approx \Delta_f \approx \Delta_{n+1} - \Delta_n$ have approximately the same size. (Pre)thermalization then immediately leads to a featureless quantum phase (II) with zero time-averaged pumping rate $P^{12} = 0$, as the total Chern numbers sum to $\sum_{n=0}^{N} C_n = \sum_{n=1}^{N-1} C_n = 0$.

The phase boundaries of the dynamical transitions are not sharp, as they originate from nonanalytical excitation processes. Nevertheless, the numerics suggest that the leading processes are approximately covered by critical frequencies $\omega_c \propto \Delta_{1/f}^{\min}$, which is roughly illustrated by assuming a proportionality constant $K_T = 0.11$ in Fig. 4.5 (dashed yellow lines). We have evaluated the gaps $\Delta_{1/f}$ of Eq. (4.18) in the origin ($\vec{\varphi} = 0$) of the synthetic 2D BZ, obtaining the minimum band gaps (see Appendix B.2)

$$\Delta_{1/f}^{\min}(\mathcal{A}) = \lambda\,|\mathbf{d}(0)|\,\Delta_{1/f}\Big(\frac{\mathcal{A}}{|\mathbf{d}(0)|}\Big)$$

for the mass parameter $M = 1.2$. The approach for the critical frequencies ω_c becomes less accurate with larger total spin numbers N, especially evident in Figs. 4.5(b) and 4.5(c). This, however, can be explained by the time-scales required for (pre)thermalization into the nonequilibrium quantum phases (see Sec. 4.3.2): with a higher number of energy bands (controlled by a larger total number of spins N), transition phases with pumping rates beyond the integer-quantized values become more pronounced. This transient effect, in turn, leads to a broadening of the phase boundaries of the dynamical transitions, which slightly distorts the approximation $\omega_c \propto \Delta_{1/f}^{\min}$. Nevertheless, the fundamental scaling behavior of the phase diagrams of Fig. 4.5 can be analyzed: both the crossover interaction strength $\mathcal{A}^{\mathrm{cr}} = \frac{2\,|\mathbf{d}(0)|}{N} = \frac{1.6}{N}$ (cf. Fig. 4.1) and the minimum band gaps $\Delta_{1/f}^{\min}/\lambda \approx \frac{0.8}{N}$ scale with the inverse of N for a larger number of environmental spins, indicating that the TBGE represents a finite size effect in our model. We have used that $|\mathbf{d}(0)| = 0.8$.

4.3.2 Transient Dynamics

In the previous section, we have shown that for a time $\lambda T = 5 \cdot 10^5$, the dynamical transitions to the different nonequilibrium quantum phases mainly depend on the relation between the frequency ω and the minimum band gap $\Delta_{1/f}^{\min}$ (see dashed yellow lines in Fig. 4.5). For a finite frequency $\omega \neq 0$, however, the breakdown of the prethermal regime strongly depends on the time-scales of the nonequilibrium dynamics. We investigate the transient dynamics for the quasiperiodically driven CSM by numerically calculating the von Neumann entropy of the central spin [NC10]:

$$S^{\mathrm{dy}}(t) = -\operatorname{Tr}_0 \left[\hat{\rho}_{0,0}^{\mathrm{dy}}(t) \, \ln[\hat{\rho}_{0,0}^{\mathrm{dy}}(t)] \right], \tag{4.34}$$

where Tr_0 denotes the trace acting on the central spin-1/2 and ln the natural matrix logarithm. We use the reduced density matrix $\hat{\rho}_{0,0}^{\mathrm{dy}}(t)$ introduced in Eq. (4.27), while in contrast to Eq. (4.28) we now also take into account the higher orders in the perturbative expansion. Within the prethermal regime, the quasiadiabatic dynamics is confined to the energy band $\mathcal{E}_{-}^{(1)}$ (see Fig. 4.1) if the system has been initialized in the ferromagnetic ground state $|\Phi_0(\vec{\varphi}_{t_0})\rangle$ (cf. Eq. (4.23)). Since the associated instantaneous eigenstate $|\Phi_0(\vec{\varphi}_t)\rangle$ corresponds to a ferromagnetic product state at all times (cf. Sec. 4.1.3), the von Neumann entropy nearly vanishes[15]: $S^{\mathrm{dy}}(t) \approx 0$. Away from the zero-frequency limit, however, there exists a critical time t_c at which the prethermal regime breaks down. The dynamics then leads to nonadiabatic excitation processes between the energy bands of Eq. (4.15), resulting in an increase of the von Neumann entropy $S^{\mathrm{dy}}(t) > 0$ for times $t > t_c$. This change enables, in principle, the determination of the critical time t_c.

The von Neumann entropy $S^{\mathrm{dy}}(t)$ described by Eq. (4.34) thus reveals the transient dynamics for the breakdown of the strong coupling regime. In the CSM, however, (pre)thermalization additionally leads to the two main stages (I) and (II), as discussed in Sec. 4.3.1. To determine the fundamental time-scales of this (pre)thermalization processes, we analyze the time-averaged von Neumann entropy

$$\bar{S}^{\mathrm{dy}}(t) = \frac{1}{t} \int_0^t \mathrm{d}t' \, S^{\mathrm{dy}}(t'). \tag{4.35}$$

This quantity provides a proper characterization of the different nonequilibrium quantum phases (I)-(II), as explicitly suggested in the Appendix B.5. In particular, the featureless states (IIa) and (IIb) can be distinguished. Thus, it can be used not only to detect the transient dynamics, but also as a diagnostic tool to confirm the discussions of Sec. 4.3.1. In Fig. 4.6, the time-averaged von Neumann entropy $\bar{S}^{\mathrm{dy}}(t)$ of Eq. (4.35) is shown as a function of time t and frequency ω for different ferromagnetic interaction strengths $\mathcal{A} > 0$ and total numbers of spins N. The remaining parameters are chosen as in the numerical computation of the time-averaged pumping rate P^{12} (see Fig. 4.5). The numerical values of $\bar{S}^{\mathrm{dy}}(t)$ roughly correspond to the predictions for the different dynamical phases derived in the Appendix B.5. The nonequilibrium quantum phases are resolved as the

[15] Although the first-order corrections in Eq. (4.28) induce non-unitary dynamics to the central spin, their contributions to the von Neumann entropy (4.34) are much smaller compared to those of the adiabatic limit.

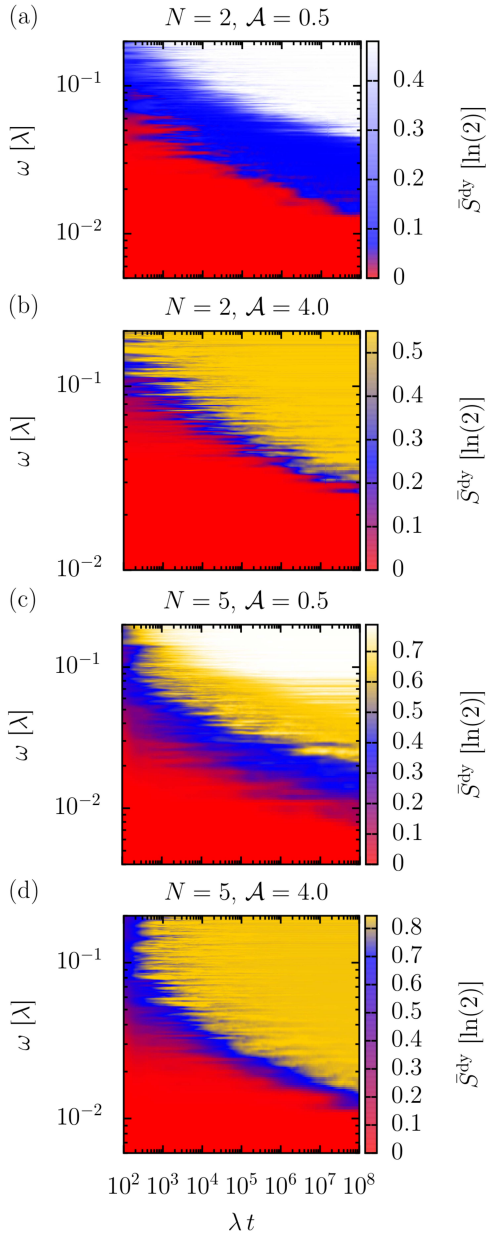

Figure 4.6: Time-averaged von Neumann entropy $\bar{S}^{\mathrm{dy}}(t)$ as a function of time $\lambda\, t$ and frequencies $\omega_1 = \omega$, $\omega_2 = \gamma\, \omega$ for different ferromagnetic interaction strengths $\mathcal{A} > 0$ and total spin numbers N. The different nonequilibrium quantum phases are resolved as the prethermal phase (red regime), the intermediate dynamical phase (I) (blue regime), the featureless phases (IIa) (orange regime) and (IIb) (white regime). The transient dynamics and fundamental time-scales of (pre)thermalization can be estimated by analyzing the phase boundaries of the dynamical transitions, yielding critical frequencies ω_c for a time $\lambda\, T = 5 \cdot 10^5$ consistent with those of Fig. 4.5.

prethermal phase (red regime), the intermediate dynamical phase (I) (blue regime), the featureless phases (IIa) (orange regime) and (IIb) (white regime). The intermediate dynamical phase (I) exhibits finite values of the time-averaged von Neumann entropy $\bar{S}^{\mathrm{dy}}(t) > 0$, arising from the nonadiabatic conditions discussed in Sec. 4.3.1. Thus, the dynamics of the central spin significantly differs from that of a single spin in the noninteracting topological regime, reflecting the decoherence effects arising from the interactions with the environment. In both cases, however, the dynamical response is described by the ensemble-averaged pumping rate $\bar{P}^{12}$ of Eq. (4.33), as explicitly shown in Fig. 4.5. For $\mathcal{A} = 4.0$, no (pre)thermalization into an "infinite-temperature" state (IIb) takes place for parameters used in Figs. 4.6(b) and 4.6(d). This follows from the fact that the high-energy bands $\mathcal{E}^{(2)}_{+,n}$ are well separated from the other energy bands for $\mathcal{A} \gg \frac{1.6}{N}$ (see also Fig. 4.1(a)). For $N = 2$ and $\mathcal{A} = 0.5$, the system immediately (pre)thermalizes from the intermediate dynamical phase (I) to the ergodic situation (IIb), as shown in Fig. 4.6(a). In this case, the minimum band gap Δ_f^{min} is much larger than the energetic separation between the ferromagnetic energy band $\mathcal{E}^{(1)}_{+}$ and the high-energy bands $\mathcal{E}^{(2)}_{+,n}$ (note that the crossover interaction strength is $\mathcal{A}^{\mathrm{cr}} = 0.8$). Nonadiabatic excitations to the energy band $\mathcal{E}^{(1)}_{+}$ then immediately populate high-energy bands $\mathcal{E}^{(2)}_{+,n}$ as well. For $N = 5$, the crossover interaction strength is $\mathcal{A}^{\mathrm{cr}} = 0.32$. An interaction strength $\mathcal{A} = 0.5$ then leads to a spectrum in which the ferromagnetic energy band $\mathcal{E}^{(1)}_{+}$ is separated from the high-energy bands $\mathcal{E}^{(2)}_{+,n}$. The system then also (pre)thermalizes to the featureless state (IIa), as demonstrated in Fig. 4.6(c). The fundamental timescales of (pre)thermalization can be estimated by analyzing the phase boundaries of the dynamical transitions: changes from red $\mapsto$ blue / blue $\mapsto$ white / blue $\mapsto$ orange regimes happen at critical times t_c and frequencies ω_c. The associated boundaries thus provide the critical frequencies ω_c as a function of time t. The logarithmic scales in Fig. 4.6 suggest that this time-dependence could be modulated by a power law. This results in critical times t_c that decrease with larger frequencies ω, while a time $\lambda T = 5 \cdot 10^5$ leads to critical frequencies ω_c that are consistent with those of the phase boundaries of the nonequilibrium phase diagrams of Fig. 4.5. In this sense, the topological frequency conversion could be employed as an indicator of thermalization in a many-body spin system.

5

Conclusion

We have shown that interactions can drastically modify the topological properties of quantum systems with dynamically-induced synthetic dimensions, with correlated topological responses that have no counterpart to the noninteracting regime. Inspired by these interaction-driven features, we have discovered a novel mechanism of topological quantization coined *topological burning glass effect* (TBGE), in which the local response of a quantum system exhibits a topological quantization that is enhanced by an integer due to its environmental coupling. Our results reflect fundamental concepts that do not depend on the details of the model, but simply refer to the quantum dynamics of a generic (interacting) system evolving quasiperiodically in parameter space. Treating these dynamics by means of a perturbative expansion around the adiabatic limit, the topological response stems from the virtual couplings between the synthetic energy bands of the instantaneous spectrum.

Before presenting our main results on the interplay between interaction and synthetic dimension, we have given an overview on the field of dynamical synthetic quantum matter. To this end, we have focused on energy pumping in quasiperiodically driven quantum systems, providing a demonstrative implementation of the aforementioned fundamental concepts. In these systems, the time-quasiperiodic dynamics can be mapped onto a higher-dimensional Floquet lattice, with a tight-binding model forming a synthetic band structure in parameter space. Focusing on a gapped energy band, the semiclassical equations of motion reveal a nontrivial Berry phase term in the frequency domain, resulting in a transverse response similar to that of a quantum Hall scenario. The Hall response in this generalized Floquet system manifests itself in a topological frequency conversion between the quasiperiodic drives, with a time-averaged pumping rate proportional to the nonzero integer classifying the synthetic Hall regime. Following this line of reasoning, it has been shown that a single spin-1/2 subjected to two fields of incommensurate temporal periodicity generates a concrete and feasible example of a *topological frequency converter* (TFC), in which the quantized rate is determined by the adiabatically defined winding number of a Chern insulator.

Based on this knowledge, we have demonstrated that correlated topological phases in synthetic dimensions already appear for the simplest generalization of the TFC,

namely two interacting spins equally exposed to two circularly polarized drives. This minimal model, which we have coined *interacting topological frequency converter* (ITFC), already offers striking topological phenomena that can only be interpreted by means of two-body spin configurations. By calculating the topological phase diagrams of the ITFC as a function of interaction strength, we have predicted an amplification of the frequency conversion as a direct manifestation of the correlated topological response. This enhancement is more pronounced as the number of interacting spins increases, which we have explicitly confirmed by extending the model to three interacting spins. Experimental realizations of the ITFC might be implemented in superconducting quantum circuits [SKK$^+$14, RNC$^+$14] or gated double *quantum dots* (QDs) [PJT$^+$05, BFT$^+$15, SPF$^+$19], the latter allowing for even more exotic couplings between spins due to spin-orbit interactions [FSC$^+$20, FVV$^+$22].

Extending the aforementioned geometrical aspects to open quantum systems, we have identified that the TBGE fundamentally modifies the correspondence between adiabatically defined topological invariants and quantized response signals. To this end, we have shown that the topologically quantized response of a quantum system coupled to its environment is magnified in a way that can not be understood from the adiabatic properties of the quantum system alone. Instead, the quantum system inherits the topological information of the total system in its non-unitary dynamics, imposing a local response that is not covered by its reduced adiabatic density matrix. We have illustrated the TBGE with the concrete example of a quasiperiodically driven *central spin model* (CSM), in which a central spin experiences a topological frequency conversion that is significantly enhanced with the number of surrounding spins. Although this choice makes sense from a pedagogical point of view, the TBGE itself is a generic phenomenon that applies to any static extension of the CSM (or equivalent models) as long as three conditions are met: (*i*) the interacting system is initialized in a (synthetic) energy band that is energetically separated from the other bands, (*ii*) the dynamics is accurately described by the first-order terms of *adiabatic perturbation theory* (APT), (*iii*) the physical observable of interest locally acts on the (small) quantum system coupled to the (larger) environment. In this sense, the details of the model are not important, which is why we expect that the TBGE exemplifies a more general principle of topological open quantum systems.

So far, topological frequency conversion has only been measured indirectly using interference patterns in *nitrogen-vacancy* (NV) centers [BCCS20] or spin polarization detections in superconducting quantum circuits [MS21]. Given this shortcoming, the amplification of the TBGE could be employed to enable the direct experimental observation of the quantized energy current, providing a complementary approach to the recent proposals made in the context of Weyl semimetals [NMR22]. As the enhanced response might be destroyed by nonadiabatic transitions, we have investigated the exact dynamics of the system by numerical calculations. This analysis has shown that the nonadiabatic breakdown occurs when the driving frequencies approach the size of the energy gap above the many-body ground state, the latter scaling with the inverse of the total number of spins in the CSM. We suggest that this scaling behavior could be compensated by counterdiabatic protocols [DR03, DR05, dC13, CPSP19], potentially improving the lifetime of the quasiadiabatic dynamics and thus making the TBGE also

accessible to a larger number of surrounding spins.

The main idea behind the dynamical synthetic quantum matter presented in this Thesis is to project the parameter space of a generic quantum system onto the momentum space of condensed matter materials. Assuming quasiperiodic modulation, this allows for the generation of Floquet counterparts of topological states of matter, such as the presented realization of a quantum anomalous Hall phase by means of the well-known Chern insulator. However, since the geometrical and topological features of the dynamical synthetic quantum matter underlie a generic mechanism that is independent of the concrete model in the physical Hilbert space, our results can in principle be extended to a variety of other topological models from solid-state physics. Following this line of reasoning, a more generic parametrization of the multi-frequency drives can induce three- or higher-dimensional Floquet spaces, in which correlation effects might reveal further topological features unique to the dynamically-induced synthetic dimensions. In this context, the correlated topological responses observed in the ITFC or the CSM could be extended to more exotic couplings between the spins. For example, interactions in lateral QDs or NV centers are not necessarily isotropic, while anisotropic interactions could lead to topological phase transitions that potentially enrich the nonequilibrium phase diagrams of the CSM. As nonadiabatic transitions to excited states of the spectrum suppress the topological response in both the ITFC and the CSM, it would be highly desirable to find mechanisms that stabilize the quasiadiabatic dynamics in these systems. In this context, many-body localization might be a promising candidate for protecting dynamical synthetic quantum matter against thermalization to an infinite temperature state [PPacHA15, LDM15, NH15, AABS19, RL20a]. In fact, this approach has already been shown to persist under quasiperiodic driving [ZMKM22, LCC22], such that it may be used for the stabilization of the TBGE in the CSM.

Appendices

A

Details about the Interacting Topological Frequency Converter

Contents

In the main text, we have explored the interplay of interaction and dynamical synthetic dimension by examining the correlated topological response of the *interacting topological frequency converter* (ITFC), a minimal platform consisting of two interacting spins exposed to two incommensurate periodic drives. The main goal of this Appendix A is to provide additional technical details about this prototypical model, including a schematic illustration of the mapping of all possible single-spin configurations at *high-symmetry points* (HSPs) to the winding number ν (Sec. A.1), an explicit analysis of the topological phase diagrams for nonvanishing interaction strength $\mathcal{J}_{x-y}$ (Sec. A.2), and the extension of the ITFC to an interacting three-spin model (Sec. A.3). Parts of this Appendix A are based on the Supplemental Material of Ref. [KPBT20].

A.1 Mapping the Spin Configuration to the Winding Number

Taking into account that the Hamiltonian (3.10) commutes with $\hat{S}_z$ at HSPs of the synthetic 2D BZ ($\mathcal{J}_{x-y} = 0$), we examine the mapping of all possible single-spin configurations at HSPs to the winding number[1] ν. A schematic illustration is presented in Fig. A.1. Besides the mappings already applied in Fig. 3.3, there exist spin configurations at HSPs in which the spin winds twice around its Bloch sphere. This stems from the fact that the quantum states at $(0, \pi)$, $(\pi, 0)$ show the same spin configuration, such that they count twice in determining the coverage of the Bloch sphere.

[1] This mapping is based on the approach introduced in Sec. 3.2.3, where the topological features of each separable state contributing to the linear combination in $|\psi_{1,0}\rangle$ are explored individually.

Spin configuration	Winding number
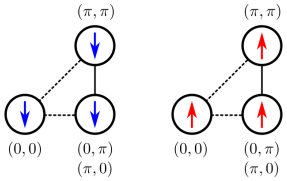	$\nu = 0$
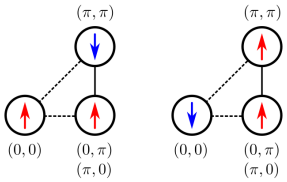	$\nu = -1$
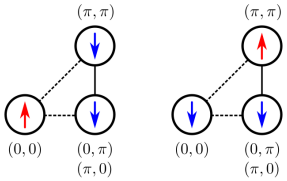	$\nu = 1$
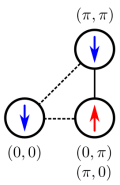	$\nu = -2$
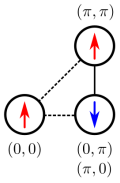	$\nu = 2$

Figure A.1: Mapping of all possible single-spin configurations at *high-symmetry points* (HSPs) to the winding number ν. Since quantum states at $(0,\pi)$, $(\pi,0)$ show the same spin configuration, they count twice in determining the coverage of the Bloch sphere. As a consequence, there exist spin configurations in which the spin winds twice around its Bloch sphere.

A.2 Topological Phase Diagrams for nonvanishing $\mathcal{J}_{\mathbf{x-y}}$

We investigate the influence of a nonvanishing interaction strength $\mathcal{J}_{x-y}$ on the topological phase diagrams of Fig. 3.7. For a finite $\mathcal{J}_{x-y} \neq 0$, the Hamiltonian (3.10) does not commute with $\hat{S}_z$ at HSPs of the synthetic 2D BZ, leading to a coupling of the ferromagnetic triplet states $|\psi_{1,1}\rangle$, $|\psi_{1,-1}\rangle$. A band inversion at HSPs then occurs between the antiferromagnetic triplet state $|\psi_{1,0}\rangle$ and a superposition of ferromagnetic triplet states $|\psi_{1,1}\rangle$ and $|\psi_{1,-1}\rangle$. Accordingly, the topology of the system can no longer be determined by considering the spin configurations at HSPs only, but needs to be explicitly calculated by the integral of Eq. (3.13). Thus, we have to diagonalize the projected Hamiltonian (3.12) for a finite $\mathcal{J}_{x-y} \neq 0$, and calculate the Chern number C_n of the respective Bloch eigenstates $|\Psi_n(\vec{\varphi})\rangle$ $\{n = 0, 1, 2\}$ by Eq. (3.13).

The resulting topological phase diagrams as a function of mass parameter M and interaction strength $\mathcal{J}_z$ are displayed in Fig. A.2 for different interaction strengths $\mathcal{J}_{x-y} \neq 0$. For a finite $\mathcal{J}_{x-y}$, the topological phases are no longer bounded by straight lines as in Fig. 3.7. Especially, phase transitions that corresponded to the horizontal lines at $|M| = 2$ and $M = 0$ now show dispersive character. Although the critical values of $\mathcal{J}_z$ and M are strongly modified by the coupling of the ferromagnetic triplet states $|\psi_{1,1}\rangle$, $|\psi_{1,-1}\rangle$, the corresponding topological invariants of the phases do not vary from those of the main text. In particular, the striking topological phenomena with odd Chern numbers $C_n = \pm 1, \pm 3$ are still present and are influenced at most only by a shift of the boundaries of the phase transitions. Accordingly, the phenomenological results of the main text are not qualitatively affected by a nonvanishing interaction strength $\mathcal{J}_{x-y}$.

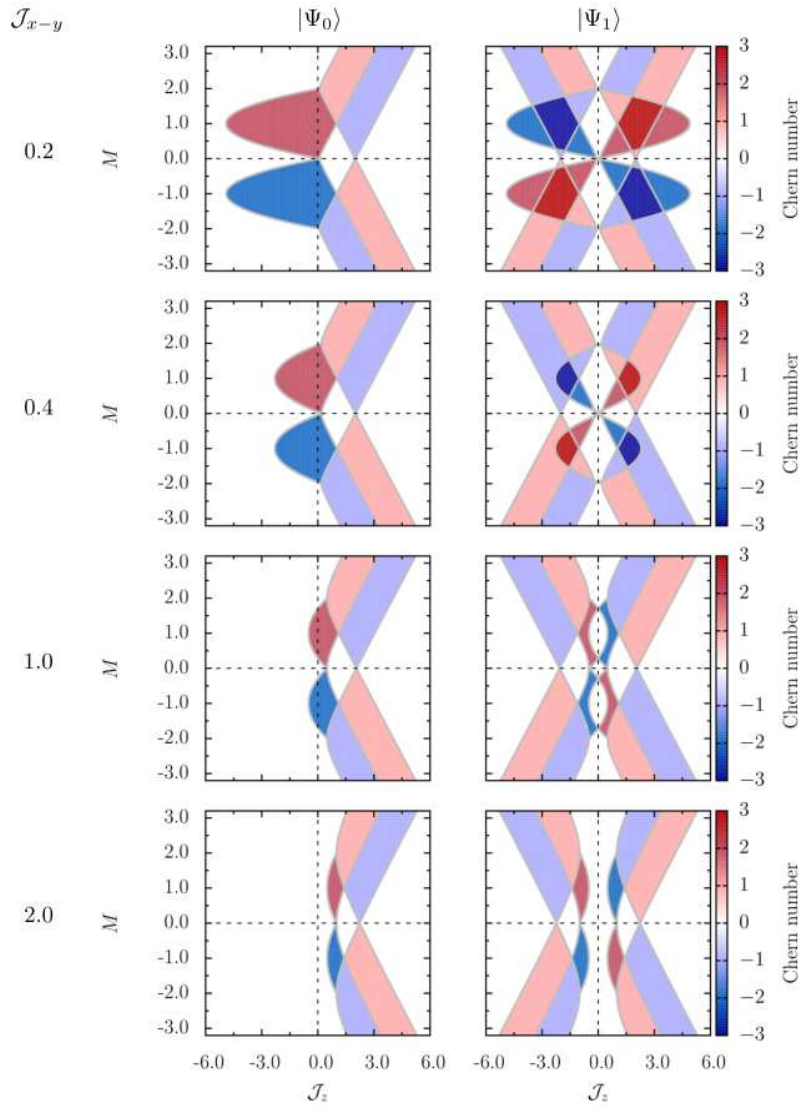

Figure A.2: Topological phase diagrams as a function of M and $\mathcal{J}_z$ for different interaction strengths $\mathcal{J}_{x-y}$. The topological phases are no longer bounded by straight lines as in Fig. 3.7, which is why the topological phase transitions are quantitatively modified by a finite $\mathcal{J}_{x-y} \neq 0$. The topological invariants of the phases, however, do not differ from those of the main text. In particular, the striking topological phenomena with odd Chern numbers $C_n = \pm 1, \pm 3$ are still present, and only influenced by a shift of the boundaries. The phenomenological results of the main text are therefore not qualitatively influenced by a finite interaction strength $\mathcal{J}_{x-y}$. *Reprinted figure with permission from Ref. [KPBT20]. Copyright (2022) by the American Physical Society.*

A.3 Extended Three-Spin Model

In the main text, we have demonstrated that the *interacting topological frequency converter* (ITFC) consisting of two interacting spins (see Fig. 3.6 for an illustration) realizes correlated topological phases in which the topological response can be enhanced by interactions for global Chern numbers $C_n = \pm 3$. In the following, we illustrate that such correlated topological phases are also to be expected with an increasing number of interacting spins, and that in these cases the associated amplification of the topological frequency conversion is even more pronounced. As a prime example, we extend the Hamiltonian (3.10) by an additional spin C and, for simplicity, concentrate on a symmetrical arrangement of the spins given by

$$\hat{H}_3(\vec{\varphi}_t) = \frac{g^* \mu_B}{2} \mathbf{B}(\vec{\varphi}_t) \left(\hat{\boldsymbol{\sigma}}_A + \hat{\boldsymbol{\sigma}}_B + \hat{\boldsymbol{\sigma}}_C\right) + \sum_{i=x,y,z} J_i \left(\hat{\sigma}^i_A \hat{\sigma}^i_B + \hat{\sigma}^i_B \hat{\sigma}^i_C + \hat{\sigma}^i_A \hat{\sigma}^i_C\right).$$

In the external field $\mathbf{B}(\vec{\varphi}_t)$ of Eq. (3.11) we again set the amplitudes to $B_{1/2} = B_c$. For the interacting three-spin model $\hat{H}_3$, the same calculations as in the main text for two spins can now be performed. In particular, the system again commutes with the total spin $[\hat{H}_3, \hat{\mathbf{S}}^2] = 0$, and the problem can be decoupled into the Hilbert subspaces with $s = 3/2$ and $s = 1/2$. Apart from a global constant, the Hamiltonian can then be written in a diagonal form: $\hat{H}_3 = \mathrm{diag}[\hat{H}_Q, \hat{H}_{D1}, \hat{H}_{D2}]$, where

$$\hat{H}_Q = \lambda' \begin{pmatrix} 3\left(\frac{B_z}{B_c} + \mathcal{J}_z\right) & \sqrt{3}\,\frac{B_-}{B_c} & \sqrt{3}\,\mathcal{J}_{x-y} & 0 \\ \sqrt{3}\,\frac{B_+}{B_c} & -\mathcal{J}_z + \frac{B_z}{B_c} & 2\,\frac{B_-}{B_c} & \sqrt{3}\,\mathcal{J}_{x-y} \\ \sqrt{3}\,\mathcal{J}_{x-y} & 2\,\frac{B_+}{B_c} & -\mathcal{J}_z - \frac{B_z}{B_c} & \sqrt{3}\,\frac{B_-}{B_c} \\ 0 & \sqrt{3}\,\mathcal{J}_{x-y} & \sqrt{3}\,\frac{B_+}{B_c} & -3\left(\frac{B_z}{B_c} - \mathcal{J}_z\right) \end{pmatrix}$$

is represented in the basis of quartet states $\{|\psi_{\frac{3}{2},\frac{3}{2}}\rangle, |\psi_{\frac{3}{2},\frac{1}{2}}\rangle, |\psi_{\frac{3}{2},-\frac{1}{2}}\rangle, |\psi_{\frac{3}{2},-\frac{3}{2}}\rangle\}$. Again, we have introduced the transverse components $B_\pm = B_x \pm i\, B_y$, the energy scale $\lambda' = \frac{g^* \mu_B B_c}{2}$, and the effective interaction strengths $\mathcal{J}_{x\pm y} = \frac{J_x \pm J_y}{\lambda'}$ and $\mathcal{J}_z = \frac{J_z}{\lambda'} - \frac{\mathcal{J}_{x+y}}{2}$ for ease of notation. The Hilbert subspace with $s = 1/2$ consists of two degenerate doublet states[2] $\{|\psi_{\frac{1}{2},\frac{1}{2}}\rangle^{(D1)}, |\psi_{\frac{1}{2},-\frac{1}{2}}\rangle^{(D1)}\}$ and $\{|\psi_{\frac{1}{2},\frac{1}{2}}\rangle^{(D2)}, |\psi_{\frac{1}{2},-\frac{1}{2}}\rangle^{(D2)}\}$, each showing the structure[3] of a noninteracting Chern insulator:

$$\hat{H}_{D1/D2} = \lambda' \begin{pmatrix} \frac{B_z}{B_c} & \frac{B_-}{B_c} \\ \frac{B_+}{B_c} & -\frac{B_z}{B_c} \end{pmatrix} - \lambda' \left(3\,\mathcal{J}_{x+y} + \mathcal{J}_z\right).$$

For this reason, we restrict ourselves to study the Hilbert subspace with $s = 3/2$, for which we diagonalize the projected Hamiltonian $\hat{H}_Q$ for a finite interaction strength $\mathcal{J}_z \neq 0$ ($\mathcal{J}_{x-y} = 0$) and determine the Chern number of the respective eigenstates $|\Psi_n(\vec{\varphi})\rangle$ $\{n = 0, 1, 2, 3\}$ according to Eq. (3.13).

[2] Note that we choose the doublet states such that they form an orthonormal basis of the associated Hilbert subspace.

[3] Except for an overall energy shift caused by $\mathcal{J}_{x+y}$ and $\mathcal{J}_z$.

The resulting topological phase diagrams as a function of mass parameter $M = B_0/B_c$ and effective interaction strength $\mathcal{J}_z$ ($\mathcal{J}_{x-y} = 0$) are displayed in Fig. A.3. Interactions lead to correlated topological phases with Chern numbers $C_n = \pm 1$, ± 2, ± 4, ± 5, which are completely prohibited in the noninteracting regime. Especially, the amplification of the topological frequency conversion is even more pronounced ($C_n = \pm 5$) than in the case of two interacting spins. Since at HSPs the system $\hat{H}_3$ commutes with $\hat{S}_z$ (because $\mathcal{J}_{x-y} = 0$), the Hamiltonian $\hat{H}_Q$ becomes diagonal in the basis of quartet states. Consequently, the topological phase transitions can be investigated in an completely analogous way as in the interacting two-spin case, which additionally illustrates that the physical interpretations of the main text are also valid for the symmetrically arranged three-spin model.

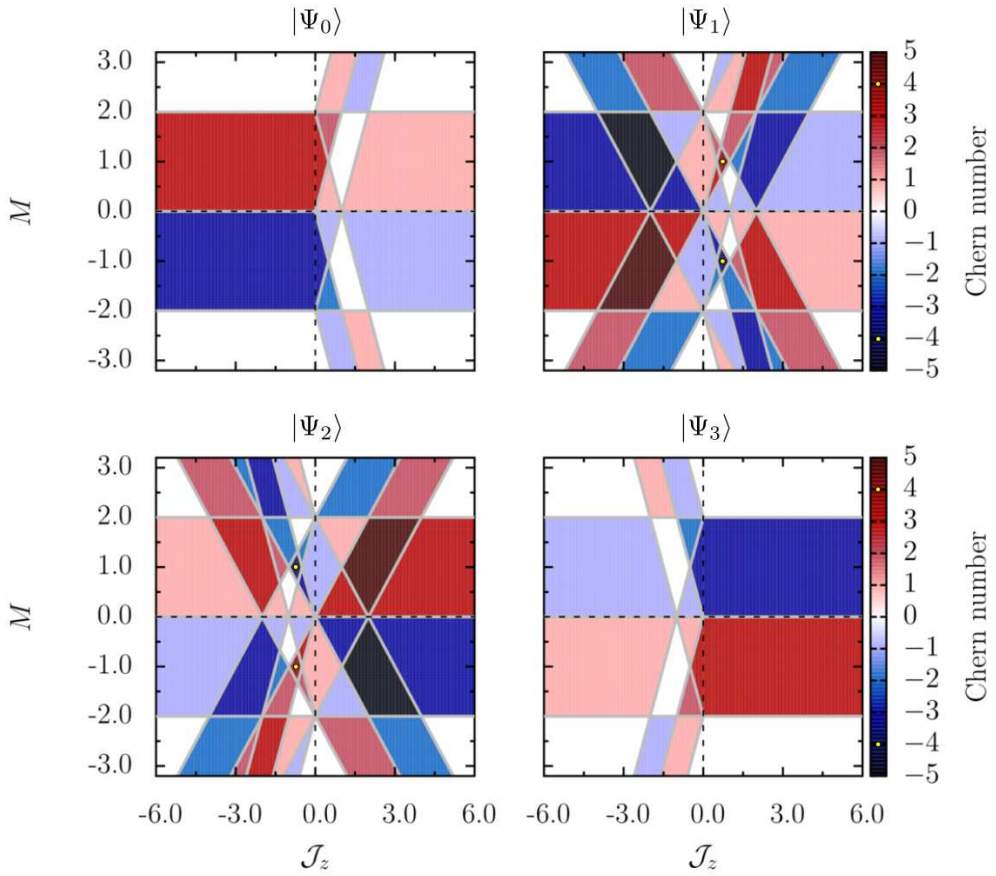

Figure A.3: Topological phase diagrams for the interacting three-spin model as a function of mass parameter M and effective interaction strength $\mathcal{J}_z$ ($\mathcal{J}_{x-y} = 0$). Since we restrict ourselves to investigate the Hilbert subspace with $s = 3/2$ (quartet states), the eigenstates of the projected Hamiltonian $\hat{H}_Q$ are given by $|\Psi_n(\vec{\varphi})\rangle$ $\{n = 0, 1, 2, 3\}$. For a better identification we have marked the phases with Chern numbers $C_n = \pm 4$ by a yellow dot. Interactions drive the system into correlated topological phases with Chern numbers $C_n = \pm 1, \pm 2, \pm 4, \pm 5$ that are forbidden in the noninteracting regime. For $C_n = \pm 5$, this leads to an amplification of the topological frequency conversion that is even more pronounced than in the case of two interacting spins. *Reprinted figure with permission from Ref. [KPBT20]. Copyright (2022) by the American Physical Society.*

B

Details about the Central Spin Model

Contents

In the main text, we have illustrated the *topological burning glass effect* (TBGE) by exploring energy pumping in the quasiperiodically driven *central spin model* (CSM). The main goal of this Appendix B is to provide additional technical details about this prototypical example. This includes the stability analysis for more generic extensions of the CSM (Sec. B.1), the determination of the minimum band gaps in the synthetic 2D *Brillouin zone* (BZ) by means of the spin wave excitations (Sec. B.2), the generalization of the TBGE to the excited states of the interacting spin system (Sec. B.3), the results for antiferromagnetic coupling strength $A < 0$ (Sec. B.4), and the argumentation why the characterization of the nonequilibrium quantum phases introduced in Sec. 4.3 is properly described by the time-averaged von Neumann entropy of the central spin-1/2 (Sec. B.5). Parts of this Appendix B are based on the Supplemental Material of Ref. [KPBT22].

B.1 Stability Analysis

We explore the quasiperiodically driven CSM for more generic couplings. To this end, we consider two concrete static extensions of Eq. (4.22) by implementing (I) inhomogeneous coupling strengths $A_k = x_k\, A$ between the central spin and the surrounding spins (see Eq. (B.1)), and (II) finite coupling strengths $I = y\, A$ between the surrounding spins (see Eq. (B.3)). By numerically calculating the instantaneous spectrum using exact diagonalization (see Fig. B.1), we argue that the TBGE is robust to these extensions.

We start with inhomogeneous coupling strengths $A_k = x_k\, A$, yielding the Hamiltonian

$$\hat{H}_{\mathrm{I}}(\vec{\varphi}_t) = g^*\, \mu_B\, \mathbf{B}(\vec{\varphi}_t) \cdot \hat{\mathbf{S}}_0 - A \sum_{k=1}^{N-1} x_k\, \hat{\mathbf{S}}_0 \cdot \hat{\mathbf{S}}_k. \tag{B.1}$$

We use the definitions of Eq. (4.22), and introduce real positive numbers $x_k \in \mathbb{R}^+$ to account for the inhomogeneity of the interaction. We analyze the energy bands $E_{\mathrm{I}}(\vec{\varphi}_t)$ of Eq. (B.1) for fixed values of the phases $\vec{\varphi}_t$, that is at a given point of the synthetic 2D BZ. In what follows, we thus suppress the subscript t from $\vec{\varphi}_t$. As in Sec. 4.1.2, we perform the transformation

$$\hat{H}'_{\mathrm{I}}(\vec{\varphi}) = \Big(\bigotimes_{i=0}^{N-1} \hat{U}^\dagger(\vec{\varphi}) \Big)\, \hat{H}_{\mathrm{I}}(\vec{\varphi})\, \Big(\bigotimes_{i=0}^{N-1} \hat{U}(\vec{\varphi}) \Big) = \lambda\, |\mathbf{d}(\vec{\varphi})| \left[\hat{S}_0^{z'} - \mathcal{A}_{\vec{\varphi}} \sum_{k=1}^{N-1} x_k\, \hat{\mathbf{S}}_0 \cdot \hat{\mathbf{S}}_k \right], \tag{B.2}$$

where we use the definitions of Eq. (4.3) and introduce the ($\vec{\varphi}$-dependent) interaction strength $\mathcal{A}_{\vec{\varphi}} = \mathcal{A}/|\mathbf{d}(\vec{\varphi})|$. Again, we assume that $|\mathbf{d}(\vec{\varphi})| \neq 0$ and $\lambda > 0$. Unlike the homogeneous case (cf. Sec. 4.1.2), the Hamiltonian $\hat{H}'_{\mathrm{I}}(\vec{\varphi})$ does not commute with the total spin $\hat{\mathbf{J}}^2$ of the surrounding spins, meaning that the total system can not be decomposed into a block diagonal form. Rather, the full Hilbert space must be considered, which is why we derive the dimensionless energy eigenvalues $\mathcal{E}_{\mathrm{I}}(\mathcal{A}_{\vec{\varphi}}) = \frac{E_{\mathrm{I}}(\vec{\varphi})}{\lambda |\mathbf{d}(\vec{\varphi})|}$ of Eq. (B.2) by exact diagonalization. Fig. B.1(a) shows the instantaneous spectrum $\mathcal{E}_{\mathrm{I}}$ as a function of ferromagnetic interaction strength $\mathcal{A}_{\vec{\varphi}} \geq 0$ and a total number of spins $N = 5$ for both homogeneous $x_k = 1$ (solid blue lines) and inhomogeneous $x_k = -\frac{k}{4} + \frac{8}{5}$ (dashed red lines) coupling strengths $A_k = x_k\, A$. Although some anti-crossings may

arise in the excited energy bands of the spectrum, the inhomogeneity of the interaction hardly affects the ferromagnetic ground state energy band. In fact, as the latter remains energetically separated from the other bands, the quasiadiabatic dynamics starting from the ferromagnetic ground state can still be described by APT (cf. Eq. (4.24)). Thus, subsequent derivations of the TBGE (cf. Eqs. (4.25) to (4.28)) are not fundamentally affected by inhomogeneous couplings.

Similar results can be found for finite coupling strengths $I = y\,A$ between the surrounding spins, described by the Hamiltonian

$$\hat{H}_{\mathrm{II}}(\vec{\varphi}_t) = g^*\,\mu_B\,\mathbf{B}(\vec{\varphi}_t)\cdot\hat{\mathbf{S}}_0 - A\left(\hat{\mathbf{S}}_0\cdot\hat{\mathbf{J}} + y\sum_{k=1}^{N-1}\hat{\mathbf{S}}_k\cdot\hat{\mathbf{S}}_{k+1}\right) \tag{B.3}$$

with $y \in \mathbb{R}_0^+$ and periodic boundary conditions $\hat{\mathbf{S}}_N = \hat{\mathbf{S}}_1$. The dimensionless energy eigenvalues $\mathcal{E}_{\mathrm{II}}$ associated with Eq. (B.3) are illustrated for $y = 0$ (solid blue lines) and $y = 0.2$ (dashed red lines) in Fig. B.1(b). Again, the ferromagnetic ground state energy band remains energetically separated from the other bands. Hence, the TBGE is robust against generalizations of the CSM, e.g. for the cases of inhomogeneous couplings between central spin and surrounding spins or a finite coupling between the surrounding spins. Note that, in Fig. B.1, we only show the lower half of the instantaneous spectrum for illustrative reasons, while the results for the remaining energy bands are not essential for the aforementioned discussion.

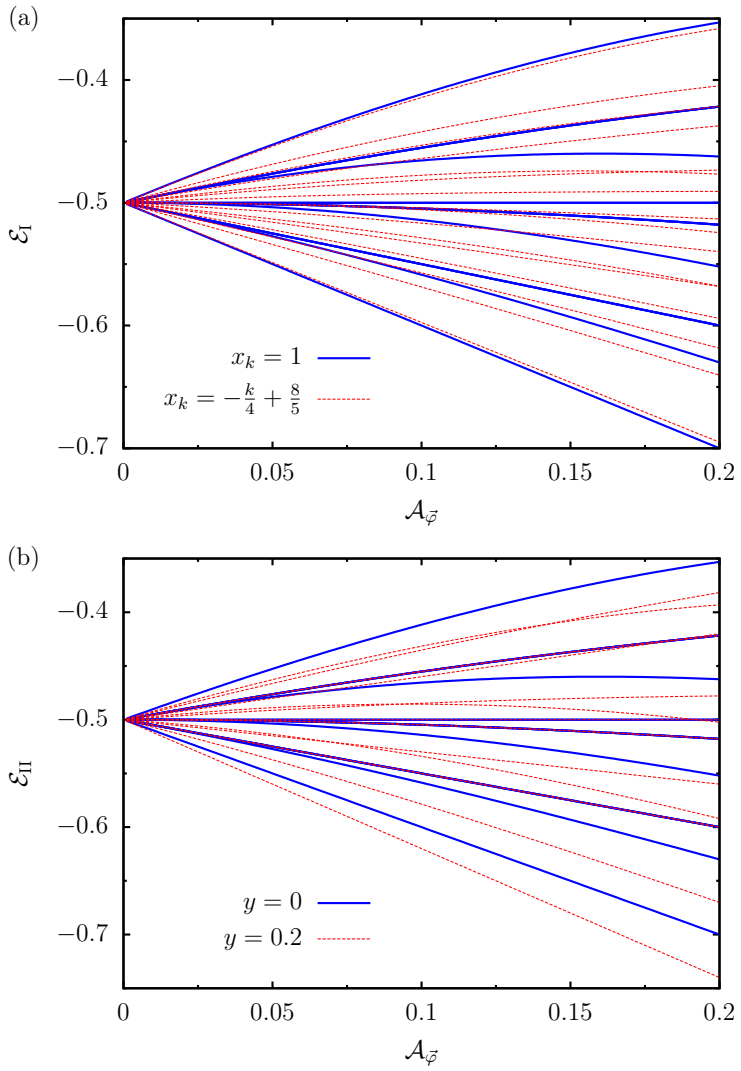

Figure B.1: Spectrum $\mathcal{E}$ as a function of interaction strength $\mathcal{A}_{\vec{\varphi}} \geq 0$ and a total number of spins $N = 5$. For illustrative reasons, only the lower half of the synthetic energy bands is shown. (a) Results for homogeneous $x_k = 1$ (solid blue lines) and inhomogeneous $x_k = -\frac{k}{4} + \frac{8}{5}$ (dashed red lines) coupling strengths $A_k = x_k\, A$. The inhomogeneity of the interaction hardly affects the ferromagnetic ground state energy band, such that its quasiadiabatic dynamics can still be described by *adiabatic perturbation theory* (APT). (b) Similar results for finite coupling strengths $I = y\, A$ between the surrounding spins with $y = 0$ (solid blue lines) and $y = 0.2$ (dashed red lines). *Reprinted figure with permission from Ref. [KPBT22]. Copyright (2022) by the American Physical Society.*

B.2 Minimum Band Gaps

The nature of spin wave excitations (see Sec. 4.1.4) can be used to derive the minimum band gaps $\Delta_{1/f}^{\min}(\mathcal{A})$ within the synthetic 2D BZ. Restricting ourselves to ferromagnetic interaction strengths $\mathcal{A} \geq 0$, we start our calculation by introducing the low-energy gaps

$$\tilde{\Delta}_1(\vec{\varphi},\mathcal{A}) = E_-^{(2)}(\vec{\varphi},-\frac{N}{2}+1) - E_-^{(1)}(\vec{\varphi}), \quad \tilde{\Delta}_f(\vec{\varphi},\mathcal{A}) = E_+^{(1)}(\vec{\varphi}) - E_-^{(2)}(\vec{\varphi},\frac{N}{2}-1), \tag{B.4}$$

which explicitly depend on the phases $\vec{\varphi} = (\varphi_1, \varphi_2)$ defined on the synthetic 2D BZ. Applying the Hellmann-Feynman theorem $\partial_{\varphi_i} E(\vec{\varphi}) = \langle \partial_{\varphi_i} \hat{H}'(\vec{\varphi}) \rangle = \lambda \, (\partial_{\varphi_i} |\mathbf{d}(\vec{\varphi})|) \, \langle \hat{S}_0^{z'} \rangle$ associated with the energy bands of Eqs. (4.13), (4.14), the extremal points within the synthetic 2D BZ can be determined by the condition

$$\frac{\partial \tilde{\Delta}_{1/f}(\vec{\varphi},\mathcal{A})}{\partial \varphi_i} = 0, \quad \text{with} \quad \frac{\partial \tilde{\Delta}_{1/f}(\vec{\varphi},\mathcal{A})}{\partial \varphi_i} = \lambda \, \Delta\chi_{1/f}\Big(\frac{\mathcal{A}}{|\mathbf{d}(\vec{\varphi})|}\Big) \, \frac{\partial |\mathbf{d}(\vec{\varphi})|}{\partial \varphi_i}.$$

For interaction strengths $\mathcal{A} > 0$, the expectation values $\Delta\chi_{1/f} \neq 0$ are not vanishing as explicitly demonstrated in Fig. 4.2(a). The extremal points are then exclusively determined by the condition $\partial_{\varphi_i} |\mathbf{d}(\vec{\varphi})| = 0$, leading to the HSPs of the synthetic 2D BZ. To find the minimum band gaps $\Delta_{1/f}^{\min}(\mathcal{A})$, the low-energy gaps (B.4) thus have to be evaluated only at these HSPs. For fixed values of the phases, the behavior of Eq. (B.4) as a function of ferromagnetic interaction strength $\mathcal{A} \geq 0$ can be illustrated in terms of the low-energy gaps (4.18):

$$\tilde{\Delta}_{1/f}(\vec{\varphi},\mathcal{A}) = \lambda \, |\mathbf{d}(\vec{\varphi})| \, \Delta_{1/f}\Big(\frac{\mathcal{A}}{|\mathbf{d}(\vec{\varphi})|}\Big). \tag{B.5}$$

Considering the associated approximations (see also Fig. 4.1(b))

$$\frac{\tilde{\Delta}_1(\vec{\varphi},\mathcal{A})}{\lambda} \approx \begin{cases} \frac{\mathcal{A}}{2} & ; \mathcal{A} \ll \frac{2\,|\mathbf{d}(\vec{\varphi}_{\min})|}{N} \\ \frac{|\mathbf{d}(\vec{\varphi})|}{N} & ; \mathcal{A} \gg \frac{2\,|\mathbf{d}(\vec{\varphi}_{\max})|}{N} \end{cases},$$

$$\frac{\tilde{\Delta}_f(\vec{\varphi},\mathcal{A})}{\lambda} \approx \begin{cases} |\mathbf{d}(\vec{\varphi})| - (N-1)\,\frac{\mathcal{A}}{2} & ; \mathcal{A} \ll \frac{2\,|\mathbf{d}(\vec{\varphi}_{\min})|}{N} \\ \frac{|\mathbf{d}(\vec{\varphi})|}{N} & ; \mathcal{A} \gg \frac{2\,|\mathbf{d}(\vec{\varphi}_{\max})|}{N} \end{cases},$$

it becomes clear that the minimum band gaps $\Delta_{1/f}^{\min}(\mathcal{A}) = \tilde{\Delta}_{1/f}(\vec{\varphi}_{\min},\mathcal{A})$ are associated with the extremal points $\vec{\varphi}_{\min}$ that result in minimal values $|\mathbf{d}(\vec{\varphi}_{\min})|$. The extremal points $\vec{\varphi}_{\min}/\vec{\varphi}_{\max}$ and associated minimal/maximal values $|\mathbf{d}(\vec{\varphi}_{\min})|/|\mathbf{d}(\vec{\varphi}_{\max})|$ are illustrated as a function of the mass parameter M in Tab. B.1. For $M = 1.2$, Eq. (B.5) then yields the minimum band gaps

$$\Delta_{1/f}^{\min}(\mathcal{A}) = \lambda \, |\mathbf{d}(0)| \, \Delta_{1/f}\Big(\frac{\mathcal{A}}{|\mathbf{d}(0)|}\Big).$$

	$M \geq 1$	$0 \leq M \leq 1$	$-1 \leq M \leq 0$	$M \leq -1$
$\vec{\varphi}_{\min}$	$(0,0)$	$(0,\pi)$, $(\pi,0)$	$(0,\pi)$, $(\pi,0)$	(π,π)
$\lvert\mathbf{d}(\vec{\varphi}_{\min})\rvert$	$\lvert M-2\rvert$	$\lvert M\rvert$	$\lvert M\rvert$	$\lvert M+2\rvert$
$\vec{\varphi}_{\max}$	(π,π)	(π,π)	$(0,0)$	$(0,0)$
$\lvert\mathbf{d}(\vec{\varphi}_{\max})\rvert$	$\lvert M+2\rvert$	$\lvert M+2\rvert$	$\lvert M-2\rvert$	$\lvert M-2\rvert$

Table B.1: Extremal points of the synthetic phases $\vec{\varphi} = (\varphi_1, \varphi_2)$ and associated minimal and maximal values $|\mathbf{d}(\vec{\varphi})|$ as a function of the mass parameter M.

B.3 Generalization to Excited States

In the main text, we have illustrated the TBGE by restricting ourselves to the dynamics originating from the ferromagnetic ground state $|\Phi_0(\vec{\varphi}_{t_0})\rangle$ (cf. Eq. (4.23)) for two main reasons. First, the adiabatic ground state $|\Phi_0(\vec{\varphi}_t)\rangle$ is a product state at all times (cf. Sec. 4.1.3), allowing a simple and descriptive topological classification of the reduced adiabatic density matrix $\hat{\rho}^{\mathrm{ad}}_{0,0}(\vec{\varphi}) = \frac{1}{2}\left(\mathbb{1} - \tilde{\mathbf{d}}(\vec{\varphi}) \cdot \hat{\boldsymbol{\sigma}}\right)$ of the central spin-1/2 (cf. Sec. 3.1.2). Second, the TBGE is most pronounced if the coupled system is initialized in its ferromagnetic ground state $|\Phi_0(\vec{\varphi}_{t_0})\rangle$, with a topological frequency conversion that is magnified by a factor N (cf. Eq. (4.32)). Initializing the system in the next excited state instead, the enhancement would decrease from N to $N-2$ (and so on). To emphasize the general applicability of the derivations of the main text, however, we also show results for the excited energy bands of the interacting spin system below. In doing so, we refer to the topological band structure derived in Sec. 4.1.3.

Considering the instantaneous eigenstates of Eq. (4.16), the reduced adiabatic density matrix of the central spin-1/2 can be derived by tracing out the environment $\hat{\mathbf{J}}$ (denoted as $\mathrm{Tr}_{\hat{\mathbf{J}}}$):

$$\hat{\varrho}^{(1)}_{0,\pm} = \mathrm{Tr}_{\hat{\mathbf{J}}}\left[\,|\mathcal{E}^{(1)}_{\pm}\rangle\langle\mathcal{E}^{(1)}_{\pm}|\,\right] = \frac{1}{2}\left(\mathbb{1}\pm\hat{\sigma}^{z'}\right), \quad \hat{\varrho}^{(2)}_{0,\pm,n} = \mathrm{Tr}_{\hat{\mathbf{J}}}\left[\,|\mathcal{E}^{(2)}_{\pm,n}\rangle\langle\mathcal{E}^{(2)}_{\pm,n}|\,\right] = \frac{1}{2}\left(\mathbb{1}\pm\chi_n\,\hat{\sigma}^{z'}\right). \tag{B.6}$$

We use the property of the partial trace

$$\mathrm{Tr}_{\hat{\mathbf{J}}}\left[\,|m_{s_0}, m_j\rangle\langle\tilde{m}_{s_0}, \tilde{m}_j|\,\right] = |m_{s_0}\rangle\langle\tilde{m}_{s_0}|\;\delta_{m_j,\tilde{m}_j},$$

and represent Eq. (B.6) within the rotated basis $\{|+\tfrac{1}{2}\rangle, |-\tfrac{1}{2}\rangle\}$ of the central spin-1/2. As the quantum number n is conserved, the reduced adiabatic density matrix $\hat{\varrho}_0$ only contains diagonal matrix elements, related to the expectation values χ of Sec. 4.1.4. In fact, this reveals the values $\chi_n(\mathcal{A}_{\vec{\varphi}})$ of Eqs. (4.17), (4.20). By performing the inverse transformation $\hat{\rho}_0 = \hat{U}(\vec{\varphi})\,\hat{\varrho}_0\,\hat{U}^{\dagger}(\vec{\varphi})$, we rotate (B.6) back into the original basis of Eq. (4.22):

$$\hat{\rho}^{(1)}_{0,\pm}(\vec{\varphi}) = \frac{1}{2}\left(\mathbb{1} \pm \tilde{\mathbf{d}}(\vec{\varphi}) \cdot \hat{\boldsymbol{\sigma}}\right), \quad \hat{\rho}^{(2)}_{0,\pm,n}(\vec{\varphi}) = \frac{1}{2}\left(\mathbb{1} + \mathbf{u}^{(2)}_{\pm,n}(\vec{\varphi}) \cdot \hat{\boldsymbol{\sigma}}\right). \tag{B.7}$$

We have introduced vectors $\mathbf{u}^{(2)}_{\pm,n}(\vec{\varphi}) = \pm\,\chi_n(\mathcal{A}_{\vec{\varphi}})\,\tilde{\mathbf{d}}(\vec{\varphi})$, and used the $SU(2)$ matrices $\hat{U}(\vec{\varphi})$ defined in the transformation of Eq. (4.3):

$$\hat{U}(\vec{\varphi})\,\hat{\sigma}^{z'}\,\hat{U}^{\dagger}(\vec{\varphi}) = \tilde{\mathbf{d}}(\vec{\varphi})\cdot\hat{\boldsymbol{\sigma}} \quad \text{with} \quad \tilde{\mathbf{d}}(\vec{\varphi}) = \frac{\mathbf{d}(\vec{\varphi})}{|\mathbf{d}(\vec{\varphi})|}.$$

The reduced adiabatic density matrix $\hat{\rho}^{(1)}_{0,\pm}$ corresponds to that of a single spin-1/2, following from the separable structure of the ferromagnetic states. Provided that $|\mathbf{d}(\vec{\varphi})| \neq 0$, a topological invariant can then be assigned to the central spin (cf. Eq. (3.7)): $\nu^{(1)}_{\pm} = \mp\nu_{gr}$ (independent on the interaction strength $\mathcal{A}$). The reduced adiabatic density matrix $\hat{\rho}^{(2)}_{0,\pm,n}$ of Eq. (B.7) is parametrized by vectors $\mathbf{u}^{(2)}_{\pm,n}(\vec{\varphi})$ proportional to the expectation values $\chi_n(\mathcal{A}_{\vec{\varphi}})$. For an interaction strength $\mathcal{A} \neq 0$, the vectors $\mathbf{u}^{(2)}_{\pm,n}(\vec{\varphi})$ exhibit an adiabatic spin polarization that passes inside the Bloch sphere. The length $|\mathbf{u}^{(2)}_{\pm,n}(\vec{\varphi})| = |\chi_n(\mathcal{A}_{\vec{\varphi}})| \leq 1$ then measures the purity of the reduced density matrix $\mathrm{Tr}_0[\hat{\rho}_0^2] = \frac{1}{2}\,(1+|\mathbf{u}|^2)$ [NC10]. As long as $|\mathbf{u}^{(2)}_{\pm,n}(\vec{\varphi})| > 0$ remains finite throughout the entire synthetic 2D BZ, topologically inequivalent states can be distinguished by the winding number [DRBZ11, BBK$^+$13, BZD15, BD15, HZB16]

$$\nu^{(2)}_{\pm,n} = \frac{1}{4\pi}\iint_0^{2\pi} \mathrm{d}^2\vec{\varphi}\,\tilde{\mathbf{u}}^{(2)}_{\pm,n}(\vec{\varphi})\left(\partial_{\varphi_1}\tilde{\mathbf{u}}^{(2)}_{\pm,n}(\vec{\varphi})\times\partial_{\varphi_2}\tilde{\mathbf{u}}^{(2)}_{\pm,n}(\vec{\varphi})\right) \quad \text{with} \quad \tilde{\mathbf{u}}^{(2)}_{\pm,n}(\vec{\varphi}) = \frac{\mathbf{u}^{(2)}_{\pm,n}(\vec{\varphi})}{|\mathbf{u}^{(2)}_{\pm,n}(\vec{\varphi})|}. \tag{B.8}$$

However, if $|\mathbf{u}^{(2)}_{\pm,n}(\vec{\varphi})| = 0$ vanishes at a given point of the synthetic 2D BZ, the topological classification of the central spin becomes undefined.

The length $|\mathbf{u}^{(2)}_{\pm,n}(\vec{\varphi})| = |\chi_n(\mathcal{A}_{\vec{\varphi}})| \leq 1$ is associated with the expectation values $\chi_n(\mathcal{A}_{\vec{\varphi}})$. In Fig. B.2, the expectation values $\chi_n(\mathcal{A}_{\vec{\varphi}})$ are shown as a function of ferromagnetic interaction strength $\mathcal{A}_{\vec{\varphi}} \geq 0$ and $N = 6$. As in Sec. 4.1.4, the underlying processes can be roughly divided into the following ranges of interaction strengths $\mathcal{A}_{\vec{\varphi}}$. For $\mathcal{A}_{\vec{\varphi}} \ll \frac{2}{N}$, the expectation values $\chi_n(\mathcal{A}_{\vec{\varphi}}) = 1 + \mathcal{O}(\mathcal{A}^2_{\vec{\varphi}})$ indicate that the central spin is hardly affected by interactions. By increasing the interaction strength to $\mathcal{A}_{\vec{\varphi}} \approx \frac{2}{N}$, the expectation values $\chi_n(\mathcal{A}_{\vec{\varphi}})$ decrease with the interaction strength $\mathcal{A}_{\vec{\varphi}}$, indicating that the central spin becomes rotated due to collective spin wave excitations. For $\mathcal{A}_{\vec{\varphi}} \gg \frac{2}{N}$, the expectation values converge to $\chi_n \approx 1 - \frac{2\,n}{N}$, showing that the central spin becomes effectively flipped for quantum numbers $n > \frac{N}{2}$. Then, expectation values $\chi_n(\mathcal{A}_{\vec{\varphi}})$ change sign at an interaction strength $\mathcal{A}_{\vec{\varphi}} = \frac{2}{2\,n-N}$, resulting in vanishing lengths $|\mathbf{u}^{(2)}_{\pm,n}(\vec{\varphi})| = |\chi_n(\mathcal{A}_{\vec{\varphi}})| = 0$. The sign analysis of $\chi_n(\mathcal{A}_{\vec{\varphi}})$ is summarized in Tab. B.2.

The topological classification of the central spin is calculated according to Eq. (B.8), leading to the results of Tab. B.3. We use that $\mathcal{A}_{\vec{\varphi}} = \mathcal{A}/|\mathbf{d}(\vec{\varphi})|$, resulting in minimal and maximal interaction strengths

$$\mathcal{A}_n^{\min} = \frac{2\,|\mathbf{d}(\vec{\varphi}_{\min})|}{2\,n-N}, \quad \mathcal{A}_n^{\max} = \frac{2\,|\mathbf{d}(\vec{\varphi}_{\max})|}{2\,n-N}. \tag{B.9}$$

We have evaluated the interaction strength $\mathcal{A}_{\vec{\varphi}}$ in the extremal points $\vec{\varphi}_{\min}/\vec{\varphi}_{\max}$ of the synthetic 2D BZ, obtaining the minimal/maximal values $|\mathbf{d}(\vec{\varphi}_{\min})|/|\mathbf{d}(\vec{\varphi}_{\max})|$ for mass parameters M (see Tab. B.1). Our results reveal that the single-spin winding

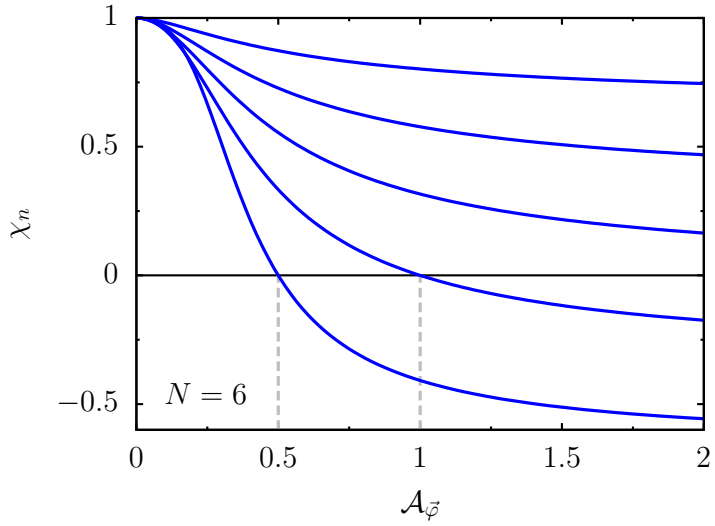

Figure B.2: Expectation values $\chi_n(\mathcal{A}_{\vec{\varphi}})$ as a function of ferromagnetic interaction strength $\mathcal{A}_{\vec{\varphi}} \geq 0$ and $N = 6$. For $\mathcal{A}_{\vec{\varphi}} \ll \frac{2}{N}$, expectation values $\chi_n(\mathcal{A}_{\vec{\varphi}}) \approx 1$ indicate that the central spin is hardly affected by interactions. For $\mathcal{A}_{\vec{\varphi}} \approx \frac{2}{N}$, the central spin becomes rotated due to collective spin wave excitations. For $\mathcal{A}_{\vec{\varphi}} \gg \frac{2}{N}$, the expectation values converge to $\chi_n \approx 1 - \frac{2\,n}{N}$, indicating that for $n > \frac{N}{2}$ the central spin becomes effectively flipped. Then, expectation values $\chi_n(\mathcal{A}_{\vec{\varphi}})$ change sign at an interaction strength $\mathcal{A}_{\vec{\varphi}} = \frac{2}{2\,n-N}$.

$\mathcal{A}_{\vec{\varphi}} \geq 0$			
$n \leq \frac{N}{2}$	$n > \frac{N}{2}$		
$\mathcal{A}_{\vec{\varphi}} < \infty$	$\mathcal{A}_{\vec{\varphi}} < \frac{2}{2\,n-N}$	$\mathcal{A}_{\vec{\varphi}} = \frac{2}{2\,n-N}$	$\mathcal{A}_{\vec{\varphi}} > \frac{2}{2\,n-N}$
$\chi_n > 0$	$\chi_n > 0$	$\chi_n = 0$	$\chi_n < 0$

Table B.2: Sign analysis of the expectation values $\chi_n(\mathcal{A}_{\vec{\varphi}})$ as a function of ferromagnetic interaction strength $\mathcal{A}_{\vec{\varphi}} \geq 0$ and quantum number n. The entry $\mathcal{A}_{\vec{\varphi}} < \infty$ symbolizes a finite interaction strength.

$\mathcal{A} \geq 0$			
$n \leq \frac{N}{2}$	$n > \frac{N}{2}$		
$\mathcal{A} < \infty$	$\mathcal{A} < \mathcal{A}_n^{\min}$	$\mathcal{A}_n^{\min} \leq \mathcal{A} \leq \mathcal{A}_n^{\max}$	$\mathcal{A} > \mathcal{A}_n^{\max}$
$\nu_{\pm,n}^{(2)} = \mp\nu_{gr}$	$\nu_{\pm,n}^{(2)} = \mp\nu_{gr}$	undefined	$\nu_{\pm,n}^{(2)} = \pm\nu_{gr}$

Table B.3: Winding number ν of the central spin as a function of ferromagnetic interaction strength $\mathcal{A} \geq 0$ and quantum number n. We have introduced minimal/maximal interaction strengths $\mathcal{A}_n^{\min}/\mathcal{A}_n^{\max}$ defined in Eq. (B.9). The entry $\mathcal{A} < \infty$ symbolizes a finite interaction strength.

number ν differs from the topological response for all quantum numbers n. In fact, each energy band produces a time-averaged pumping rate $P_n^{12} = -P_n^{21} = \frac{C_n}{2\pi}\,\omega_1\,\omega_2$ determined by the total Chern number $C_n = (N-2\,n)\,\nu_{gr}$ (cf. Sec. 4.1.3). Considering the quasiadiabatic dynamics confined to an excited energy band $\mathcal{E}^{(2)}_{\pm,n}$, this can lead to a situation where the topological quantization of the local response P_n^{12} exists even though the winding number ν of the central spin is undefined.

The previous observations can be straightforwardly extended to antiferromagnetic interaction strengths $\mathcal{A}_{\vec{\varphi}} \leq 0$ using the property of the expectation values

$$\chi_n(\mathcal{A}_{\vec{\varphi}}) = \chi_{N-n}(-\mathcal{A}_{\vec{\varphi}}).$$

B.4 Antiferromagnetic Interaction Strength

We examine the instantaneous spectrum and the nonequilibrium phase diagrams of the quasiperiodically driven CSM for an antiferromagnetic interaction strength $\mathcal{A} < 0$. Analogous to the ferromagnetic case (see Fig. 4.1(a)), the energy bands (4.15) can be energetically ordered for an antiferromagnetic interaction strength. Fig. B.3 shows the schematic structure of the instantaneous spectrum $\mathcal{E}$ as a function of antiferromagnetic interaction strength $\mathcal{A}_{\vec{\varphi}} \leq 0$. The antiferromagnetic ground state corresponds to $|\mathcal{E}^{(2)}_{-,N-1}\rangle$, followed by low-energy states $|\mathcal{E}^{(2)}_{-,n}\rangle$ with gradually decreasing number n. Note that the number $n = 1, 2, \ldots, N-1$ of flipped spins is again defined with respect to the ferromagnetic state $m_s = -\frac{N}{2}$. The high-energy excited states $|\mathcal{E}^{(2)}_{+,n}\rangle$ are located between the ferromagnetic states $m_s = -\frac{N}{2}$ and $m_s = \frac{N}{2}$, with the latter again separated by the Zeeman energy term equal to 1 (in units of $\lambda\,|\mathbf{d}(\vec{\varphi})|$). We restrict ourselves to gaps

$$\Delta_I(\mathcal{A}_{\vec{\varphi}}) = \mathcal{E}^{(2)}_{-,N-2}(\mathcal{A}_{\vec{\varphi}}) - \mathcal{E}^{(2)}_{-,N-1}(\mathcal{A}_{\vec{\varphi}}),$$
$$\Delta_{II} = \mathcal{E}^{(1)}_{-}(\mathcal{A}_{\vec{\varphi}}) - \mathcal{E}^{(2)}_{-,1}(\mathcal{A}_{\vec{\varphi}}), \quad \Delta_{III}(\mathcal{A}_{\vec{\varphi}}) = \mathcal{E}^{(2)}_{+,1}(\mathcal{A}_{\vec{\varphi}}) - \mathcal{E}^{(1)}_{-}(\mathcal{A}_{\vec{\varphi}}), \quad \text{(B.10)}$$

which are relevant for the formation of the dynamical topological quantum phases in the antiferromagnetic case. For $\mathcal{A}_{\vec{\varphi}} \ll -\frac{2}{N}$, the gaps converge to $\Delta_I \approx \Delta_{III} \approx \frac{1}{N}$ due to collective spin wave excitations, while $\Delta_{II} \propto \mathcal{A}_{\vec{\varphi}}$ indicates that the energy difference between low- $|\mathcal{E}^{(2)}_{-,n}\rangle$ and high-lying states $|\mathcal{E}^{(2)}_{+,n}\rangle$ goes again linearly with the interaction strength $\mathcal{A}_{\vec{\varphi}}$. The corresponding nonequilibrium phase diagrams as a function of antiferromagnetic interaction strength $\mathcal{A} < 0$ and frequency ω are shown in Fig. B.4 for different total numbers of spins N. The numerical methods and associated parameters are chosen as in Fig. 4.5, except that the system is initially prepared in the antiferromagnetic ground state energy band $\mathcal{E}^{(2)}_{-,N-1}$. Provided the quasiadiabatic dynamics is confined to the energy band $\mathcal{E}^{(2)}_{-,N-1}$, the time-averaged pumping rate P^{12} is proportional to the total Chern number $C_{N-1} = (2-N)\,\nu_{gr}$ (red regimes). An ensemble-averaged pumping rate $\bar{P}^{12} = \frac{\nu_{gr}}{2\pi}\,\omega_1\,\omega_2$ (see Eq. (4.33)) identical to the noninteracting case (blue regimes) can be observed for interaction strengths $\mathcal{A}_{\vec{\varphi}} < 0$ that induce energy gaps $\Delta_{II} \ll \Delta_{III}$ (see Fig. B.3): populations in the low-energy bands $\mathcal{E}^{(2)}_{-,n}$ and the ferromagnetic energy band $\mathcal{E}^{(1)}_{-}$ become equal within an intermediate

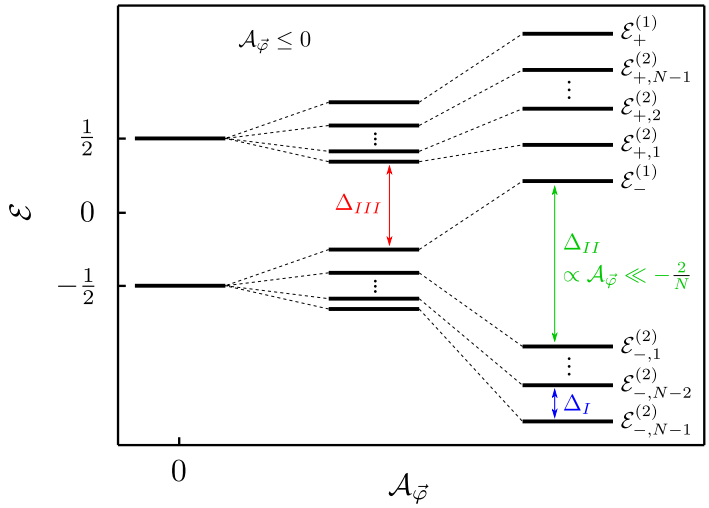

Figure B.3: Spectrum $\mathcal{E}$ as a function of interaction strength $\mathcal{A}_{\vec{\varphi}} \leq 0$. The ground state corresponds to $|\mathcal{E}^{(2)}_{-,N-1}\rangle$, followed by low-energy states $|\mathcal{E}^{(2)}_{-,n}\rangle$ with decreasing number n. High-energy excited states $|\mathcal{E}^{(2)}_{+,n}\rangle$ are located between states $m_s = -\frac{N}{2}$ and $m_s = \frac{N}{2}$, the latter separated by the Zeeman energy term equal to 1 (in units of $\lambda\,|\mathbf{d}(\vec{\varphi})|$). For $\mathcal{A}_{\vec{\varphi}} \ll -\frac{2}{N}$, the low-energy states $|\mathcal{E}^{(2)}_{-,n}\rangle$ are well separated ($\propto \mathcal{A}_{\vec{\varphi}}$) from the other states. Gaps Δ_{I-III} relevant for the nonequilibrium evolution (see Fig. B.4) are schematically illustrated, while gaps $\Delta_{II} = \Delta_{III}$ are exactly the same for an interaction strength $\mathcal{A}_{\vec{\varphi}} = -\frac{2}{N}$. *Reprinted figure with permission from Ref. [KPBT22]. Copyright (2022) by the American Physical Society.*

(pre)thermal regime, while transitions to the high-energy band $\mathcal{E}^{(2)}_{+,1}$ are suppressed. For $\Delta_{II} \gtrapprox \Delta_{III}$, (pre)thermalization immediately leads to a featureless quantum phase with zero time-averaged pumping rate $P^{12} = 0$ (white regimes), as the total Chern numbers sum to $\sum_{n=1}^{N-1} C_n = \sum_{n=0}^{N} C_n = 0$. Gaps $\Delta_{II} = \Delta_{III}$ are exactly the same for $\mathcal{A}_{\vec{\varphi}} = -\frac{2}{N}$, which makes this especially relevant for interaction strengths $\mathcal{A}_{\vec{\varphi}} \ll -\frac{2}{N}$. However, (pre)thermalization into a featureless quantum state can also be observed in general for interaction strengths $\mathcal{A}_{\vec{\varphi}} < 0$ that induce low-energy gaps $\Delta_I \ll \Delta_{II}$, completely independent of gaps Δ_{III}. As in Sec. 4.3.1, the exact dynamics suggests that the leading nonadiabatic excitation processes are approximately covered by critical frequencies $\omega_c \propto \Delta^{\min}_{I-III}$, which is roughly illustrated by assuming a proportionality constant $K = 0.11$ in Fig. B.4 (dashed yellow lines). Again, we have evaluated the gaps Δ_{I-III} of Eq. (B.10) in the origin ($\vec{\varphi} = 0$) of the synthetic 2D BZ, obtaining the minimum band gaps

$$\Delta^{\min}_{I-III}(\mathcal{A}) = \lambda\,|\mathbf{d}(0)|\,\Delta_{I-III}\Big(\frac{\mathcal{A}}{|\mathbf{d}(0)|}\Big).$$

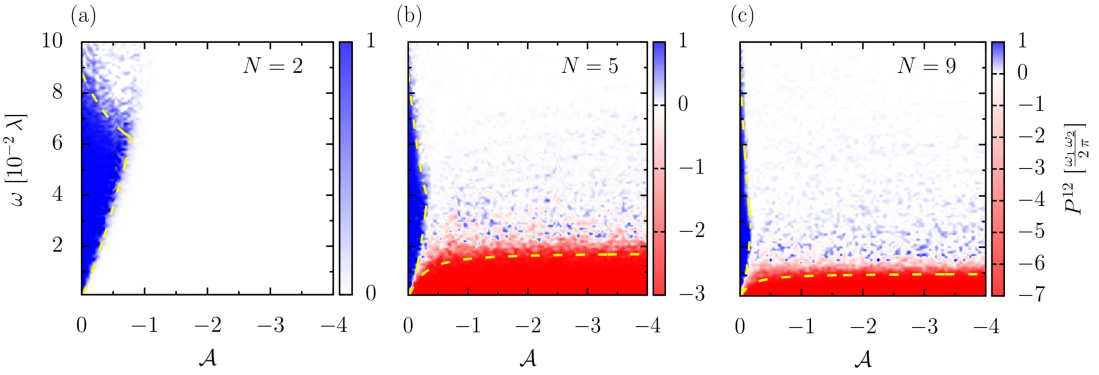

Figure B.4: Nonequilibrium phase diagrams as a function of interaction strength $\mathcal{A} < 0$ and frequencies $\omega_1 = \omega$, $\omega_2 = \gamma\,\omega$ for different total spin numbers N. The system is initially prepared in the antiferromagnetic ground state energy band $\mathcal{E}^{(2)}_{-,N-1}$. Numerical methods and associated parameters are chosen as in Fig. 4.5. Provided the quasiadiabatic dynamics is confined to the energy band $\mathcal{E}^{(2)}_{-,N-1}$, the time-averaged pumping rate P^{12} is proportional to the total Chern number $C_{N-1} = (2-N)\,\nu_{gr}$ (red regimes). Nonadiabatic excitation processes can in turn lead to dynamical transitions to intermediate/featureless quantum phases with pumping rates $\bar{P}^{12} = \frac{\nu_{gr}}{2\,\pi}\,\omega_1\,\omega_2$ (blue regimes)/$P^{12} = 0$ (white regimes). The critical frequencies ω_c scale with the associated gaps (see Fig. B.3), roughly illustrated by phase boundaries $\omega_c = 0.11\,\Delta^{\mathrm{min}}_{I-III}$ (dashed yellow lines). *Reprinted figure with permission from Ref. [KPBT22]. Copyright (2022) by the American Physical Society.*

B.5 Approximated von Neumann Entropy

We propose that the time-averaged von Neumann entropy $\bar{S}^{\mathrm{dy}}(t)$ of Eq. (4.35) provides a proper characterization of the different nonequilibrium quantum phases (I)-(II). We show this by comparing the numerical values of $\bar{S}^{\mathrm{dy}}(t)$ with the phase-averaged von Neumann entropy of the relevant instantaneous state populations of the CSM. Although the latter calculations only account for the instantaneous spectrum, the associated ansatz actually leads to a reasonable approximation of the numerical results of $\bar{S}^{\mathrm{dy}}(t)$ (see Fig. 4.6).

As discussed in Sec. 4.3.2, the strong coupling regime breaks down at some critical time t_c for a finite frequency $\omega \neq 0$. The dynamics then leads to nonadiabatic excitation processes between the energy bands of Eq. (4.15). Starting from the ferromagnetic ground state energy band $\mathcal{E}^{(1)}_{-}$, the breakdown of the prethermal regime occurs in two main stages. (I) The exact quantum state shows equal time-averaged overlaps with the instantaneous eigenstates of the energy bands $\mathcal{E}^{(1)}_{-}$ and $\mathcal{E}^{(2)}_{-,r}$. Considering the instantaneous eigenstates of Eq. (4.16), this situation can be modeled by a linear combination with equal contributions from the associated state vectors:

$$|\psi^{-}_{n}\{\mathcal{A}_{\vec{\varphi}}, \theta^{-}_{1\ldots n}\}\rangle = \frac{1}{\sqrt{n+1}}\left(|\mathcal{E}^{(1)}_{-}\rangle + \sum_{r=1}^{n} \mathrm{e}^{\mathrm{i}\theta^{-}_{r}}\ |\mathcal{E}^{(2)}_{-,r}\rangle\right). \tag{B.11}$$

Within this ansatz, we introduce phases $\theta^{-}_{r} \in [0, 2\pi[$, which can be considered as free parameters of the modulation. The approach of Eq. (B.11) corresponds to the

intermediate dynamical phase (I) for the number $n = N - 1$. Similarly, the remaining phases (IIa) and (IIb) are modulated by linear combinations

$$|\psi_N\{\mathcal{A}_{\vec{\varphi}}, \theta^-_{1\ldots N-1}, \theta_N\}\rangle = \frac{1}{\sqrt{N+1}} \Big(\sqrt{N}\ |\psi^-_{N-1}\{\mathcal{A}_{\vec{\varphi}}, \theta^-_{1\ldots N-1}\}\rangle + \mathrm{e}^{\mathrm{i}\theta_N}\ |\mathcal{E}^{(1)}_+\rangle \Big), \quad \text{(B.12)}$$

and

$$|\psi^+_n\{\mathcal{A}_{\vec{\varphi}}, \theta^-_{1\ldots N-1}, \theta_N, \theta^+_{n\ldots N-1}\}\rangle = \frac{1}{\sqrt{2N+1-n}} \times \\ \times \Big(\sqrt{N+1}\ |\psi_N\{\mathcal{A}_{\vec{\varphi}}, \theta^-_{1\ldots N-1}, \theta_N\}\rangle + \sum_{r=n}^{N-1} \mathrm{e}^{\mathrm{i}\theta^+_r}\ |\mathcal{E}^{(2)}_{+,r}\rangle \Big), \quad \text{(B.13)}$$

where we introduce the additional phases $\theta_N \in [0, 2\pi[$, $\theta^+_r \in [0, 2\pi[$. In Eq. (B.13), the "infinite-temperature" state (IIb) corresponds to the quantum number $n = 1$.

We analytically derive the von Neumann entropy of the central spin for the instantaneous state populations of Eqs. (B.11), (B.12) and (B.13):

$$\mathcal{S}\{\mathcal{A}_{\vec{\varphi}}, \boldsymbol{\theta}\} = -\,\mathrm{Tr}_0 \Big[\hat{\varrho}_0\{\mathcal{A}_{\vec{\varphi}}, \boldsymbol{\theta}\}\ \ln\big(\hat{\varrho}_0\{\mathcal{A}_{\vec{\varphi}}, \boldsymbol{\theta}\}\big) \Big], \quad \text{(B.14)}$$

where Tr_0 denotes the trace acting on the central spin-1/2 and ln the natural matrix logarithm. We have introduced the reduced density matrix of the central spin-1/2

$$\hat{\varrho}_0\{\mathcal{A}_{\vec{\varphi}}, \boldsymbol{\theta}\} = \mathrm{Tr}_{\hat{\mathbf{J}}} \left[|\psi\{\mathcal{A}_{\vec{\varphi}}, \boldsymbol{\theta}\}\rangle\langle\psi\{\mathcal{A}_{\vec{\varphi}}, \boldsymbol{\theta}\}| \right] = \frac{1}{2} \left(\mathbb{1} + \mathbf{u}\{\mathcal{A}_{\vec{\varphi}}, \boldsymbol{\theta}\}\, \hat{\boldsymbol{\sigma}}' \right) \quad \text{(B.15)}$$

by tracing out the environmental spins $\hat{\mathbf{J}}$ of the host material (denoted as $\mathrm{Tr}_{\hat{\mathbf{J}}}$). The reduced density matrix of Eq. (B.15) is parametrized by vectors $\mathbf{u}\{\mathcal{A}_{\vec{\varphi}}, \boldsymbol{\theta}\}$ that explicitly depend on the interaction strength $\mathcal{A}_{\vec{\varphi}}$ and set of phases $\boldsymbol{\theta}$, which contain the associated parameters $\{\theta^-_r,\ \theta_N,\ \theta^+_r\}$ of Eqs. (B.11), (B.12) and (B.13). Analytical expressions for $\mathbf{u}\{\mathcal{A}_{\vec{\varphi}}, \boldsymbol{\theta}\}$ are derived using the property of the partial trace

$$\mathrm{Tr}_{\hat{\mathbf{J}}} \Big[|m_{s_0}, m_j\rangle\langle\tilde{m}_{s_0}, \tilde{m}_j| \Big] = |m_{s_0}\rangle\langle\tilde{m}_{s_0}|\ \delta_{m_j,\tilde{m}_j},$$

the instantaneous eigenstates derived in Eq. (4.16), and the nonvanishing matrix elements within the rotated basis $\{|+\tfrac{1}{2}\rangle, |-\tfrac{1}{2}\rangle\}$ of the central spin-1/2:

$$\mathrm{Tr}_{\hat{\mathbf{J}}} \Big[|\mathcal{E}^{(1)}_\pm\rangle\langle\mathcal{E}^{(1)}_\pm| \Big] = \frac{1}{2} \Big(\mathbb{1} \pm \hat{\sigma}^{z'} \Big), \quad \text{(B.16)}$$

$$\mathrm{Tr}_{\hat{\mathbf{J}}} \Big[|\mathcal{E}^{(1)}_-\rangle\langle\mathcal{E}^{(2)}_{\pm,r}| \Big] = \sqrt{\frac{1 \pm \chi_r}{2}}\ \frac{\hat{\sigma}^{x'} - \mathrm{i}\,\hat{\sigma}^{y'}}{2}\ \delta_{r,1}, \quad \text{(B.17)}$$

$$\mathrm{Tr}_{\hat{\mathbf{J}}} \Big[|\mathcal{E}^{(1)}_+\rangle\langle\mathcal{E}^{(2)}_{\pm,r}| \Big] = \mp\sqrt{\frac{1 \mp \chi_r}{2}}\ \frac{\hat{\sigma}^{x'} + \mathrm{i}\,\hat{\sigma}^{y'}}{2}\ \delta_{r,N-1}, \quad \text{(B.18)}$$

$$\mathrm{Tr}_{\hat{\mathbf{J}}} \Big[|\mathcal{E}^{(2)}_{\pm,r}\rangle\langle\mathcal{E}^{(2)}_{\pm,v}| \Big] = \frac{1}{2} \Big(\mathbb{1} \pm \chi_r\, \hat{\sigma}^{z'} \Big)\, \delta_{r,v} \mp \\ \mp \sqrt{\frac{1 \pm \chi_r}{2}} \sqrt{\frac{1 \mp \chi_v}{2}}\ \frac{\hat{\sigma}^{x'} + \mathrm{i}\,\hat{\sigma}^{y'}}{2}\ \delta_{v,r-1} \mp \sqrt{\frac{1 \mp \chi_r}{2}} \sqrt{\frac{1 \pm \chi_v}{2}}\ \frac{\hat{\sigma}^{x'} - \mathrm{i}\,\hat{\sigma}^{y'}}{2}\ \delta_{v,r+1}, \quad \text{(B.19)}$$

$$\mathrm{Tr}_{\hat{\mathbf{j}}}\left[\,|\mathcal{E}^{(2)}_{\pm,r}\rangle\langle\mathcal{E}^{(2)}_{\mp,v}|\,\right] = \frac{\sqrt{1-\chi_r^2}}{2}\,\hat{\sigma}^{z'}\,\delta_{r,v}\pm$$
$$\pm\sqrt{\frac{1\pm\chi_r}{2}}\sqrt{\frac{1\pm\chi_v}{2}}\,\frac{\hat{\sigma}^{x'}+\mathrm{i}\,\hat{\sigma}^{y'}}{2}\,\delta_{v,r-1}\mp\sqrt{\frac{1\mp\chi_r}{2}}\sqrt{\frac{1\mp\chi_v}{2}}\,\frac{\hat{\sigma}^{x'}-\mathrm{i}\,\hat{\sigma}^{y'}}{2}\,\delta_{v,r+1}. \quad \text{(B.20)}$$

The matrix elements illustrate which combinations of the instantaneous eigenstates of Eq. (4.16) contribute to the von Neumann entropy $\mathcal{S}\{\mathcal{A}_{\vec{\varphi}},\boldsymbol{\theta}\}$ of Eq. (B.14). Performing the calculations for the linear combination (B.11), we obtain

$$\mathbf{u}^-_n\{\mathcal{A}_{\vec{\varphi}},\theta^-_{1\ldots n}\} = \frac{1}{n+1}\left[\sqrt{2\,(1-\chi_1)}\begin{pmatrix}\cos(\theta^-_1)\\-\sin(\theta^-_1)\\0\end{pmatrix}+\right.$$
$$\left.+\sum_{r=1}^{n-1}\sqrt{(1+\chi_r)\,(1-\chi_{r+1})}\begin{pmatrix}\cos(\theta^-_{r+1}-\theta^-_r)\\-\sin(\theta^-_{r+1}-\theta^-_r)\\0\end{pmatrix}-(1+n\,\bar{\chi}_n)\begin{pmatrix}0\\0\\1\end{pmatrix}\right], \quad \text{(B.21)}$$

where we introduce the summarized expectation value $\bar{\chi}_n = \frac{1}{n}\sum_{r=1}^{n}\chi_r$. The first term of Eq. (B.21) stems from the lower solution of the off-diagonal matrix elements (B.17), which arise from overlaps between the instantaneous eigenstates $|\mathcal{E}^{(1)}_-\rangle$ and $|\mathcal{E}^{(2)}_{-,1}\rangle$. The second term originates from the lower solution of the off-diagonal matrix elements (B.19), which correspond to overlaps between neighboring low-energy states $|\mathcal{E}^{(2)}_{-,r}\rangle$ and $|\mathcal{E}^{(2)}_{-,r+1}\rangle$. The last term is obtained from the lower solutions of the diagonal matrix elements (B.16) and (B.19), taking into account the direct contributions of the instantaneous eigenstates $|\mathcal{E}^{(1)}_-\rangle$ and $|\mathcal{E}^{(2)}_{-,r}\rangle$. Similarly, we derive the analytical expression

$$\mathbf{u}_N\{\mathcal{A}_{\vec{\varphi}},\theta^-_{1\ldots N-1},\theta_N\} = \frac{1}{N+1}\left[N\,\mathbf{u}^-_{N-1}\{\mathcal{A}_{\vec{\varphi}},\theta^-_{1\ldots N-1}\}+\right.$$
$$\left.+\sqrt{2\,(1+\chi_{N-1})}\begin{pmatrix}\cos(\theta_N-\theta^-_{N-1})\\-\sin(\theta_N-\theta^-_{N-1})\\0\end{pmatrix}+\begin{pmatrix}0\\0\\1\end{pmatrix}\right] \quad \text{(B.22)}$$

for the linear combination (B.12). The first term of Eq. (B.22) results from the contributions of the intermediate dynamical phase (I). The second term originates from the lower solution of the off-diagonal matrix elements (B.18), which take into account the overlaps between the instantaneous eigenstates $|\mathcal{E}^{(2)}_{-,N-1}\rangle$ and $|\mathcal{E}^{(1)}_+\rangle$. The last term represents the direct contribution of the instantaneous eigenstate $|\mathcal{E}^{(1)}_+\rangle$, given by the upper solution of the diagonal matrix elements (B.16). For the linear combination

(B.13), further calculations lead to

$$\begin{aligned}\mathbf{u}_n^+\{\mathcal{A}_{\vec{\varphi}},\theta^-_{1\ldots N-1},\theta_N,\theta^+_{n\ldots N-1}\} = \frac{1}{2N+1-n}\Bigg[&(N+1)\,\mathbf{u}_N\{\mathcal{A}_{\vec{\varphi}},\theta^-_{1\ldots N-1},\theta_N\}+\\ &+\sqrt{2\,(1+\chi_1)}\,\delta_{n,1}\begin{pmatrix}\cos(\theta_1^+)\\-\sin(\theta_1^+)\\0\end{pmatrix}-\sqrt{2\,(1-\chi_{N-1})}\begin{pmatrix}\cos(\theta_N-\theta^+_{N-1})\\-\sin(\theta_N-\theta^+_{N-1})\\0\end{pmatrix}+\\ &+(1-\delta_{n,1})\sum_{r=n}^{N-1}\sqrt{(1+\chi_r)\,(1+\chi_{r-1})}\begin{pmatrix}\cos(\theta_r^+-\theta_{r-1}^-)\\-\sin(\theta_r^+-\theta_{r-1}^-)\\0\end{pmatrix}+\\ &+\delta_{n,1}\sum_{r=2}^{N-1}\sqrt{(1+\chi_r)\,(1+\chi_{r-1})}\begin{pmatrix}\cos(\theta_r^+-\theta_{r-1}^-)\\-\sin(\theta_r^+-\theta_{r-1}^-)\\0\end{pmatrix}-\\ &-\sum_{r=n}^{N-2}\Bigg[\sqrt{(1-\chi_r)\,(1-\chi_{r+1})}\begin{pmatrix}\cos(\theta_{r+1}^--\theta_r^+)\\-\sin(\theta_{r+1}^--\theta_r^+)\\0\end{pmatrix}+\\ &+\sqrt{(1-\chi_r)\,(1+\chi_{r+1})}\begin{pmatrix}\cos(\theta_{r+1}^+-\theta_r^+)\\-\sin(\theta_{r+1}^+-\theta_r^+)\\0\end{pmatrix}\Bigg]+\\ &+\Big(2\sum_{r=n}^{N-1}\sqrt{1-\chi_r^2}\,\cos(\theta_r^--\theta_r^+)+(N-n)\,\underline{\chi}_n\Big)\begin{pmatrix}0\\0\\1\end{pmatrix}\Bigg],\end{aligned}\tag{B.23}$$

with the summarized expectation value $\underline{\chi}_n = \frac{1}{N-n}\sum_{r=n}^{N-1}\chi_r$. The individual terms of Eq. (B.23) can be interpreted analogously to Eqs. (B.21) and (B.22), while additional overlaps between low- $|\mathcal{E}^{(2)}_{-,r}\rangle$ and high-energy states $|\mathcal{E}^{(2)}_{+,v}\rangle$ result in diagonal and off-diagonal contributions originating from the matrix elements (B.20).

After calculating the von Neumann entropy $\mathcal{S}\{\mathcal{A}_{\vec{\varphi}},\boldsymbol{\theta}\}$ of Eq. (B.14) for the instantaneous state populations of Eqs. (B.11), (B.12) and (B.13), we exploit the following idea: (pre)thermalization leads to a sampling of all possible phase combinations during the nonequilibrium dynamics. The time-averaged von Neumann entropy $\bar{S}^{\mathrm{dy}}(t)$ of Eq. (4.35) can then be approximated by selecting the relevant instantaneous state population and integrating (B.14) along the set of phases $\boldsymbol{\theta}$:

$$\bar{\mathcal{S}}(\mathcal{A}) = \frac{1}{(2\pi)^{p+2}}\iint_0^{2\pi}\mathrm{d}^2\vec{\varphi}\int\cdots\int_0^{2\pi}\mathrm{d}^p\boldsymbol{\theta}\,\mathcal{S}\Big\{\frac{\mathcal{A}}{|\mathbf{d}(\vec{\varphi})|},\boldsymbol{\theta}\Big\}.\tag{B.24}$$

We have introduced the number $p\in\mathbb{N}$, which corresponds to the dimension of the phase vector $\boldsymbol{\theta}$ containing the parameters $\{\theta_r^-,\,\theta_N,\,\theta_r^+\}$ of Eqs. (B.11), (B.12) and (B.13). In Eq. (B.24), we have additionally integrated along the phases of the ($\vec{\varphi}$-dependent) interaction strength $\mathcal{A}_{\vec{\varphi}} = \mathcal{A}/|\mathbf{d}(\vec{\varphi})|$, which accounts for the sampling of the synthetic 2D BZ during the time-evolution of the quantum state. In Fig. B.5, the phase-averaged von Neumann entropy $\bar{\mathcal{S}}(\mathcal{A})$ of Eq. (B.24) is shown as a function of ferromagnetic interaction strength $\mathcal{A}>0$ for different total numbers of spins N. We have performed

the integration numerically, and have chosen the mass parameter $M = 1.2$ as in the main text. We have calculated the phase-averaged von Neumann entropy $\bar{\mathcal{S}}(\mathcal{A})$ for the different instantaneous state populations of Eqs. (B.11), (B.12) and (B.13): blue/green lines correspond to linear combinations (B.11)/(B.13), the red line corresponds to the linear combination (B.12). The solid lines of Fig. B.5 then represent the different dynamical stages (I)-(II). Assuming that the relevant instantaneous state population is selected, the numerical values of the time-averaged von Neumann entropy $\bar{S}^{\mathrm{dy}}(t)$ of Eq. (4.35) are reasonably approximated by the phase-averaged von Neumann entropy $\bar{\mathcal{S}}(\mathcal{A})$ of Eq. (B.24). This, in turn, suggests that $\bar{S}^{\mathrm{dy}}(t)$ provides a proper characterization of the different nonequilibrium quantum phases (I)-(II). We have used that the von Neumann entropy of Eq. (B.14) is invariant under the transformation defined in Eq. (4.3).

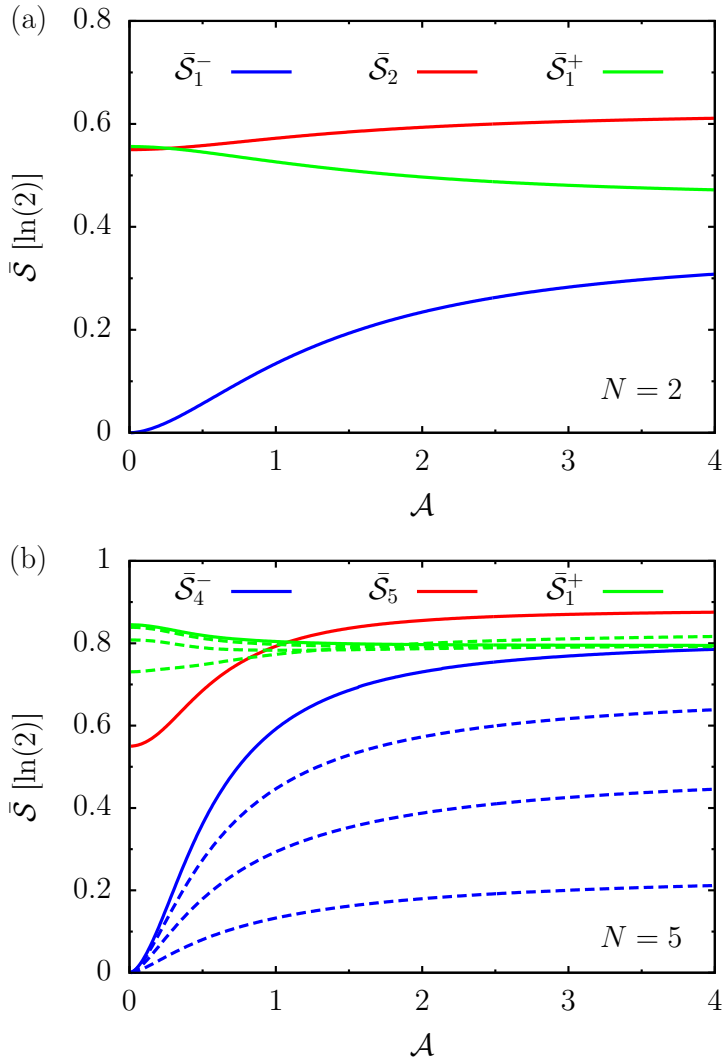

Figure B.5: Phase-averaged von Neumann entropy $\bar{\mathcal{S}}(\mathcal{A})$ as a function of ferromagnetic interaction strength $\mathcal{A} > 0$ and total numbers of spins (a) $N = 2$ and (b) $N = 5$. The integration has been performed numerically, and a mass parameter $M = 1.2$ has been chosen as in the main text. The phase-averaged von Neumann entropy $\bar{\mathcal{S}}(\mathcal{A})$ is calculated for the different instantaneous state populations of Eqs. (B.11), (B.12) and (B.13): blue/green lines correspond to linear combinations (B.11)/(B.13), the red line corresponds to the linear combination (B.12). Solid lines then represent the different dynamical stages (I)-(II). Once the relevant instantaneous state population is selected, the time-averaged von Neumann entropy $\bar{S}^{\mathrm{dy}}(t)$ of Eq. (4.35) is reasonably approximated by the phase-averaged von Neumann entropy $\bar{\mathcal{S}}(\mathcal{A})$. This, in turn, suggests that $\bar{S}^{\mathrm{dy}}(t)$ provides an appropriate characterization of the different nonequilibrium quantum phases (I)-(II).

Acronyms

APT	*adiabatic perturbation theory*
BZ	*Brillouin zone*
CSM	*central spin model*
HSP	*high-symmetry point*
IVP	*initial value problem*
LDE	*linear differential equation*
NV	*nitrogen-vacancy*
QD	*quantum dot*
TBGE	*topological burning glass effect*
TFC	*topological frequency converter*
ITFC	*interacting topological frequency converter*

Bibliography

[AABS19] D. A. Abanin, E. Altman, I. Bloch, and M. Serbyn. *Colloquium: Many-body localization, thermalization, and entanglement.* Rev. Mod. Phys. **91**, 021001 (2019). doi:10.1103/RevModPhys.91.021001. [p. 87]

[AB59] E. Adams and E. Blount. *Energy bands in the presence of an external force field—II: Anomalous velocities.* J. Phys. Chem. Solids **10**, 286 (1959). doi:10.1016/0022-3697(59)90004-6. [p. 29]

[AM76] N. W. Ashcroft and N. D. Mermin. *Solid State Physics.* Holt, Rinehart and Winston, New York (1976). [pp. 2, 6, 14, 18, 21, 26, 29, 30]

[AMV18] N. P. Armitage, E. J. Mele, and A. Vishwanath. *Weyl and Dirac semimetals in three-dimensional solids.* Rev. Mod. Phys. **90**, 015001 (2018). doi:10.1103/RevModPhys.90.015001. [p. 2]

[Awr14] J. Awrejcewicz. *Ordinary Differential Equations and Mechanical Systems.* Springer, Cham (2014). [pp. 14, 15]

[Bal15] L. E. Ballentine. *Quantum Mechanics: a modern development.* World Scientific, New Jersey, 2nd ed. (2015). [pp. 11, 48, 62]

[BBK+13] C.-E. Bardyn, M. A. Baranov, C. V. Kraus, E. Rico, A. İmamoğlu, P. Zoller, and S. Diehl. *Topology by dissipation.* New Journal of Physics **15**, 085001 (2013). doi:10.1088/1367-2630/15/8/085001. [p. 105]

[BBP04] H.-P. Breuer, D. Burgarth, and F. Petruccione. *Non-Markovian dynamics in a spin star system: Exact solution and approximation techniques.* Phys. Rev. B **70**, 045323 (2004). doi:10.1103/PhysRevB.70.045323. [pp. 63, 65]

[BCCS20] E. Boyers, P. J. D. Crowley, A. Chandran, and A. O. Sushkov. *Exploring 2D Synthetic Quantum Hall Physics with a Quasiperiodically Driven Qubit.* Phys. Rev. Lett. **125**, 160505 (2020). doi:10.1103/PhysRevLett.125.160505. [pp. 3, 4, 46, 86]

[BCOR09] S. Blanes, F. Casas, J. Oteo, and J. Ros. *The Magnus expansion and some of its applications.* Phys. Rep. **470**, 151 (2009). doi:10.1016/j.physrep.2008.11.001. [p. 20]

[BD15] J. C. Budich and S. Diehl. *Topology of density matrices.* Phys. Rev. B **91**, 165140 (2015). doi:10.1103/PhysRevB.91.165140. [p. 105]

[BDP15] M. Bukov, L. D'Alessio, and A. Polkovnikov. *Universal high-frequency behavior of periodically driven systems: from dynamical stabilization to Floquet engineering.* Advances in Physics **64**, 139 (2015). doi:10.1080/00018732.2015.1055918. [pp. 14, 19, 20, 24]

[Ber84] M. V. Berry. *Quantal phase factors accompanying adiabatic changes.* Proc. R. Soc. London, Ser. A **392**, 45 (1984). doi:10.1098/rspa.1984.0023. [pp. 2, 6, 7, 9, 12, 26, 27, 30]

[BES13] B. M. Brown, M. S. P. Eastham, and K. M. Schmidt. *Periodic Differential Operators.* Birkhäuser, Basel (2013). [pp. 14, 15, 16]

[BF28] M. Born and V. Fock. *Beweis des Adiabatensatzes.* Z. Phys. **51**, 165 (1928). doi:10.1007/BF01343193. [pp. 7, 8, 9]

[BFT+15] B. Bertrand, H. Flentje, S. Takada, M. Yamamoto, S. Tarucha, A. Ludwig, A. D. Wieck, C. Bäuerle, and T. Meunier. *Quantum Manipulation of Two-Electron Spin States in Isolated Double Quantum Dots.* Phys. Rev. Lett. **115**, 096801 (2015). doi:10.1103/PhysRevLett.115.096801. [pp. 36, 47, 59, 86]

[BH13] B. A. Bernevig and T. L. Hughes. *Topological Insulators and Topological Superconductors.* Princeton University Press, Princeton, NJ (2013). [pp. 2, 20]

[BHZ06] B. A. Bernevig, T. L. Hughes, and S.-C. Zhang. *Quantum Spin Hall Effect and Topological Phase Transition in HgTe Quantum Wells.* Science **314**, 1757 (2006). doi:10.1126/science.1133734. [pp. 3, 20, 36, 37, 39]

[Blo29] F. Bloch. *Über die Quantenmechanik der Elektronen in Kristallgittern.* Z. Phys. **52**, 555 (1929). doi:10.1007/BF01339455. [pp. 2, 6, 12, 14, 18, 21, 26, 29, 30]

[Blo62] E. Blount. *Formalisms of Band Theory.* Solid State Phys. **13**, 305 (1962). doi:10.1016/S0081-1947(08)60459-2. [p. 29]

[BMK+03] A. Bohm, A. Mostafazadeh, H. Koizumi, Q. Niu, and J. Zwanziger. *The Geometric Phase in Quantum Systems.* Springer, Berlin (2003). [pp. 6, 13, 30]

[BNT+09] G. Balasubramanian, P. Neumann, D. Twitchen, M. Markham, R. Kolesov, N. Mizuochi, J. Isoya, J. Achard, J. Beck, J. Tissler, V. Jacques, P. R. Hemmer, F. Jelezko, and J. Wrachtrup. *Ultralong spin coherence time in isotopically engineered diamond.* Nat. Mater. **8** (2009). doi:10.1038/nmat2420. [p. 61]

[BZ06] B. A. Bernevig and S.-C. Zhang. *Quantum Spin Hall Effect.* Phys. Rev. Lett. **96**, 106802 (2006). doi:10.1103/PhysRevLett.96.106802. [p. 20]

[BZD15] J. C. Budich, P. Zoller, and S. Diehl. *Dissipative preparation of Chern insulators.* Phys. Rev. A **91**, 042117 (2015). doi:10.1103/PhysRevA.91.042117. [p. 105]

[CB09] W. A. Coish and J. Baugh. *Nuclear spins in nanostructures.* Phys. Stat. Sol. (B) **246**, 2203 (2009). doi:10.1002/pssb.200945229. [pp. 59, 60]

[CDBF19] P. W. Claeys, C. Dimo, S. D. Baerdemacker, and A. Faribault. *Integrable spin-1/2 Richardson-Gaudin XYZ models in an arbitrary magnetic field*. J. Phys. A **52**, 08LT01 (2019). doi:10.1088/1751-8121/aafe9b. [pp. 3, 58, 59, 61]

[CDS19] N. R. Cooper, J. Dalibard, and I. B. Spielman. *Topological bands for ultracold atoms*. Rev. Mod. Phys. **91**, 015005 (2019). doi:10.1103/RevModPhys.91.015005. [pp. 2, 14, 19]

[CDSM13] J. Cayssol, B. Dóra, F. Simon, and R. Moessner. *Floquet topological insulators*. Phys. Status Solidi RRL **7**, 101 (2013). doi:10.1002/pssr.201206451. [pp. 2, 14, 19, 24]

[CF21] J. Cayssol and J. N. Fuchs. *Topological and geometrical aspects of band theory*. J. Phys.: Materials **4**, 034007 (2021). doi:10.1088/2515-7639/abf0b5. [pp. 2, 6, 12, 29, 33, 58]

[Che46] S. S. Chern. *Characteristic Classes of Hermitian Manifolds*. Annals of Mathematics **47**, 85 (1946). doi:10.2307/1969037. [pp. 2, 20, 33, 42]

[Chi99] C. Chicone. *Ordinary Differential Equations with Applications*. Springer, New York (1999). [pp. 14, 15, 16]

[CLM22] C.-Z. Chang, C.-X. Liu, and A. H. MacDonald. *Colloquium: Quantum anomalous Hall effect*. arXiv:2202.13902 (2022). doi:10.48550/arXiv.2202.13902. [pp. 37, 39]

[CLY+20] Q. Chen, H. Liu, M. Yu, S. Zhang, and J. Cai. *Dynamical decoupling for realization of topological frequency conversion*. Phys. Rev. A **102**, 052606 (2020). doi:10.1103/PhysRevA.102.052606. [pp. 3, 46]

[CMC19] P. J. D. Crowley, I. Martin, and A. Chandran. *Topological classification of quasiperiodically driven quantum systems*. Phys. Rev. B **99**, 064306 (2019). doi:10.1103/PhysRevB.99.064306. [pp. 3, 46]

[CMC20] P. J. D. Crowley, I. Martin, and A. Chandran. *Half-Integer Quantized Topological Response in Quasiperiodically Driven Quantum Systems*. Phys. Rev. Lett. **125**, 100601 (2020). doi:10.1103/PhysRevLett.125.100601. [pp. 3, 46]

[CN95] M.-C. Chang and Q. Niu. *Berry Phase, Hyperorbits, and the Hofstadter Spectrum*. Phys. Rev. Lett. **75**, 1348 (1995). doi:10.1103/PhysRevLett.75.1348. [pp. 6, 13, 26, 29, 30]

[CN96] M.-C. Chang and Q. Niu. *Berry phase, hyperorbits, and the Hofstadter spectrum: Semiclassical dynamics in magnetic Bloch bands*. Phys. Rev. B **53**, 7010 (1996). doi:10.1103/PhysRevB.53.7010. [pp. 6, 13, 26, 29, 30]

[Con08] L. Conlon. *Differentiable Manifolds*. Birkhäuser, Boston, 2nd ed. (2008). [p. 13]

[COR01] F. Casas, J. A. Oteo, and J. Ros. *Floquet theory: exponential perturbative treatment.* J. Phys. A: Math. Gen. **34**, 3379 (2001). doi:10.1088/0305-4470/34/16/305. [p. 20]

[CPSP19] P. W. Claeys, M. Pandey, D. Sels, and A. Polkovnikov. *Floquet-Engineering Counterdiabatic Protocols in Quantum Many-Body Systems.* Phys. Rev. Lett. **123**, 090602 (2019). doi:10.1103/PhysRevLett.123.090602. [p. 86]

[Cro89] F. H. Croom. *Principles of Topology.* Saunders College Publishing, Philadelphia (1989). [p. 1]

[CSDF+21] A. Chatterjee, P. Stevenson, S. De Franceschi, A. Morello, N. P. de Leon, and F. Kuemmeth. *Semiconductor qubits in practice.* Nat. Rev. Phys. **3**, 157 (2021). doi:10.1038/s42254-021-00283-9. [pp. 4, 38, 58, 59, 61]

[CT04] S.-I. Chu and D. A. Telnov. *Beyond the Floquet theorem: generalized Floquet formalisms and quasienergy methods for atomic and molecular multiphoton processes in intense laser fields.* Phys. Rep. **390**, 1 (2004). doi:10.1016/j.physrep.2003.10.001. [pp. 3, 6, 13, 26, 27]

[CW08] J. Clarke and F. K. Wilhelm. *Superconducting quantum bits.* Nature **453**, 1031 (2008). doi:10.1038/nature07128. [p. 38]

[dC13] A. del Campo. *Shortcuts to Adiabaticity by Counterdiabatic Driving.* Phys. Rev. Lett. **111**, 100502 (2013). doi:10.1103/PhysRevLett.111.100502. [p. 86]

[DGJbuO11] J. Dalibard, F. Gerbier, G. Juzeliūnas, and P. Öhberg. *Colloquium: Artificial gauge potentials for neutral atoms.* Rev. Mod. Phys. **83**, 1523 (2011). doi:10.1103/RevModPhys.83.1523. [p. 2]

[DiV00] D. P. DiVincenzo. *The Physical Implementation of Quantum Computation.* Fortschr. Phys. **48**, 771 (2000). doi:10.1002/1521-3978(200009)48:9/11¡771::AID-PROP771¿3.0.CO;2-E. [pp. 59, 60]

[DMD+13] M. W. Doherty, N. B. Manson, P. Delaney, F. Jelezko, J. Wrachtrup, and L. C. Hollenberg. *The nitrogen-vacancy colour centre in diamond.* Phys. Rep. **528**, 1 (2013). doi:10.1016/j.physrep.2013.02.001. [pp. 4, 38, 58, 59, 61]

[DPS04] J. Dukelsky, S. Pittel, and G. Sierra. *Colloquium: Exactly solvable Richardson-Gaudin models for many-body quantum systems.* Rev. Mod. Phys. **76**, 643 (2004). doi:10.1103/RevModPhys.76.643. [pp. 3, 58, 59, 61]

[DR03] M. Demirplak and S. A. Rice. *Adiabatic Population Transfer with Control Fields.* J. Phys. Chem. A **107**, 9937 (2003). doi:10.1021/jp030708a. [p. 86]

[DR05] M. Demirplak and S. A. Rice. *Assisted Adiabatic Passage Revisited.* J. Phys. Chem. B **109**, 6838 (2005). doi:10.1021/jp040647w. [p. 86]

[DR14] L. D'Alessio and M. Rigol. *Long-time Behavior of Isolated Periodically Driven Interacting Lattice Systems.* Phys. Rev. X **4**, 041048 (2014). doi:10.1103/PhysRevX.4.041048. [p. 24]

[DRBZ11] S. Diehl, E. Rico, M. A. Baranov, and P. Zoller. *Topology by dissipation in atomic quantum wires.* Nature Physics **7**, 971 (2011). doi:10.1038/nphys2106. [p. 105]

[EA15] A. Eckardt and E. Anisimovas. *High-frequency approximation for periodically driven quantum systems from a Floquet-space perspective.* New J. Phys. **17**, 093039 (2015). doi:10.1088/1367-2630/17/9/093039. [pp. 3, 6, 13, 14, 18, 19, 20, 22, 23, 24, 26, 27, 37]

[Eck17] A. Eckardt. *Colloquium: Atomic quantum gases in periodically driven optical lattices.* Rev. Mod. Phys. **89**, 011004 (2017). doi:10.1103/RevModPhys.89.011004. [pp. 14, 18, 19, 22, 23, 24, 37]

[Ehr27] P. Ehrenfest. *Bemerkung über die angenäherte Gültigkeit der klassischen Mechanik innerhalb der Quantenmechanik.* Zeitschrift für Physik **45**, 455 (1927). doi:10.1007/BF01329203. [pp. 11, 48, 62]

[EJ96] A. Ekert and R. Jozsa. *Quantum computation and Shor's factoring algorithm.* Rev. Mod. Phys. **68**, 733 (1996). doi:10.1103/RevModPhys.68.733. [pp. 59, 60]

[Eul36] L. Euler. *Solutio problematis ad geometriam situs pertinentis.* Commentarii Academiae Scientiarum Imperialis Petropolitanae **8**, 128 (1736). URL `https://archive.org/details/commentariiacade08impe/page/128/mode/2up`. [p. 1]

[Fed69] H. Federer. *Geometric Measure Theory.* Springer, Berlin (1969). [p. 42]

[Flo83] G. Floquet. *Sur les équations différentielles linéaires à coefficients périodiques.* Ann. École Norm. Sup. **12**, 47 (1883). doi:10.24033/asens.220. [pp. 4, 6, 14, 16]

[Foc28] V. Fock. *Über die Beziehung zwischen den Integralen der quantenmechanischen Bewegungsgleichungen und der Schrödingerschen Wellengleichung.* Z. Phys. **49**, 323 (1928). doi:10.1007/BF01337922. [p. 9]

[FSC+20] G. Frank, Z. Scherübl, S. Csonka, G. Zaránd, and A. Pályi. *Magnetic degeneracy points in interacting two-spin systems: Geometrical patterns, topological charge distributions, and their stability.* Phys. Rev. B **101**, 245409 (2020). doi:10.1103/PhysRevB.101.245409. [pp. 47, 86]

[FVV+22] G. Frank, D. Varjas, P. Vrana, G. Pintér, and A. Pályi. *Topological charge distributions of an interacting two-spin system.* Phys. Rev. B **105**, 035414 (2022). doi:10.1103/PhysRevB.105.035414. [pp. 47, 86]

[Gau76] M. Gaudin. *Diagonalisation d'une classe d'hamiltoniens de spin.* J. Phys. France **37**, 1087 (1976). doi:10.1051/jphys:0197600370100108700. [pp. 3, 58, 59, 61]

[GBZ16] N. Goldman, J. C. Budich, and P. Zoller. *Topological quantum matter with ultracold gases in optical lattices.* Nat. Phys. **12**, 639 (2016). doi:10.1038/nphys3803. [pp. 2, 14, 19]

[GD14] N. Goldman and J. Dalibard. *Periodically Driven Quantum Systems: Effective Hamiltonians and Engineered Gauge Fields.* Phys. Rev. X **4**, 031027 (2014). doi:10.1103/PhysRevX.4.031027. [pp. 19, 24]

[GH98] M. Grifoni and P. Hänggi. *Driven quantum tunneling.* Phys. Rep. **304**, 229 (1998). doi:10.1016/S0370-1573(98)00022-2. [pp. 14, 18, 22, 23]

[GJÖS14] N. Goldman, G. Juzeliūnas, P. Öhberg, and I. B. Spielman. *Light-induced gauge fields for ultracold atoms.* Rep. Prog. Phys. **77**, 126401 (2014). doi:10.1088/0034-4885/77/12/126401. [pp. 2, 14, 19]

[GP12] V. Gritsev and A. Polkovnikov. *Dynamical quantum Hall effect in the parameter space.* Proceedings of the National Academy of Sciences **109**, 6457 (2012). doi:10.1073/pnas.1116693109. [pp. 4, 6, 7, 11, 12]

[Gri13] D. J. Griffiths. *Introduction to Electrodynamics.* Pearson, Boston, 4th ed. (2013). [p. 13]

[Gro97] L. K. Grover. *Quantum Mechanics Helps in Searching for a Needle in a Haystack.* Phys. Rev. Lett. **79**, 325 (1997). doi:10.1103/PhysRevLett.79.325. [pp. 59, 60]

[GS18] D. J. Griffiths and D. F. Schroeter. *Introduction to Quantum Mechanics.* Cambridge University Press, Cambridge, 3rd ed. (2018). [pp. 7, 11, 17, 26, 44, 47, 48, 62]

[Hal88] F. D. M. Haldane. *Model for a Quantum Hall Effect without Landau Levels: Condensed-Matter Realization of the "Parity Anomaly".* Phys. Rev. Lett. **61**, 2015 (1988). doi:10.1103/PhysRevLett.61.2015. [pp. 2, 3, 6, 20, 33, 36, 37, 39, 58]

[Hal15] B. C. Hall. *Lie Groups, Lie Algebras, and Representations.* Springer, Cham, 2nd ed. (2015). [p. 15]

[HCT83] T.-S. Ho, S.-I. Chu, and J. V. Tietz. *Semiclassical many-mode floquet theory.* Chem. Phys. Lett. **96**, 464 (1983). doi:10.1016/0009-2614(83)80732-5. [pp. 3, 6, 13, 26, 27]

[HK10] M. Z. Hasan and C. L. Kane. *Colloquium: Topological insulators.* Rev. Mod. Phys. **82**, 3045 (2010). doi:10.1103/RevModPhys.82.3045. [pp. 2, 20]

[HKP+07] R. Hanson, L. P. Kouwenhoven, J. R. Petta, S. Tarucha, and L. M. K. Vandersypen. *Spins in few-electron quantum dots.* Rev. Mod. Phys. **79**, 1217 (2007). doi:10.1103/RevModPhys.79.1217. [pp. 4, 38, 58, 59, 60, 61]

[Hol16] M. Holthaus. *Floquet engineering with quasienergy bands of periodically driven optical lattices.* J. Phys. B: At. Mol. Opt. Phys. **49**, 013001 (2016). doi:10.1088/0953-4075/49/1/013001. [pp. 14, 18, 19, 22, 24]

[HZB16] Y. Hu, P. Zoller, and J. C. Budich. *Dynamical Buildup of a Quantized Hall Response from Nontopological States.* Phys. Rev. Lett. **117**, 126803 (2016). doi:10.1103/PhysRevLett.117.126803. [p. 105]

[JMD+14] G. Jotzu, M. Messer, R. Desbuquois, M. Lebrat, T. Uehlinger, D. Greif, and T. Esslinger. *Experimental realization of the topological Haldane model with ultracold fermions.* Nature **515**, 237 (2014). doi:10.1038/nature13915. [p. 20]

[JNM02] T. Jungwirth, Q. Niu, and A. H. MacDonald. *Anomalous Hall Effect in Ferromagnetic Semiconductors.* Phys. Rev. Lett. **88**, 207208 (2002). doi:10.1103/PhysRevLett.88.207208. [pp. 29, 39]

[JW06] F. Jelezko and J. Wrachtrup. *Single defect centres in diamond: A review.* Phys. Stat. Sol. (A) **203**, 3207 (2006). doi:10.1002/pssa.200671403. [pp. 4, 38, 58, 59, 61]

[Kat50] T. Kato. *On the Adiabatic Theorem of Quantum Mechanics.* J. Phys. Soc. Jpn. **5**, 435 (1950). doi:10.1143/JPSJ.5.435. [pp. 7, 8]

[KAT01] L. P. Kouwenhoven, D. G. Austing, and S. Tarucha. *Few-electron quantum dots.* Rep. Prog. Phys. **64**, 701 (2001). doi:10.1088/0034-4885/64/6/201. [pp. 4, 38, 58, 59, 60, 61]

[KBRD10] T. Kitagawa, E. Berg, M. Rudner, and E. Demler. *Topological characterization of periodically driven quantum systems.* Phys. Rev. B **82**, 235114 (2010). doi:10.1103/PhysRevB.82.235114. [pp. 20, 21]

[KBWM+08] M. König, H. Buhmann, L. W. Molenkamp, T. Hughes, C.-X. Liu, X.-L. Qi, and S.-C. Zhang. *The Quantum Spin Hall Effect: Theory and Experiment.* J. Phys. Soc. Jpn. **77**, 031007 (2008). doi:10.1143/JPSJ.77.031007. [pp. 2, 20]

[KDP80] K. v. Klitzing, G. Dorda, and M. Pepper. *New Method for High-Accuracy Determination of the Fine-Structure Constant Based on Quantized Hall Resistance.* Phys. Rev. Lett. **45**, 494 (1980). doi:10.1103/PhysRevLett.45.494. [pp. 2, 25, 32, 33, 58]

[Kit71] C. Kittel. *Introduction to Solid State Physics.* Wiley, New York, NY, 4th ed. (1971). [pp. 2, 6, 14, 18, 21, 26, 29, 30]

[KL54] R. Karplus and J. M. Luttinger. *Hall Effect in Ferromagnetics*. Phys. Rev. **95**, 1154 (1954). doi:10.1103/PhysRev.95.1154. [p. 29]

[KL57] W. Kohn and J. M. Luttinger. *Quantum Theory of Electrical Transport Phenomena*. Phys. Rev. **108**, 590 (1957). doi:10.1103/PhysRev.108.590. [p. 29]

[KL13] C. Kloeffel and D. Loss. *Prospects for Spin-Based Quantum Computing in Quantum Dots*. Annu. Rev. Condens. Matter Phys. **4**, 51 (2013). doi:10.1146/annurev-conmatphys-030212-184248. [pp. 59, 60, 61]

[KLR+12] Y. E. Kraus, Y. Lahini, Z. Ringel, M. Verbin, and O. Zilberberg. *Topological States and Adiabatic Pumping in Quasicrystals*. Phys. Rev. Lett. **109**, 106402 (2012). doi:10.1103/PhysRevLett.109.106402. [p. 3]

[KM05a] C. L. Kane and E. J. Mele. *Quantum Spin Hall Effect in Graphene*. Phys. Rev. Lett. **95**, 226801 (2005a). doi:10.1103/PhysRevLett.95.226801. [p. 20]

[KM05b] C. L. Kane and E. J. Mele. *Z_2 Topological Order and the Quantum Spin Hall Effect*. Phys. Rev. Lett. **95**, 146802 (2005b). doi:10.1103/PhysRevLett.95.146802. [p. 20]

[KNG+18] M. H. Kolodrubetz, F. Nathan, S. Gazit, T. Morimoto, and J. E. Moore. *Topological Floquet-Thouless Energy Pump*. Phys. Rev. Lett. **120**, 150601 (2018). doi:10.1103/PhysRevLett.120.150601. [pp. 3, 46]

[KOB+11] T. Kitagawa, T. Oka, A. Brataas, L. Fu, and E. Demler. *Transport properties of nonequilibrium systems under the application of light: Photoinduced quantum Hall insulators without Landau levels*. Phys. Rev. B **84**, 235108 (2011). doi:10.1103/PhysRevB.84.235108. [p. 20]

[Koh85] M. Kohmoto. *Topological invariant and the quantization of the Hall conductance*. Ann. Phys. **160**, 343 (1985). doi:10.1016/0003-4916(85)90148-4. [pp. 2, 6, 33, 58]

[KP08] S. G. Krantz and H. R. Parks. *Geometric Integration Theory*. Birkhäuser, Boston (2008). [p. 42]

[KPBT20] S. Körber, L. Privitera, J. C. Budich, and B. Trauzettel. *Interacting topological frequency converter*. Phys. Rev. Research **2**, 022023(R) (2020). doi:10.1103/PhysRevResearch.2.022023. [pp. 3, 34, 36, 47, 48, 50, 51, 52, 54, 92, 95, 98]

[KPBT22] S. Körber, L. Privitera, J. C. Budich, and B. Trauzettel. *Topological burning glass effect*. Phys. Rev. B **106**, L140304 (2022). doi:10.1103/PhysRevB.106.L140304. [pp. 3, 34, 58, 59, 67, 71, 72, 78, 79, 80, 100, 102, 108, 109]

[KRZ13] Y. E. Kraus, Z. Ringel, and O. Zilberberg. *Four-Dimensional Quantum Hall Effect in a Two-Dimensional Quasicrystal*. Phys. Rev. Lett. **111**, 226401 (2013). doi:10.1103/PhysRevLett.111.226401. [p. 3]

[KS17] A. B. Khanikaev and G. Shvets. *Two-dimensional topological photonics*. Nat. Photonics **11**, 763 (2017). doi:10.1038/s41566-017-0048-5. [p. 2]

[Kub57] R. Kubo. *Statistical-Mechanical Theory of Irreversible Processes. I. General Theory and Simple Applications to Magnetic and Conduction Problems*. J. Phys. Soc. Jpn. **12**, 570 (1957). doi:10.1143/JPSJ.12.570. [pp. 2, 6, 26, 33, 58]

[KWB+07] M. König, S. Wiedmann, C. Brüne, A. Roth, H. Buhmann, L. W. Molenkamp, X.-L. Qi, and S.-C. Zhang. *Quantum spin Hall insulator state in HgTe quantum wells*. Science **318**, 766 (2007). doi:10.1126/science.1148047. [p. 20]

[Lau81] R. B. Laughlin. *Quantized Hall conductivity in two dimensions*. Phys. Rev. B **23**, 5632 (1981). doi:10.1103/PhysRevB.23.5632. [pp. 2, 6, 33, 58]

[LCC21] D. M. Long, P. J. D. Crowley, and A. Chandran. *Nonadiabatic Topological Energy Pumps with Quasiperiodic Driving*. Phys. Rev. Lett. **126**, 106805 (2021). doi:10.1103/PhysRevLett.126.106805. [pp. 3, 46]

[LCC22] D. M. Long, P. J. D. Crowley, and A. Chandran. *Many-body localization with quasiperiodic driving*. Phys. Rev. B **105**, 144204 (2022). doi:10.1103/PhysRevB.105.144204. [p. 87]

[LD98] D. Loss and D. P. DiVincenzo. *Quantum computation with quantum dots*. Phys. Rev. A **57**, 120 (1998). doi:10.1103/PhysRevA.57.120. [pp. 59, 60]

[LDM14] A. Lazarides, A. Das, and R. Moessner. *Equilibrium states of generic quantum systems subject to periodic driving*. Phys. Rev. E **90**, 012110 (2014). doi:10.1103/PhysRevE.90.012110. [p. 24]

[LDM15] A. Lazarides, A. Das, and R. Moessner. *Fate of Many-Body Localization Under Periodic Driving*. Phys. Rev. Lett. **115**, 030402 (2015). doi:10.1103/PhysRevLett.115.030402. [p. 87]

[Lee13] J. M. Lee. *Introduction to Smooth Manifolds*. Springer, New York, 2nd ed. (2013). [p. 13]

[LJS14] L. Lu, J. D. Joannopoulos, and M. Soljačić. *Topological photonics*. Nat. Photonics **8**, 821 (2014). doi:10.1038/nphoton.2014.248. [p. 2]

[LRG11] N. H. Lindner, G. Refael, and V. Galitski. *Floquet topological insulator in semiconductor quantum wells*. Nat. Phys. **7**, 490 (2011). doi:10.1038/nphys1926. [p. 20]

[LSP+18] M. Lohse, C. Schweizer, H. M. Price, O. Zilberberg, and I. Bloch. *Exploring 4D quantum Hall physics with a 2D topological charge pump.* Nature **553**, 55 (2018). doi:10.1038/nature25000. [p. 3]

[LSZ+16] M. Lohse, C. Schweizer, O. Zilberberg, M. Aidelsburger, and I. Bloch. *A Thouless quantum pump with ultracold bosonic atoms in an optical superlattice.* Nat. Phys. **12**, 350 (2016). doi:10.1038/nphys3584. [p. 3]

[LZQ16] C.-X. Liu, S.-C. Zhang, and X.-L. Qi. *The Quantum Anomalous Hall Effect: Theory and Experiment.* Annual Review of Condensed Matter Physics **7**, 301 (2016). doi:10.1146/annurev-conmatphys-031115-011417. [pp. 37, 39]

[Mah00] G. D. Mahan. *Many-Particle Physics.* Kluwer, Boston, 3rd ed. (2000). [pp. 2, 6, 26, 33, 58]

[Mes62] A. Messiah. *Quantum Mechanics*, vol. 2. North-Holland, Amsterdam (1962). [pp. 7, 8]

[Moo10] J. E. Moore. *The birth of topological insulators.* Nature **464**, 194 (2010). doi:10.1038/nature08916. [pp. 2, 20]

[Mor16] F. Morgan. *Geometric Measure Theory: a beginner's guide.* Academic Press, Amsterdam, 5th ed. (2016). [p. 42]

[MRH17] I. Martin, G. Refael, and B. Halperin. *Topological Frequency Conversion in Strongly Driven Quantum Systems.* Phys. Rev. X **7**, 041008 (2017). doi:10.1103/PhysRevX.7.041008. [pp. 3, 6, 14, 26, 27, 29, 30, 33, 34, 36, 37, 39, 53]

[MS21] D. Malz and A. Smith. *Topological Two-Dimensional Floquet Lattice on a Single Superconducting Qubit.* Phys. Rev. Lett. **126**, 163602 (2021). doi:10.1103/PhysRevLett.126.163602. [pp. 3, 4, 46, 77, 86]

[MSS01] Y. Makhlin, G. Schön, and A. Shnirman. *Quantum-state engineering with Josephson-junction devices.* Rev. Mod. Phys. **73**, 357 (2001). doi:10.1103/RevModPhys.73.357. [p. 38]

[MSS+20] J. W. McIver, B. Schulte, F.-U. Stein, T. Matsuyama, G. Jotzu, G. Meier, and A. Cavalleri. *Light-induced anomalous Hall effect in graphene.* Nat. Phys. **16**, 38 (2020). doi:10.1038/s41567-019-0698-y. [p. 20]

[Mun00] J. R. Munkres. *Topology.* Prentice-Hall, Upper Saddle River, NJ, 2nd ed. (2000). [p. 1]

[NC10] M. A. Nielsen and I. L. Chuang. *Quantum Computation and Quantum Information.* Cambridge University Press, Cambridge, 10th anniversary ed. (2010). [pp. 37, 40, 51, 58, 59, 60, 74, 75, 82, 105]

[NGG+21] F. Nathan, R. Ge, S. Gazit, M. Rudner, and M. Kolodrubetz. *Quasiperiodic Floquet-Thouless Energy Pump*. Phys. Rev. Lett. **127**, 166804 (2021). doi:10.1103/PhysRevLett.127.166804. [pp. 3, 46]

[NH15] R. Nandkishore and D. A. Huse. *Many-Body Localization and Thermalization in Quantum Statistical Mechanics*. Annual Review of Condensed Matter Physics **6**, 15 (2015). doi:10.1146/annurev-conmatphys-031214-014726. [p. 87]

[NMR19] F. Nathan, I. Martin, and G. Refael. *Topological frequency conversion in a driven dissipative quantum cavity*. Phys. Rev. B **99**, 094311 (2019). doi:10.1103/PhysRevB.99.094311. [pp. 3, 37, 46]

[NMR22] F. Nathan, I. Martin, and G. Refael. *Topological frequency conversion in Weyl semimetals*. arXiv:2201.07804 (2022). doi:10.48550/arXiv.2201.07804. [p. 86]

[NRRM20] F. Nathan, G. Refael, M. S. Rudner, and I. Martin. *Quantum frequency locking and downconversion in a driven qubit-cavity system*. Phys. Rev. Research **2**, 043411 (2020). doi:10.1103/PhysRevResearch.2.043411. [pp. 3, 37, 46]

[NSO+10] N. Nagaosa, J. Sinova, S. Onoda, A. H. MacDonald, and N. P. Ong. *Anomalous Hall effect*. Rev. Mod. Phys. **82**, 1539 (2010). doi:10.1103/RevModPhys.82.1539. [pp. 29, 39]

[NTT+16] S. Nakajima, T. Tomita, S. Taie, T. Ichinose, H. Ozawa, L. Wang, M. Troyer, and Y. Takahashi. *Topological Thouless pumping of ultracold fermions*. Nat. Phys. **12**, 296 (2016). doi:10.1038/nphys3622. [p. 3]

[OA09] T. Oka and H. Aoki. *Photovoltaic Hall effect in graphene*. Phys. Rev. B **79**, 081406(R) (2009). doi:10.1103/PhysRevB.79.081406. [p. 20]

[OK19] T. Oka and S. Kitamura. *Floquet Engineering of Quantum Materials*. Annual Review of Condensed Matter Physics **10**, 387 (2019). doi:10.1146/annurev-conmatphys-031218-013423. [pp. 2, 14, 19, 24, 25]

[OP19] T. Ozawa and H. M. Price. *Topological quantum matter in synthetic dimensions*. Nat. Rev. Phys. **1**, 349 (2019). doi:10.1038/s42254-019-0045-3. [p. 2]

[OPA+19] T. Ozawa, H. M. Price, A. Amo, N. Goldman, M. Hafezi, L. Lu, M. C. Rechtsman, D. Schuster, J. Simon, O. Zilberberg, and I. Carusotto. *Topological photonics*. Rev. Mod. Phys. **91**, 015006 (2019). doi:10.1103/RevModPhys.91.015006. [p. 2]

[OPG+16] T. Ozawa, H. M. Price, N. Goldman, O. Zilberberg, and I. Carusotto. *Synthetic dimensions in integrated photonics: From optical isolation to*

four-dimensional quantum Hall physics. Phys. Rev. A **93**, 043827 (2016). doi:10.1103/PhysRevA.93.043827. [p. 2]

[PG90] R. E. Prange and S. M. Girvin. *The Quantum Hall Effect*. Springer, New York, 2nd ed. (1990). [pp. 2, 25, 32, 33, 58]

[PJT+05] J. R. Petta, A. C. Johnson, J. M. Taylor, E. A. Laird, A. Yacoby, M. D. Lukin, C. M. Marcus, M. P. Hanson, and A. C. Gossard. *Coherent Manipulation of Coupled Electron Spins in Semiconductor Quantum Dots*. Science **309**, 2180 (2005). doi:10.1126/science.1116955. [pp. 36, 47, 59, 86]

[PPacHA15] P. Ponte, Z. Papić, F. m. c. Huveneers, and D. A. Abanin. *Many-Body Localization in Periodically Driven Systems*. Phys. Rev. Lett. **114**, 140401 (2015). doi:10.1103/PhysRevLett.114.140401. [p. 87]

[PR18] Y. Peng and G. Refael. *Topological energy conversion through the bulk or the boundary of driven systems*. Phys. Rev. B **97**, 134303 (2018). doi:10.1103/PhysRevB.97.134303. [pp. 3, 46]

[PR21] C. Psaroudaki and G. Refael. *Photon pumping in a weakly-driven quantum cavity–spin system*. Annals of Physics **435**, 168553 (2021). doi:10.1016/j.aop.2021.168553. [pp. 3, 37, 46]

[PZO+15] H. M. Price, O. Zilberberg, T. Ozawa, I. Carusotto, and N. Goldman. *Four-Dimensional Quantum Hall Effect with Ultracold Atoms*. Phys. Rev. Lett. **115**, 195303 (2015). doi:10.1103/PhysRevLett.115.195303. [p. 2]

[QHZ08] X.-L. Qi, T. L. Hughes, and S.-C. Zhang. *Topological field theory of time-reversal invariant insulators*. Phys. Rev. B **78**, 195424 (2008). doi:10.1103/PhysRevB.78.195424. [pp. 2, 4, 20, 33, 36, 37, 39, 40, 42]

[QRP21] Z. Qi, G. Refael, and Y. Peng. *Universal nonadiabatic energy pumping in a quasiperiodically driven extended system*. Phys. Rev. B **104**, 224301 (2021). doi:10.1103/PhysRevB.104.224301. [pp. 3, 46]

[QWZ06] X.-L. Qi, Y.-S. Wu, and S.-C. Zhang. *Topological quantization of the spin Hall effect in two-dimensional paramagnetic semiconductors*. Phys. Rev. B **74**, 085308 (2006). doi:10.1103/PhysRevB.74.085308. [pp. 3, 4, 20, 36, 37, 39, 40]

[QZ10] X.-L. Qi and S.-C. Zhang. *The quantum spin Hall effect and topological insulators*. Physics Today **63**, 33 (2010). doi:10.1063/1.3293411. [pp. 2, 20]

[QZ11] X.-L. Qi and S.-C. Zhang. *Topological insulators and superconductors*. Rev. Mod. Phys. **83**, 1057 (2011). doi:10.1103/RevModPhys.83.1057. [pp. 2, 20]

[Res00] R. Resta. *Manifestations of Berry's phase in molecules and condensed matter*. J. Phys.: Condens. Matter **12**, R107 (2000). doi:10.1088/0953-8984/12/9/201. [pp. 9, 13]

[RGB+11] A. Rozhkov, G. Giavaras, Y. P. Bliokh, V. Freilikher, and F. Nori. *Electronic properties of mesoscopic graphene structures: Charge confinement and control of spin and charge transport*. Phys. Rep. **503**, 77 (2011). doi:10.1016/j.physrep.2011.02.002. [pp. 60, 61]

[RL20a] M. S. Rudner and N. H. Lindner. *Band structure engineering and non-equilibrium dynamics in Floquet topological insulators*. Nat. Rev. Phys. **2**, 229 (2020a). doi:10.1038/s42254-020-0170-z. [pp. 2, 14, 19, 24, 87]

[RL20b] M. S. Rudner and N. H. Lindner. *The Floquet Engineer's Handbook*. arXiv:2003.08252 (2020b). doi:10.48550/arXiv.2003.08252. [pp. 14, 23, 24, 37]

[RLBL13] M. S. Rudner, N. H. Lindner, E. Berg, and M. Levin. *Anomalous Edge States and the Bulk-Edge Correspondence for Periodically Driven Two-Dimensional Systems*. Phys. Rev. X **3**, 031005 (2013). doi:10.1103/PhysRevX.3.031005. [pp. 20, 21]

[RNC+14] P. Roushan, C. Neill, Y. Chen, M. Kolodrubetz, C. Quintana, N. Leung, M. Fang, R. Barends, B. Campbell, Z. Chen, B. Chiaro, A. Dunsworth, E. Jeffrey, J. Kelly, A. Megrant, J. Mutus, P. J. J. O'Malley, D. Sank, A. Vainsencher, J. Wenner, T. White, A. Polkovnikov, A. N. Cleland, and J. M. Martinis. *Observation of topological transitions in interacting quantum circuits*. Nature **515**, 241 (2014). doi:10.1038/nature13891. [pp. 4, 36, 47, 77, 86]

[ROP08] G. Rigolin, G. Ortiz, and V. H. Ponce. *Beyond the quantum adiabatic approximation: Adiabatic perturbation theory*. Phys. Rev. A **78**, 052508 (2008). doi:10.1103/PhysRevA.78.052508. [pp. 4, 6, 7, 10, 11]

[RT10] P. Recher and B. Trauzettel. *Quantum dots and spin qubits in graphene*. Nanotechnology **21**, 302001 (2010). doi:10.1088/0957-4484/21/30/302001. [pp. 4, 38, 58, 59, 60, 61]

[RZP+13] M. C. Rechtsman, J. M. Zeuner, Y. Plotnik, Y. Lumer, D. Podolsky, F. Dreisow, S. Nolte, M. Segev, and A. Szameit. *Photonic Floquet topological insulators*. Nature **496**, 196 (2013). doi:10.1038/nature12066. [p. 20]

[Sam73] H. Sambe. *Steady States and Quasienergies of a Quantum-Mechanical System in an Oscillating Field*. Phys. Rev. A **7**, 2203 (1973). doi:10.1103/PhysRevA.7.2203. [pp. 4, 6, 14, 22, 23]

[Sch26] E. Schrödinger. *An Undulatory Theory of the Mechanics of Atoms and Molecules*. Phys. Rev. **28**, 1049 (1926). doi:10.1103/PhysRev.28.1049. [pp. 7, 17, 26, 44]

[Sch07] F. Schwabl. *Quantum Mechanics*. Springer, Berlin, 4th ed. (2007). [pp. 11, 37, 47]

[SCLD14] R. Schirhagl, K. Chang, M. Loretz, and C. L. Degen. *Nitrogen-Vacancy Centers in Diamond: Nanoscale Sensors for Physics and Biology*. Annu. Rev. Phys. Chem. **65**, 83 (2014). doi:10.1146/annurev-physchem-040513-103659. [pp. 4, 38, 58, 59, 61]

[SG08] R. J. Schoelkopf and S. M. Girvin. *Wiring up quantum systems*. Nature **451**, 664 (2008). doi:10.1038/451664a. [p. 38]

[Sha08] R. Shankar. *Principles of Quantum Mechanics*. Springer, New York, 2nd ed. (2008). [pp. 7, 17, 26, 37, 44, 47]

[Shi65] J. H. Shirley. *Solution of the Schrödinger Equation with a Hamiltonian Periodic in Time*. Phys. Rev. **138**, B979 (1965). doi:10.1103/PhysRev.138.B979. [pp. 4, 6, 14, 19, 24]

[Sho94] P. W. Shor. Algorithms for quantum computation: discrete logarithms and factoring. In *Proceedings 35th Annual Symposium on Foundations of Computer Science*, page 124 (1994). doi:10.1109/SFCS.1994.365700. [pp. 59, 60]

[Sid13] T. C. Sideris. *Ordinary Differential Equations and Dynamical Systems*. Atlantis Press, Amsterdam (2013). [pp. 14, 15, 16]

[Sim83a] B. Simon. *Holonomy, the Quantum Adiabatic Theorem, and Berry's Phase*. Phys. Rev. Lett. **51**, 2167 (1983a). doi:10.1103/PhysRevLett.51.2167. [pp. 2, 6, 33, 58]

[Sim83b] L. Simon. *Lectures on Geometric Measure Theory*, vol. 3. Proc. Centre Math. Anal. Austral. Nat. Univ., Canberra: Australien National University, Centre for Mathematical Analysis (1983b). [p. 42]

[SKK+14] M. D. Schroer, M. H. Kolodrubetz, W. F. Kindel, M. Sandberg, J. Gao, M. R. Vissers, D. P. Pappas, A. Polkovnikov, and K. W. Lehnert. *Measuring a Topological Transition in an Artificial Spin-1/2 System*. Phys. Rev. Lett. **113**, 050402 (2014). doi:10.1103/PhysRevLett.113.050402. [pp. 4, 36, 47, 77, 86]

[SKL03] J. Schliemann, A. Khaetskii, and D. Loss. *Electron spin dynamics in quantum dots and related nanostructures due to hyperfine interaction with nuclei*. J. Phys.: Condens. Matter **15**, R1809 (2003). doi:10.1088/0953-8984/15/50/r01. [pp. 59, 60, 61]

[SN99] G. Sundaram and Q. Niu. *Wave-packet dynamics in slowly perturbed crystals: Gradient corrections and Berry-phase effects*. Phys. Rev. B **59**, 14915 (1999). doi:10.1103/PhysRevB.59.14915. [pp. 6, 13, 26, 29, 30]

[SN21] J. J. Sakurai and J. Napolitano. *Modern Quantum Mechanics*. Cambridge University Press, Cambridge, 3rd ed. (2021). [pp. 11, 37]

[SPF+19] Z. Scherübl, A. Pályi, G. Frank, I. E. Lukács, G. Fülöp, B. Fülöp, J. Nygård, K. Watanabe, T. Taniguchi, G. Zaránd, and S. Csonka. *Observation of spin–orbit coupling induced Weyl points in a two-electron double quantum dot*. Commun. Phys. **2**, 108 (2019). doi:10.1038/s42005-019-0200-2. [pp. 36, 47, 59, 86]

[SYZ22] K. Schwennicke and J. Yuen-Zhou. *Enantioselective Topological Frequency Conversion*. J. Phys. Chem. Lett. **13**, 2434 (2022). doi:10.1021/acs.jpclett.1c04161. [pp. 3, 46]

[TBLB07] B. Trauzettel, D. V. Bulaev, D. Loss, and G. Burkard. *Spin qubits in graphene quantum dots*. Nat. Phys. **3**, 192 (2007). doi:10.1038/nphys544. [pp. 60, 61]

[TBR+16] P. Titum, E. Berg, M. S. Rudner, G. Refael, and N. H. Lindner. *Anomalous Floquet-Anderson Insulator as a Nonadiabatic Quantized Charge Pump*. Phys. Rev. X **6**, 021013 (2016). doi:10.1103/PhysRevX.6.021013. [pp. 20, 21]

[Tes12] G. Teschl. *Ordinary Differential Equations and Dynamical Systems*. American Mathematical Society, Providence, R.I. (2012). [pp. 14, 15, 16]

[Tho83] D. J. Thouless. *Quantization of particle transport*. Phys. Rev. B **27**, 6083 (1983). doi:10.1103/PhysRevB.27.6083. [pp. 2, 25, 36]

[Tho98] D. J. Thouless. *Topological Quantum Numbers in Nonrelativistic Physics*. World Scientific, Singapore (1998). [pp. 2, 13, 32, 33, 58]

[TKNdN82] D. J. Thouless, M. Kohmoto, M. P. Nightingale, and M. den Nijs. *Quantized Hall Conductance in a Two-Dimensional Periodic Potential*. Phys. Rev. Lett. **49**, 405 (1982). doi:10.1103/PhysRevLett.49.405. [pp. 2, 6, 20, 25, 33, 42, 58]

[TLAR03] A. M. Tyryshkin, S. A. Lyon, A. V. Astashkin, and A. M. Raitsimring. *Electron spin relaxation times of phosphorus donors in silicon*. Phys. Rev. B **68**, 193207 (2003). doi:10.1103/PhysRevB.68.193207. [p. 61]

[UMA+13] B. Urbaszek, X. Marie, T. Amand, O. Krebs, P. Voisin, P. Maletinsky, A. Högele, and A. Imamoglu. *Nuclear spin physics in quantum dots: An optical investigation*. Rev. Mod. Phys. **85**, 79 (2013). doi:10.1103/RevModPhys.85.79. [pp. 59, 60, 61]

[Van18] D. Vanderbilt. *Berry Phases in Electronic Structure Theory*. Cambridge University Press, Cambridge (2018). [pp. 2, 6, 13, 30, 33, 58]

[VCC20] T. Villazon, A. Chandran, and P. W. Claeys. *Integrability and dark states in an anisotropic central spin model*. Phys. Rev. Research **2**, 032052 (2020). doi:10.1103/PhysRevResearch.2.032052. [p. 59]

[VCP+20] T. Villazon, P. W. Claeys, M. Pandey, A. Polkovnikov, and A. Chandran. *Persistent dark states in anisotropic central spin models*. Sci. Rep. **10**, 16080 (2020). doi:10.1038/s41598-020-73015-1. [p. 59]

[Vol03] G. E. Volovik. *The Universe in a Helium Droplet*. Oxford University Press (2003). [pp. 2, 4, 36, 37, 39, 40]

[VPM16] A. Verdeny, J. Puig, and F. Mintert. *Quasi-Periodically Driven Quantum Systems*. Z. Naturforsch. A **71**, 897 (2016). doi:10.1515/zna-2016-0079. [pp. 3, 6, 13, 26, 27]

[Wan60] G. H. Wannier. *Wave Functions and Effective Hamiltonian for Bloch Electrons in an Electric Field*. Phys. Rev. **117**, 432 (1960). doi:10.1103/PhysRev.117.432. [p. 25]

[Wan62] G. H. Wannier. *Dynamics of Band Electrons in Electric and Magnetic Fields*. Rev. Mod. Phys. **34**, 645 (1962). doi:10.1103/RevModPhys.34.645. [p. 25]

[WBD+17] P. Weinberg, M. Bukov, L. D'Alessio, A. Polkovnikov, S. Vajna, and M. Kolodrubetz. *Adiabatic perturbation theory and geometry of periodically-driven systems*. Phys. Rep. **688**, 1 (2017). doi:10.1016/j.physrep.2017.05.003. [pp. 4, 6, 7, 10, 11, 12]

[Wen17] X.-G. Wen. *Colloquium: Zoo of quantum-topological phases of matter*. Rev. Mod. Phys. **89**, 041004 (2017). doi:10.1103/RevModPhys.89.041004. [pp. 2, 13, 32]

[Wil70] S. Willard. *General Topology*. Addison Wesley Longman Publishing Co, Reading, Massachusetts (1970). [p. 1]

[Wil11] C. P. Williams. *Explorations in Quantum Computing*. Springer, London, 2nd ed. (2011). [pp. 59, 60]

[WM02] J. Wesenberg and K. Mølmer. *Mixed collective states of many spins*. Phys. Rev. A **65**, 062304 (2002). doi:10.1103/PhysRevA.65.062304. [pp. 63, 65]

[WYH+15] H. Weng, R. Yu, X. Hu, X. Dai, and Z. Fang. *Quantum anomalous Hall effect and related topological electronic states*. Advances in Physics **64**, 227 (2015). doi:10.1080/00018732.2015.1068524. [pp. 37, 39]

[XCN10] D. Xiao, M.-C. Chang, and Q. Niu. *Berry phase effects on electronic properties*. Rev. Mod. Phys. **82**, 1959 (2010). doi:10.1103/RevModPhys.82.1959. [pp. 2, 6, 7, 9, 12, 13, 29, 30, 33, 58]

[YF17] B. Yan and C. Felser. *Topological Materials: Weyl Semimetals*. Annual Review of Condensed Matter Physics **8**, 337 (2017). doi:10.1146/annurev-conmatphys-031016-025458. [p. 2]

[YN05] J. Q. You and F. Nori. *Superconducting Circuits and Quantum Information*. Physics Today **58**, 42 (2005). doi:10.1063/1.2155757. [p. 38]

[ZDM+13] F. A. Zwanenburg, A. S. Dzurak, A. Morello, M. Y. Simmons, L. C. L. Hollenberg, G. Klimeck, S. Rogge, S. N. Coppersmith, and M. A. Eriksson. *Silicon quantum electronics*. Rev. Mod. Phys. **85**, 961 (2013). doi:10.1103/RevModPhys.85.961. [pp. 4, 38, 58, 59, 61]

[ZHG+18] O. Zilberberg, S. Huang, J. Guglielmon, M. Wang, K. P. Chen, Y. E. Kraus, and M. C. Rechtsman. *Photonic topological boundary pumping as a probe of 4D quantum Hall physics*. Nature **553**, 59 (2018). doi:10.1038/nature25011. [p. 3]

[ZMKM22] H. Zhao, F. Mintert, J. Knolle, and R. Moessner. *Localization persisting under aperiodic driving*. Phys. Rev. B **105**, L220202 (2022). doi:10.1103/PhysRevB.105.L220202. [p. 87]

Acknowledgements

First and foremost, I would like to thank my supervisor Björn Trauzettel, from whose outstanding and comprehensive expertise in the field of mesoscopic physics I have learned a lot over the past years. Due to your keen perception, you were always able to provide me with new inspiration for my scientific work, while giving me a free hand in pursuing my own research interests. Especially, I would like to emphasize your professional and at the same time cordial leadership, so that I always enjoyed going to university. Moreover, I am very grateful that you gave me the opportunity to participate in various international conferences and schools, such as the wonderful Capri Spring School or the ENB meeting in the small and lovely town of Brixen.

I would also like to express my special thanks to Lorenzo Privitera, who paved the way for my research topic and provided me with significant support during the first years of my PhD. It was a great pleasure to work with you, and I am very appreciative to learn about Floquet physics from such a capable and kind physicist. Particularly at the beginning, you took a lot of time to guide me through the programming codes, which allowed me to perform the necessary numerical simulations as well as to discover my passion for coding. Even though you left academia, you continued to support and motivate me whenever I became frustrated. This is not something that can be taken for granted, thank you very much for that.

Further, it was a great honor to collaborate with Jan Carl Budich, whose extraordinary expertise in the field of open quantum systems contributed significantly to the interpretation of our results. It was fascinating to see that you always asked the right questions, even though I didn't notice it at first glance. With your wealth of experience and exceptional verbosity, you have greatly improved our manuscripts.

A general thanks goes to all my colleagues at the chair of TP4, who created a very pleasant and professional working atmosphere. I am convinced that you were instrumental in making me feel comfortable during my time as a PhD student. Especially, I want to mention Daniel Breunig, who inducted me into the world of high-performance computing in his role as TP4-IT administrator. Special appreciation also goes to our secretary Nelly Meyer, providing helpful assistance in all bureaucratic matters and immediately taking the necessary steps in urgent situations such as a forgotten re-enrollment deadline.

Last but not least, I would like to thank my entire family, but particularly my parents Brigitte and Franz Körber, and my sisters Sonja Schmitt and Susanne Schlier. With your boundless patience, you always stand behind me even in difficult times. Brigitte and Franz, you encouraged me in every decision and made my undergraduate studies in Würzburg even possible with your great support. Finally, my heartfelt gratitude goes to my girlfriend Sabine Hegwein, who accompanied me through all the good and bad times of my doctoral studies. Thank you so much for your unconditional loyalty in all circumstances.